MECHANICAL SYNTHESIS OF MAGNESIUM ALLOYS FOR HYDROGEN STORAGE

by

Luis Felipe Contreras Vásquez

A thesis submitted to
The University of Birmingham
For the degree of
DOCTOR OF PHILOSOPHY

School of Metallurgy and Materials
College of Engineering and Physical Sciences
University of Birmingham

September 2017

SYNOPSIS

Synthesis, characterisation and hydrogen sorption properties of a variety of magnesium based hydrides were investigated in this work. The structure of these composites was studied using X-ray diffraction (XRD) and Raman spectroscopy.

The thermal stability and decomposition reactions of the Mg-based hydrides was studied using differential scanning calorimetry (DSC) and thermogravimetric analysis (TGA), coupled with a mass spectrometer (MS) to determine the gaseous products released during heating. Compositional changes and reversibility were investigated in detail using in-situ XRD under Ar and H_2.

Mechanical milling of magnesium hydride (MgH_2) under Ar and H_2 resulted in a reduction of the crystallite size from 207 nm for the as received to 18 nm for 10 h milled MgH_2. For the first time was reported the effect of Raman spectroscopy on milled MgH_2 demonstrating that milled samples were Raman active. Hydrogen desorption temperatures were decreased ~120 °C (DSC) with increasing milling time (10 h), however, hydrogen capacity was decreased ~6.55 wt. % (TGA).

Hydrogenation of Li-Mg alloy was investigated via reactive milling in 100 bar H_2, after 1 h milling Li-Mg phase was hydrogenated forming LiH and MgH_2. Hydrogen desorption was observed at 250 °C (DSC), releasing 0.19 wt. % (TGA). Although, the desorption temperature was decreased, the amount of hydrogen released is insignificant and is hard to consider for on-board applications.

Mechanical milling of sodium hydride (NaH) and magnesium hydride (MgH_2) under Ar and H_2 lead to the formation of sodium magnesium ternary hydride ($NaMgH_3$). Thermal decomposition occurred at ~ 325 °C with a mass change of 5 wt. %, associated with the evolution of hydrogen.

Hydrogen desorption occurred in two-step reactions. Rehydrogenation of the $NaMgH_3$ hydride was observed at 250 °C and 10 bar H_2.

Mechanical milling of lithium hydride (LiH) substituted into $NaMgH_3$ hydride resulted in the formation of a quaternary $Li_xNa_{1-x}MgH_3$ hydride with molar compositions (x=0, 0.2, 0.5, 0.8). Thermal decomposition started at 250 °C, releasing a total amount of 5 wt% of H_2. Decomposition reactions occurred in two and three steps. Furthermore, reversibility of the main phase was achieved at 250 °C and 10 bar H_2.

Milling calcium hydride (CaH_2) and MgH_2 lead to the formation of calcium magnesium (Ca-Mg-H) ternary hydride. Hydrogen sorption characteristics showed a dehydrogenation temperature of 325 °C (DSC) with a total amount of 2.24 wt.% H_2 evolution up to 500 °C. However, dehydrogenation of CaH_2 was not completed even at 500 °C. Thermal decomposition suggested two steps reactions. Reversibility was successfully achieved at 365 °C and 10 bar H_2.

LiH and NaH were substituted into the Ca-Mg-H to form quaternary hydrides with composition $M_xCa_{1-x}MgH_4$. Hydrogen sorption properties showed desorption temperatures between 300 °C and 385°C with a maximum of 3.5 wt.% H_2 released. Thermal decomposition proceeded in three-step reaction. Nonetheless, complete dehydrogenation was not achieved.

Overall, this investigation has demonstrated for a variety of Mg-based hydrides that reducing crystallite size has a positive effect in the sorption properties, unfortunately, none of the materials and composites investigated in this work meet the targets for light-duty vehicles set out by the Department of Energy (DoE). However, other applications such as heat storage might be of interest.

ACKNOWLEDGEMENTS

First of all, I would like to thank Almighty GOD for the opportunity to be at this stage of my life, successfully accomplishing one more goal, embarking into a new dream. Thank you for the wisdom, perseverance, love and faith given through Jesus Christ and the Holy Spirit to walk firmly and not tumble. All the Glory Must be to The Lord.

Special thanks dedicated to you my beloved wife, for your patience, love, support, and sacrifices. For leaving everything and everyone behind, to help me to accomplish this degree. I can certainly say that without you by my side, I would not be able to be where I am now. Thank you for giving me the best gift one can dream of, a beautiful angel that completely changed my perception of what life is. I love you both, and I am grateful for the time, love and laughs shared with me during these years. I am blessed to have you.

Thank you to my family for the love, support, and prayers. You encouraged me to keep going forward no matter what, backed me up as a family and showed me the importance of having GOD in my life.

Thank you to my supervisor Professor David Book for his guidance and support on every stage of this work and for the opportunity to be part of the Hydrogen group at the University of Birmingham.

Thank you to Dr. Reed, Mr. Simon Cannon, Dr. Joshua Vines, Dr. Luke Hughes, Dr. Sheng Guo and all my fellows at hydrogen group, for their help and share knowledge of the equipment. Thank you for all the food shared during our social hours.

I also would like to extend my thanks to the Government of Ecuador through the SENESCYT for the grant awarded to study my postgraduate degree at the University of Birmingham.

CONTENTS

LIST OF FIGURES

LIST OF TABLES

CHAPTER I

1. INTRODUCTION

This thesis will cover the use of magnesium alloys for hydrogen storage in mobile applications. The following chapter contains the background and some context for the project.

1.1 Introduction

The XX and early XXI centuries have seen a remarkable growth of the global economies and living standards, world's population is predicted to increase to 11.2 billion by 2100. (UN, 2015). The great engine of this development has been access to energy. Nearly 80% of the energy supply has been based on fossil fuels (coal, natural gas, petroleum, and liquefied gas-oil) while the other 20% is divided between renewable energy and nuclear power (Ren 21, 2011). Increases in worldwide energy demand, and negative effects of fossil fuels (climate change related to greenhouse emissions and health problems), have led to a drive for new technological approaches and renewable sources of energy, which will reduce dependency on fossil fuels. Thus, a balance between energy production, and greenhouse gases emitted during the conversion of energy, needs to be established.

With the need for energy growing every day, there are some key factors to be considered:

- **Environmental Issues**. - Greenhouse gases emitted during the conversion of energy from fossil fuels is causing many of the environmental problems the world is now facing – including climate change (e.g. increasing global atmospheric temperatures((RSoC), 2016)), air pollution, and oil spills..
- **Dependency on fossil fuels**. - Global economy is completely dependent on fossil fuels. Recent reports from International Energy Agency (IEA) estimated that global energy demand is about to increase by a third from 2012 to 2035, considering that reserves of

fossil fuels are finite resources, there is a global need for new energy sources which can replace the current dependency on fossil fuels ((IEA), 2016)

- **High demand and Price**. - Since the beginning of the industrialisation age, energy consumption has increased day by day (BP, 2016). Heating, cooling systems, electronics, and mainly all our daily activities are based on energy consumption. The oil price fluctuation in the last 3 years, in addition to the limitation of fossil fuels reserves; estimates give an approximate of 60 years for the gas reserves, 40 years for oil reserves and 100 years for the coal reserves to run out, leads to the rise of the global concern about what options do we have to supply a greatly increasing demand for energy((EIA), 2017).

Considering the supply and environmental limitations of fossil fuels ((EF), 2010, BP, 2016), there is a need to find new ways to supply energy in an efficient and eco-friendly way. Many multinational companies in conjunction with leaders of the most developed countries have put much effort into coming up with a solution to replace the matrix of power production. Some of the most promising are:

- Enhanced solar panels (PV) with improved storage capacity and higher efficiency. There are three main PV solar cell types: Monocrystalline; more expensive but higher efficiency, typically 13-17 %, Polycrystalline; cheaper, but lower efficiency, usually 11-15 % and a system which combines one of the two previous panels with a thin-film; costly but efficiency exceeds 17 % ((DOE), 2014, Wikipedia, 2015).
- Geothermal Energy, capturing the underground energy from the Earth (Parker, 2014).
- Tidal Power, using the motion of the ocean tides, currents and waves to produce electricity with a prospective potential for future power and electricity generation (Goldman, 2012).

- Wind turbines, designed for generating power in extreme weather conditions and areas with low winds (IceWind RW/CW) (Matheson, 2014, ICEWIND, 2017).

Although, these technologies seem promising as future energy resources, each one has its drawbacks. For instance, (PV) solar panels won't be as efficient in countries where the sunlight is not constant or is very low. Besides, renewable resources (solar, geothermal, tidal, wind) depend on abundant and constant source of energy which would depend on the location of the systems. On the other hand, one of the main problems renewable energies are facing nowadays is the lack of enhanced storage systems that retain the energy produced from the sunlight, wind, waves or the earth (Pacesila et al., 2016, Sen and Ganguly, 2016, Töpler, 2016).

The production of energy from renewable sources is intermittent and depends on different ambient factors. Thus, sometimes produced energy is higher than the normal demand for consumption, other times less. If energy produced by renewable sources were to satisfy energy requirements, all these drawbacks should be overcome, and any surplus energy stored efficiently and utilised in periods of higher demand.

Hydrogen has attracted attention over the last decade as a promising candidate to substitute fossil fuels and fulfil the needs of the increasing demand of energy (Töpler, 2016). The following section summarises the pros and cons of hydrogen technology as a viable energy vector.

1.2 Hydrogen as Energy vector

Hydrogen is the simplest of all earth elements; it is made up of 1 proton and 1 electron. It is most commonly found as water, and in very small amounts in the atmosphere (Hydropol, 2017)

Hydrogen is considered a potential energy vector because of several reasons. First, its abundance. Hydrogen is the most abundant chemical substance in the universe (Palmer, 2008). Second, its oxidation only generates water as a product (e.g. in a fuel cell). Thirdly, it possesses a higher content of energy per unit mass than natural gas or gasoline (Medellín, 2006). Figure 1.1 illustrates the advantages of H_2 over traditional fossil fuels in terms of it energy per mass content: 33.3 (kWh/kg) for H_2 compared to 13.9 and 12.4 (kWh/kg) for natural gas and liquid hydrocarbons, respectively (Schlapbach and Züttel, 2001, Borgschulte et al., 2008).

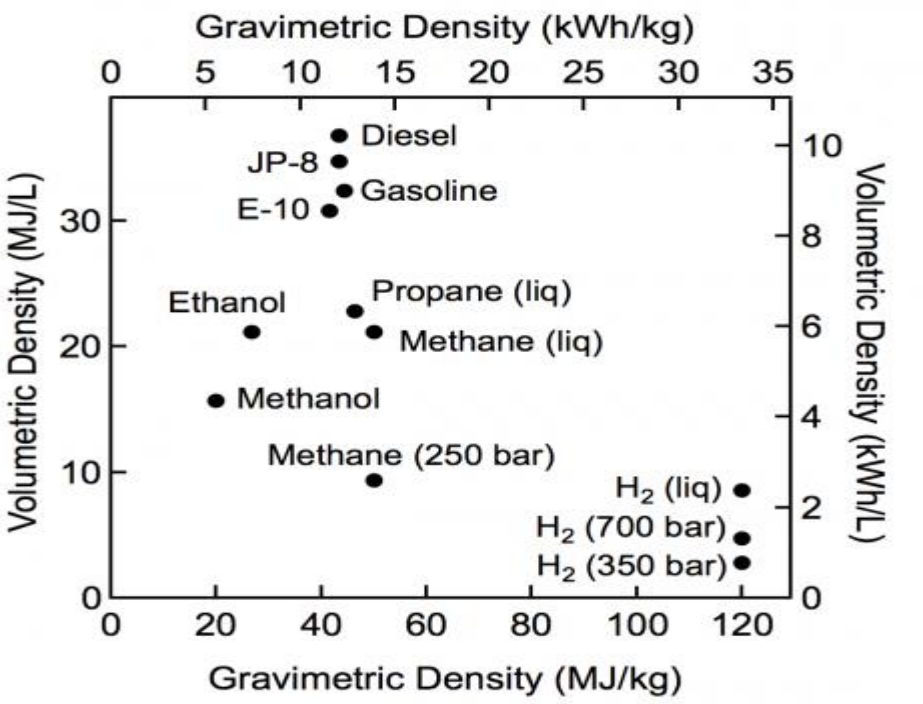

Figure 1.1 Comparison of specific energy (energy per mass or gravimetric density) and energy density (energy per volume or volumetric density) for several fuels. (Schlapbach and Züttel, 2001)

Moreover, hydrogen can be produced from renewable sources (i.e. electrolysis, biomass, PV technologies), potentially reducing the use of fossil fuels and therefore, contributing to overcome energetic and environmental issues (Turner, 2004).

Despite all the above-mentioned benefits of this technology, hydrogen energy it is not yet commercially viable due to several political, socio-economic, technological and scientific limitations which need to be overcome.

Politically and economically, replacing fossil fuels as main energy source represents a big challenge for the hydrogen technology, due to the globally well-established infrastructure around the distribution of the fuel and its derivatives. Moreover, the energy densities of the fossil fuels in terms of volumetric and gravimetric capacities are the highest known up to date. Despite those facts, countries such as Japan (Japanese National Institute of Advanced Industrial Science and Technology), the US Department of Energy (DOE) have developed hydrogen research programmes to start looking over the transition to a "hydrogen economy" ((DOE), 2006)'(Cunningham, 2006).

In terms of technology development, several problems are to be considered such as: Production – hydrogen does not naturally exist in molecular form and needs to be obtained from different sources. Although modern technologies allow the production of hydrogen using renewable sources (i.e. electrolysis, biomass, wind, solar panels) the majority of the hydrogen produced globally is obtained from fossil fuels, mainly natural gas reformation (Padró and Putsche, 1999). However, this method is the most efficient and the cheapest, hydrogen obtained from gasification is not exempt from CO_2 emissions and thus, cannot be considered as viable long-term solution.

Another known technology for hydrogen production such us the Electrolysis of water; where hydrogen and oxygen are splitted through electric current (preferably obtained from renewable energy sources), biological, high-temperature and photo-electrochemical water splitting, are available offering potential pathways into more efficient and CO_2 free hydrogen production. (Energy)

Transportation and distribution – Hydrogen is currently transported over roadways in special tanks, in liquid (-253 ^{o}C cryogenic liquid tankers) and gas (350/700 bar tube trailers), by pipeline or metal hydrides loaded onto mobile units. Nevertheless, each of these methods require special vessels (pressure proofed, insulated) influencing directly into their cost.

Therefore, for the widespread use of hydrogen, is necessary to develop new materials for lower-cost hydrogen compression/liquefaction technology and more energy-efficient innovative methods, for instance, using metal hydrides, in addition to adequate infrastructures (An, 2002, Wurster, 2002).

Storage – Gas, liquid, and in chemical compounds are the most common ways to store hydrogen. However, these methods present major disadvantages which limit its applicability; to store hydrogen gas in tanks requires extremely high pressures (at least 700 bar).

Liquid hydrogen is stored in cryogenic containers and the process of liquefaction requires a great amount of energy estimated by Peschka W. (Peschka and Peschka, 1992) of 10 kWh/kg which is around 2-3 times higher than the energy needed for compressed hydrogen.

Hydrogen can be stored in metal hydrides and reversibly obtained when needed at certain temperature and pressure. More detailed information about the different methods will be discussed further in section 1.3 and subsequent sections. However, the storage methods available nowadays do not meet the specifications for industrial applications and scaling up (Schlapbach and Züttel, 2001).

Utilization (Final use) – In terms of efficiency, simplicity and emissions in mobile applications, fuel cell technology is leading the development. Using hydrogen to achieve high performances and efficiency up to > 60 % converting chemical energy of hydrogen into electric energy without combustion giving water as by-product Figure 1.2 shows the schematic of a proton exchange membrane fuel cell (PEMFC).

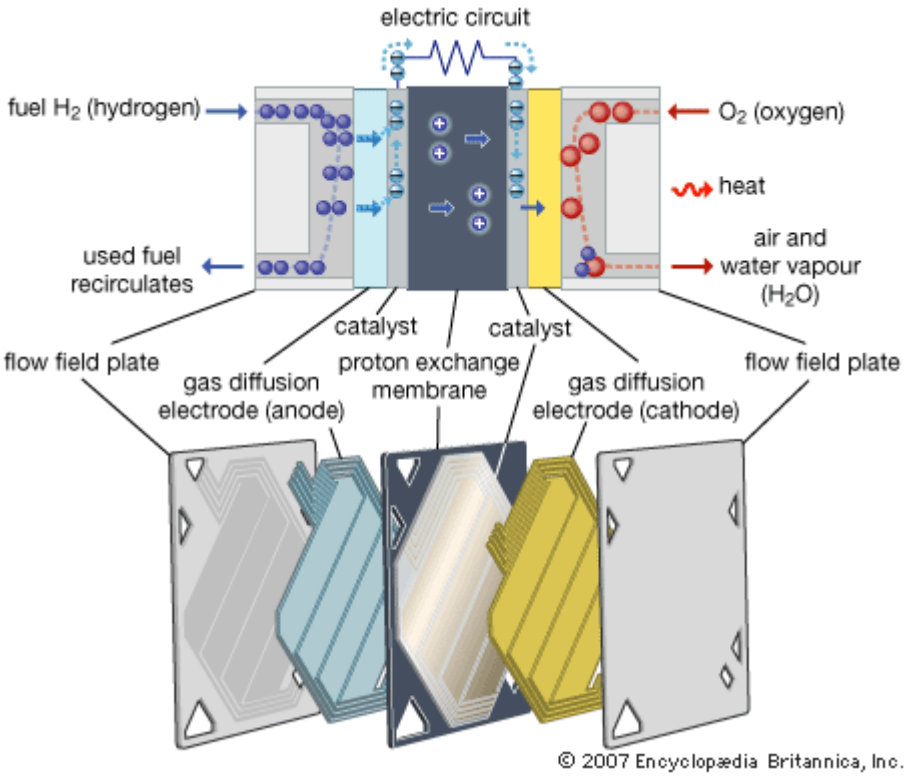

Figure 1.2 Schematic function mechanism of a PEMFC(Britannica, 2007)

Nevertheless, the main drawback of this technology is the costs that can range from £2000 kW to £7000 kW. In comparison with cheaper technologies, the costs of fuel cell technology need to be reduced to $10/kWh approximately £6/kWh by 2020 according to the DoE targets (Energy, (FCT), 2012, US Department of Energy, 2000). In addition, currently utilised fuel cells have problems such as short life, reliability, slow dynamic responses and hydrogen supply (Schmittinger and Vahidi, 2008). Another inconvenience is the lack of a safe, compact and efficient mean of storage for the hydrogen, mainly for on-board hydrogen storage in light-duty vehicles (Jorgensen, 2011).

Hydrogen storage is considered the main drawback of the hydrogen technology and all the above discussed challenges need to be overcome if we were to head towards a sustainable hydrogen economy.

1.3 Hydrogen Storage

Hydrogen is a low-density gas at room temperature (0.08 g/l at 1 bar) and has an extremely low energy per volume unit (0.003 kWh/l) making it very difficult to store. If we compare for example these values with the common used fossil fuels (i.e. natural gas 0.008 kWh/l, coal 35 kWh/l or hydrocarbons 10.5 kWh/l) we see that the quantity of energy per volume unit of hydrogen is much lower than the fossil fuels sources. Figure 1.3 shows a comparison between energy storage densities using different technologies and hydrogen.

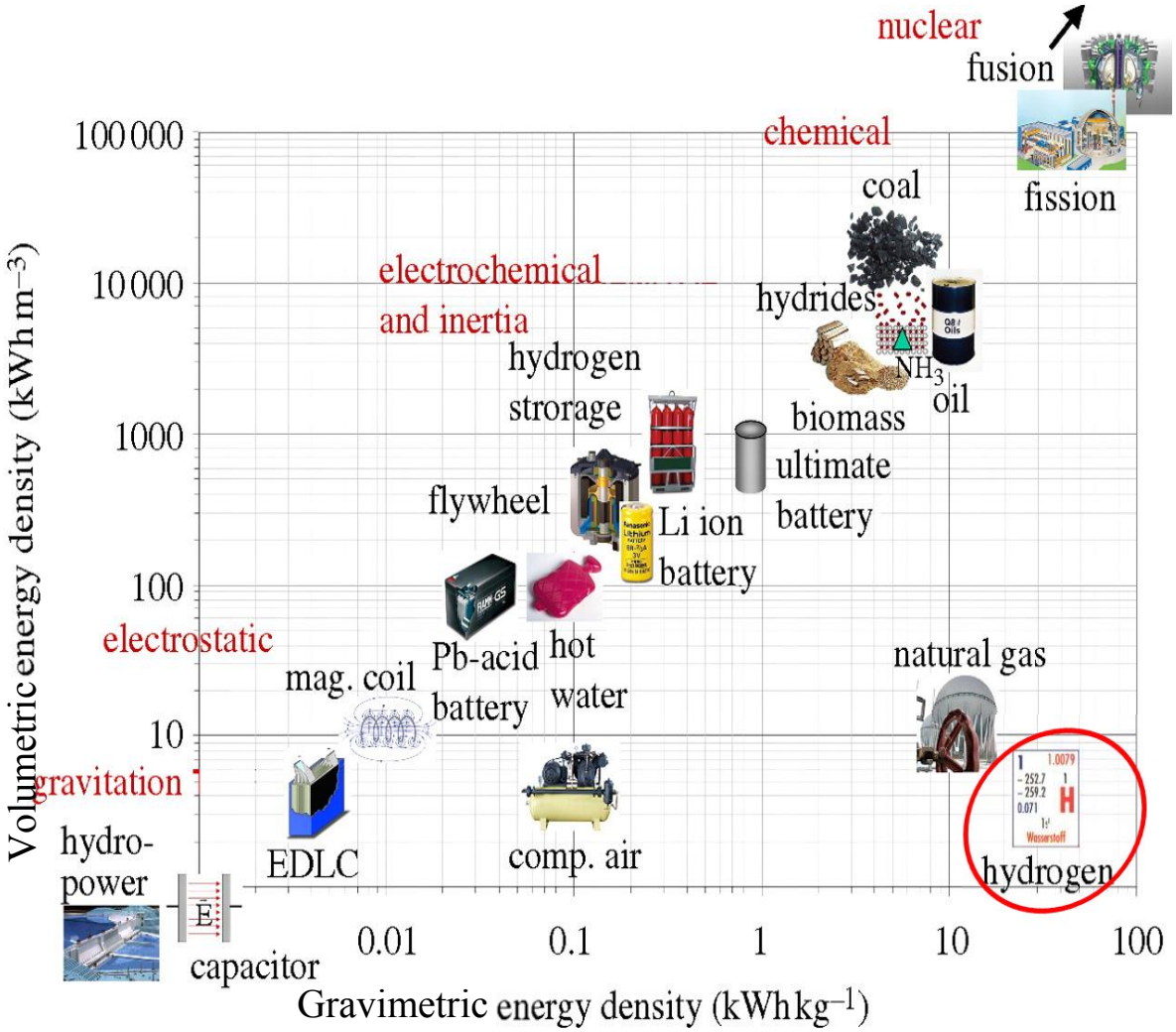

Figure 1.3 Volumetric against gravimetric energy storage densities of different energy carriers. Hydrogen shows very low volumetric density, but a very high gravimetric energy density (Züttel et al., 2010)

For example, an electric car coupled with a fuel cell can cover a range of 400 km with 4 kg of hydrogen. Nevertheless, its volume would occupy approximately 45 m^3, corresponding to a spherical balloon of approximately 5 m diameter (Schlapbach and Zuttel, 2001), which would be extremely impractical. Therefore, the development of enhanced hydrogen storage systems is a demanding and crucial task for the commercialisation of hydrogen technology. Figure 1.4 shows the volume of gas in relation to a typical car, where significant reduction in volume can be achieved by liquefying, compressing, or absorbing hydrogen.

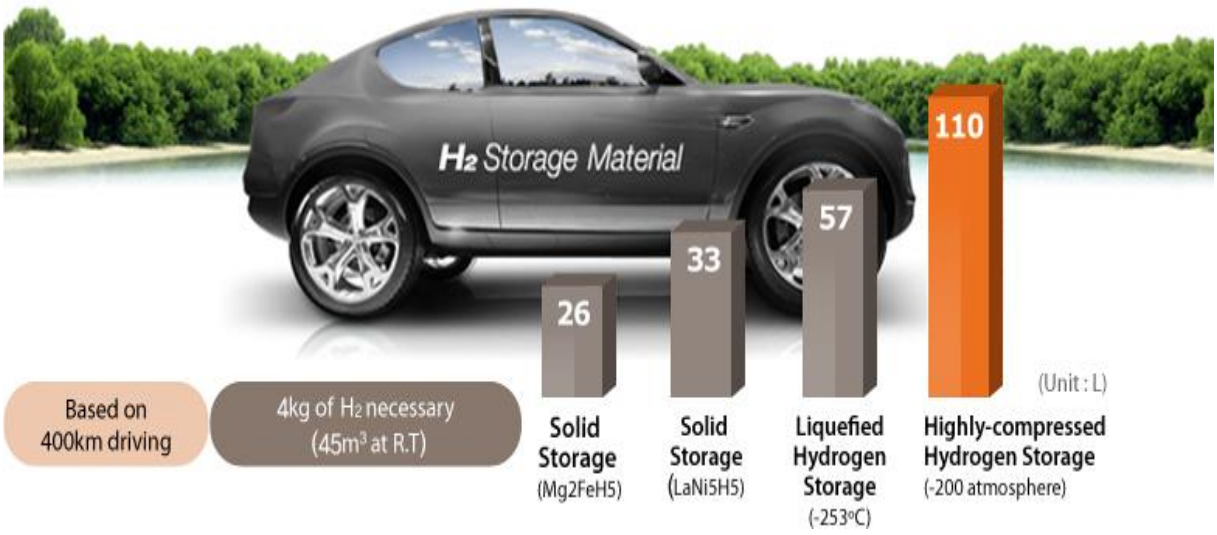

Figure 1.4 Relative volumes required to store 4 kg of hydrogen based on a 400 km driving range using different techniques (Hanwha, 2013)

The US Department of Energy (DoE) has set reference targets for on-board storage systems to be commercially feasible. Table 1.1 summarises the main criteria the system must satisfy. Unfortunately, until now none of the storage systems currently used meets these criteria. An increasing number of materials and systems for hydrogen storage are being studied (Prabhukhot Prachi and Wagh Mahesh, 2016) and developed by research groups (universities) and private industry in collaboration with governmental bodies to try to meet the set targets.

Table 1.1 Targets for on-board hydrogen storage for light duty fuel cell vehicle (DoE) *((DOE), 2012a)*

Storage Parameter	Units	2020	Ultimate
System Gravimetric Capacity Usable, specific-energy from H_2 (net useful energy/max system mass) [b]	kWh/kg (kg H_2/kg system)	1.8 (0.055)	2.5 (0.075)
System Volumetric Capacity Usable energy density from H_2 (net useful energy/max system volume) [b]	kWh/L (kg H_2/L system)	1.3 (0.040)	2.3 (0.070)
Storage System Cost	$/kWh net	10	8
	($/kg $H_{2\ stored}$)	333	266
• Fuel cost [c]	$/gge at pump	2-4	2-4
Durability/Operability			
• Operating ambient temperature [d]	°C	-40/60 (sun)	-40/60 (sun)
• Min/max delivery temperature	°C	-40/85	-40/85
• Operational cycle life (1/4 tank to full)	Cycles	1500	1500
• Min delivery pressure from storage system	bar (abs)	5	3
• Max delivery pressure from storage system	bar (abs)	12	12
• Onboard Efficiency [e]	%	90	90
• "Well" to Powerplant Efficiency [e]	%	60	60
Charging / Discharging Rates			
• System fill time (5 kg)	min	3.3	2.5
	(kg H_2/min)	(1.5)	(2.0)
• Minimum full flow rate	(g/s)/kW	0.02	0.02
• Start time to full flow (20 °C)	s	5	5
• Start time to full flow (-20 °C)	s	15	15
• Transient response at operating temperature 10%-90% and 90%-0%	s	0.75	0.75
Fuel Quality (H_2 from storage) [f]	% H_2	SAE J2719 and ISO/PDTS 14687-2 (99.97% dry basis)	
Environmental Health & Safety			
• Permeation & leakage [g]	-	Meets or exceeds applicable standards, for example SAE J2579	
• Toxicity	-		
• Safety	-		
• Loss of usable H_2 [h]	(g/h)/kg $H_{2\ stored}$	0.05	0.05

a Targets are based on the lower heating value of hydrogen, without consideration of the conversion efficiency of the fuel cell power plant.
b "Net useful energy" or "net" excludes unusable energy
c Stated ambient temperature.
d Delivery temperature refers to the inlet temperature of the hydrogen to the fuel cell.
e Hydrogen storage systems must be able to deliver hydrogen meeting acceptable hydrogen quality standards
f Total hydrogen lost into the environment as H2
g Total hydrogen lost from the storage system

Traditional storage methods are simple and well-known, high pressure gas and cylinders of liquid are commonly used in industrial facilities and laboratories to handle hydrogen. These options are mainly feasible for stationary storage of hydrogen, where the volume and weights are not a constraint, for instance in large plants.

For mobile applications (on-board storage) on the contrary to stationary storage, both weight and volume are a major restriction. Capacity and cycling under accessible conditions of 0-100 °C and 1-10 bar are the challenges to overcome in order to provide an efficient and long- term solution to the fossil fuels.

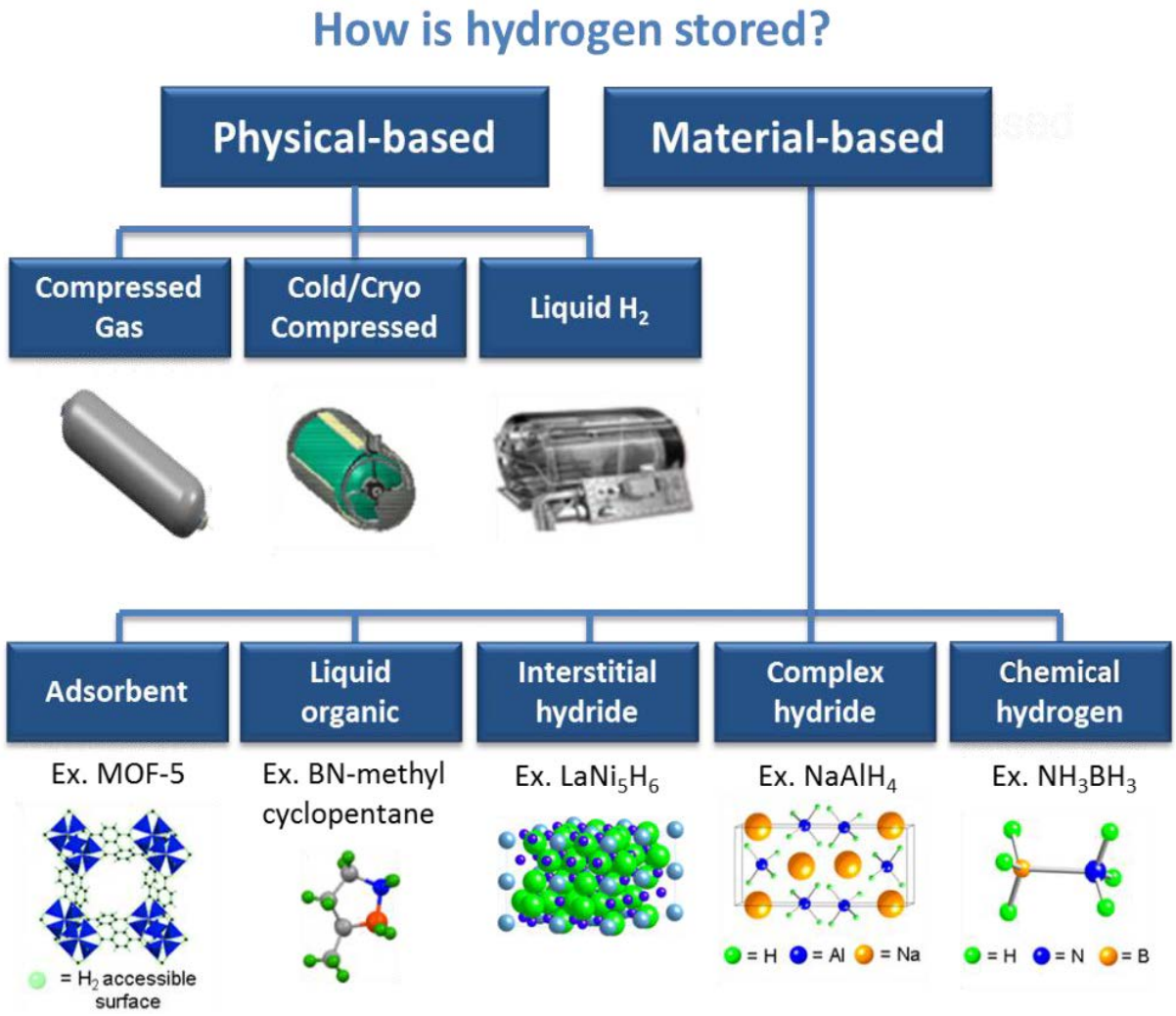

Figure 1.5 Potential storage systems that can meet the targets for on-board light duty vehicles((DOE), 2012b)

The studies of hydrogen storage systems can be divided into two main groups: 1) Physical-based storage – where liquid, compressed gas with increased hydrogen density and insulated pressure tanks may allow the DOE target to be met and 2) material-based storage – with sorbents, chemical hydrogen storage materials and metal hydrides can contribute to meet the DOE criteria. Figure 1.5 shows the different storage systems that can meet the targets for on-board light duty vehicles((DOE), 2012b).

Figure 1.6 shows current hydrogen storage systems in terms of gravimetric and volumetric hydrogen capacities being investigated. The most effective materials are the ones that have the maximum volumetric and gravimetric densities. Black and red dots correspond to the 2015 and ultimate system targets from the DOE. Whereas, the red dashed circle corresponds to the materials target, in the case of this research MgH_2. Therefore, to satisfy the ultimate system targets a material should exceed 6.5 wt% gravimetric hydrogen density, and 70 kg H_2 m^{-3}.

From Figure 1.6, it is evident that CH_4, liquefied hydrogen, $LiBH_4$ are good candidates. However, several disadvantages such as liberation of toxic gases and high operation temperatures limit the application of these compounds.

On the other hand, materials such as $BaReH_9$ and Mg_2FeH_6 present outstanding volumetric capacities although their gravimetric density does not meet the criteria for on-board applications. MgH_2 shows good volumetric capacity and the gravimetric density, therefore, this material might be potentially used for hydrogen storage applications. This thesis will focus in the study of Mg-based compounds.

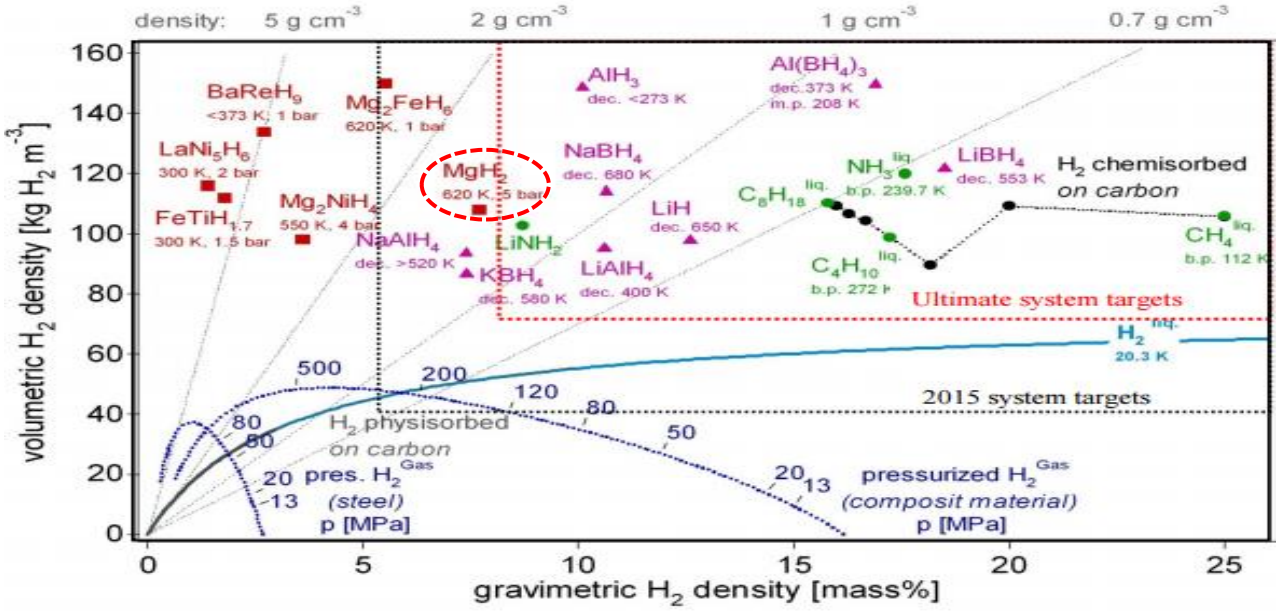

Figure 1.6 Volumetric and Gravimetric densities of a series of investigated materials for hydrogen storage. Modified from(Züttel, 2003). Red – metal hydrides. Purple – complex hydrides. Green – carbon based hydrides (Züttel, 2003). Red dashed circle – materials target

1.3.1 Physical-based storage

1.3.1.1 Compressed Gas Hydrogen Storage

Compressed gas is the most mature method for hydrogen storage due to the well-established infrastructure and development of its technology. For example, its used in the Toyota Mirai which comprises an innovative system of 2 tanks made of carbon fibre-reinforced, it can store approximately 5 kg H_2 at 700 bar with a total gravimetric capacity of 5.7 wt.% and an internal volume of 122.4 L, the refuelling time takes approximately 3 min with a driving range of 490 km(Toyota, 2015). Although, this technology is simple and well-known, safety and efficiency represent the main drawbacks.

Volumetric capacity of a 700-bar tank is 0.026 kg H_2/L, this value is significantly lower than the target proposed from the DOE 0.070 kg H_2/L(Hua et al., 2011, (DOE), 2012a). In addition,

overall efficiency of this technology is decreased by approximately 14 % at 800 bar due to the extra energy required for H_2 pressurisation(Westerwaal and Haije, 2008).

Safety concerns represent another limitation of this method given that hydrogen tanks can be highly flammable in an event of collision. Although, modern technology allowed enhancing significantly the protection of the vessels creating a 3-layer cylinders with impact resistance, safety still represents one of the biggest concerns linked with this kind of hydrogen storage (Davis, 2001)

Therefore, safety and low volumetric hydrogen density of these tanks need to be improved to comply with the ultimate targets for on-board hydrogen storage.

3.1.1.2 Liquid Hydrogen Storage

Liquid hydrogen is an alternative for storing hydrogen. Nevertheless, a substantial amount of energy around 8-16 kWh/kg H_2 is necessary to maintain the temperatures < 250 °C which is the condition for a cryogenic storage. This energy intensive process is 2-3 times more expensive than for compressed hydrogen. Moreover, it is susceptible to "boil-off" losses as a result of heat leaks when the system reaches its critical temperature. Depending on the size and shape of the storage tanks the hydrogen boils-off proportional to the surface to volume ratio. For instance double walled spherical storage tanks with a volume of 100 m^3 boils off 0.2 % of liquid hydrogen per day (Eberle et al., 2009, Wolf, 2010, Züttel et al., 2010, Züttel et al., 2011). This method is practical in aerospace applications mainly, whereas, for on-board applications becomes expensive and unlikely to achieve high efficiencies.

Recent studies have combined the compression and liquefaction methods (cryo-compressed hydrogen). This tank is volumetrically more compact than conventional comprising 0.041 kg H_2/L and a gravimetric capacity of 5.6 wt.%. Nevertheless, it has a penalty in the efficiency (41 %) which is too low to meet the DOE (60 %) specifications(Ahluwalia et al., 2010).

1.3.2 Material-based Storage

1.3.2.1 Physisorption

Physisorption consists of the interaction (physical bonding) of gas molecules (hydrogen) to the surface of a liquid or solid material at low temperatures due to van der Waals attractions. The bonding energy of these forces is very low accounting for an approximate of 6 kJ/mol H_2 which requires very low temperatures typically -196 °C (77 K)(Walker, 2008, Thomas, 2007). The most common materials employed for this kind of storage are porous materials due to the large surface areas, e.g. activated carbon; showing adsorption values of 5.5 wt% H_2 at -196 °C (Yürüm et al., 2009), carbon nanotubes, zeolites; with a maximum gravimetric storage of 2 wt. % at 16 bar (Langmi et al., 2003), and Metal-Organic Frameworks (MOFs); exhibiting a total of 7.5 wt. % H_2 capacity at -196 °C and 70 bar H_2 (MOF-177) and 34 g/L on a volumetric basis (IRMOF-20) (Rosi et al., 2003, Wong-Foy et al., 2006) .

The major advantage of this storage method is the low operating pressure, rapid sorption kinetics, and relatively low material cost and stability. Nevertheless, the small hydrogen capacity and low operation temperatures, make impractical the application of these materials for storing hydrogen.

1.3.2.2 Chemical Reactions with Water

Hydrogen is produced through the reaction of chemical compounds with water. Drawback of this method consists on the management of the by-products generated which need to be removed from the vehicle and rehydrogenated separately.

Compounds such as MgH_2 have been studied for the hydrolysis reaction, given that, when they are in contact with water form magnesium hydroxide ($Mg(OH)_2$) and hydrogen (equation 1.1) (Züttel, 2004). The maximum amount of released hydrogen obtained with through this reaction is 10.6 wt.%, although, it requires external rehydrogenation.

$$MgH_2 + 2H_2O \rightarrow Mg(OH)_2 + 2H_2 \quad (1.1)$$

Another reaction for hydrolysis considered is that of $NaBH_4$ with water as shown in equation (1.2). $NaBH_4$ can be safely delivered or stored as liquid or powder at ambient temperature (Umegaki et al., 2009). This reaction shows a high gravimetric capacity (10.9 wt. %) and rapid kinetics, however as with the magnesium hydride, rehydrogenation cannot be performed on-board limiting their commercialisation.

$$NaBH_4 + 2H_2O \rightarrow NaBO_2 + 4H_2 \quad (1.2)$$

1.3.2.3 Complex Hydrides

These materials have been extensively studied due to the high gravimetric densities (up to 18 wt.% for $LiBH_4$) (Züttel, 2003, Orimo et al., 2007). Alanates $[AlH_4]$-, amides $[NH_2]$- and borohydrides [BH4]- (Group I and II salts) in which hydrogen is covalently bonded to central atoms in complex anions are the most common examples of these hydrides. These negative charges can be compensated by cations of most alkali and alkaline-earth metals such as Li, Na, Mg(Grochala and Edwards, 2004, Nakamori et al., 2008, Orimo et al., 2007).

Complex hydrides are interesting hydrogen storage candidates, although more research is needed in terms of desorption temperatures, reversibility and release of by-product gas(es) to meet the DOE targets for on-board storage.

1.3.2.4 Metal hydrides

Metallic hydrides are the safest form of hydrogen storage. The principle of this method is that certain metals and metallic alloys have the property to form reversibly when they react with hydrogen, forming metal hydrides that decompose on heating to specific temperatures or by increasing the pressure releasing hydrogen.

The hydride forms exposing the metal to a high-pressure hydrogen atmosphere, which leads to the absorption of the hydrogen atoms into the crystal lattice. This process is shown in Figure 1.7.(Guervós Sánchez, 2003, Atkins, 2010)

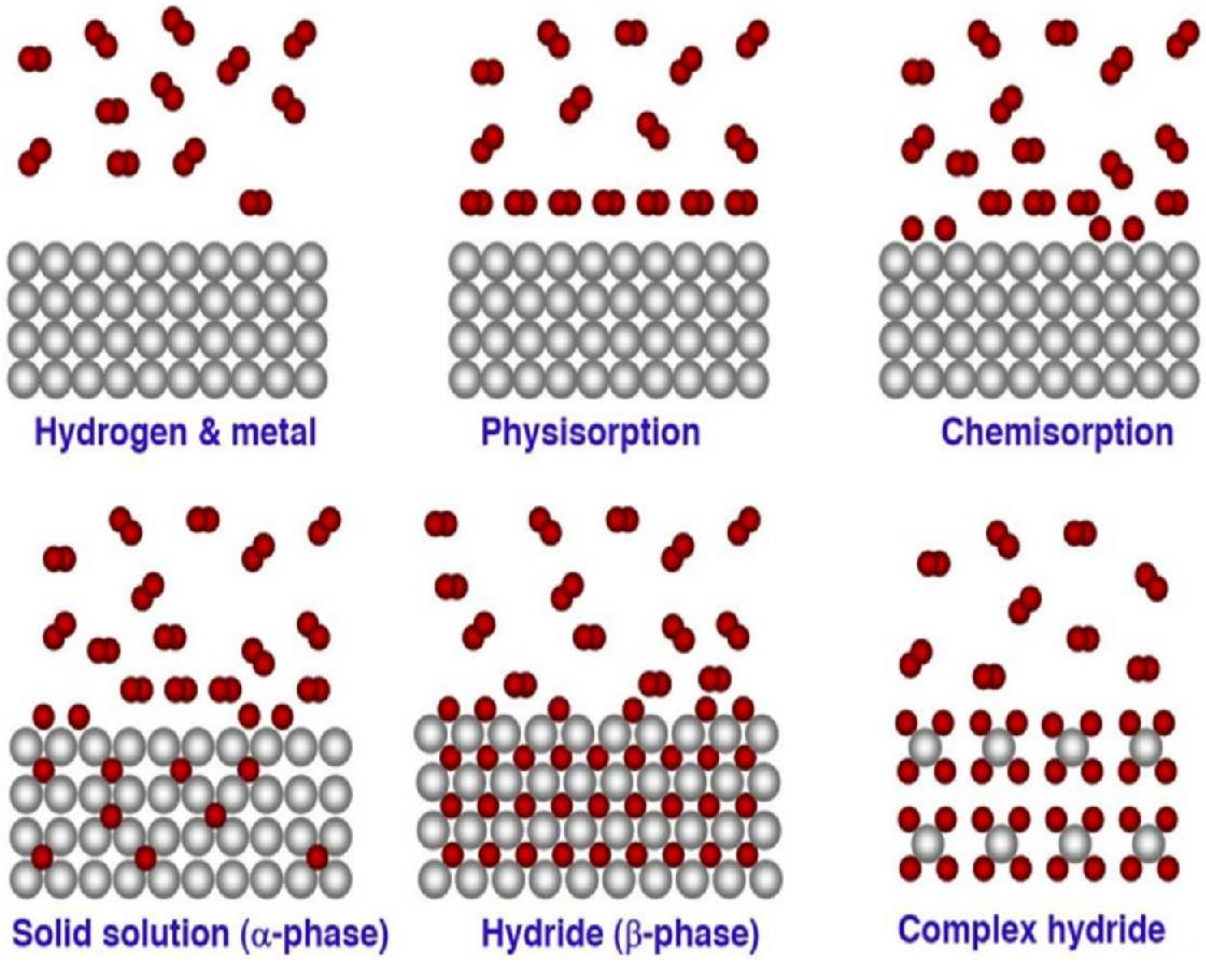

Figure 1.7 Schematic diagram of possible hydrogen bonding states in hydrogen storage materials. (Orimo et al., 2007)

The different stages involved in the hydrogen absorption process in a metal are described below:

1. Molecular hydrogen (H_2) move toward the metal surface. The interactions between the molecular hydrogen and the metal (M-H) are of van der Waals type, therefore the hydrogen molecule is physisorbed.
2. Molecular hydrogen dissociates onto the metal surface ($H_2 \rightarrow H+H$) to form a chemical M-H bond. This process is known as chemisorption and the energy required for the same will depend on the elements at the metal surface.
3. Atomic hydrogen diffuses to the interstitial sites of the metal and dissolves exothermically to form a solid solution (α-phase) at a low H concentration ($H/M<0.1$). This phase has the same structure as the host metal and can be accompanied with lattice expansion to let the hydrogen atoms accommodate in the structure (Zutel, 2003).
4. Increasing the hydrogen pressure, the hydride phase (β-phase) starts to form as more hydrogen is absorbed. This produce strong H-H interactions due to the substantial lattice expansion. This leads to a plateau region in the isotherms where both phases (α and β) coexist and the H concentration can radically increase with minor changes in the temperature or pressure. The length of the equilibrium (plateau) determined the quantity of stored hydrogen, this is of interest for hydrogen storage applications.
5. Once pure phase is achieved, the H concentration increases with the pressure. This indicates the dissolution of H into the hydride.

The **desorption** process is inverse to the above described process for absorption therefore:

1. Decomposition of the hydride phase
2. Diffusion through the metal.
3. Hydrogen atoms overstep the metal surface.
4. Hydrogen atoms recombine to form H_2 ($H+H \rightarrow H_2$)
5. Release of hydrogen.

The reaction of hydrogen with a metal/alloy (M) to form a metal hydride (MH_x) is represented by the following formula(Sandrock and Bowman, 2003):

$$M + (x/2)\ H_2 \leftrightarrow MH_x + \text{heat} \qquad (1.3)$$

The thermodynamic behaviour of a hydride can be shown by pressure composition temperature curve (PCT) analysis (Figure 1.8).

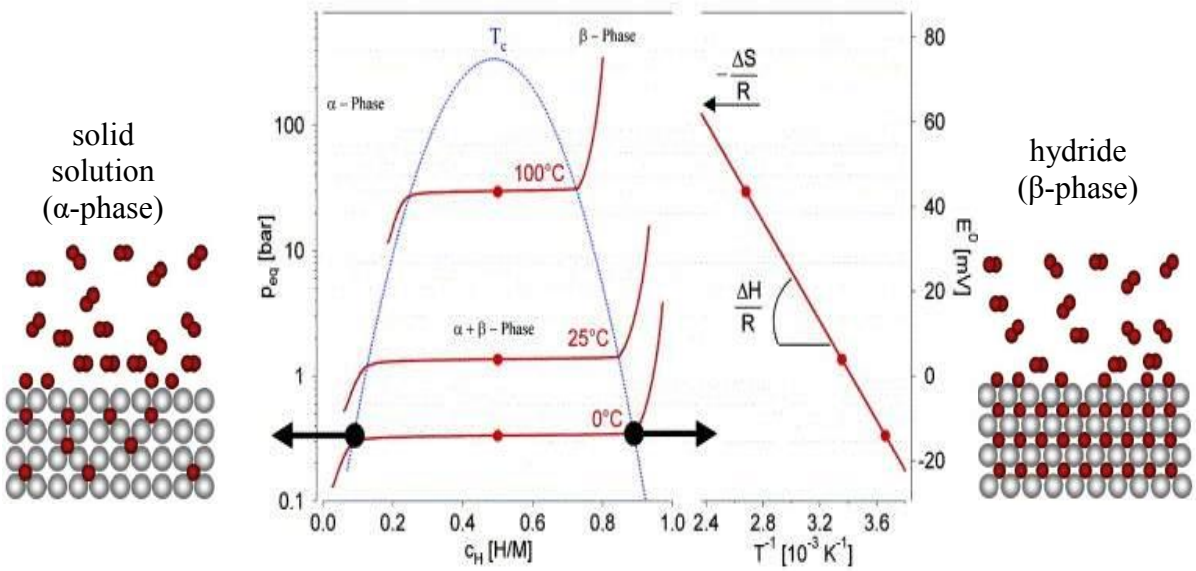

Figure 1.8 Pressure composition isotherm plot of $LaNi_5$ (left), van't Hoff plot (right) (Züttel, 2003, Guo, 2015).

From the PCT curves analysis can be inferred that the relationship between pressure (P_{eq}) at which the reaction (absorption, desorption) is produced and the temperature (T) can be expressed by the van't Hoff equation:

$$\ln P/Po = \Delta H/RT - \Delta S/R \qquad (1.4)$$

where, ΔH and ΔS are the enthalpy and entropy changes of the phase transformation, P_0 is the standard pressure of 1 bar, P corresponds to the plateau pressure at T (K) and R is the universal gas constant (8.3145 J/mol K).

Values for the enthalpy of formation for the $LaNi_5$ = -158.9 kJ/mol is negative given that the formation reaction of hydrides (absorption) is an exothermic reaction and the decomposition (desorption) of its phase is an endothermic reaction. Particularly, the enthalpy is an important measurement of the stability of the phase bonding (M-H) in the hydrides and allows the comparison with the stability of other compounds. To reach an equilibrium (plateau) pressure of 1 bar at 27 °C, ΔH should be equal to 39.2 kJ/mol H_2 (Guo, 2015, Züttel, 2003).

When thermal management is required, an important consideration is to have a small enthalpy. The lower the enthalpy, the less energy is required for the dehydrogenation of the sample. Hence, lower temperatures of desorption can be achieved.

Special attention has been paid to the intermetallic hydrides, due to their favourable kinetics, high volumetric hydrogen density and good rehydrogenation properties after several cycles at low pressure and temperature. The formation reaction of an intermetallic compound can be described as:

$$A_yB_z + xH_2 \leftrightarrow A_yB_zH_{2x} + \Delta Q \quad (1.5)$$

Where, metal A is usually a transition metal, or a rare earth metal forming a stable hydride, B is a transition metal and does not form a stable hydride but helps to catalyse the dissociation of the H_2 molecule, and ΔQ represents the released heat upon absorption of hydrogen(Züttel, 2003).

Up to the present time, MgH_2 is considered one of the most promising metal hydrides given that theoretically it can store 7.7 wt.% of H_2 and has a high energy density (9 MJ/kg) Mg(Zhu et al., 2006a). The main drawback of MgH_2 is its: high thermal stability; because of its bonding which has sometimes being described as partially covalent, requiring high temperatures for the hydrogen desorption, and slow hydrogen sorption kinetics (Sakintuna et al., 2007).

A more thorough review of MgH_2 is provided in Chapter 2.

1.4 Summary

It is important to highlight the need to develop new technologies to move away from fossil fuels dependency, this chapter contains a rapid review of some of the most promising renewable sources of energy for the future that can help on the transition to a more sustainable source of energy, to comply with increasing demand.

Hydrogen and its properties were presented as a potential candidate to a clean energy vector given that its oxidation generates as a product, only water (e.g. in a fuel cell) and because has the highest content of energy per unit mass in comparison to natural gas or gasoline. However, the main downside of hydrogen is the high cost of the technology and to overcome issues such as fossil fuels free production, transport, infrastructure (end use) and storage.

Different technologies for hydrogen storage were described, including a general review of the advantages and disadvantages. At this point, none of the current storage methods fulfil the economic and technical demands for on-board applications.

Physical methods are the most common solution for hydrogen storage, due to the simplicity and well-established infrastructure, although the space occupied by the large size tanks, the high cost of manufacturing, very high/very low pressures and safety concerns are challenges.

Material-based hydrogen storage could represent a more sustainable solution, if the targets for an improved H_2 gravimetric capacity, faster kinetics, temperature ranges and reversibility are met. In addition, the cost of manufacturing and production must be lowered.

From these material-based compounds, MgH_2 stood out as a prospective candidate to fulfil the required criteria for on-board storage in light-duty vehicles. However, slow kinetics and high desorption temperature limits its application. Therefore, this thesis will cover the investigation of Mg-based hydrides for hydrogen storage.

It is important to mention that this chapter does not represent an extensive review of all the hydrogen storage materials due to the vast of literature available on the topic and is a summary

of the most relevant materials of each method. Table 1.2 summarises the 6 hydrogen storage methods including some of the technical characteristics such as hydrogen capacity, operating temperatures and other properties.

Table 1.2 Summary of the hydrogen storage methods and some technical characteristics. Adapted from *(Pickering, 2014, Harris et al., 2004, Züttel, 2004, Züttel, 2003)*, RT means "room temperature". Values herein described correspond to the materials representing each method.

Hydrogen Storage Methods		Volumetric density (kg/m^3 H_2)	Gravimetric density (wt%)	Operating temperature (°C)	Operating pressure (bar)	High purity hydrogen	Reversibility	Remarks
Physical-based	Compressed Hydrogen	>40	13	25 (RT)	700	Yes	Yes	Simple, well stablished but needs energy and is costly
	Liquid Hydrogen	71	Tank size depending	< 250	1	Yes	Yes	Susceptible to "boil off"
	Chemical reaction with water	>150	< 40	25 (RT)	1	No	No	No direct rehydrogenation
Material-based	Physisorption	20	~1.5	-196	100	Yes	Yes	Low operation temperatures
	Complex Hydrides	150	>18*	>100	1	No	Some	high pressures required for absorption and high temperatures for desorption
	Metal Hydrides	150	~2	25 (RT)	1	Yes	Yes	low H_2 capacity (heavy metals)

CHAPTER II

2. Mg-BASED HYDRIDES

2.1 Introduction

Magnesium (Mg) and particularly magnesium hydride (MgH_2) is considered a potential candidate for hydrogen storage due to its: high gravimetric capacity (7.6 wt.% H_2); relatively good volumetric capacity (for a metal hydride, 110 kg/m^3 H_2); and reversibility. Moreover, Mg in a relatively abundant metal (8^{th} most frequent element in Earth occupying a 2.7 wt.%) and therefore its cost is relatively low ($3 per kg)(Burstow, 2002, Dornheim et al., 2007).

However, the major drawback is its high desorption temperature (over 300 °C) associated with the high stability of the Mg-H bonds, resulting in slow hydrogen sorption kinetics. Furthermore, Mg is highly reactive with air (Zaluska et al., 1999). These downsides prevent its practical application as a hydrogen storage medium. There are different studies focused on the alteration of the hydrogen storage properties by: alloying with other metals, to modify the enthalpy of hydride formation (Reilly Jr and Wiswall Jr, 1968); introducing a catalyst, to enhance the surface absorption and desorption of hydrogen (Liang et al., 1999, Grigorova et al., 2005, Barkhordarian et al., 2004, Hanada et al., 2006b); refining the microstructure by forming a thin film (Jain et al., 2010a, Schulz et al., 1999) or by mechanical milling powder in order to reduce crystallite size (Schulz et al., 1995, Zaluska et al., 1999, Suryanarayana, 2001b). Nevertheless, alloying with other metals e.g. adding Ni, usually causes a decrease in gravimetric capacity. Hence, there is a need to develop novel and enhanced Mg-based hydrides with lower stability (reduced ΔH) without substantially reducing the gravimetric hydrogen storage capacity.

2.2 Mg/MgH_2 Structures

Numerous studies regarding MgH_2 systems have been performed on the structural modification of the material. These studies have led to a more comprehensive understanding of the phase transitions involved in the formation and dehydrogenation of MgH_2.

Pure magnesium presents a hexagonal closed packed (HCP) structure corresponding to the $P6_3/mmc$ space group. Magnesium forms a hydride as shown in equation 2.1:

$$Mg + H_2 \leftrightarrow MgH_2 \quad (2.1)$$

When hydrogen starts to be absorbed by Mg a solid solution of H in Mg is formed. H atoms sit in the tetrahedral interstitial sites in the Mg lattice (up to ~0.07 at.% H at 643 °C at 1 bar pressure)(San-Martin and Manchester, 1987). When more H is absorbed, a body centre tetragonal structure with space group $P4_2/mnm$ (rutile-type TiO_2) is formed by the α-MgH_2 at low temperatures and ambient pressure(Noritake et al., 2002, Moriwaki et al., 2006).

β-MgH_2 described by Bastide et al. shows a hexagonal (pseudocubic) phase CaF_2 type structure, was first detected as a mixture with α-MgH_2 at 650 °C at 4GPa(Bastide et al., 1980). Er et al. and Vajeeston et al. suggested that β-MgH_2 may be present as a purely cubic phase, and be formed from γ-MgH_2 at ~4 GPa(Vajeeston et al., 2006, Er et al., 2010).

Experimental works reported by Vajeeston et al. and Moriwaki et al. showed the unstable orthorhombic δ-MgH_2 (Pbc_21) space group may be formed from the transition of β-MgH_2 at ~7 GPa.

γ-MgH_2 phase is orthorhombic with Pbcn space group and α-PbO_2 structure, it forms from the conversion of α-MgH_2 at high pressure of 2.5-8 GPa and temperatures ranging from 250-900 °C (Bortz et al., 1999, Bastide et al., 1980). Table 2.1 gives a summary of the different MgH_2 phases.

Table 2.1 Summary of the different MgH_2 phases experimentally determined; blue spheres show Mg atoms, Red spheres are H atoms. Modified from*(Reardon, 2014)*.

Phase Prefix	Structure Type	Space Group	Unit Cell
Alpha (α)	Tetragonal, Rutile-type TiO_2	*P4/mnm*	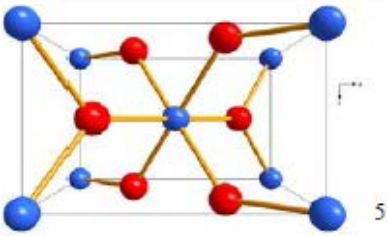
Beta (β)	Hexagonal (pseudocubic) modified CaF_2	$Pa\bar{3}$	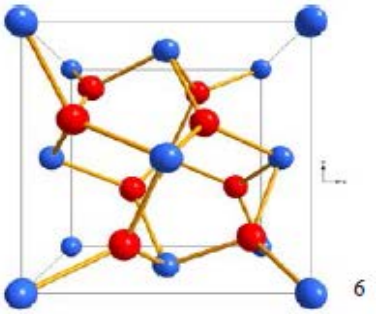
Delta (δ)	Orthorhombic	Pbc_21	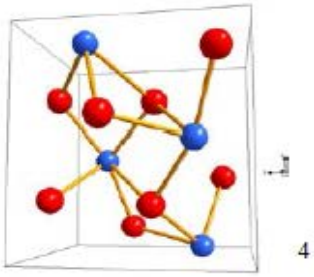
Gamma (γ) (mixture with α)	Orthorhombic α-PbO_2	*Pbcn*	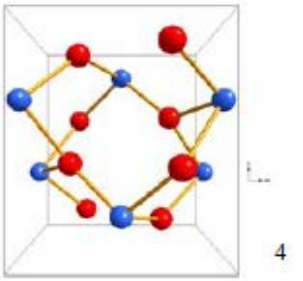

The bonding of H in MgH_2 was investigated by Noritake et al. and showed that involves a mixture of covalent and ionic bonding. Weak Mg-H and H-H covalent bonds may help the hydrogenation and dehydrogenation properties of MgH_2(Noritake et al., 2002).

2.3 Hydrogen Storage Properties

2.3.1 Kinetics

Slow absorption/desorption kinetics are one of the major issues of MgH_2, this effect is evidenced by the multiple energy barriers. For the absorption, the reaction on the surface involves: physisorption, as hydrogen molecule approaches the surface and interacts via van der Waals forces; chemisorption, in which the hydrogen dissociates into H atoms that diffuse into the metal; and hydride formation, which can be described by nucleation and growth models. The desorption process proceeds inversely to the absorption: Mg has to be nucleated and H atoms diffuse to the surface of the metal, recombining into hydrogen molecules (Dornheim et al., 2007, Martin et al., 1996). Different approaches can be taken to improve the absorption kinetics, for example: microstructural modifications such as grain and particle size reduction can reduce the diffusion path lengths for hydrogen; and/or the use of suitable catalysts to lower the surface barriers to dissociation and re-association of molecular hydrogen.

2.3.1.1 Effect of Microstructural Modification

It is has been reported that for complete hydrogenation of Mg, the particle size of the material must be < 30-50 μm (Zaluska et al., 1999). Ball milling has been used to try to modify and therefore reduce temperature of hydrogenation and/or increase sorption kinetics of MgH_2. Through ball milling: the particle and grain size can be reduced, the surface area increased, and the number of defects (which act as active sites for hydrogen absorption reactions) increased (Jain et al., 2010b). Moreover high-energy ball milling under hydrogen allows the formation of hydride phases or phase changes(Suryanarayana, 2001b).

In 1999 Huot et al. reported that after 2 h milling MgH_2, an approximate of 4 % of α-phase transformed into metastable γ-phase and reverted to α-MgH_2 after first hydrogenation(Huot et

al., 1999). Dornheim et al. milled MgH_2 for 20 h showing an estimated crystallite size of 20 nm (Dornheim et al., 2006) in comparison to the as received material (~280 nm). Significant decrease of absorption kinetics was demonstrated by Huhn et al. after annealing Mg at 300 °C, this shows a grain growth of approximately 200 nm(Huhn et al., 2005). Studies performed by Varin et al. on the effect of ball milling MgH_2 (Degussa-Goldschmidt) from 25 min to 100 h, show the changes in particles after milling obtaining smaller size particles. After 5 hours milling, the grain and particle sizes were significantly reduced from ~280 nm to ~12 nm and ~40 μm to ~1 μm, respectively. Increasing the milling time to 20 h resulted in a further grain and particle size decrease of about 10 nm and 0.6 μm. Although, some bigger particles were detected due to agglomeration, no representative lattice strain was noticed. A total reduction on the onset temperature from the DSC; performed in argon at a heating rate of 4 C/min, was achieved from 406 °C (as received MgH_2) to 342 °C (100 h milled MgH_2). A growth of approximately 53 μm was obtained without comprising the absorption kinetics (Varin et al., 2010).

One of the disadvantages of this synthesis method is the contamination of the material during the milling and handling process. Due to the high sensitivity of Mg to oxygen, MgO is typically formed on the Mg surface. This oxidation layer may affect the hydrogenation/dehydrogenation properties of the material(Fournier et al., 2002). Even though, MgH_2 kinetics have been improved, the temperature for desorption (300 °C) inhibit is practical use for on-board applications.

2.3.1.2 Catalysis and additives

Another route to enhance the sorption properties of MgH_2 is the use of suitable catalysts or additives. Several investigations have investigated the effects of additives. Liang et al studied

the catalytic effect on the reaction kinetics of MgH_2 on the base of transition metals as Ti, V, Mn, Fe and Ni elements. MgH_2–Ti presented the best results in terms of absorption kinetics at 250 °C, whereas, the lowest desorption temperature was attained with the MgH_2–V at 200 °C (Liang et al., 1999). Moreover, Oelerich et al. investigated the effect of adding 5 mol % V_2O_5 on the MgH_2 and obtained desorption rates of about 8 times faster those for the pure material (Oelerich et al., 2001).

Further studies have demonstrated hydrogenation at room temperature absorbing a total of 4.5 wt % H_2 at pressure <10 bar within 15 seconds when milling MgH_2 with 1 mol % Nb_2O_5 additive for 20 h and a total of 5.3 wt. % H_2 desorption at 160 °C after 100 min(Hanada et al., 2006a).

Another additive with comparable effects (Figure 2.1) was reported by Cui et al. on the base of Mg coated with multivalence Ti catalysts, reaching a total desorption of 6.7 wt. % H_2 within 15 min at 250 °C as shown in figure 2.2(Cui et al., 2013).

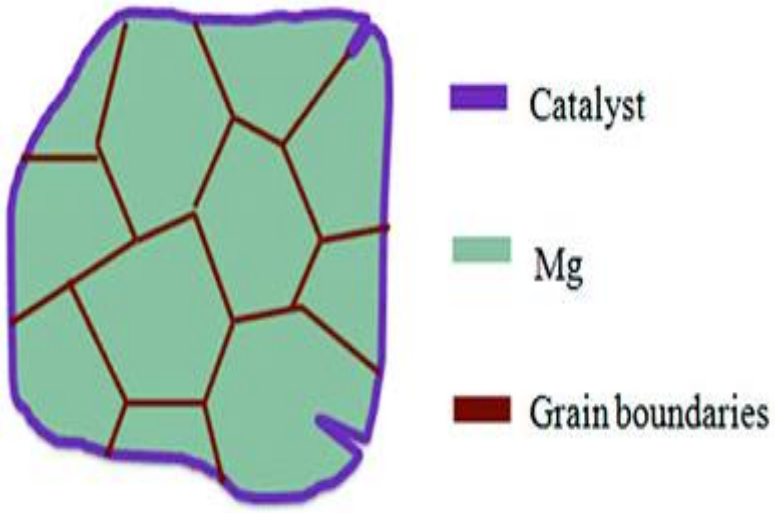

Figure 2.1 Schematic structural illustration of catalyst layer covered on Mg particle. Reproduced from(Cui et al., 2013)

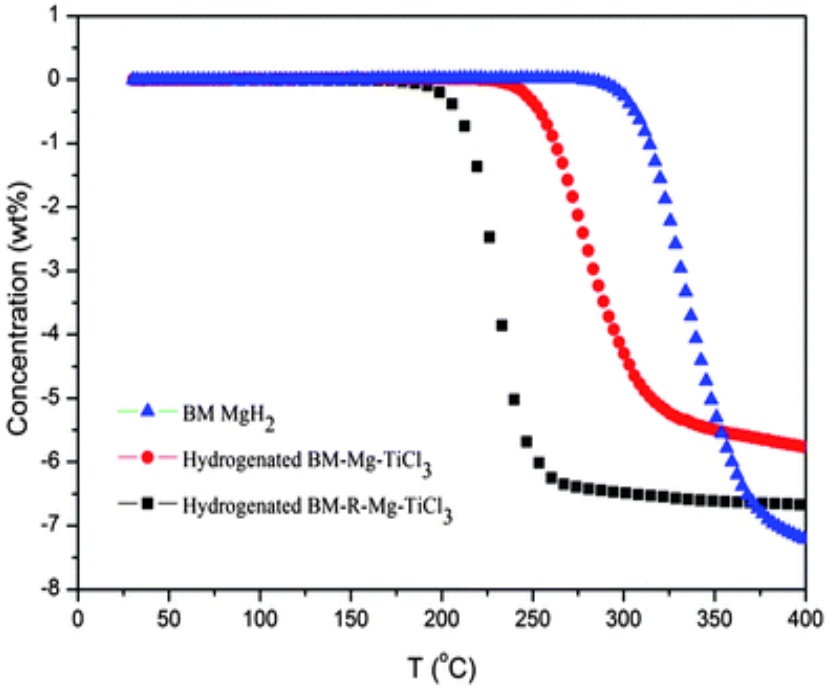

Figure 2.2 Temperature-Programmed Desorption (TPD) profiles for the ball-milled MgH_2 in Ar at a heating rate of 5 °C/min, fully hydrogenated BM-R sample and BM sample. Reproduced from*(Cui et al., 2013)*.

In conclusion, it has been evidenced that hydrogen sorption kinetics in Mg has been improved by the methods explained in the above review. However, the thermodynamic properties are still a constraint for the practical application of the MgH_2 and need to be thoroughly studied.

2.3.2 Thermodynamic behaviour

There are plenty of suitable hydride candidates with the capacity to absorb/desorb hydrogen at ambient conditions. However, all the hydrides with high gravimetric capacities show poor reversibility or need extremely high hydrogen pressures. Moreover, they are too stable. The acceptable value of reaction enthalpy has been established between 20 and 30 kJ/mol H_2. (Paskevicius et al., 2010) Therefore, the alteration of thermodynamic properties is a key point for the implementation of light-weight hydrides as hydrogen storage materials. Figure 2.3 show hydrides with high gravimetric capacities plotted against their hydrogen reaction enthalpies.

For the purpose of this thesis we will refer to the investigations of MgH_2, the other M-H compounds are beyond the scope of this work, and its properties will not be studied. Thermodynamic properties of MgH_2 have been exhaustively researched using different methods and models(Zhao-Karger et al., 2010, Bogdanović et al., 1999a, Bououdina et al., 2006, Paskevicius et al., 2010, Shevlin and Guo, 2013, Vajo et al., 2007).

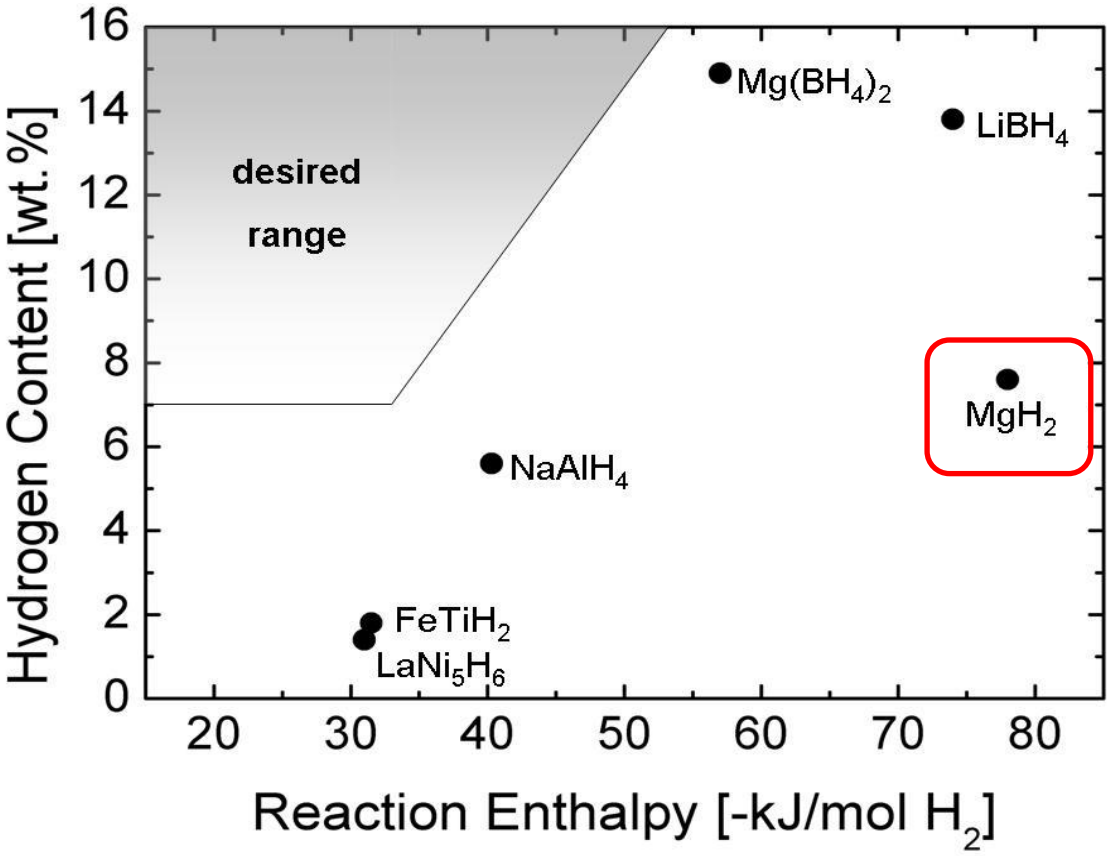

Figure 2.3 Theoretically achievable reversible storage capacities and reaction enthalpies of selected hydrides. $LaNi_5H_6$ and $FeTiH_2$ are taken as examples for conventional room temperature hydrides. The reaction enthalpies and achievable hydrogen storage capacities are ΔH = -31 kJ/mol H_2, $C_{H,max}$ = 1.4 wt.% for $LaNi_5H_6$ and for the Fe-Ti system ΔH = -31.5 kJ/mol H_2, $C_{H,max}$ = 1.8 wt.%(average over two reaction steps with $\Delta H(FeTiH_2)$ = -28 kJ/mol H_2 and $\Delta H(FeTiH)$ = -35 kJ/mol H_2 respectively)(Buchner and Povel, 1982). The respective values for $NaAlH_4$ are ΔH = -40.5 kJ/mol H_2, $C_{H,max}$ = 5.6 wt.%(average over two reaction steps with $\Delta H(NaAlH_4)$ = -37 kJ/mol H_2 and $\Delta H(NaAl_3H_6)$ = -47 kJ/mol H_2 (Bogdanović et al., 2009) , for MgH_2: ΔH = -75 kJ/mol H_2 and $C_{H,max}$ = 7.6 wt.%(Lu et al., 2009), for $LiBH_4$: ΔH = -74 kJ/mol H_2 (Mauron et al., 2008) and $C_{H,max}$ = 18.5 wt.%, for $Mg(BH_4)_2$: ΔH = -57 kJ/mol H_2 (Li et al., 2008) and $C_{H,max}$ = 14.9 wt.%. Reproduced from (Dornheim, 2011)

Thermal stability of the hydride is one of the main characteristics that need to be modified in order to enhance MgH_2 desorption temperatures. Hence, enthalpy of decomposition needs to be lowered, the aim is to find a reversible material under ambient temperature and pressure.

The enthalpy of formation of MgH_2 was reported to be ΔH_f = -75 kJ/mol H_2 and the entropy ΔS_f = 132.2 J K^{-1} mol^{-1} H_2 (Bogdanović et al., 1999b). However, the dissociation and recombination of H_2 molecules at its surface are rather poor and must follow a solid-state diffusion mechanism, resulting in a high desorption temperature.

The formation of alloys with different stabilities is one of the most common ways of modifying the thermodynamics of MgH_2. The reaction enthalpy can be lowered by destabilising the hydride state or stabilising the dehydrogenated state (Figure 2.4 a). Thus, the reaction enthalpy is increased by stabilising the hydride and/or destabilising the dehydrogenated state as shown in Figure 2.4 b (Dornheim, 2011).

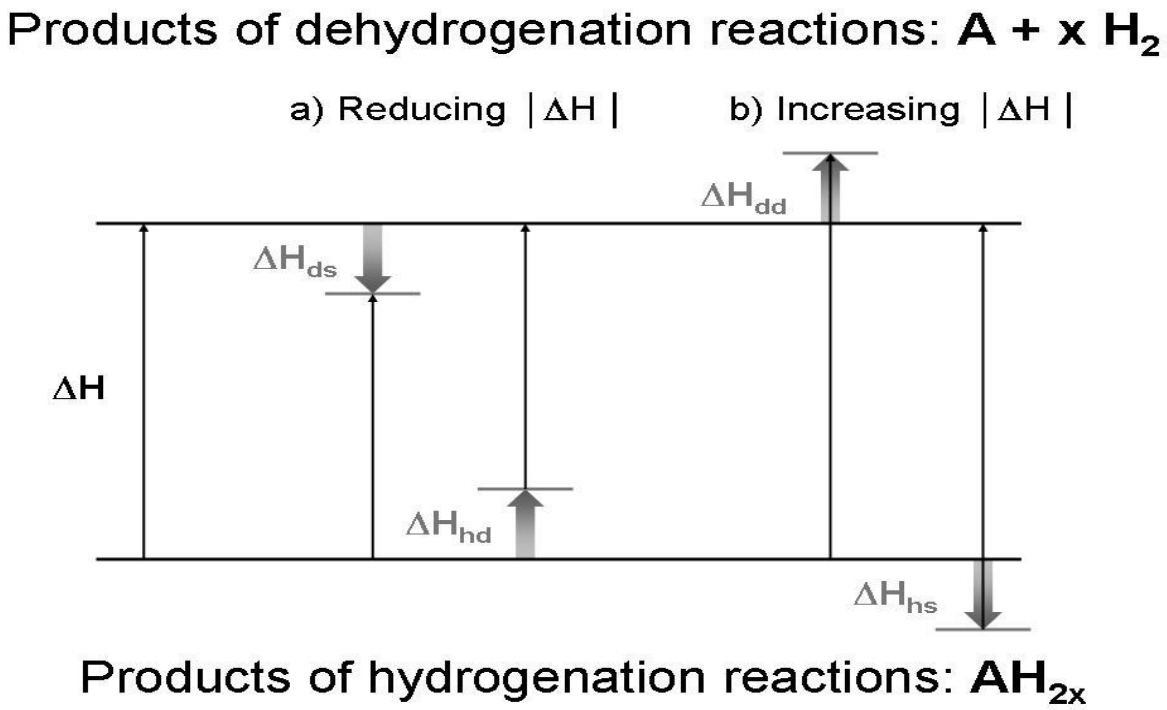

Figure 2.4 Modification of the thermodynamic properties of M-H by altering the stability of the hydrogenated or dehydrogenated state. Reproduced from *(Dornheim, 2011)*.

From the most representative metal hydrides with thermodynamic modifications Mg-Ni stood out as potential hydrogen storage system. Reilly et al. reported that Mg_2NiH_4 shows an enthalpy of formation equal to -64 kJ/mol H_2 with a desorption temperature of ~240 °C. This temperature is much lower than the 300 °C required for the pure MgH_2. Nevertheless, there is a penalty in the gravimetric capacity which is reduced to 3.6 wt. % H_2 (Reilly Jr and Wiswall Jr, 1968). Klassen et al. substituted the Ni by Cu and achieved a further reduction in the desorption temperature of about 10 °C for the $Mg_2Ni_{0.5}Cu_{0.5}$ hydride in comparison to the Mg_2NiH_4 (Klassen et al., 2001).

Darnaudery et al. and later Tsushio et al. reported similar stabilities to those of Mg_2NiH_4 in quaternary hydrides formed with transition metals $Mg_2Ni_{0.75}M_{0.25}$ were M= (V, Cr, Fe, Co, and Zn) and M= (Cr, Fe, Co, Mn) respectively. The reaction enthalpy was decreased to -50 kJ/mol H_2. However, a very low gravimetric capacity was obtained from those hydrides accounting for about 0.9 wt % H_2 ($MgNi_{0.86}Cr_{0.03}$) (Darnaudery et al., 1983, Tsushio et al., 1998).

Room temperature hydrogen desorption was accomplished by Terashita et al. studies in the $(Mg_{1-x}Ca_x)Ni_2$ (x=0.32) compound. The enthalpy and entropy of this hydride was determined to be equal to ΔH=-37kJ/mol H_2 and ΔS= -94 J K^{-1} mol^{-1} H_2. Unfortunately, the hydrogen storage capacity is limited to 1.4 wt % H_2 (Terashita et al., 2001).

Klassen et al. investigated the effect of milling MgH_2 with elemental metals (Al, Si, Ca, Co, Cu). The formation of new phases was detected only on compounds mixed with Si and Cu. Nevertheless, due to the compact structure of these hydrides high temperatures and pressures (>300 °C, >50 bar H_2) were required for dehydrogenation (Hannink and Hill, 2006).

MgCa has been studied due to the favourable Laves crystal structure, giving a formation enthalpy of ΔH_f = -42 kJ/mol H_2 (Dornheim et al., 2007). However, very stable Ca phases due to the CaH_2 formation limit the reversibility and desorption under moderate conditions.

2.3.3 Ternary Hydrides

Ternary metal hydrides have been of interest for advanced hydrogen storage systems, a promising route to lower the reaction enthalpies of MgH_2 is to mix the hydride with alkali/alkaline-earth metals (Gingl et al., 1992a, Gingl et al., 1992b). Table 2.2 summarises the different group of ternary hydrides that can be formed from literature reviews.

From Table 2.2 was observed there are a vast number of synthesised and characterised Mg-based ternary hydrides comprising alkali/alkaline-earth metals. However, the relatively low hydrogen capacity (except for the underlined hydrides), and the high temperature required for desorption (~400 °C) reduce its applicability for hydrogen storage.

For the purpose of this thesis Mg-based ternary hydrides mixed with LiH, NaH, CaH_2 will be investigated due to their light weight and potential hydrogen capacity. A brief review of the most important properties of each of these mixtures will be given below.

Table 2.2 Summary of the different group of ternary hydrides that can be formed from literature reviews.

Compound	Structure	Space group	Theor. H_2 (wt%)	g H_2/L
$NaMgH_3$	Orthorhombic	*Pnma*	6	88.3
$KMgH_3$	Cubic	*Pm-3m*	4.6	77.1
K_2MgH_4	Tetragonal	*I4/mmm*	3.8	59.9
$RbMgH_3$	Hexagonal	*P6$_3$/mmc*	2.7	69.7e
Rb_2MgH_4	Orthorhombic	*Pnma*	2	45.5
Rb_3MgH_5	Tetragonal	*I4/mcm*	1.8	42.7
$Rb_4Mg_3H_{10}$	Orthorhombic	*Cmca*	2.4	56.9
$CsMgH_3$ (hp) [a]	Trigonal	*R-3m*	1.9	60
$CsMgH_3$ (lp)	Orthorhombic	*Pmmn*	1.9	56.9
Cs_2MgH_4 (hp) [a]	Tetragonal	*I4/mmm*	1.2	48.5
Cs_2MgH_4 (lp)	Orthorhombic	*Pnma*	1.4	40
Cs_3MgH_5	Tetragonal	*I4/mcm*	1.2	37.1
$Cs_4Mg_3H_{10}$ [a]	Orthorhombic	*Cmca*	1.6	52.7
$Ca_4Mg_3H_{14}$	Hexagonal	*P-62m*	5.7	98.9
$Ca_{19}Mg_8H_{54}$ [a]	Cubic	*Im-3*	5.4	100.9
$SrMgH_4$	Orthorhombic	*Cmc2$_1$*	3.5	88.5
$Sr_2Mg_3H_{10}$	Monoclinic	*C2/m*	3.9	95.1
Sr_2MgH_6 [a]	Trigonal	*P-3m1*	2.9	91.3
Ba_2MgH_6	Trigonal	*P-3m1*	2	78.3
$Ba_2Mg_3H_{10}$	Monoclinic	*C2/m*	2.8	86.5
$Ba_6Mg_7H_{26}$	Orthorhombic	*Immm*	2.6	83.7

hp = high-pressure modification; *lp* = low-pressure modification; *a* = synthesized under high hydrostatic pressure.

2.3.3.1 Na-Mg-H (Sodium Magnesium Hydride)

Sodium Magnesium Hydride $NaMgH_3$ has been extensively researched both experimentally and through theoretical modelling (Bouamrane et al., 2000, Bouamrane et al., 2001, Rönnebro et al., 2000, Ikeda et al., 2005a, Fornari et al., 2007, Ikeda et al., 2007a, Ikeda et al., 2007b, Komiya et al., 2008, Vajeeston et al., 2008, Bouhadda et al., 2010, Pottmaier et al., 2011, Reardon et al., 2013, Chaudhary et al., 2015). The interest of this material lies in its ability to

store 6 wt. % H_2 that can be reversibly formed under certain conditions of temperature and pressure (Ikeda et al., 2005a). The synthesis and characterisation of this compound was first reported by Bouamrane et al. through a reaction of a mixture of Mg and NaH at 480 °C for 24 hours under 10 bar H_2 pressure (Bouamrane et al., 2000). Further investigations lead by Ikeda et al. reported the synthesis of $NaMgH_3$ hydride through mechanical milling MgH_2 and NaH for 20 h under a hydrogen atmosphere (Ikeda et al., 2005a). Experimental investigations, showed that $NaMgH_3$ is able to desorb approximately 6 wt. % H_2 at 400 °C running in an argon atmosphere at a heating rate of 5 °C/min. Dehydrogenation proceeded via a two-step reaction as shown in equation 2.2 and 2.3. Furthermore, it was able to reabsorb hydrogen from the decomposed phases of Mg and Na under 10 bar H_2 pressure and 400 °C.

$$NaMgH_3 \rightarrow NaH + Mg + H_2 \quad (2.2)$$

$$NaH + Mg + H_2 \rightarrow Na + Mg + 3/2H_2 \quad (2.3)$$

More recent investigations reported by Pottmaier et al. confirmed the formation of $NaMgH_3$ ternary phase via mechanical milling NaH and MgH_2 for 5 h under 10 bar hydrogen where the two-step desorption was confirmed by DSC and in-situ XRD techniques. Rehydrogenation of the decomposed NaH and MgH_2 was detected at 350 °C and 5 bar H_2 (Pottmaier et al., 2011). Later, Reardon et al. described the facile synthesis of $NaMgH_3$ via reactive milling for 5 h under a nitrogen atmosphere, dehydrogenation was accomplished via a two-step reaction, and a total of 4.7 wt. % H_2 was desorbed at 372 °C (Reardon et al., 2013).

Although, $NaMgH_3$ shows a high capacity to desorb hydrogen and good reversibility, desorption temperatures (400 ^oC) remain high in comparison to catalysed MgH_2 (200 ^oC), therefore, to be considered as a potential hydrogen storage candidate, temperature of decomposition need to be reduced. A more comprehensive study of this material will be covered in Chapter 6.

2.3.3.2 Ca-Mg-H (Calcium Magnesium Hydrides)

The study of the ternary hydrides $Ca_{19}Mg_8H_{54}$ (cubic) and $Ca_4Mg_3H_{14}$ (hexagonal) was reported due to its relatively high hydrogen storage capacity (5.4 and 5.7 wt. % H_2 respectively)(Nomura et al., 1978, Gingl et al., 1992a, Huang et al., 1992a, Nesper and Miller, 1993, Huang et al., 1995a, Bertheville and Yvon, 1999, Nobuki et al., 2007, Asano et al., 2009, Sartori et al., 2009, Reardon, 2014). Ternary Ca hydrides with group I, (e.g. Li, Na, K) were also investigated (Vajeeston et al., 2010, Bouamrane et al., 2001). Work on $CaLi_2$ alloys demonstrated that no ternary Ca-Li hydride phase could be detected. Nevertheless, it was reported that the diffusion of Li into the systems allows a faster hydrogenation of the Ca and Li to form the respective hydrides (Liu et al., 2009). More recent studies, reported the synthesis and structures of alkali metal hydrides type $MCaH_x$ where M= Li, K, Na, Rb, Cs using high pressure sintering methods under H_2 (~95 bar) (Matar et al., 2011, Vajeeston et al., 2010). Ca-Mg hydrides have been synthesised from $CaMg_2$ alloy at direct high-pressure (~90 bar) and temperature (465 °C) and from the reaction of the CaH_2 and MgH_2 using the same conditions as above, forming $Ca_4Mg_3H_{14}$ and $Ca_{19}Mg_8H_{54}$ (Gingl et al., 1992a, Bertheville and Yvon, 1999). The ternary phase $Ca_4Mg_3H_{14}$ was described for the first time by Gingl et al. in a mixture of Mg, MgH_2 and CaH_2 under high pressure (~53 bar) and high temperature (~410°C) for 6 days (Gingl et al., 1992a). Later, Yvon and Bertheville defined the $Ca_{19}Mg_8H_{54}$ ternary phase in a mixture of CaH_2 and MgH_2 (2:1 ratio) in a multi-anvil cell for 3 h which was iso-structural to $Yb_{19}Mg_8D_{54}$ (Bertheville and Yvon, 1999).

Further investigations on the ternary hydride systems comprising Ca-Mg hydrides performed by Santori et al. showed the formation of $Ca_{19}Mg_8H_{54}$ and $Ca_4Mg_3H_{14}$ phases from their work on Mg-Al-Ca-H system by reactive ball milling; but never as a single phase (Sartori et al., 2009).

Reardon et al. reported the mechanochemical synthesis of Ca-Mg-H via mechanical milling CaH_2 and MgH_2 for 5 h under a nitrogen atmosphere. The investigations revealed that smaller atoms such as Li and Na might be inserted into the Ca-Mg-H system facilitating the hydrogenation and dehydrogenation of the same(Reardon, 2014).

Although there are reports on the synthesis and formation of Ca-Mg-H ternary hydrides, there is very little information on the dehydrogenation reactions and reversibility, key aspects to consider for hydrogen storage applications(Huot et al., 2003). Moreover, the relatively low gravimetric hydrogen capacity (< 5 wt. %) limits its applicability for mobile applications.

In this thesis, (chapter 8) will cover the synthesis, hydrogen sorption properties and reversibility of Ca-Mg-H ternary hydrides via mechanical milling.

2.3.3.3 Li-Mg-H (Lithium Magnesium Hydrides)

Li-Mg-H systems are interesting candidates for hydrogen storage due to their high theoretical gravimetric hydrogen density. Theoretical approaches predict the formation of two possible phases $LiMgH_3$ and Li_2MgH_4 with a theoretical H_2 capacity of 8.8 and 9.5 wt. % respectively(Vajeeston et al., 2008, Li et al., 2011). For instance, Chen et. al. through first principle methods (computational method), predicted the thermodynamic stability of both mixtures ($LiMgH_3$, Li_2MgH_4) at room temperature. Many attempts have been performed to try to synthesize this ternary hydride using various methods and techniques(Ikeda et al., 2005b, Vajeeston et al., 2008, Smith et al., 2010, Li et al., 2011, Guo, 2015, Pfrommer et al., 1994). However, to date, none of the experimental studies have been able to synthesise these predicted hydrides.

Ikeda et al.(Ikeda et al., 2005b) attempted to synthesise the Li-Mg-H hydride via mechanical milling LiH and MgH_2 under H_2 for 20 h. However, after the characterisation of the milled

material no traces of the targeted ternary phase was found. Later, Vajeeston et al.(Vajeeston et al., 2008), Pfrommer et. al(Pfrommer et al., 1994) and Li et al.(Li et al., 2011) predicted a trigonal structure with an R3c space group ($LiTaO_3$–type) for the $LiMgH_3$ ternary hydride, and an orthorhombic with a Pbam space group (Na_2MgCl_4-type) for the Li_2MgH_4 hydride from computational methods (first principle methods). It was found that the synthesis from MgH_2 and LiH is not stable and therefore not energetically favourable.

Further research carried out by Li et al.(Li et al., 2011) Attempting to insert H atoms into the ordered sites of Mg-Li phases to synthesise the ternary hydride were not successful. Recent studies by Smith et al.(Smith et al., 2010) found that Li-doped MgH_2 at any Li concentration is thermodynamically metastable with respect to the separation into LiH and MgH_2. Guo (Guo, 2015) reported the hydrogenation of Li-Mg ribbon (composition of 97 at% Li and 3 at% Mg) into LiH and $Mg_{(1-x)}Li_xH_2$ (x = ~0.04) using high pressure milling. Furthermore, decomposition of Li-Mg hydrided samples was described and a hydrogen desorption temperature was lowered from 900 to 470 °C.

Li-Mg-H could be a potential candidate for hydrogen storage given that Li and Mg are light-weight metals with high hydrogen capacity. Nevertheless, to date, there are only theoretical predictions of the $LiMgH_3$ and Li_2MgH_4. These phases have not yet been reported to have been experimentally synthesised.

Chapter 5 of this research shows the experimental investigation of Li-Mg-H hydride synthesis and hydrogen sorption properties of the ball milled Li-Mg ribbon.

2.3.4 Destabilisation of ternary hydrides by light-weight metals substitution.

The addition/substitution of light-weight metals into ternary hydrides has been proven to destabilise the desorption temperature of the ternary hydrides. Among the light-weight materials from the periodic table of elements, in this thesis Li and Na metals were chosen due to its atomic weight and potential gravimetric capacities when substituted into the ternary hydrides. There are plenty of information on substituted materials into ternary hydrides to enhance the hydrogen sorption properties for hydrogen storage applications.(Kohno et al., 2000) However, this work will focus in the Li substitution into Na-Mg-H and Ca-Mg-H ternary phases. Moreover, the studies of the Na substitution into the Ca-Mg-H are included.

2.3.4.1 Li substitution into Na-Mg-H hydride

The formation ability of $Li_xNa_{1-x}MgH_3$ (x= 0, 0.5 and 1) was first reported by Ikeda et al.(Ikeda et al., 2005b). The hydride system was obtained via reactive milling LiH, NaH and MgH_2 under H_2 for 20 h, where was found that the diffraction peaks of the structure shifted to higher angles due to the partial substitution of Na by Li. Later on, the same authors suggested that Li substitution into $NaMgH_3$ could lower the desorption temperature of the ternary compound $NaMgH_3$(Ikeda et al., 2007b).

DFT calculations carried out by Xiao et al.(Xiao et al., 2009) on the thermodynamic properties of the quaternary $Li_xNa_{1-x}MgH_3$ hydride predicted that Li substitution into $NaMgH_3$ composite will have a favourable destabilising effect due to the smaller ionic size of Li in comparison to Na.

More recent work on $NaMgH_3$ destabilisation performed by Martinez Coronado et al. (Martínez-Coronado et al., 2012), showed the synthesis of $Na_{1-x}Li_xMgH_3$ (x=0, 0.25 and 0.5) hydride through high-pressure synthesis at 20 Kbar and 750 °C, it was concluded that hydrogen desorption temperatures of the system decrease from 435 to 420 °C as Li is introduced into the system due to the lower stability of the Li-substituted samples as shown in Figure 2.5.

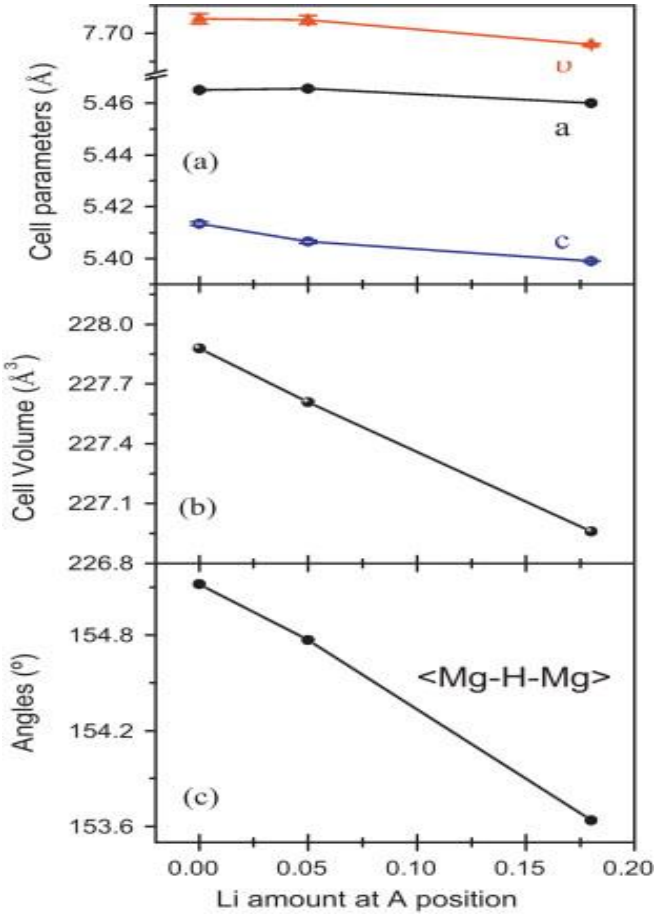

Figure 2.5 (a) the unit-cell parameter, (b) cell volume, and (c) tilting angle for $Na_{1-x}Li_xMgH_3$ as a function of the amount of Li at the A position of the perovskite. Reproduced from (Martínez-Coronado et al., 2012)

Reports on the structure, thermal analysis and dehydriding kinetic properties of $Na_{1-x}Li_xMgH_3$ (x=0, 0.5 and 1) performed by Wang et al.(Wang et al., 2016) showed that Li with nominal composition 0.5 has better dehydriding kinetic properties and releases a larger amount of hydrogen (4.11 wt% at 365 °C) in comparison to the ternary $NaMgH_3$ (3.42 wt.% at 365 °C).

2.3.4.2 Li and Na substitution into Ca-Mg-H hydrides

To the best of the author's knowledge there are no previous literature reports on this specific quaternary hydride composition. Following the studies reported by Reardon H. (Reardon, 2014) in Ca-Mg-H ternary hydride systems via mechanical milling under a nitrogen atmosphere, and the suggestions given in previous literature (Reardon, 2014, Yvon and Bertheville, 2006) of the favourable effect of Li substitution into ternary hydrides, light-weight metals such as Li and Na will be introduced into Ca-Mg-H phase in order to investigate the properties of the substituted quaternary hydrides. Therefore, in this thesis (Chapter 8) will be reported the synthesis, structure, thermal analysis, dehydriding properties and rehydrogenation properties of the systems comprising $Li_xCa_{1-x}MgH_4$ (x=0.2) hydride system and $Na_xCa_{1-x}MgH_4$ (x=0.2) using mechanical milling under an inert atmosphere.

2.4 Magnesium-based hydrides applications.

In addition to hydrogen storage for mobile applications, Mg-based hydrides can be used in other types of energy storage that do not necessarily require a low operating temperature and fast kinetics, such as: thermal energy storage (e.g. solar energy, waste heat from industrial processes, etc.); stationary hydrogen storage (mass storage); and batteries (solid state rechargeable Mg, Mg-air)(Bogdanović et al., 2009, Chusid et al., 2003). Mg based hydrides offer high capacity to store heat at temperatures around 400 °C. The energy density (up to 2257 kJ/kg), the cycling stability (10000 cycles) of these hydride systems is much higher than current heat storage systems (Reiser et al., 2000).

Magnesium hydride as heat storage can be safely used up to 440 °C; going over this temperature results in capacity losses.

One of the technologies that has attracted attention, is solar power energy storage. For electricity production from solar heat power plants, thermal storage is essential. Mg-based hydrides offer the necessary conditions of temperature and capacity, in addition to its low cost and good cycling stability. There are however, other ways of storing thermal energy i.e. molten salts. Nonetheless, with lower gravimetric densities (153 kJ/Kg for molten salts) and poor cycling stability.(Liu and Rao, 2017) Schematic of MgH_2 heat store is illustrated in Figure 2.6.

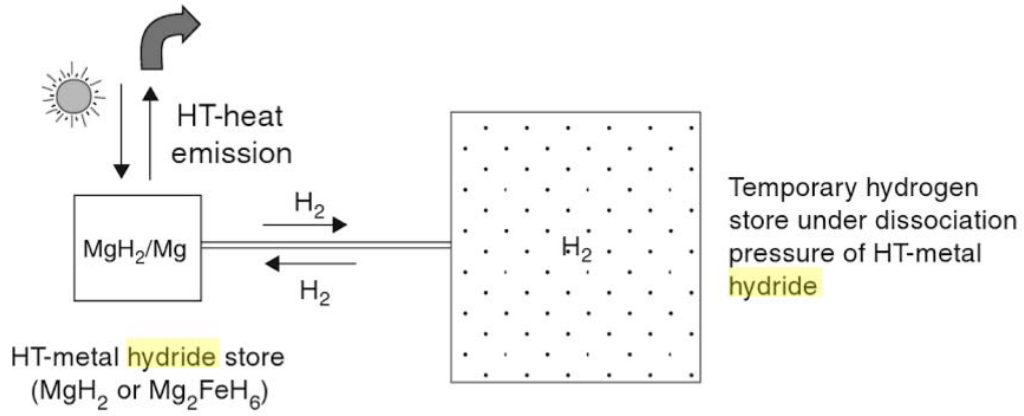

Figure 2.6 Schematic of MgH_2 heat store in a pressure container. Reproduced from (Kilner et al., 2012)

On the other hand, McPhy Energy patented a novel composite for mass storage based on MgH_2, phase change materials and expanded natural graphite which releases heat from the absorption reaction and this can be reversed for the desorption (Figure 2.7). Therefore, energy needed to store hydrogen is very low which meaning lower costs, but also lower carbon footprint through the lifetime of using McPhy's solid-state hydrogen storage solutions. Moreover, it is easy to use, does not require the presence of specialist or expensive maintenance. Making this a very interesting candidate in terms of scalable applications(McPhy).

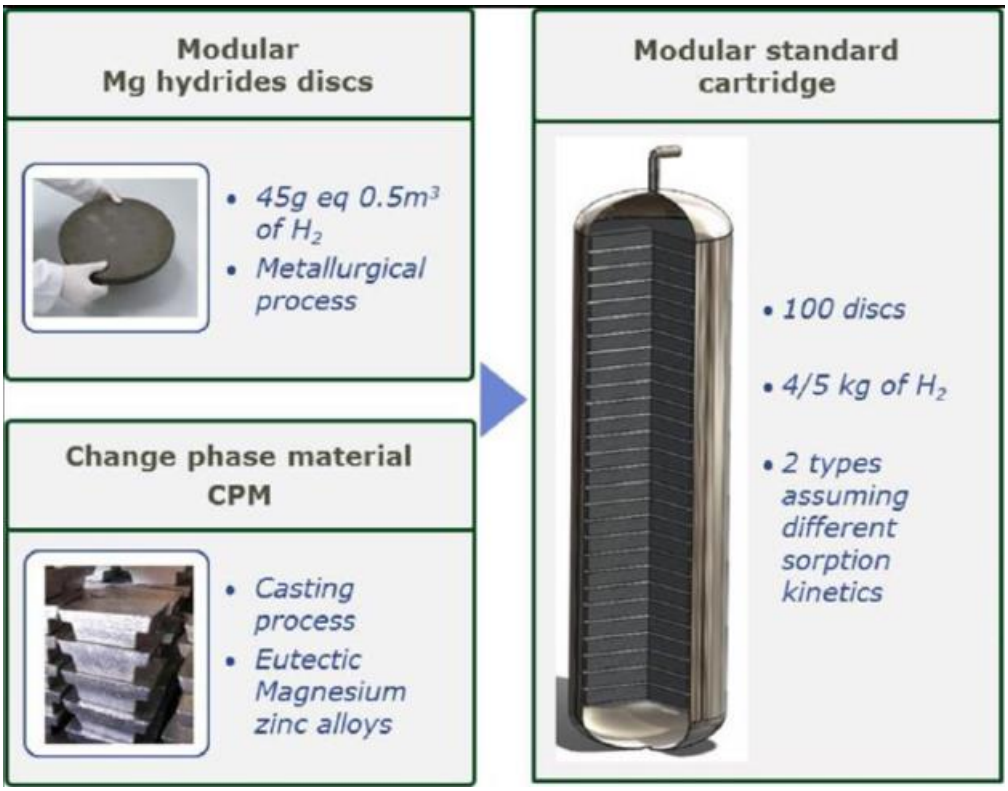

Figure 2.7 McPhy modular standard cartridge based on Mg hydrides discs. Reproduced from (Jehan and Fruchart, 2013)

2.5 Summary

Mg-based hydrides are interesting materials for diverse applications due to the relative low cost and abundance of Mg. The primary application described in this thesis is hydrogen storage. MgH_2 is a potential candidate to comply with the targets for on-board hydrogen storage in light-duty vehicles proposed by The US Department of Energy (DOE), given that possesses a relatively high hydrogen capacity of 7.6 wt. %, in addition to the good rehydrogenation ability achieved under certain conditions of temperature and pressure. Nevertheless, the kinetic reactions of absorption/desorption are rather slow and need to be enhanced. Moreover, hydrogen desorption temperatures of around 400 °C are too high for on-board hydrogen storage, hence, need to be lowered to 60 °C to boost its practical usage.

Different approaches to improve the kinetic and thermodynamic behaviour of the material have been covered in the literature. In this chapter, the effect of microstructural modification; through mechanical milling and the addition of catalytics and alloying additives to enhance the sorption kinetics of MgH_2 was described. It was elucidated that the kinetics can be accelerated by reducing the particle and crystallite sizes of the material and adding a catalyst(s) such as Nb_2O_5 or Ti. Although, MgH_2 phase remained stable and required high temperatures for desorption. Furthermore, thermodynamic destabilisation of MgH_2 was investigated and found that alloying MgH_2 with alkali/alkaline-earth metals might lower its reaction enthalpies. However, the hydrogen gravimetric densities were reduced, so decreasing its potential hydrogen capacity.

Consequently, synthesis of Mg-based ternary and quaternary hydrides with light-weight metals was covered as a possible approach to overcome thermodynamic limitations of MgH_2; hydrides comprising Na-Mg-H, Ca-Mg-H, Li-Mg-H, Li-Na-Mg-H, Na-Ca-Mg-H, Li-Ca-Mg-H systems were investigated and will be reported in this work.

Lastly, other MgH_2 applications were explored such as: thermal energy storage, where the working decomposition temperature of the material does not limit its applicability.

2.6 Aims and Objectives

The aim of this research is to investigate the hydrogen sorption mechanisms and thermodynamic behaviour of Mg-based hydrides, in order to try to produce novel materials with improved properties, i.e. with lower hydrogen desorption temperature (< 400 ^{o}C), high hydrogen content (> 5 wt. % H_2) and easily reversible.

With that purpose, this work will aim:

- ✓ To understand the structural and thermal properties of mechanically milled magnesium hydride samples synthesised under different times and atmospheres, using XRD, Raman, and DSC-TGA measurements. Special attention will be given to the vibrational changes characterised by Raman spectrometry.

- ✓ To investigate the structural changes and hydrogen sorption mechanisms of a Li-Mg alloy (ribbon form) synthesised via reactive milling. Particular attention, will be paid on the milled products to observe if theoretical Li-Mg-H ternary hydrides were formed.

- ✓ A comprehensive study of the structural, thermal properties and reversibility of Mg-Na-H and Ca-Mg-H ternary hydrides synthesised by high energy mechanical milling mixtures of MgH_2, NaH and CaH_2 using DSC-TGA-MS and ex/in situ XRD measurements. The milling process was carried out in an argon atmosphere alone, preventing the use of high pressure hydrogen techniques which are currently used for the synthesis of the materials.

- ✓ Investigate the effects of Li substitution into Na-Mg-H ternary hydrides synthesised via mechanical milling (Ar) in the decomposition reactions. Structural changes will be studied using Ex-situ XRD, and the compositional changes during heating will be assessed using DSC-TGA-MS and In-situ XRD.

- ✓ Attempt to synthesise novel Li-Ca-Mg-H and Na-Ca-Mg-H hydrides by high-energy milling of LiH, NaH, CaH_2 and MgH_2. Structural changes, hydrogen sorption properties and reversibility will be tested using Ex/In situ XRD and DSC-TGA-MS.

CHAPTER III

3. EXPERIMENTAL METHODS

3.1 Introduction

The experimental scheme (Figure 3.1) was divided into: (1) starting materials; (2) synthesis of the material through mechanical milling; (3) structural characterisation, via X-ray diffraction (XRD), scanning electron microscopy/energy dispersive X-ray spectroscopy (SEM/EDS) and Raman spectroscopy; (4) thermal decomposition, via differential scanning calorimetry (DSC) and thermogravimetric analysis (TGA) coupled with a Mass Spectrometer (MS); and (5) reversibility.

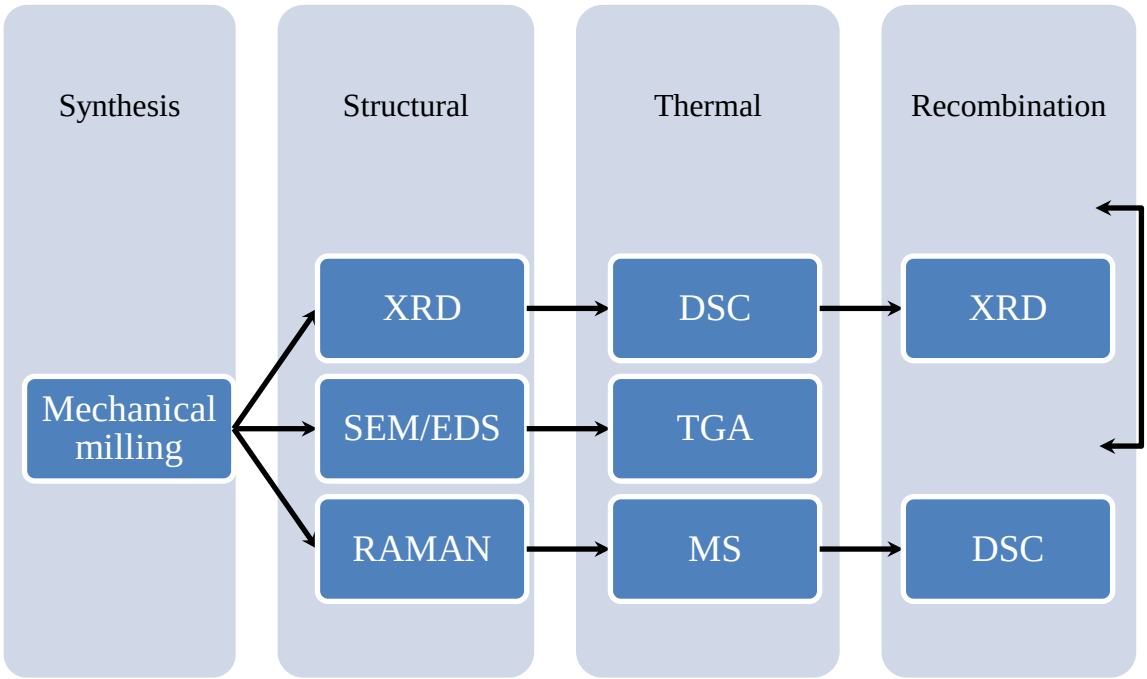

Figure 3.1 Experimental techniques used in the project

3.2 Starting Materials

Table 3.1 shows the commercial starting materials used, with their respective purity, morphology and provider. Starting materials are considered reactive due to their easy (hydro)-oxidation when they are in contact with air. This has a negative effect on their hydrogen storage properties. Therefore, materials were stored and handled inside an argon filled glove box with oxygen concentration less than 0.5% parts per million to prevent contamination.

Table 3.1 Starting materials for the formation of the hydrides.

No.	Element	Formula	Morphology	Grain (crystallite) size (nm)	Purity (%)	Provider
1	Magnesium Hydride	MgH_2	Powder	~67	~95±5 (Mg)	Goldschmidt
2	Lithium Hydride	LiH	Powder	~53	~95±5 (Li)	Sigma Aldrich
3	Sodium Hydride	NaH	Powder	~50	~95±5 (Na)	Sigma Aldrich
4	Calcium Hydride	CaH_2	Chunks	N/A	~95±5 (Ca)	Sigma Aldrich
5	Magnesium -Lithium Alloy	MgLi	Ribbon	N/A		Illika

3.3 Synthesis of the material

Mechanical milling was used to synthesise the different Mg-based hydrides due to its ability: to form new compounds; for powder size reduction; and to modify microstructures, e.g. grain size reduction.

3.3.1 Mechanical milling

For this work a Retsch Planetary Ball Mill PM400 (Figure 3.2) which contains four grinding pots and one main disk was used. The pots containing the mixtures (powders) and the milling balls are placed on the main disk and rotate around their own axis; the main disk rotates in an opposite direction, therefore, the centrifugal force act in opposite directions causing there to be impacts between milling balls and between milling balls and the inner walls of the pots. Very often powder particles will be impacted between balls and between balls and the inner walls.

Figure 3.2 Schematic a) Retsch Planetary Ball Mill PM400, b) Hardened steel milling pot 250 ml, c) Hardened steel high-pressure milling pot 220 ml. (swagelok ball valve, max pressure 150 bar)

This effect can lead to chemical reactions between powders and/or morphological changes. Even though, this method presents several advantages for the synthesis of materials such as: producing very fine powder (2 to 20 nm in size), continuous operation, and relatively low cost (Stolle, 2014), one of the main drawbacks is the amount of impurities that the high-energy collisions (balls and pot) introduce into the powder.(Suryanarayana, 2001b)

The grade of contamination will depend on the conditions used for the milling (e.g. time, number of balls, speed). Suryanarayana (Suryanarayana, 2001b) reported that, 1-4 wt. % Fe is normally present as an impurity in the case of steel milling media. . Hence, a certain level of Fe contamination is assumed to be present in all the samples prepared in this work.

The maximum pressure of the gas used was 100 bar (H_2), loaded into a hardened steel milling pot 220 ml volume. High pressure hydrogen milling technique can help to prevent the decomposition of the mixtures during the milling process, and could induce solid-gas reactions between the reactive gases (e.g.H_2) (Suryanarayana, 2001a)

Table 3.2 shows the parameters selected for the synthesis of the different Mg-based mixtures. Different milling pots, balls and atmospheres were used in the sample preparation. Milling times were based on previous studies (Guo, 2015, Reardon et al., 2013, Reardon, 2014). To minimise overheating during the milling, 15 minutes of milling was followed by a 15-minutes rest period.

Table 3.2 Parameters for the ball milled samples

Materials	Milling Time (h)	Milling Speed (rpm)	Ball to Powder Ratio	Pot volume (ml)/ball's diameter (mm)	Atmosphere
MgH_2	2,5,10	250	10:1	220/10	1 bar Ar, 100 bar H_2
Li-Mg Ribbon	0.25 ,0.5, 1	100	50:1	220/10	1 bar Ar, 100 bar H_2
NaH, MgH_2	2,3,5	400	70:1	250/10	1 bar Ar, 100 bar H_2
NaH,LiH, MgH_2	2,10,15	400	50:1	250/10	1 bar Ar
CaH_2, MgH_2	2,5,10	400	75:1	250/10	1 bar Ar
CaH_2, LiH, MgH_2	5, 10, 15	400	75:1	250/10	1 bar Ar
CaH_2, NaH, MgH_2	5,10,15	400	75:1	250/10	1 bar Ar

3.4 Structural Characterisation

Characterisation techniques employed in this work for the analysis of the as-received, as-milled material are described, using X-ray diffraction (in/ex-situ XRD), scanning electron microscopy (SEM), and vibrational spectroscopy (Raman).

3.4.1 X-ray Diffraction

X-ray powder diffraction is a very powerful technique used for phase identification of crystalline materials and provides information on unit cell dimensions. XRD function is based on constructive interference between monochromatic X-rays and a crystalline sample. To obtain a constructive interference, the interaction of the sample with the incident X-ray must satisfy Bragg's Law (Equation.3.1)

$$n\lambda=2d \sin \theta \quad (3.1)$$

Where, n is an integer number (reflection order), λ is the wavelength, d is the interplanar spacing of a crystal, θ is the angle between scattering planes at which a diffraction peak is observed (Bragg's angle) and the incident ray.

Figure 3.3 illustrates the Bragg's Law reflection; the X-rays are produced by a beam of electrons generated in a cathode ray tube by heating a filament, filtered to produce monochromatic radiation, collimated to concentrate and directed onto the sample at a controlled incident angle (θ). Constructive interference of the scattered waves λ occurs when two parallel beams show a difference in path length equal to a multiple of the wavelength (nλ), therefore satisfying Bragg's law. If this law is not fulfilled, then destructive interference occurs.

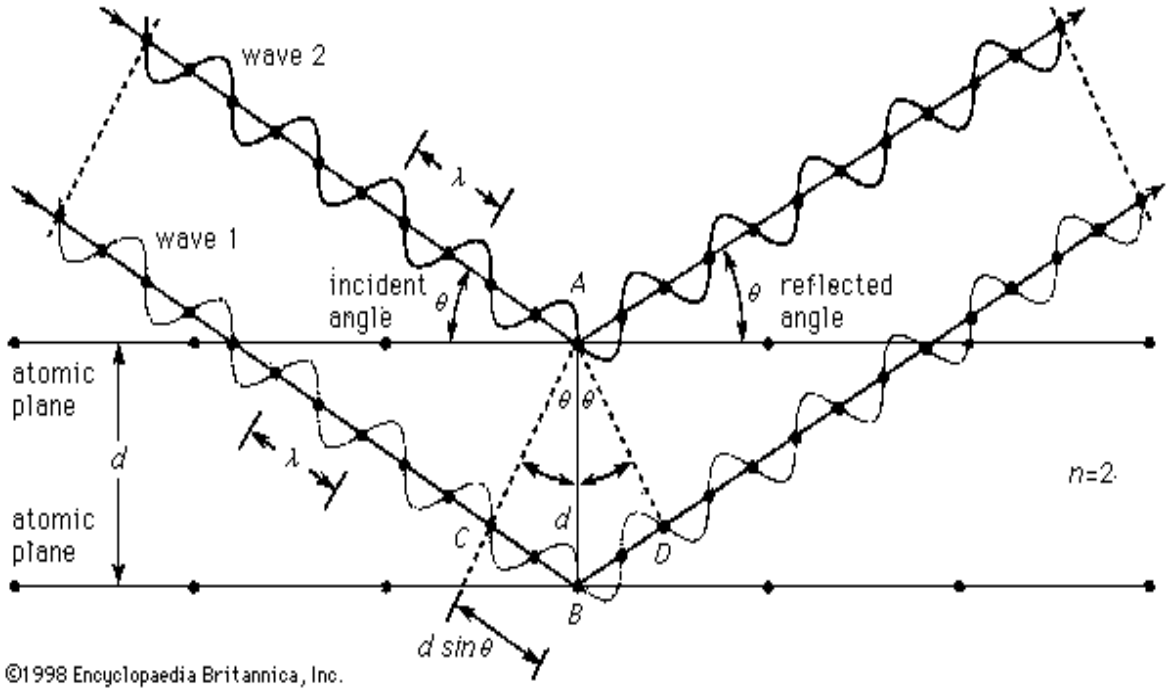

Figure 3.3 Bragg's Law reflection. Two beams with identical wavelength and phase approach a crystalline solid and are scattered off two different atoms within it. The lower beam traverses an extra length of 2dsinθ. Constructive interference occurs when this length is equal to an integer multiple of the wavelength of the radiation. Dots on X-rays represent constructive interference *(Britannica, 1999)*.

3.4.1.1 Powder X-ray diffraction

Powder X-ray diffraction can allow qualitative and quantitative estimation of the phase compositions in addition to determine the structure of crystalline materials. In this work, all the XRD measurements were performed using a Bruker D8 Advance X-ray Diffractometer (Figure 3.4).

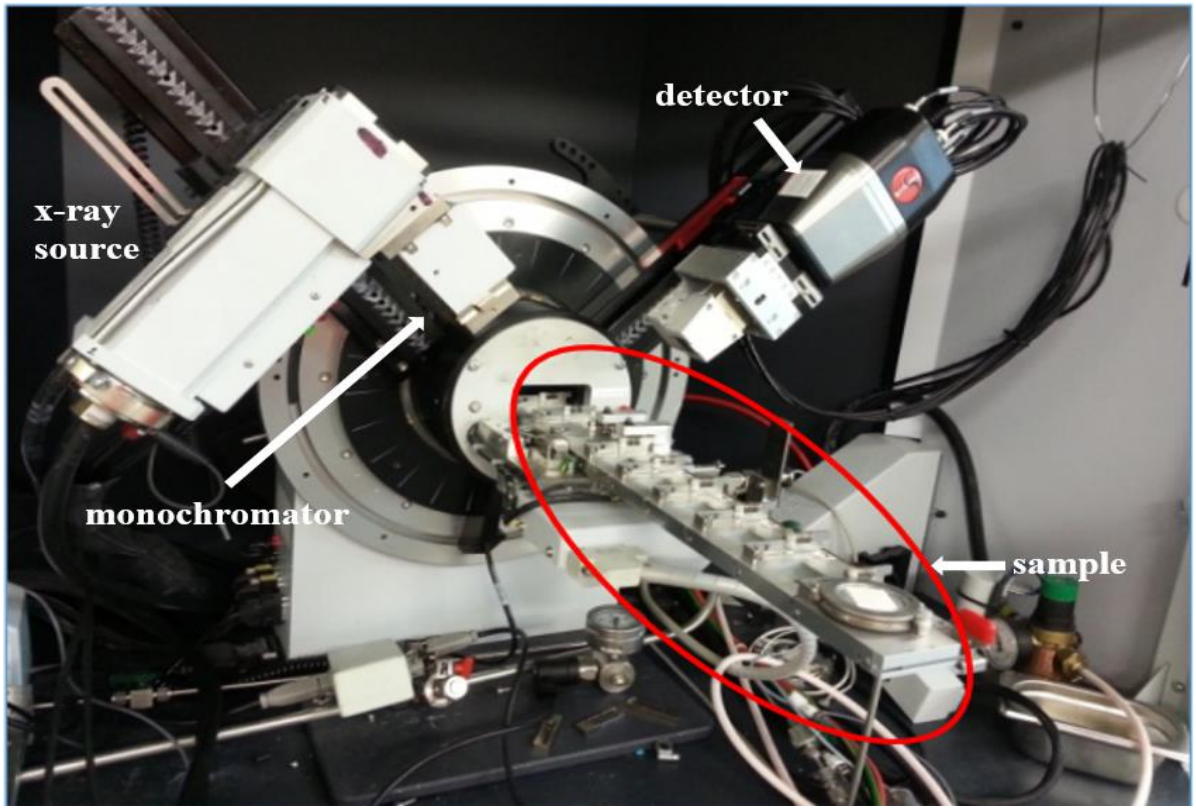

Figure 3.4 Bruker D8 advanced XRD with a 9-position multi-changer sample stage, reproduced *(Hughes, 2016)*

Monochromatic X-rays were generated with a Cu-Kα radiation (λ=0.154 nm) source with a Göbel mirror. It is assumed that powder samples contain randomly oriented crystallites, the X-rays diffraction occurs across all the existing crystallographic planes. A Vantec sensitive detector (PSD) was used to record the intensity of diffracted X-rays as a function of the angle 2θ. All ex-situ measurements at room temperature were performed under an argon inert

atmosphere using a Kapton airtight dome-shaped sample holder in order to prevent air or water contamination. Some powder samples were ground using a mortar and pestle after decomposing in order to gain a better homogeneity with the surface and inside of bulk powder. Data was collected between 5 and 90° 2θ with scanning times of 25 minutes for each sample.

3.4.1.2 In-Situ X-ray diffraction

In-situ characterisation was performed using a D8 Advance XRD coupled with an Anton Paar XRK900 reactor chamber (Figure 3.5), in order to study the compositional and structural changes of the phase(s) in the samples as a function of pressure and/or temperature. Moreover, to get a better understanding of the dehydrogenation mechanisms of samples investigated in this work. Samples were loaded into an alumina or boron nitride crucible and handled inside an argon-filled glove box to prevent air contamination.

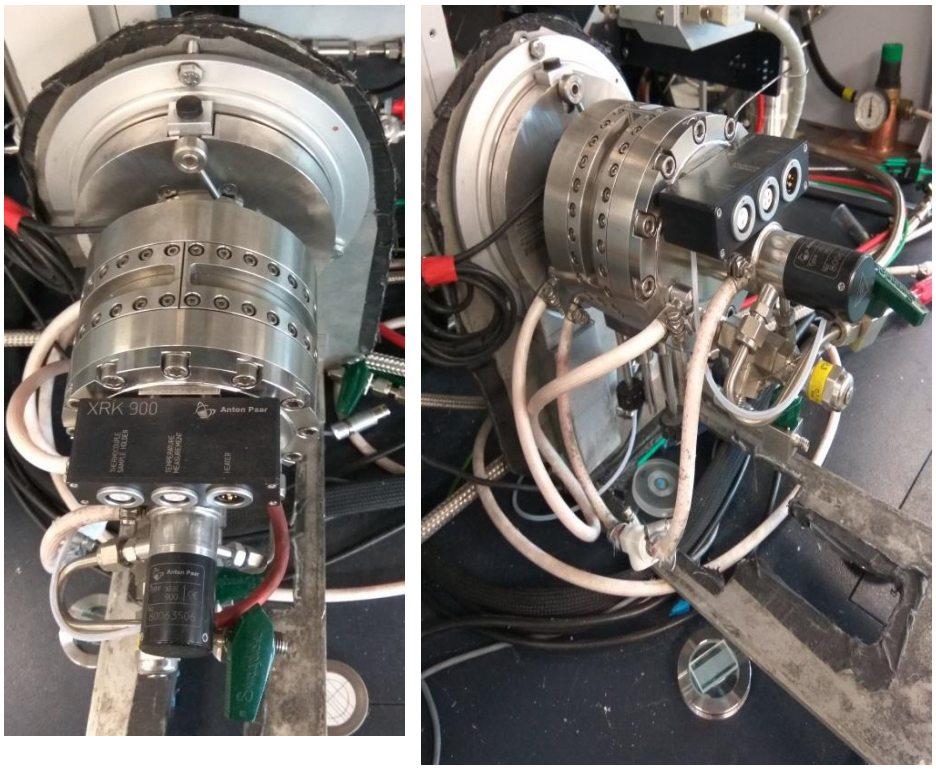

Figure 3.5 Schematic Bruker D8 advanced XRD with an Anton Paar XRK900 reactor chamber.

In-situ measurements were performed by heating the samples at a rate of 12 °C/min under a helium or hydrogen atmospheres (flowing at 100 ml/min at 3 bar pressure or 10 bar). Scans were taken isothermally from 5 to 90° 2θ range and step size of 0.02° with a total scan time of approximately 43 minutes.

3.4.1.3 X-ray diffraction data analysis

Diffraction patterns were firstly analysed by comparison with data from the literature or crystal structure databases obtained from the Inorganic Crystal Structure Database using EVA software (equipped with PDF – 2 database) (EVA, 2016, ICSD, 2017). A Pseudo-Rietveld refinement was performed in this project in order to get a qualitative analysis (determine the contribution of each phase in the milled materials) using TOPAS-Academic and jEdit software (Topas, 2017) with reference data obtained from the Inorganic Crystal Structure Database (ICSD). The background was modelled using a Chebyshev function. Peak shapes were fitted using the Pseudo-Voight function (Snellings et al., 2010). The lattice parameters were adapted, following the atomic parameters. To obtain a more accurate fitting all points before 25° 2θ were excluded from the refinement.

In the refinement, a pattern experimentally obtained was adjusted to a given pattern from the ICSD database. The parameters to build the calculated pattern were fitted to minimise the difference between the given and the calculated data. Thus, giving an accurate qualitative and quantitative of the composition of the sample. Nevertheless, temperature fluctuations, quality of the XRD data, crystallinity of the sample and grain size might affect the precision and accuracy of this method.

3.4.2 Raman Spectroscopy

Raman spectroscopy is a photonic technique that provides chemical and structural composition of materials allowing its identification. This technique is used for the study of vibrational modes in a system. Raman spectroscopy is based on the illumination of monochromatic light onto a sample and the analysis of the scattered light. Most of the scattered light has the same frequency as the incident light, however for a small fraction there can be a change in frequency due to an interaction with the sample. This scattered light that presents frequencies different to the incident radiation is known as Raman scattering. In other words, for the Raman scattering to occur needs to be an interaction between light and molecular vibrations. This is comparable to the infrared (IR) spectroscopy, although different rules apply. For instance, some vibrations will be visible in the Raman spectrum and not in the IR spectrum i.e. carbon atoms on the structure of a diamond. Figure 3.6 illustrates the schematic of the energy transfer in the Raman scattering.

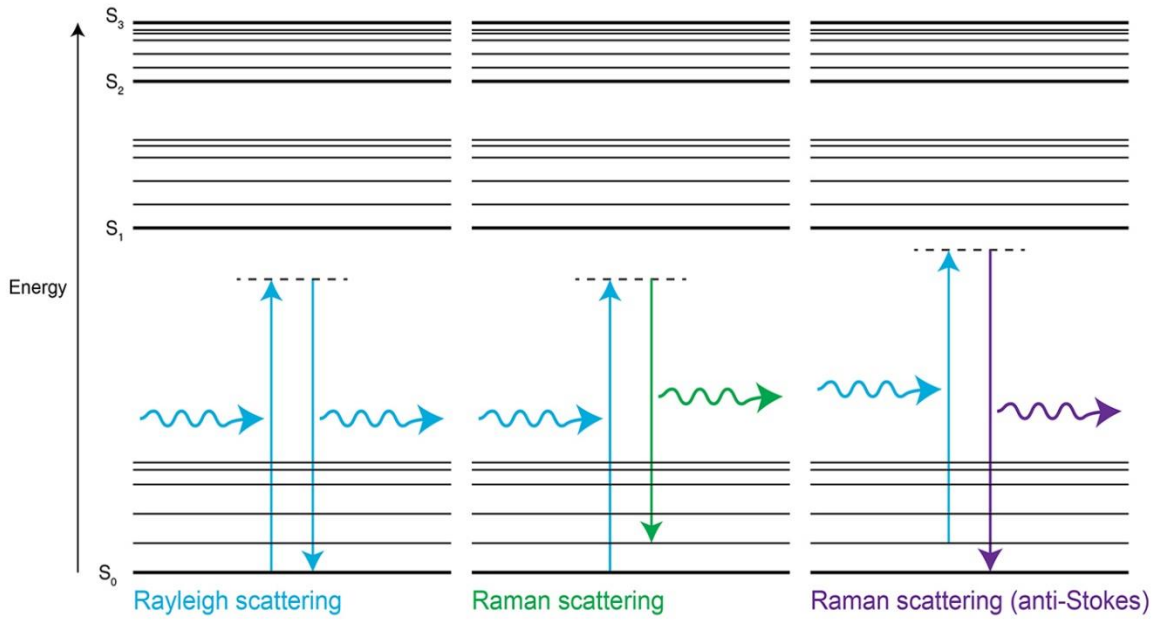

Figure 3.6 Rayleigh and Raman scattering energy diagram. S0, S1, S2 are electronic energy levels, with higher energy vibrational levels. The dashed lines represent virtual states.

If the photon transfers energy to stimulate the molecule from a base (starting) state to a virtual state and then falls to a higher energy vibrational state, the scattered photon will present lower energy than the incident photon showing a Stoke scattering. On the other hand, if the molecule is in an excited vibration state and is scattered to a basis state, then the vibrational energy will be shifted to the scattered photon with higher energy; compared to the incident photon, this effect is called anti-Stokes scattering. Commonly, Stokes scattering has a stronger effect than anti-Stokes, hence, only this one is recorded. For a molecule to exhibit a Raman "active" effect, the incident light should induce a change in its polarization. Therefore, the most intense peaks in a spectrum are result of symmetrical vibrations.

In this work, Raman spectra of the samples were collected using a Renishaw InViaReflex Raman spectrometer with a confocal microscope (Figure 3.6). The incident light (λ= 488, 635 nm) laser beam was focused onto the sample and the emitted light was channelled back through the objective and then filtered through a holographic notch filter where all photons along the laser line with a shift of ±100 cm^{-1} are removed (Rayleigh scattering). The residual photons were focused through a series of lenses and slits before being separated using a grating (2400, 1800 lines/mm) prior detection by a charge-coupled device (CCD).

Samples were loaded in an argon inert atmosphere (glove box) to avoid air contamination; an aluminium crucible containing around 15mg of sample was placed in an Instec sample cell HCS621V. Analysis of the samples was carried out using Renishaw Wire 3.4 (RENISHAW, 2016) and Igor Pro software (WaveMetrics, 2017).

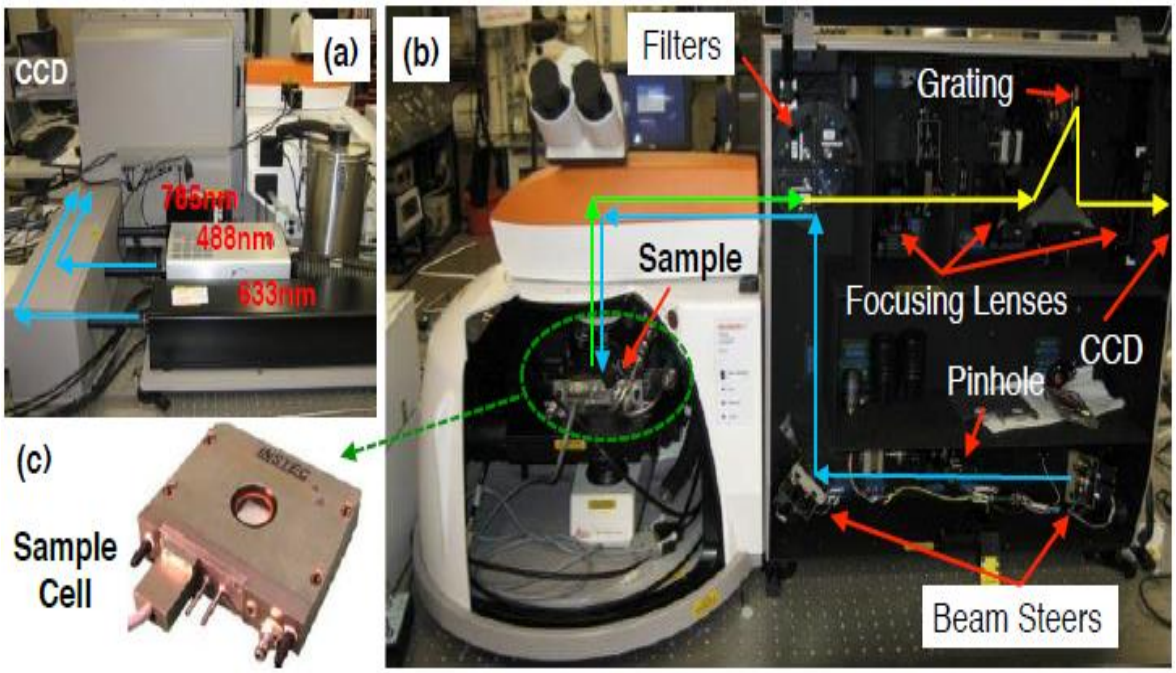

Figure 3.7 (a) Laser source, (b) Renishaw inVia Raman Microscope, (c) Instec HCS621 sample cell. Blue line: incident beam, green line: scattered beam, yellow line: remaining beam after removal of the Rayleigh scattering. Reproduced from *(Reed, 2010)*

3.4.3 Microscopy

Scanning Electron Microscope (SEM) Figure 3.7 was used in this research to identify the microstructural characteristics of the materials. This technique is based on different types of interactions that take place between an electron beam and a given material. In a SEM electrons are generated in a hot tungsten filament, accelerated by a magnetic field along the barrel of the microscope and then collimated in a beam through electromagnetic lenses, the focal length is determined by altering the voltage. Electrons can interact with the samples in different ways:

1) They can pass through the sample with no interaction
2) Interact with the electron cloud of the sample, creating low energy secondary electrons obtained from superficial areas (<50 eV), these are insensitive to elements and allows images to be obtained in which contrast will depend on the topography of the material.

3) Collide with the nucleus of the samples, creating high-energy backscattered electrons, which allow different densities and phases in the sample to be identified.

In addition, the SEM used in this research was coupled with a EDS or EDX feature, which allows chemical composition in a sample to be measured using energy dispersive spectroscopy. For all the SEM work a JEOL 6060LV, coupled with an Oxford Instruments detector and INCA EDS software, was used to obtain the images and analysis of the samples. Images were obtained with 20 kV, spot size of 50 nm, and working distance of 10 mm for EDS. All samples were loaded and mounted in an argon atmosphere to avoid contamination and then transferred to the loading platform of the SEM manually (Atteberry, 2009).

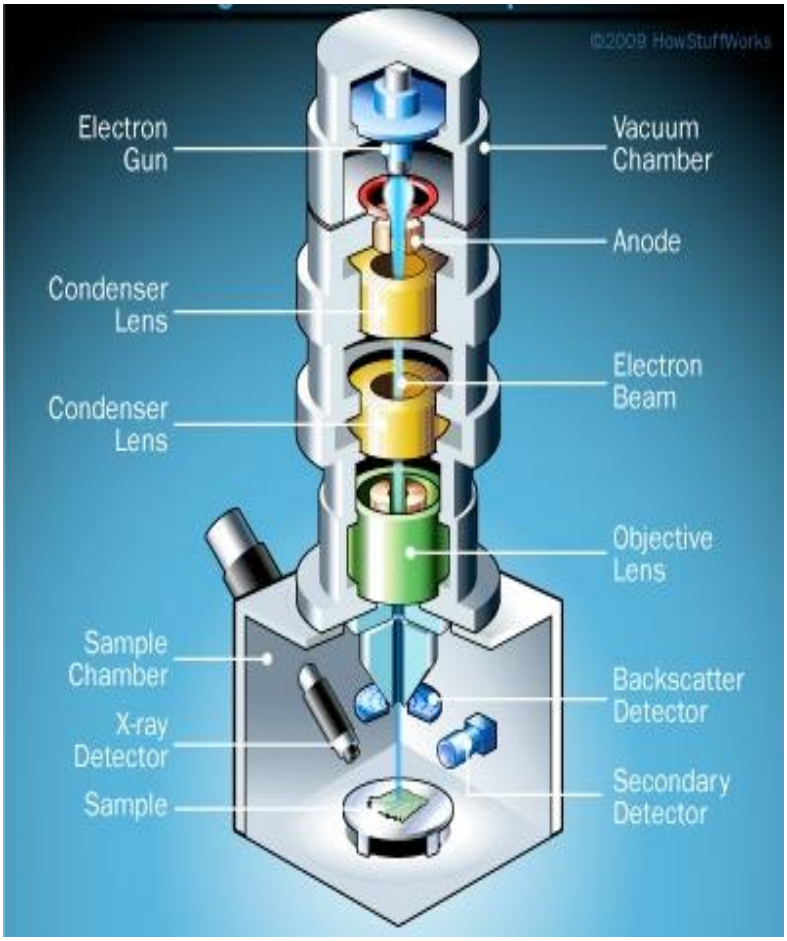

Figure 3.8 Schematic of scanning electron microscope (SEM) ***(Atteberry, 2009)***

3.5 Thermal Decomposition

Thermal decomposition of the samples was investigated using techniques of differential scanning calorimetry (DSC) and thermogravimetric analysis (TGA) coupled with a mass-spectrometer (MS). These techniques are based in the change of heat flow (DSC) and mass (TGA) during heating/cooling of a determined material, and are associated with endo/exo thermic events respectively, such as phase transitions, compounds formation and hydrogen release.

3.5.1 Differential Scanning Calorimetry (DSC)

This technique measures the difference of heat flows between one sample and one reference when they are heated or cooled at a constant speed. This difference of heat flow gives a peak that corresponds to an exothermic or endothermic event (i.e. phase changes, hydrogen release) that undergoes the studied material (Höhne et al., 1996).

In this work, a Netzsch DSC 204 HP was used, a sample and reference were placed on a disk-shaped sensor in a furnace (Figure 3.8). The heat is transferred homogenously through the disks to the sample and reference. When the sample undergoes a thermal event or presents a diverse heat capacity, the following difference in heat flow causes slopes at the thermal resistances of the sensor area (Hemminger and Sarge, 1998). These slopes are recorded by sensitive temperature sensors which measure the difference in the heat flow. The deviations are plotted as exothermal or endothermal peaks.

To achieve accurate measurements a temperature calibration was performed using standard metals (In, Bi, Sn, Pb, and Zn) with known melting points within the temperature range of the DSC. In addition, a baseline with exactly the same conditions to be used during the measurement was executed in order to reduce the effect of the background between the sample and the reference.

The Netzsch DSC 204 HP was located in a flowing argon glove box. Around 10-15mg of sample was loaded into an aluminium crucible. Measurements were performed from room temperature upon 500 °C at a heating rate of 2 °C/min and 3 bar Ar flowing at 100 ml/min.

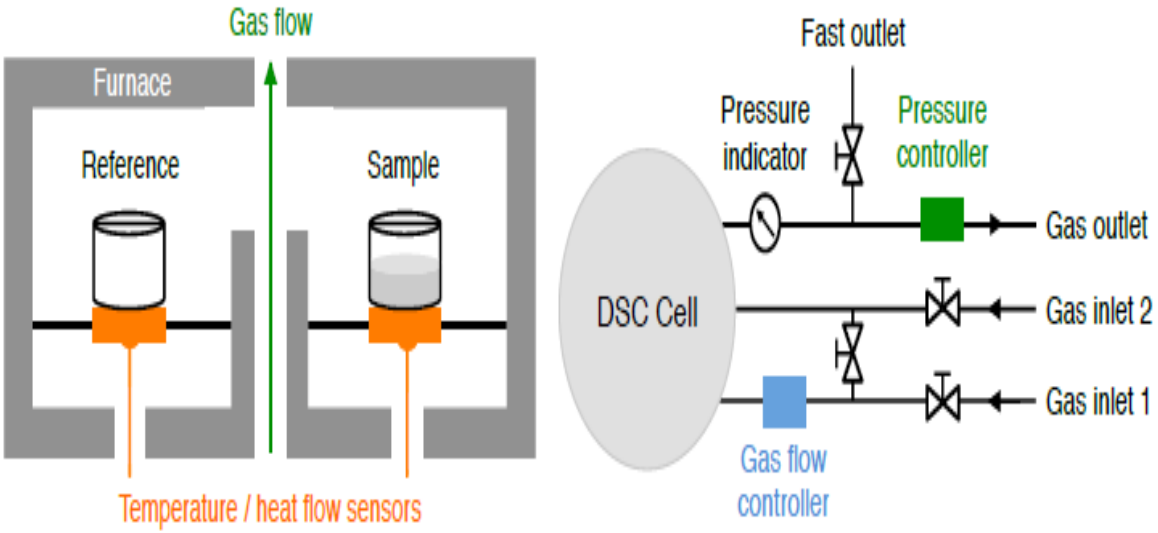

Figure 3.9 Left: Schematic of heat flux DSC cell, Right: high pressure DSC system (Netzsch DSC 204 HP) with input gas. Reproduced from(Guo, 2015).

3.5.2 Thermogravimetric Analysis (TGA)

Thermogravimetric analysis was carried out in this work to investigate the mass loss of samples. TGA (Figure 3.9) measures the mass change(s) of the material as a function of temperature and time. The equipment consists of a microbalance, a furnace and a controller, where samples can be weighed and heated/cooled at the same time. Samples are placed inside the furnace onto a thermocouple in an enclosed system to control the atmosphere. An inert gas (Ar) flows in through the gas port below the sample and all the desorbed gases during the heating/cooling process are carried to the mass spectrometer through exhausts above the sample.

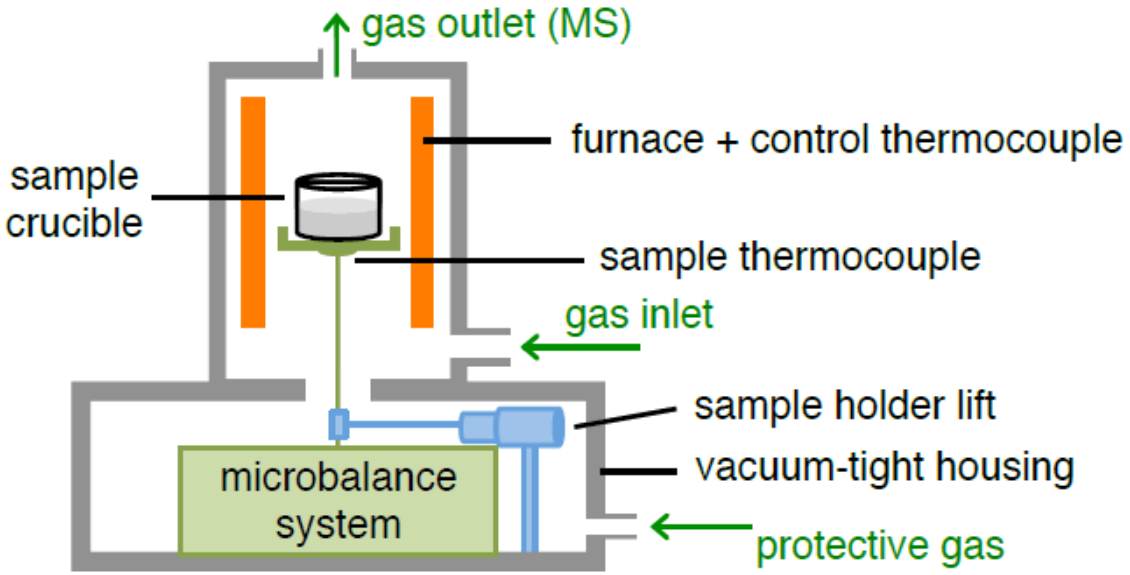

Figure 3.10 Schematic simplified internal view of a Netzsch TG 209 analyser. Reproduced from (Guo, 2015)

Calibration was performed in order to achieve accurate measurements and was carried out for the temperature and mass with standard materials (KNO_3, In, Bi, Sn, Zn and Al) and calcium oxalate, respectively. Moreover, a baseline with exact the same conditions to be performed during the measurements was executed using an empty sample holder to minimise the buoyancy effect upon heating.

In this work, a Netzsch TG 209 connected to a mass spectrometer was used to analyse and record thermogravimetric changes and the evolution of gas(es) during the heating/cooling process. The TGA was mounted inside an argon-filled glove box; all the samples were handled and prepared in an inert (Ar) atmosphere to avoid contact with air or water. Samples of around 15-20 mg were loaded into an alumina crucible with a lid, and heated at 2 °C/min and approximately 1 bar Ar flowing at 40 ml/min.

3.5.3 Mass Spectrometry

Mass Spectrometry is an analytical technique that allows the study of compounds of diverse nature: organic, inorganic or biological and obtain qualitative or quantitative information. Through mass spectrometry analysis, it is possible to obtain information on the molecular mass, structural information or to detect the presence of a compound and/or to quantify its concentration. To do this, it is necessary to ionize the molecules and obtain the ions formed in the gas phase. The generated ions are accelerated to an analyser and separated according to their mass/charge ratio (m/z) through the application of electric fields, magnetic fields or simply by determining the time of arrival to a detector. The ions that reach the detector produce an electrical signal that is processed, expanded and sent to a computer. The obtained register is called mass spectrum and represents the ionic abundances obtained as a function of the mass/charge ratio of the detected ions.

In this work, a Hidden Analytical HAL IV Mass spectrometer; connected to a Netzsch 209 TGA analyser, was used to analyse the evolution of gas(es) from thermal decomposition from thermogravimetric analysis as shown in Figure 3.10.

Two different types of detectors were used in this research:

1) Secondary Electron Multiplier used to detect low concentration gases due to a very large sensitivity.
2) Faraday cup used to monitor large gas concentrations.

The mass spectrometer was calibrated to measure the concentrations of Argon (m/z=40) faraday detector, H_2O (m/z = 18) faraday detector, O_2 (m/z = 32) faraday detector, and H_2 (m/z = 2) SEM detector.

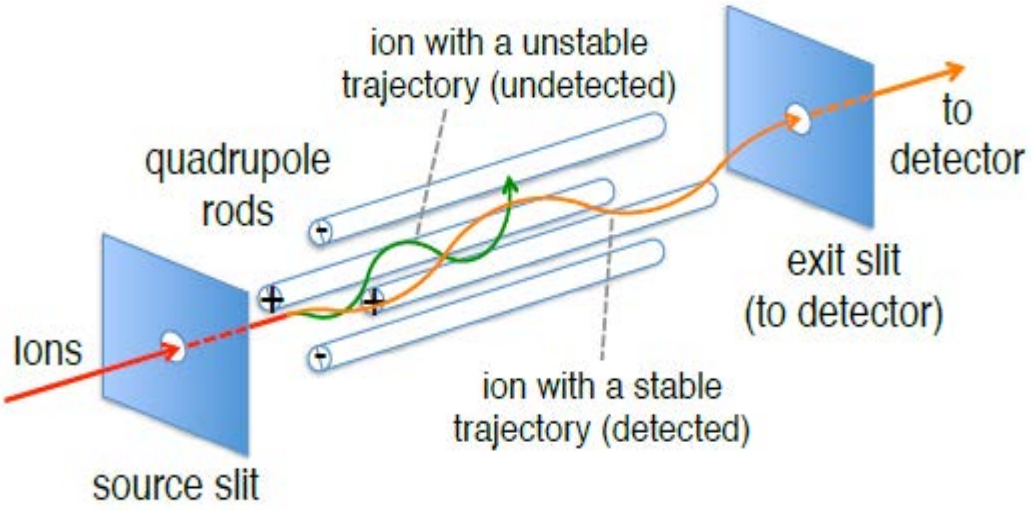

Figure 3.11 Schematic of a Hidden Analytical HAL IV Mass spectrometer

CHAPTER IV

4. MAGNESIUM HYDRIDE

4.1 Introduction

Magnesium hydride (MgH_2) combines a high H_2 capacity of 7.6 wt% with the benefit of abundantly available magnesium and low cost (Zaluska et al., 2001, Imamura et al., 2005, Zaluski et al., 1997, Zhu et al., 2006b, Cansizoglu and Karabacak, 2009) with good reversibility (Fukai, 1993). The main disadvantages of MgH_2 as a hydrogen store is the high desorption enthalpy (-75 kJ/mol), a high reactivity when exposed to air (Zaluska et al., 1999), and thermodynamic stability (desorption temperature of 300 °C at 1bar H_2 (Imamura et al., 2005)). MgH_2 requires a relatively high operating temperature which is too high for practical on-board vehicular applications (Bogdanović et al., 1999b).

Many efforts have been focussed on Mg-based hydrides to try to reduce the desorption temperature and to accelerate the re/dehydrogenation reactions. This can be accomplished by using catalysts to improve the absorption/desorption kinetics and also by reducing the grain size of the hydride by ball-milling with elements which reduce the stability of the hydrides (Reule et al., 2000). The literature review of the different composites and techniques was discussed in Chapter 2.

This chapter will cover the effect of milling magnesium hydride under different atmospheres (Ar and H_2) for 2, 5 and 10h in attempt to enhance the sorption kinetics of the pristine material. It is known from the literature that milling MgH_2 improves the thermal desorption of the hydride. Therefore, this investigation compares results of previous literature reports with values experimentally achieved in this work.

The study will be divided into three sections. Initially, the structural properties of the milled material will be investigated through XRD and Raman spectroscopy to understand any differences in composition and bonding. Then, decomposition mechanisms will be assessed through thermal analysis DSC and TGA. Finally, the products formed through decomposition will be analysed using in-situ XRD.

4.2 Characterisation of as-received and milled MgH_2

The as-received MgH_2 diffraction is shown in Figure 4.1, which reveals that the MgH_2 powder consists of 98.3 wt. % α-MgH_2 (tetragonal structure, space group $p4_2/mnm$ 136) (Bortz et al., 1999) and 1.7 wt. % Mg; the Mg probably due to incomplete hydrogenation during the manufacturing process. The lattice parameters of the material (Figure 4.2) were refined using TOPAS software and are summarised in Table 4.1

Figure 4.1 illustrates the structure of the milled material for 2, 5 and 10h in Ar obtained from X-ray diffraction. The 2h milled MgH_2 diffraction shows the formation of a new phase consistent with γ-MgH_2 (orthorhombic, Pbcn) (Nayak and Verma, 2016) in addition, to the α-MgH_2 and Mg phases.

Refinement of the milled material was performed to determine the percentage of each phase present in the sample and is shown in Figure 4.3. From there, it is possible to assign 87 wt. % to α-MgH_2 phase, 7 wt. % to Mg phase and the remaining 5 wt. % to γ-MgH_2 phase.

When milling MgH_2 for 5h in Ar, the same reflections related to α and γ MgH_2 and Mg phases were detected. Nevertheless, the intensity of the peaks was reduced and an evident broadening was observed.

The lattice parameters of the 5h milled sample (Figure 4.4) show that the sample is formed of 86 wt. % α-MgH_2, 9 wt. % γ-MgH_2, 2 wt. % Mg and 4 wt. % MgO; the MgO is possibly formed due to oxidation of Mg during milling.

On further milling MgH_2 for 10h in Ar, reflections of Mg, α and γ MgH_2, and MgO appear broader and less intense, no other phases were detected.

The refinement carried on the milled sample (Figure 4.5), indicated that 10h milled MgH_2 contains γ-MgH_2 accounting for 38 wt. %, α-MgH_2 56 wt. % and Mg (2 wt.%), MgO (4 wt. %) are the remaining crystalline material.

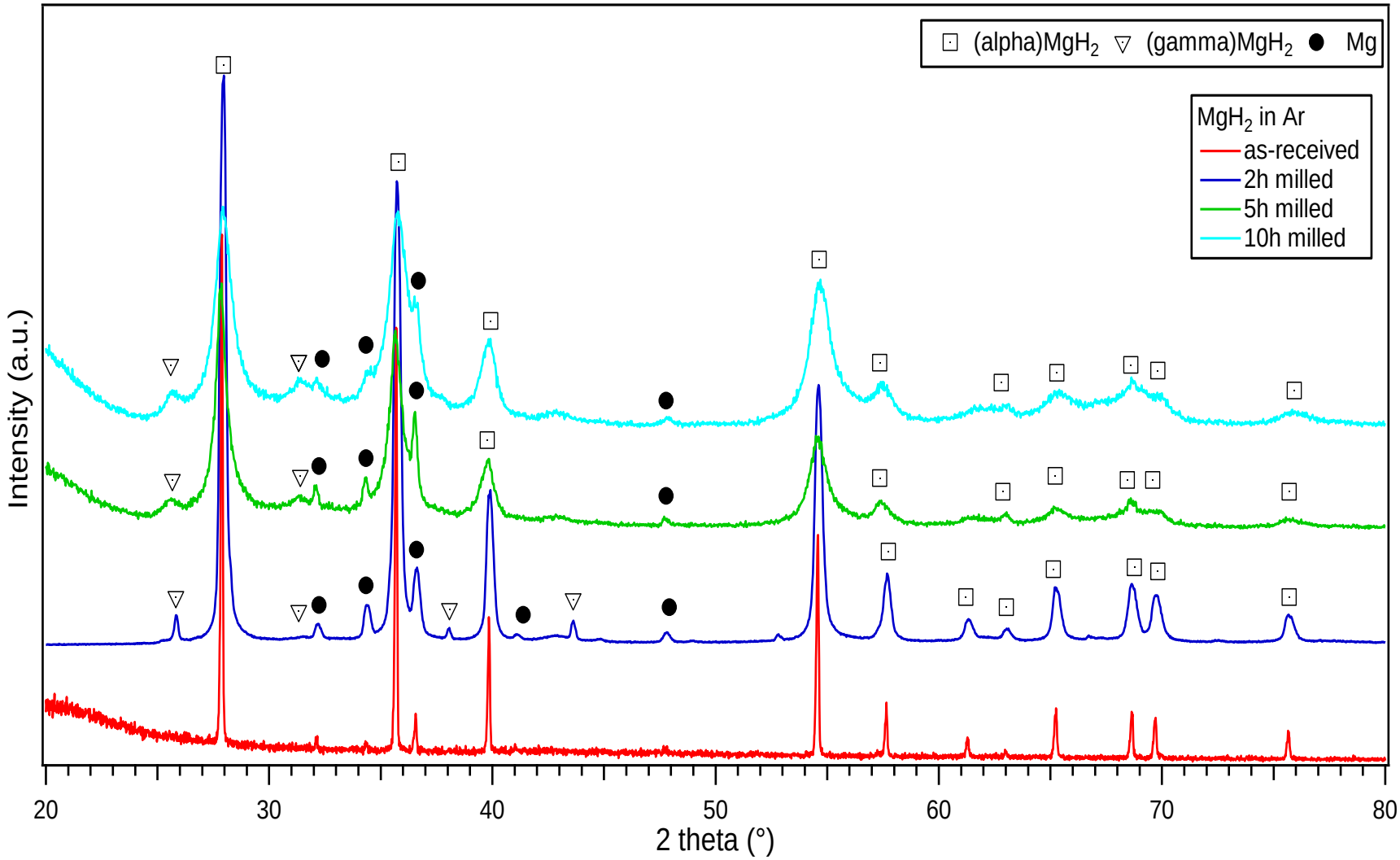

Figure 4.1 XRD patterns of the as-received and 2, 5 and 10h milled MgH_2 in Ar.

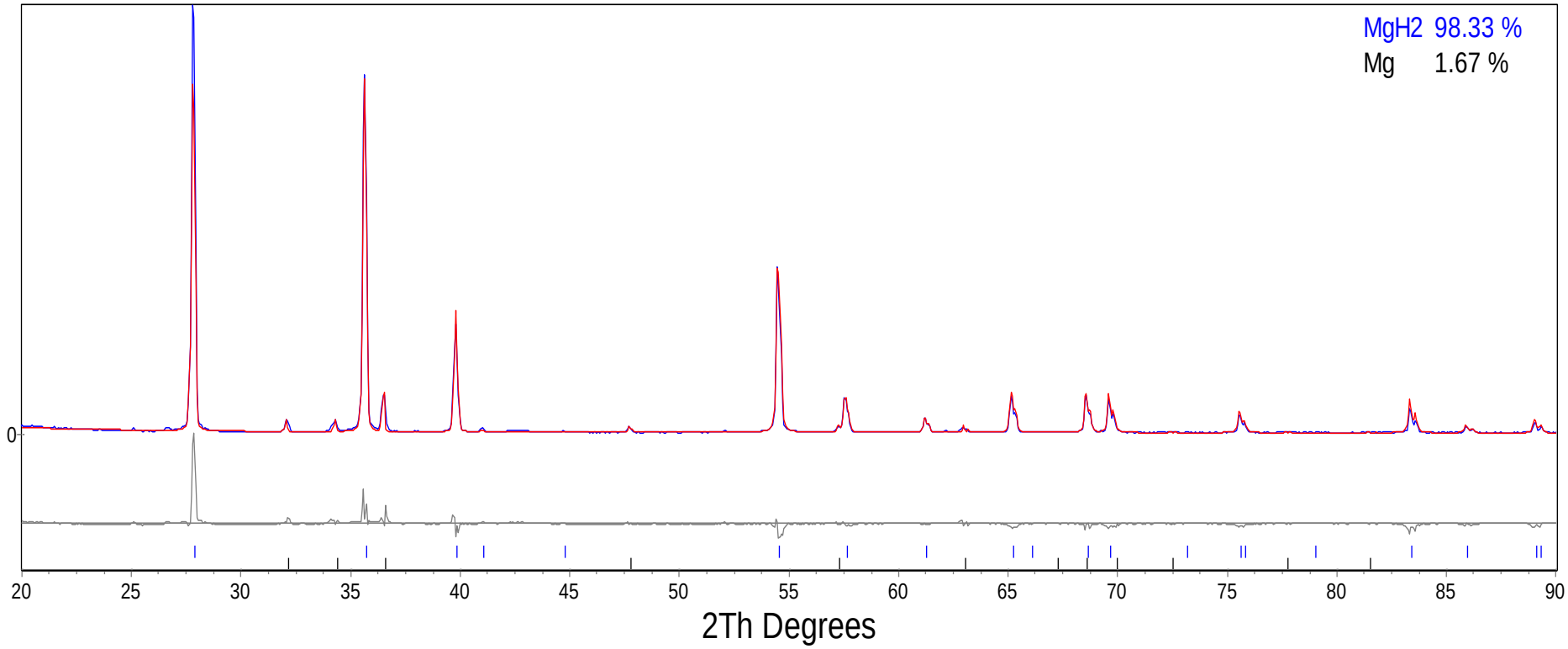

Figure 4.2 Rietveld refinement profile for the as-received MgH_2, blue line shows the observed data, the calculated data is represented by the red line and the difference is plotted underneath shown by the grey line. Values before 20 (2θ°) did not show any representative peaks and therefore are neglected. Goodness of fit 1.958.

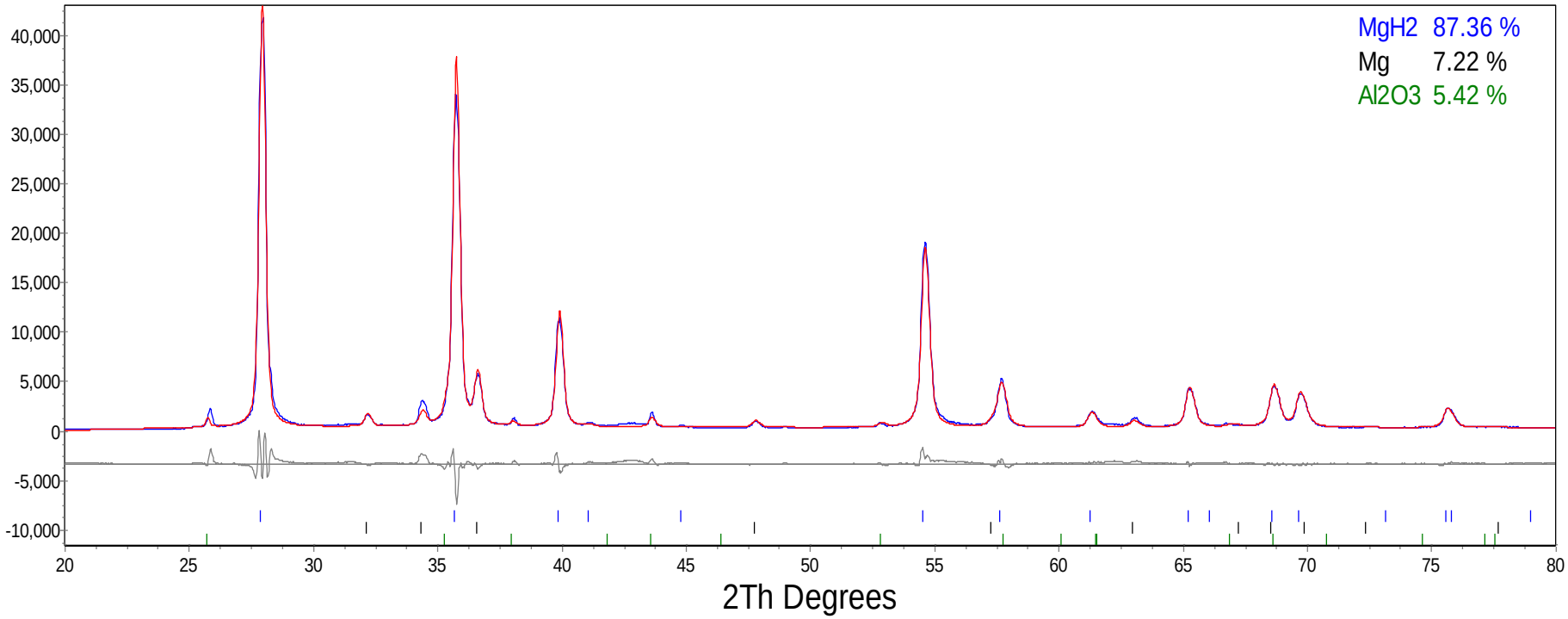

Figure 4.3 Rietveld refinement profile for the 2h milled MgH_2 in Ar, blue line shows the observed data, the calculated data is represented by the red line and the difference is plotted underneath shown by the grey line. Values before 20 (2θ°) did not show any representative peaks and therefore are neglected. Goodness of fit 1.862

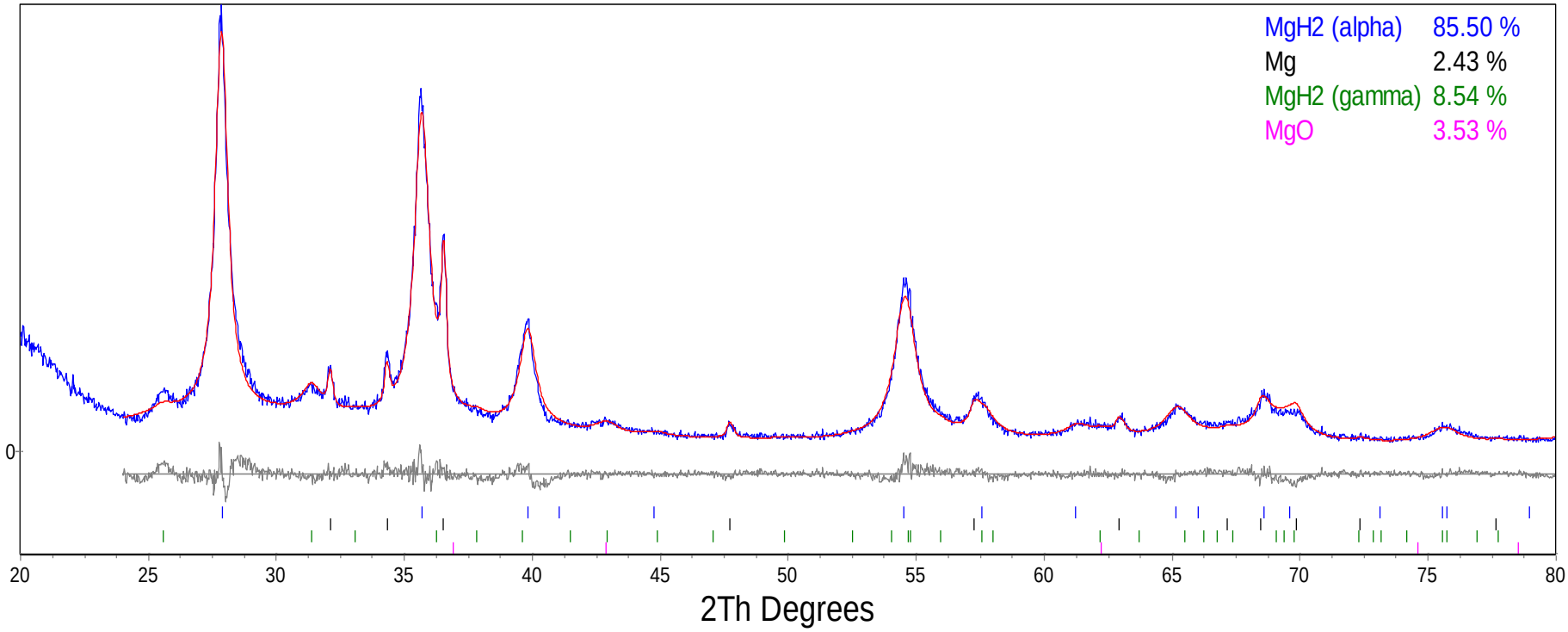

Figure 4.4 Rietveld refinement profile for the 5h milled MgH_2 in Ar, blue line shows the observed data, the calculated data is represented by the red line and the difference is plotted underneath shown by the grey line. Values before 20 (2θ°) did not show any representative peaks and therefore are neglected. Goodness of fit 1.396

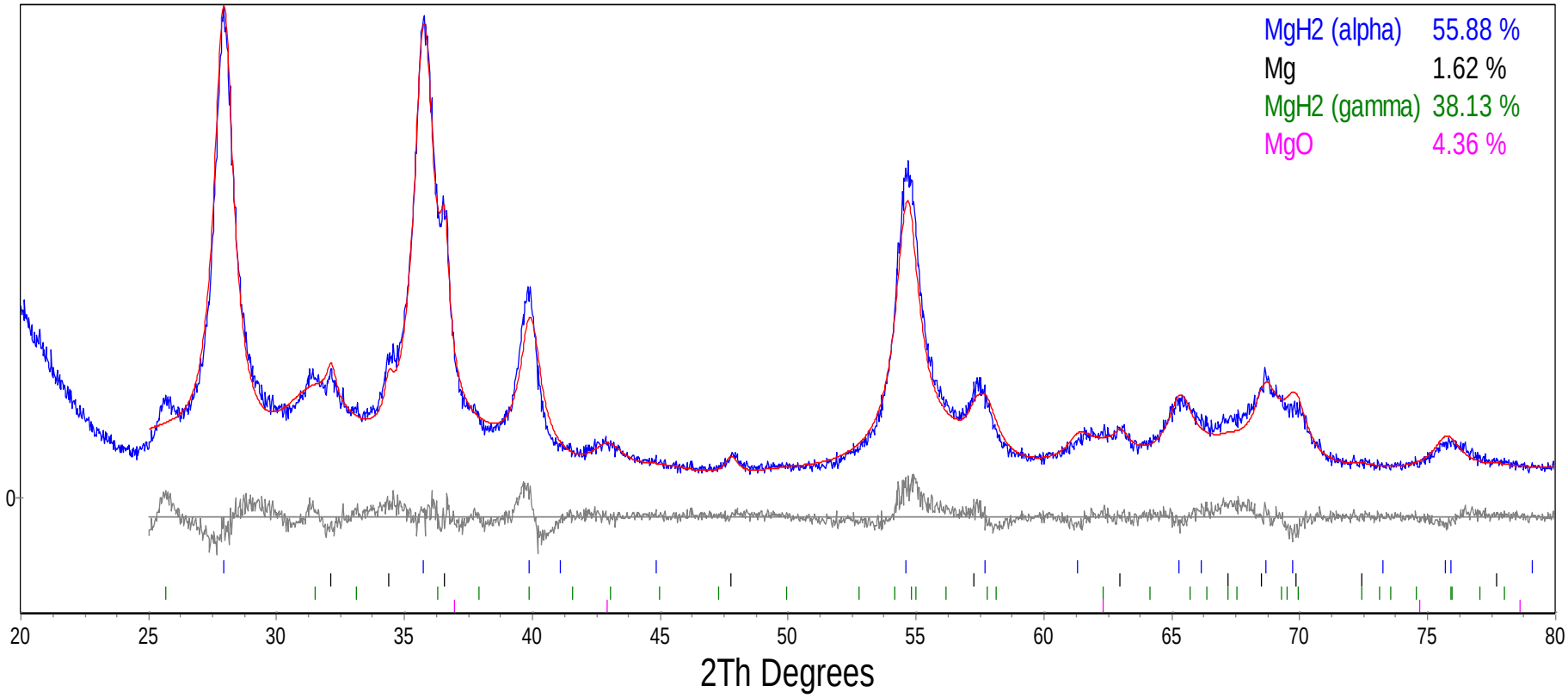

Figure 4.5 Rietveld refinement profile for the 10h milled MgH2 in Ar, blue line shows the observed data, the calculated data is represented by the red line and the difference is plotted underneath shown by the grey line. Values before 20 (2θ°) did not show any representative peaks and therefore are neglected. Goodness of fit 1.751

On the other hand, samples milled in 100 bar H_2 were characterised and their reflections are shown in Figure 4.6. MgH_2 milled in H_2 for 2h shows diffractions related to α-MgH_2, γ-MgH_2, Mg and MgO phases. In comparison to the as received material, peak intensity is reduced and peaks become broader.

The refinement of the sample is shown in Figure 4.7 and shows the values of each phases present in the milled material. It contains 79.4 wt. % α-MgH_2, 13.1 wt. % γ-MgH_2, 2.2 wt.% Mg and the remaining corresponds to MgO.

The sample milled for 5h in 100 bar H_2 show lower intensities for α-MgH_2 and Mg peaks, whereas, γ-MgH_2 and MgO intensities become more intense. The refinement of the sample (Figure 4.8) shows that the material is formed of 71.2 wt. % α-MgH_2, 23.04 wt.(Porto et al., 1967) % γ-MgH_2, 0.6 wt. % Mg and the remaining 5.2 wt. % is MgO.

When milling MgH_2 for 10h in 100 bar H_2, reflections of the γ-MgH_2 and MgO show an increased intensity, while α-MgH_2 and Mg peak intensities further decrease, showing a broadening in the peaks. No other phases were detected from the XRD.

The refinement of the 10h milled sample is shown in Figure 4.9 and allows the quantification of phases. In this case α-MgH_2 accounts for 76.4 wt. %, γ-MgH_2 shows 16 wt. %, Mg 2.5 wt.% and MgO represent the remaining crystalline material.

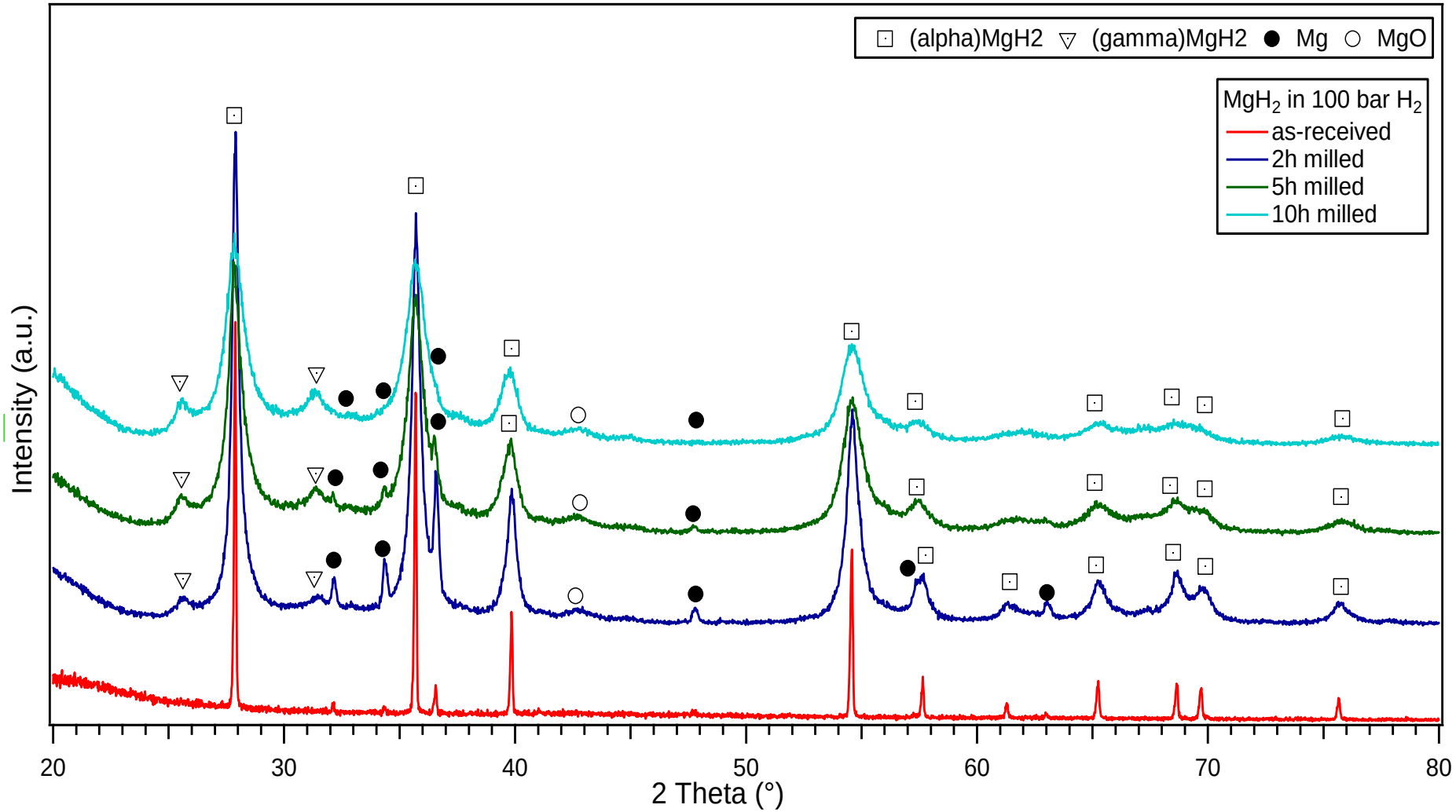

Figure 4.6 XRD reflections of as-received and 2, 5 and 10h milled MgH_2 in 100 bar H_2.

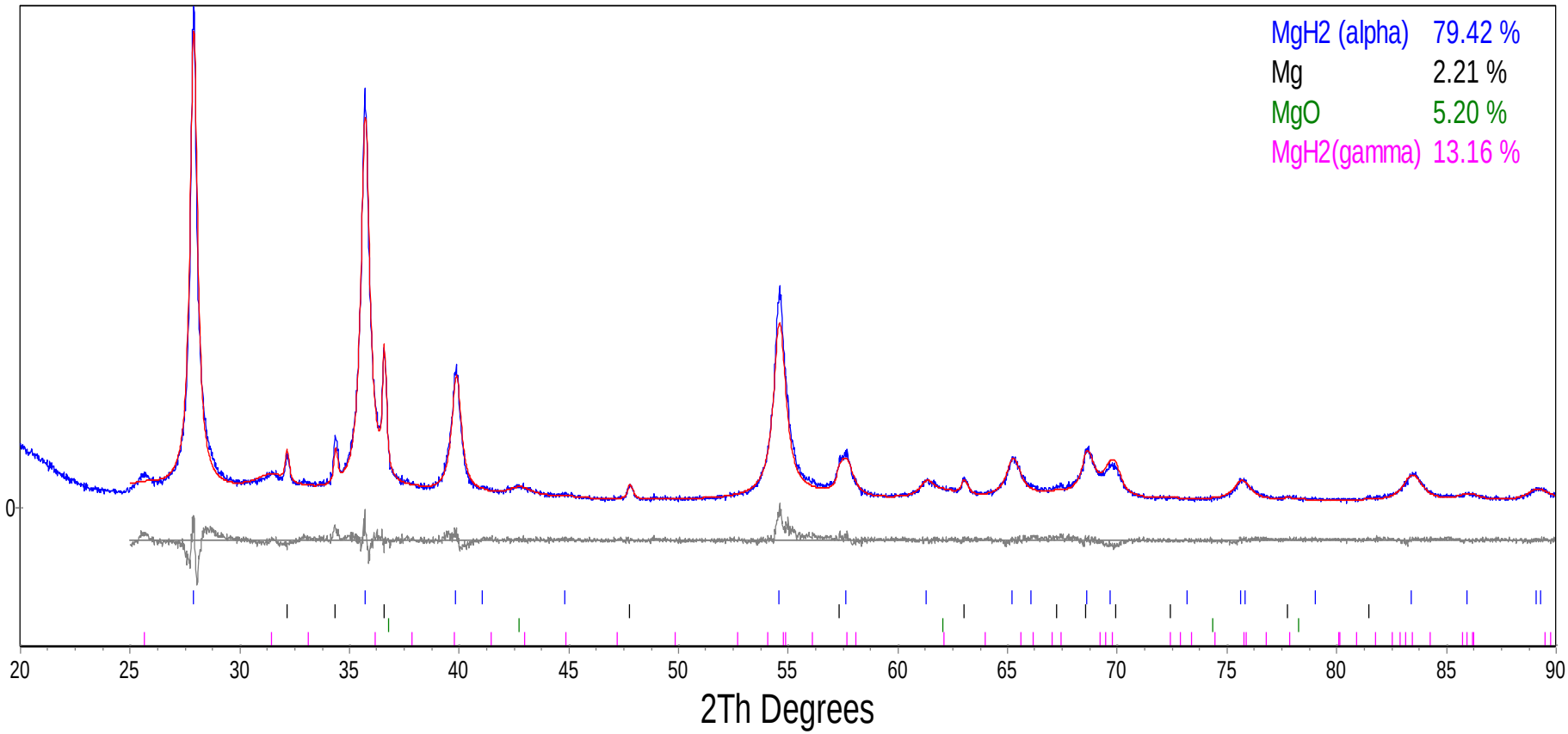

Figure 4.7 Rietveld refinement profile for the 2h milled MgH_2 in 100 bar H_2, blue line shows the observed data, the calculated data is represented by the red line and the difference is plotted underneath shown by the grey line. Diffractions before 20 (20°) did not show any representative peaks and therefore are neglected. Goodness of fit 1.579.

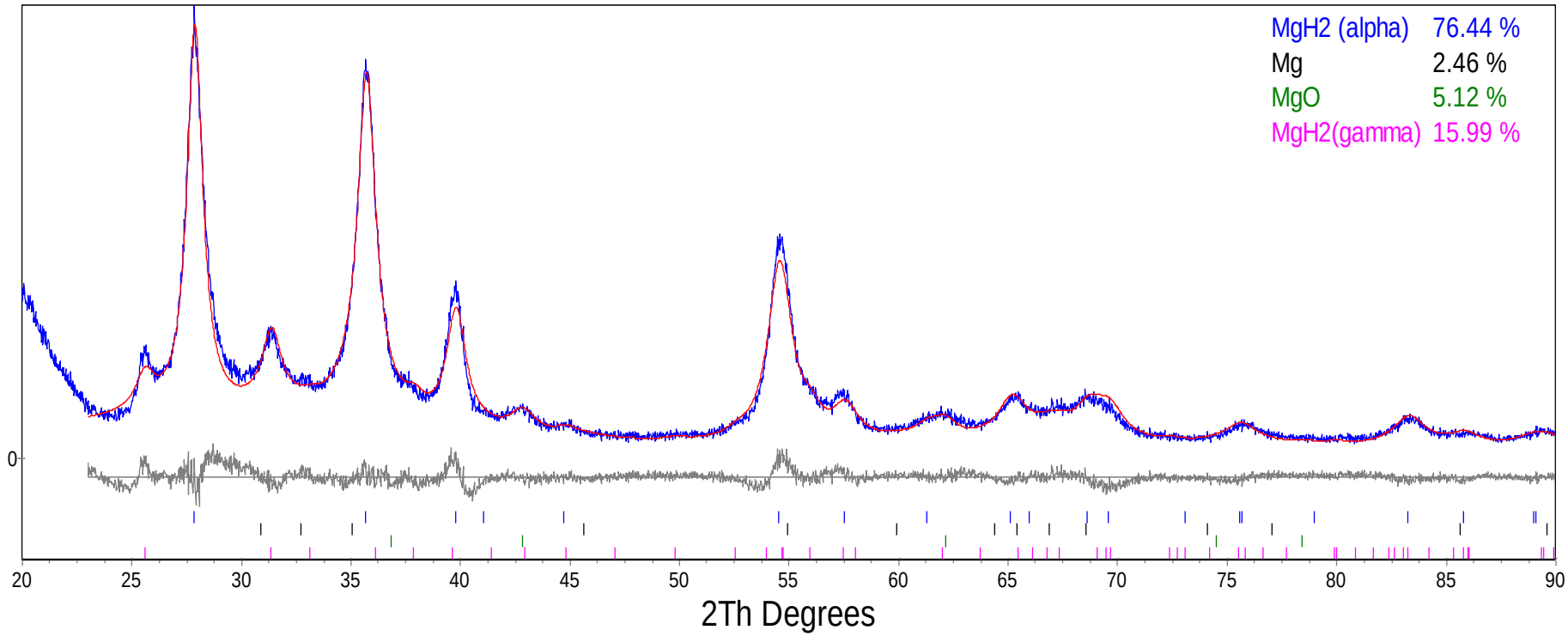

Figure 4.8 Rietveld refinement profile for the 5h milled MgH2 in 100 bar H2, blue line shows the observed data, the calculated data is represented by the red line and the difference is plotted underneath shown by the grey line. Diffractions before 20 (2θ°) did not show any representative peaks and therefore are neglected. Goodness of fit 1.622.

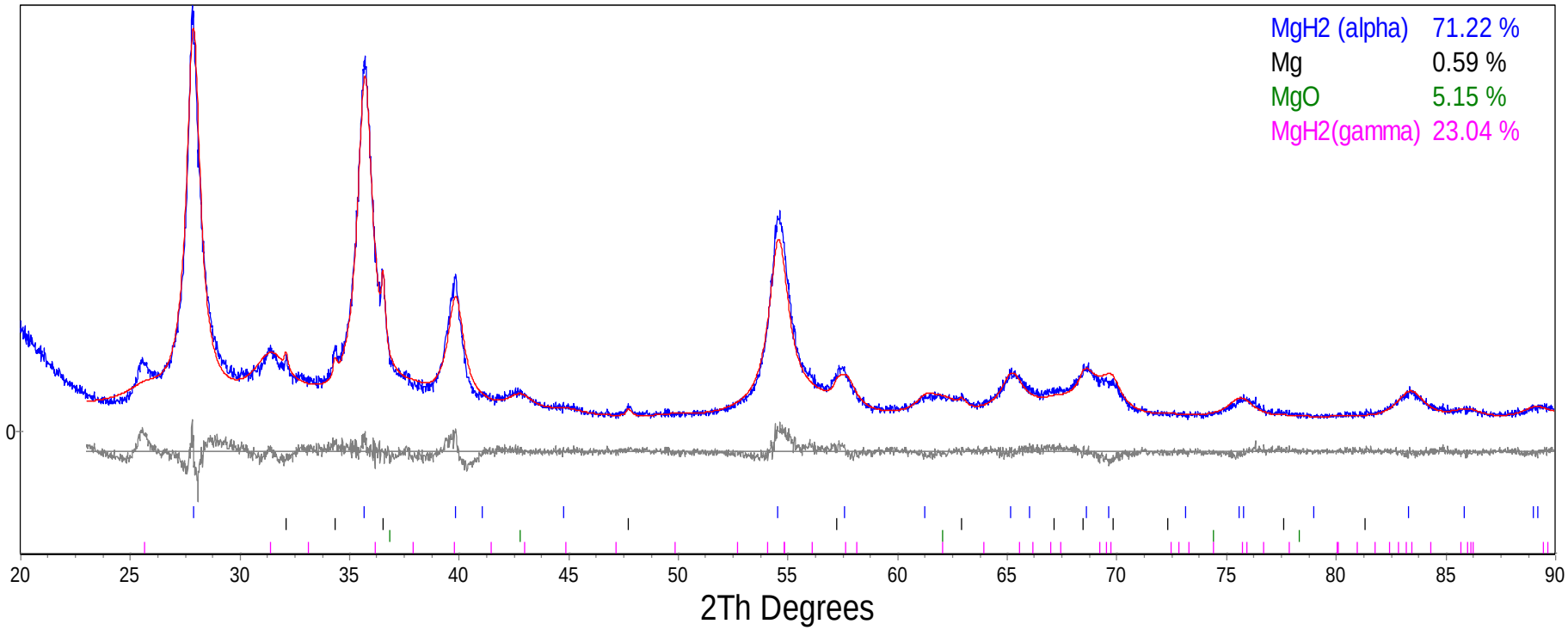

Figure 4.9 Rietveld refinement profile of the 10h milled MgH_2 in 100 bar H_2, blue line shows the observed data, the calculated data is represented by the red line and the difference is plotted underneath shown by the grey line. Diffractions before 20 (2θ°) did not show any representative peaks and therefore are neglected. Goodness of fit 1.556

The unit cell parameters of the as received and milled MgH_2 in Ar and H_2 are summarised in Table 4.1. Furthermore, to enable an easier interpretation of the lattice parameters and cell volumes of samples milled under Ar and H_2, complementary plots illustrated in Figure 4.10 and 4.11 were constructed. From this, it is observed that α-MgH_2 has a tetragonal structure with space group P42/mnm, Mg has a hexagonal structure with space group $P6_3/mmc$ space group and γ-MgH_2 shows an orthorhombic structure with space group Pbcn.

The lattice a and c after milling MgH_2 for 2h in Ar increase in size up to 5h, on further milling for 10h the unit cell contracts. The same tendency is followed for the other phases present in the samples milled in Ar.

On the contrary, unit parameters and cell volumes of the MgH_2 samples milled under 100 bar H_2 increase with the milling even after milling the sample for 10h.

The change in lattice parameters could be related to several factors such as deformation or substitution due to the milling. In this case, is most likely that is due to a reduction in the crystallite sizes of the samples as the milling time increases as shown in Figure 4.12.

Table 4.1 Summary of the unit cell parameters of the as-received and milled MgH_2 for 2, 5 and 10h in Ar and H_2 atmospheres.

	Milling Time	α-MgH_2			γ-MgH_2				Mg		
		Lattice parameters (Å)		Cell Volume (Å^3)	Lattice parameters (Å)			Cell Volume (Å^3)	Lattice parameters (Å)		Cell Volume (Å^3)
		a	c		a	b	c		a	c	
Ar	2	4.523± 0.002	3.025± 0.001	61.87± 0.05	4.545± 0.007	5.413± 0.009	4.953± 0.008	121.89± 0.03	3.215± 0.001	5.220± 0.002	46.72± 0.04
	5	4.524± 0.001	3.024± 0.001	61.91± 0.02	4.546± 0.007	5.414± 0.009	4.954± 0.008	121.94± 0.03	3.216± 0.001	5.220± 0.001	46.77± 0.02
	10	4.516± 0.001	3.021± 0.001	61.63± 0.02	4.519± 0.012	5.405± 0.012	4.946± 0.011	120.84± 0.06	3.216± 0.001	5.216± 0.003	46.71± 0.03
H_2	2	4.520± 0.001	3.023± 0.001	61.77± 0.01	4.528± 0.010	5.407± 0.012	4.961± 0.011	121.48± 0.04	3.212± 0.001	5.216± 0.001	46.62± 0.01
	5	4.524± 0.001	3.024± 0.001	61.90± 0.01	4.531± 0.006	5.403± 0.007	4.966± 0.007	121.58± 0.03	3.217± 0.001	5.221± 0.001	46.81± 0.02
	10	4.528± 0.001	3.023± 0.001	61.97± 0.02	4.546± 0.003	5.408± 0.004	4.969± 0.005	122.16± 0.02	3.339± 0.001	5.47± 0.02	52.86± 0.03
as-received		4.518± 0.001	3.023± 0.001	61.72± 0.02					3.211± 0.001	5.209± 0.001	46.53± 0.01

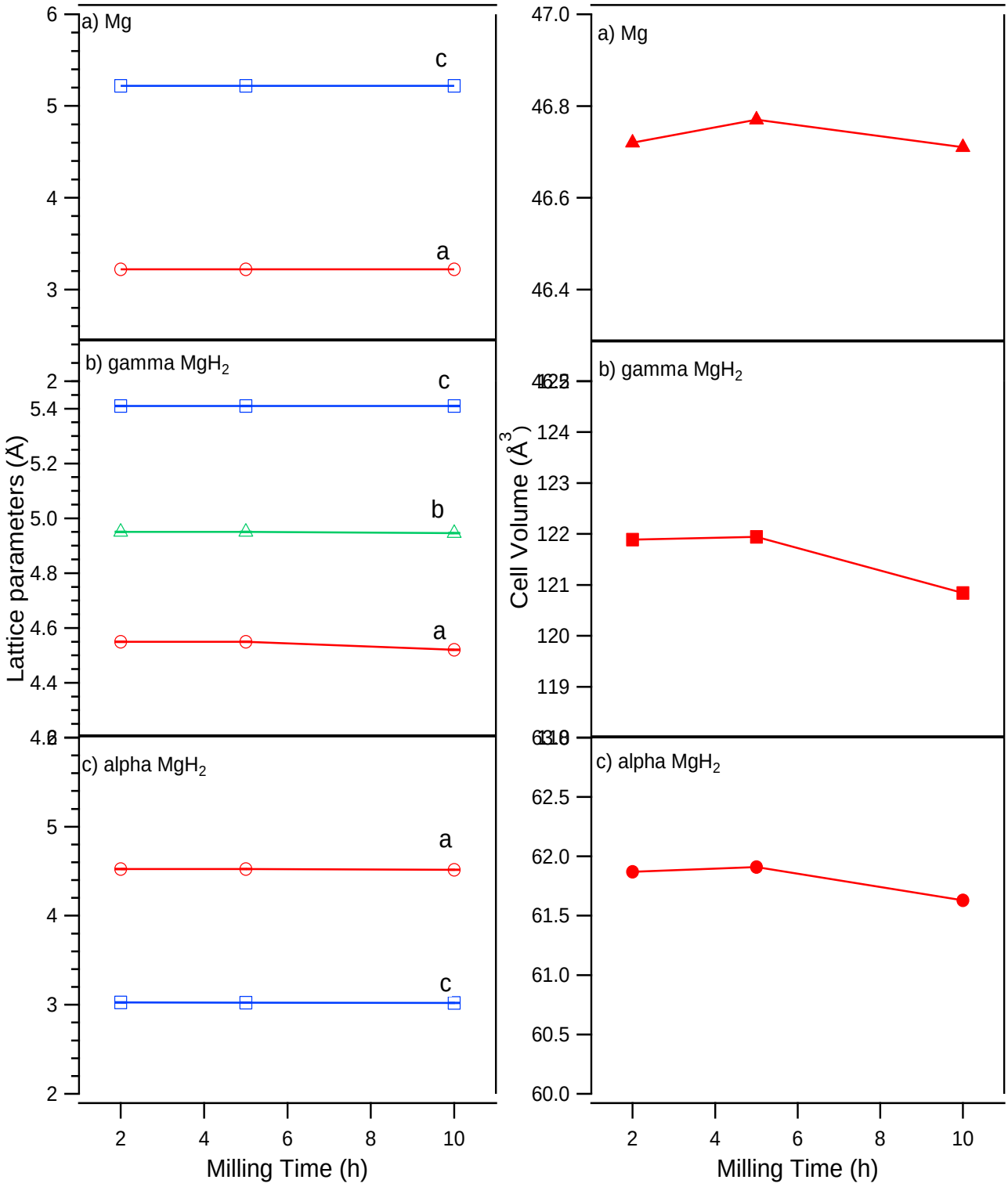

Figure 4.10 Lattice parameters and cell volumes of the 2, 5, 10 h MgH_2 milled in Ar a) Mg, b) γ-MgH_2 and c) α-MgH_2 plotted in function of the milling time. Where error bars are not shown, they are smaller than data symbols. Solid lines are a guide for the eye.

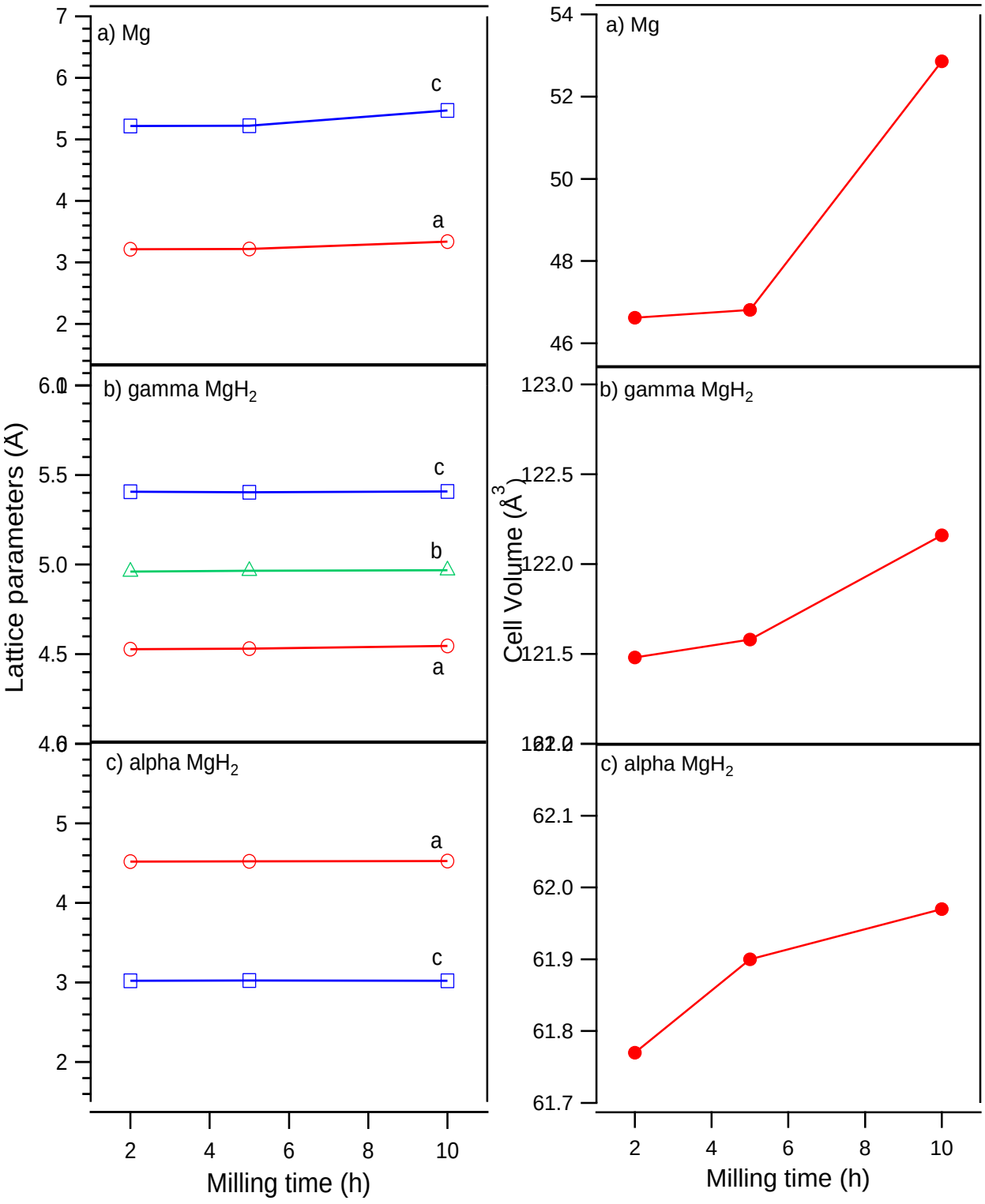

Figure 4.11 Lattice parameters and cell volumes of the 2, 5, 10 h MgH_2 milled in 100 bar H_2 a) Mg, b) γ-MgH_2 and c) α-MgH_2 plotted in function of the milling time. Where error bars are not shown, they are smaller than data symbols. Solid lines are a guide for the eye.

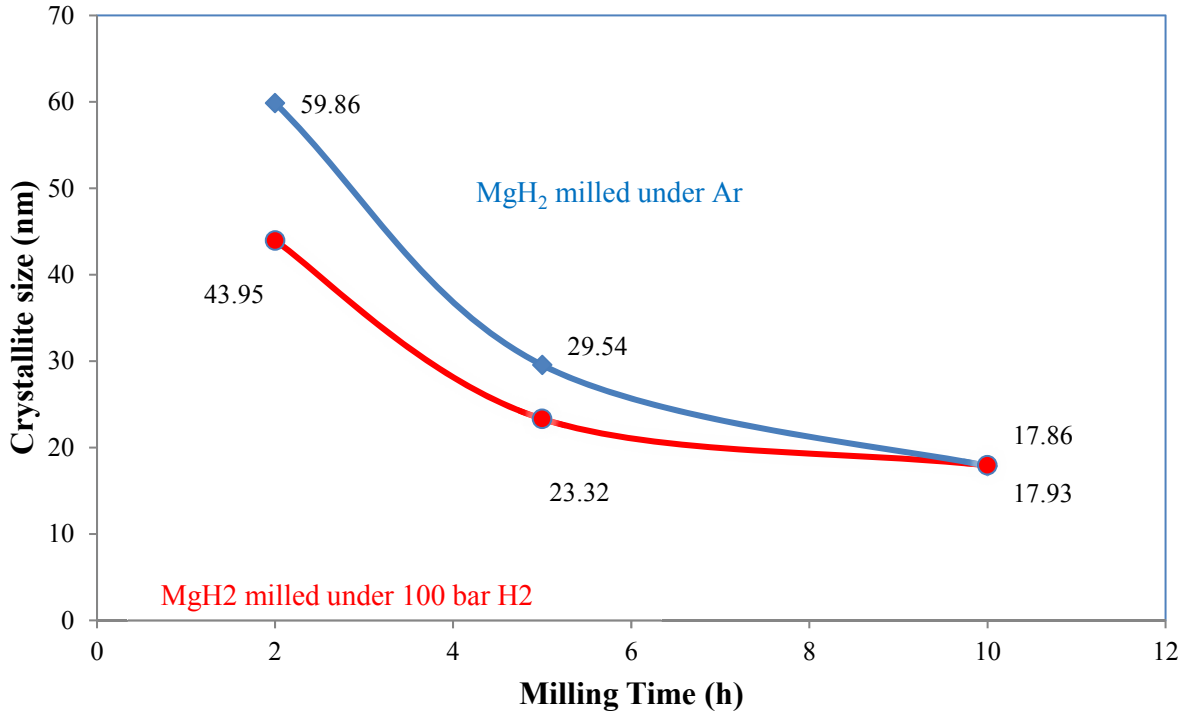

Figure 4.12 Estimated crystallite size vs milling time for MgH_2 samples milled under Ar and 100 bar H_2 for 2, 5 and 10 h.

Raman spectrum for the as-received MgH_2 is shown in Figure 4.13. Porto et al.(Porto et al., 1967) showed that there are four Raman active vibrational modes B_{1g}, E_g, A_{1g}, and B_{2g}. The B_{2g} mode was very weak, almost unresolvable with the E_g and A_{1g} modes being the strongest. Santisteban et al.(Santisteban et al., 2000) applied this model to the hydride measuring three modes. As-received MgH_2 vibrational spectrum reported by Book and Reed (Reed and Book, 2011) will be used in this investigation.

The Raman vibrations of the as-milled MgH_2 samples in Ar are illustrated in Figure 4.14. The samples milled for 5 and 10h did not show any representative peaks. Therefore, are not plotted in the graph. As for the 2h milled sample, Raman spectrum shows 3 peaks at 318.3, 947.1 and 1264 cm^{-1} linked to B_{1g}, E_g and A_{1g} modes respectively. These results agree well with the modes

reported in the literature for the as-received material. (Reed and Book, 2011, Porto et al., 1967, Santisteban et al., 2000, Kuzovnikov et al., 2013)

Consequently, Raman spectroscopy was performed in the 2, 5 and 10h milled samples in 100 bar H_2 as shown in Figure 4.15. The 2h milled sample, show an intense background noise, nevertheless, it is possible to detect the 3 vibrational modes located at 317.8 (B_{1g}), 947.6 (E_g) and 1257.9 (A_{1g}).

Similar vibrations are observed in the 5h and 10h milled samples, although, in both of these samples there are additional vibrations peaking at 179.6, 253.5, 586.9 and 657.3 cm^{-1}, which may be related to γ–MgH_2 phase vibrations according to investigations reported by Kuzovnikov et al.(Kuzovnikov et al., 2013), where intense peaks were achieved at 186 and 660 cm^{-1}. In addition, some other weak peaks were observed at 313 and 509 cm^{-1}.

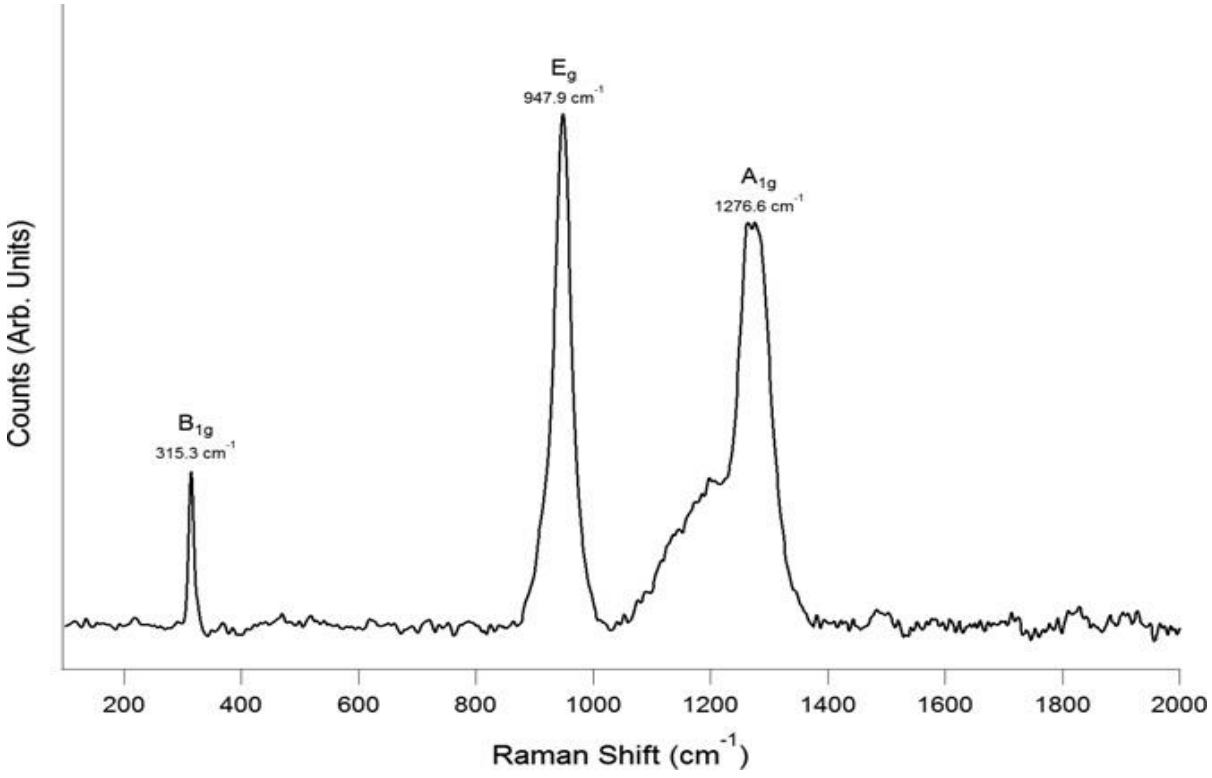

Figure 4 13 Raman spectrum of as-received MgH_2 using the 633 nm excitation laser. Reproduced from *(Reed and Book, 2011)*

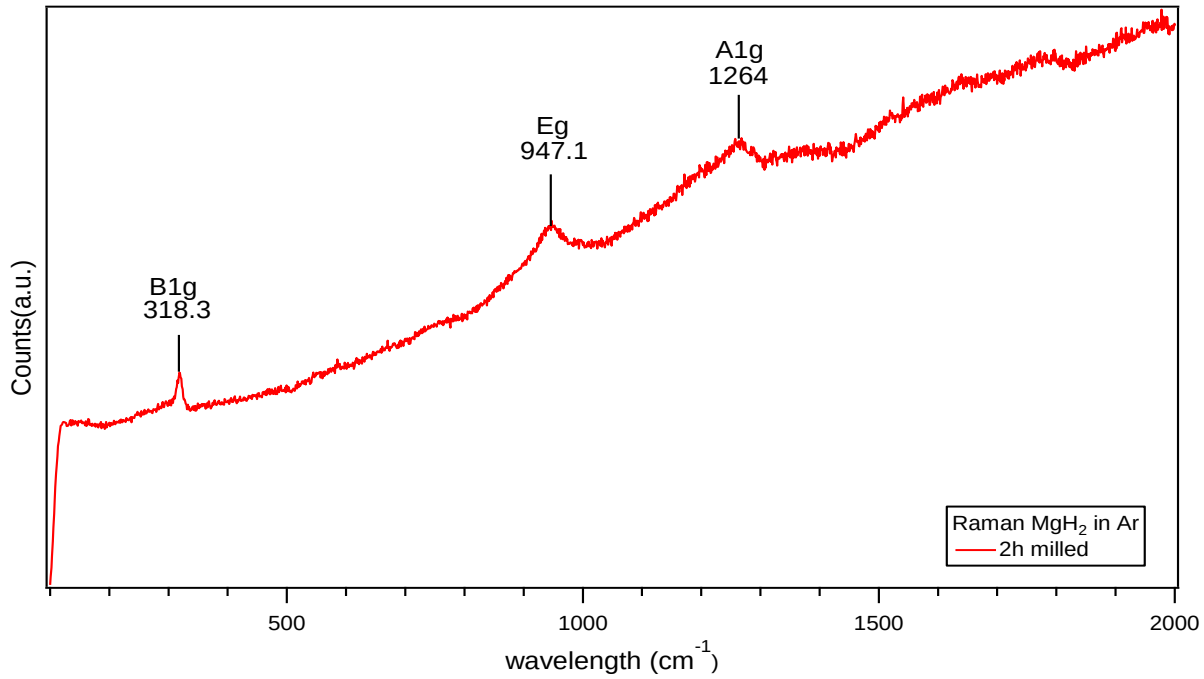

Figure 4.14 Raman spectrum of the 2h milled MgH_2 in Ar using the 633 nm excitation laser.

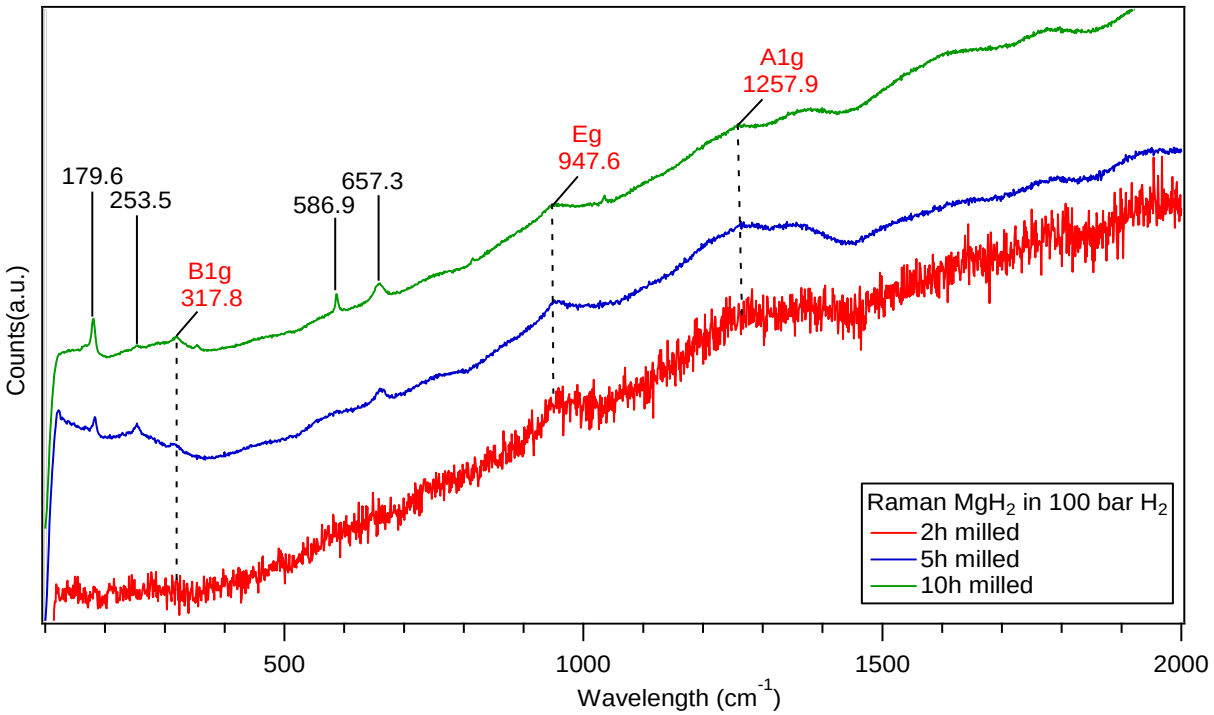

Figure 4.15 Raman spectrum of the 2, 5 and 10h milled MgH_2 in 100 bar H_2 using the 633 nm excitation laser.

Raman modes reported in previous studies and obtained experimentally in this work are summarised in Table 4.2. It is important to highlight that to the best of the author's knowledge the Raman modes for the 2, 5 and 10h milled MgH_2 in Ar and 100 bar H_2 are reported for the first time.

Table 4.2 Summary of the as-received and 2, 5 and 10h milledMgH_2 in Ar and 100 bar H_2 Raman modes compared to previous reports.

Atmosphere	Milling time (h)	Raman Modes			Other Raman modes	
		α-MgH2			γ-MgH2 (Kuzovnikov et al., 2013)	
		B_{1g} (cm^{-1})	E_g (cm^{-1})	A_{1g} (cm^{-1})		
Ar	2	318.3	947.1	1264		
	5, 10	-	-	-		
H2	2	317.8	947.6	1257.9		
	5, 10	317.8	947.6	1257.9	586.9	657.3
					179.6	253.5
as-received(Reed and Book, 2011)		315.3	947.9	1276.6		
(Santisteban et al., 2000)		300	950	1276		

4.3 Thermal Decomposition

DSC was performed to investigate the decomposition reactions and temperatures of the as-received and milled samples in Ar and 100 bar H_2. Figure 4.16 (a) shows the DSC curves of the as-received and as-milled MgH_2 for 2, 5 and 10 h in Ar. The as received hydride, show one large endothermic curve starting at around 370 °C, peaking at 392 °C. This is related to the

decomposition of MgH_2 into Mg, releasing H_2, the desorption is completed at 415 °C. TGA measurements (Figure 4.16 (b)) performed on the as-received material show a total desorption of 6.8 wt. % H_2 up to 410 °C, compared to 7.6 wt.% expected for the complete decomposition of the as-received MgH_2 (Jain et al., 2010a), it is evident that the expected H_2 capacity is decreased. This effect can be explained due to the impurities of the as-received material; containing a small fraction of Mg which is leading to less hydrogen desorption capacity, besides other impurities associated with the handling of the material.

Sample milled for 2h in Ar shows that dehydrogenation starts at around 300 °C and reaches a maximum at 350 °C, only one single endothermic reaction is observed, linked to the dehydrogenation of MgH_2. A total amount of 6.60 wt. % H_2 desorption was observed at 400 °C from the TGA.

On the 5h milled sample in Ar, DSC presents one strong endothermic reaction starting at approximately 290 °C, centred at 332.8 °C followed by a shoulder peaking at 340.5 °C up to 387.3 °C; this corresponded to a total amount of 6.52 wt. % H_2 released. The shoulder observed in this sample might be associated with the decomposition of α-MgH_2 phase given that this phase decomposes at higher temperatures (Varin et al., 2006) than γ-MgH_2.

The 10h milled material in Ar exhibits one-step desorption with an onset temperature of 251.8 °C and the main peak at 322.9 °C. A total amount of 5.69 wt. % H_2 evolution was detected up to 356.9 °C when the reaction was ended. The strong endothermic reaction observed from the DSC is linked to the decomposition of the MgH_2 into Mg releasing H_2.

A summary of the onset, peak and final temperatures experimentally obtained from the DSC and TGA of the MgH_2 samples milled in Ar are plotted in Figure 4.18.

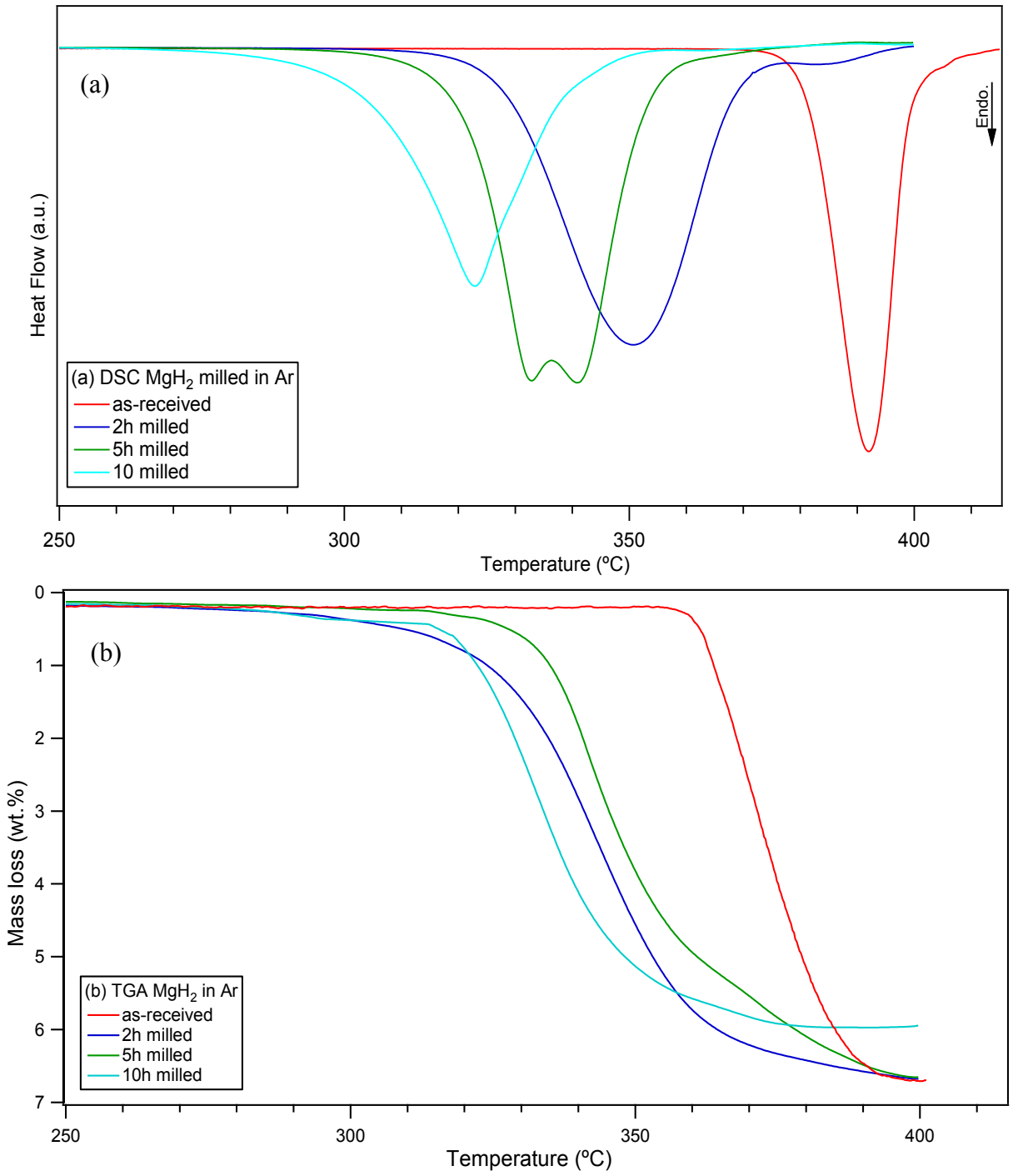

Figure 4.16 (a) DSC, (b) TGA measurements of as-received and 2, 5 and 10h mechanically milled MgH_2 in Ar. All measurements were performed at a heating rate of 2 °C/min under flowing 3 bar Ar at 100 ml/min (DSC) and at 1 bar Ar flowing at 40 ml/min (TGA). Temperatures before 250 °C do not show any representative peaks and thus, DSC and TGA curves are plotted from 250 up to 415 °C.

In terms of hydrogen desorption capacity, it is known that as the milling increases, the capacity decreases. (Ares et al., 2007) Thus, the 10h milled sample shows 5.7 wt. % desorbed which is lower than the experimental H_2 capacity obtained in this work for the as-received (6.7 wt.%), 2h milled (6.5 wt.%) and 5h milled (6.3 wt. %) Mg hydrides in Ar. On the other hand, it is observed that the onset temperature is reduced from 370 °C (as-received MgH_2) to 251.8 °C for the 10h milled material. Thus, demonstrating the effect of the milling in the decomposition temperatures of the samples.

Consequently, samples milled under H_2 were investigated through DSC and TGA measurements. Figure 4.17 (a) shows the DSC endotherms of the as-received and as-milled samples for 2, 5 and 10h under 100 bar H_2. TGA measurements for the same samples are illustrated in Figure 4.17 (b) presenting the mass loss of H_2 against the temperature.

The 2h milled sample in H_2 exhibits a single step dehydrogenation reaction. The desorption peak starts to desorb H_2 at around 278.8 °C, the endotherm shows it main deflection at 340.8 °C. This corresponds to the desorption of a total amount of 6.65 wt.% of H_2 up to 389.5 °C. The reaction proceeds as shown in equation 4.1.

$$MgH_2 \Rightarrow Mg + H_2 \qquad (4.1)$$

The dehydrogenation of the MgH_2 that had been milled for 5h in H_2 starts at around 251.8 °C peaking at 334.5 °C followed by a sluggish shoulder up to 363.8 °C; this corresponded to a total amount of 6.61 wt. % of H_2 released up to 387.8 °C. The shoulder detected in the desorption may be associated with the decomposition of the α-MgH_2 which occurs at higher temperatures than the γ -MgH_2 (Varin et al., 2006).

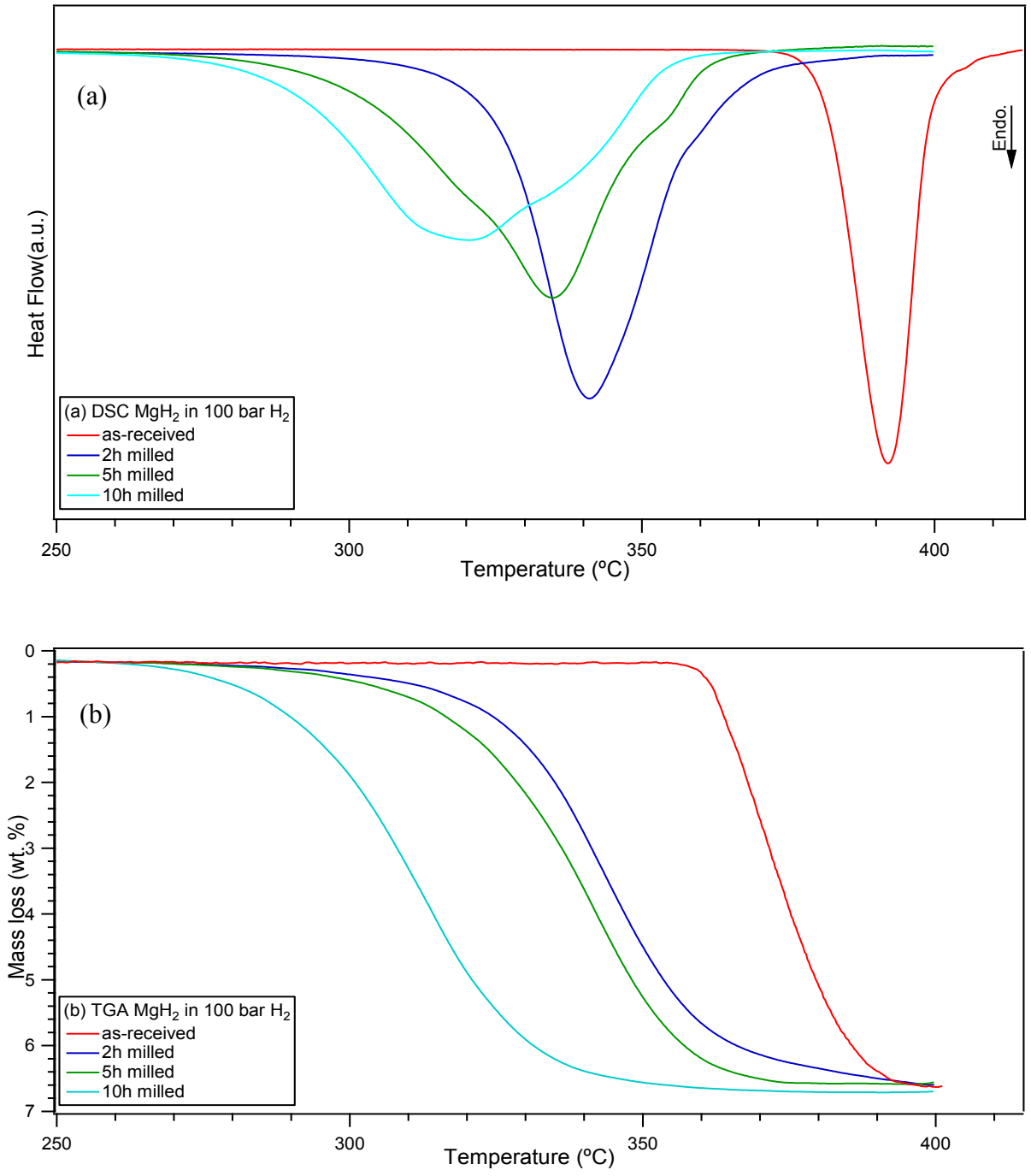

Figure 4.17 (a) DSC, (b) TGA measurements of as-received and 2, 5 and 10h mechanically milled MgH_2 in 100 bar H_2. All measurements were performed at a heating rate of 2 °C/min under flowing 3 bar Ar at 100 ml/min (DSC) and at 1 bar Ar flowing at 40 ml/min (TGA). Temperatures before 250 °C do not show any representative peaks and thus, DSC and TGA curves are plotted from 250 °C to 415 °C where the reactions were completed.

The MgH_2 milled for 10h in H_2 sample also displays one single endotherm starting at 249.6 °C and reaches a maximum at 319.4 °C followed by a small shoulder at 371.6 °C.

The total amount of H_2 evolution equals 6.55 wt. %. Again, the shoulder presented in this sample is related to the dehydrogenation of the γ-MgH_2 phase as previously discussed.

Figure 4.19 illustrates the onset, peak and final temperatures of the milled MgH_2 samples in 100 bar H_2 versus the milling time (2,5 and 10 h).

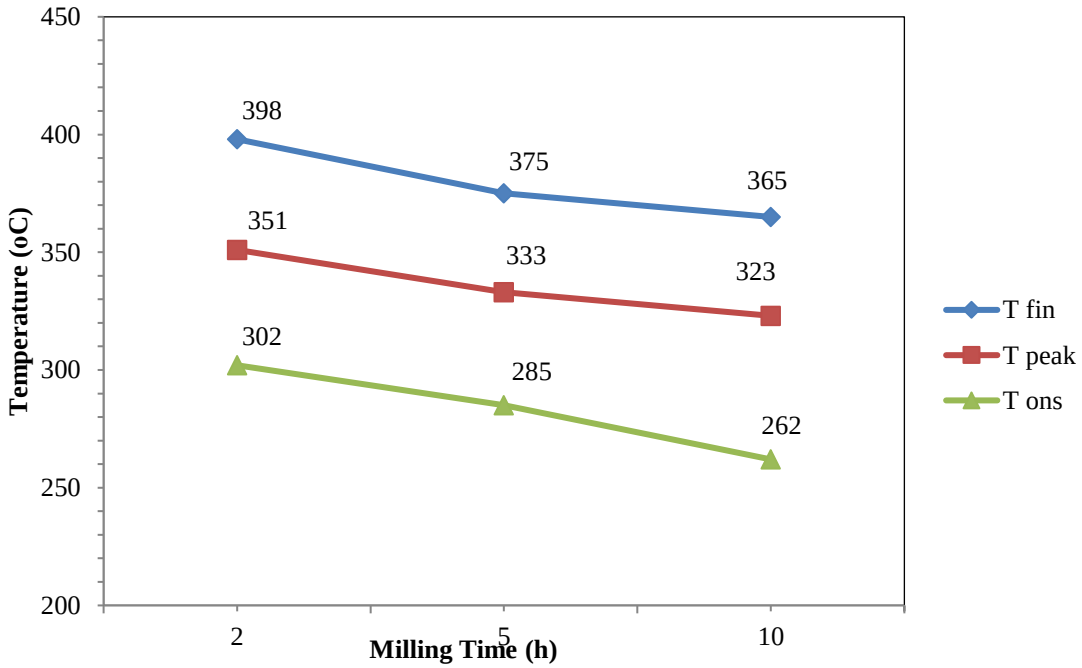

Figure 4.18 Hydrogen desorption temperatures (onset, peak, final) vs milling time of mechanically milled MgH_2 under Ar for 2, 5 and 10 h.

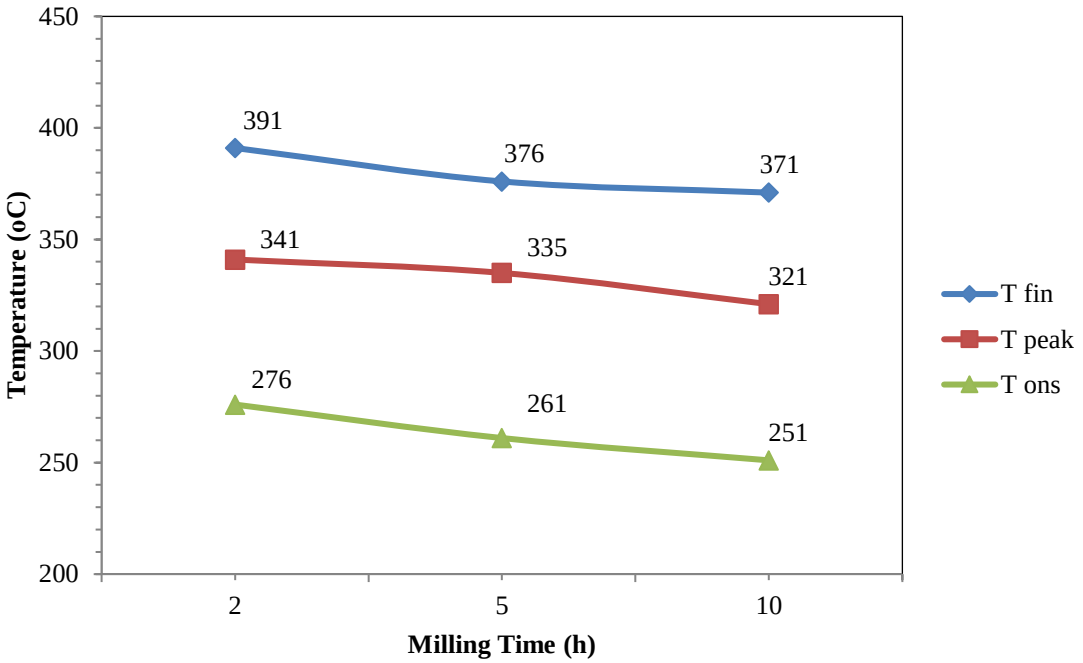

Figure 4.19 Hydrogen desorption temperatures (onset, peak, final) vs milling time of mechanically milled MgH_2 under 100 bar H_2 for 2, 5 and 10 h.

4.4 Analysis of Decomposition Products

The analysis of the products after decomposing the sample were investigated by in-situ X-ray diffraction in order to understand the phase changes and reactions as a function of temperature. Figure 4.20 illustrates the in-situ XRD of MgH_2 that had been milled for 2h in Ar loaded in a boron nitride sample holder heated at 2 °C/min in He flowing at 100 ml/min with patterns taken isothermally every 25 °C intervals between room temperature (RT) and 400 °C. It is worthwhile to mention that the in-situ measurements were performed only in one milled sample given that the decomposition of the 5 and 10h milled samples in Ar and H_2 followed the same dehydrogenation path.

At room temperature, the sample contains only MgH_2 and some Mg. Refinement performed to evaluate the quantity of each crystalline material in the sample confirmed the two phases, in addition to reflections related to the corundum sample holder. MgH_2 corresponded to 92 wt. %,

Mg showed a 3 wt. % of the sample, whereas the remaining crystalline material (5 wt. %) was linked with the diffractions of the sample holder.

On further heating up to 225 °C, the 2θ diffractions of MgH_2 increase with the temperature, while the Mg reflections slightly decrease. This effect on the Mg may be linked with the formation of an MgO phase. Refinement performed showed that sample contains 80 wt. % of MgH_2, 2 wt.% of Mg and the remaining crystalline material (18 wt. %) corresponds to MgO.

At 250 °C, MgH_2 phase starts to decompose showing an abrupt decrease in peak intensity, whereas Mg reflections intensity increase. MgO peaks become more intense as well. When refining the sample, it is observed that MgH_2 occupies only a 47 wt. % of the sample, while Mg accounts for 17 wt. % of the sample. This decomposition temperature agrees well with TGA dehydrogenation.

When increasing the temperature to 300 °C, Mg phase become stronger and it is shown in the peak intensity. MgH_2 phase is still present at this temperature. However, its intensity is decreased even further, this is evident due to the size of the peaks. Refinement performed on the sample at this temperature confirmed our observations showing that Mg phase occupies a total of 34 wt. % of the sample, while MgH_2 phase accounts for only 3 wt. %. The remaining crystalline material is associated to the oxidation of the Mg phase.

From 325 °C to 400 °C the only reflections remaining are Mg and MgO increasing in intensity with increasing temperature, which demonstrates that MgH_2 has completely decomposed into Mg releasing hydrogen which is correlates with the DSC and TGA results. When refining the sample at 400 °C, Mg phase accounts for 27 wt. % of the total crystalline material, whereas, MgO occupies a 66 wt.%. The strong reflections of MgO phase, can be explained due to a small leak in the instrument which causes the Mg to oxidase on heating.

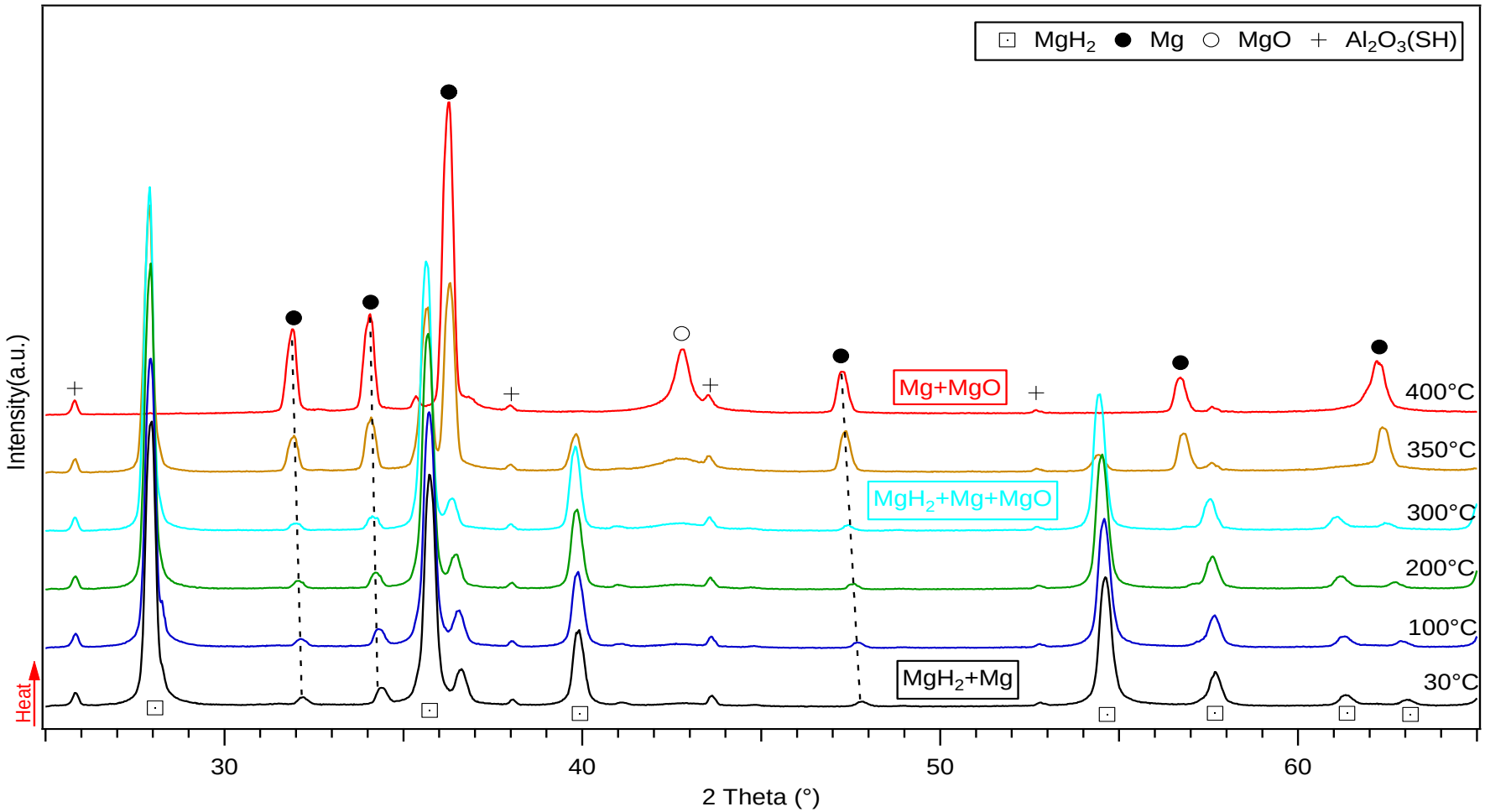

Figure 4.20 In-situ XRD diffractions of the 2h milled MgH2 in Ar, heated at 2 °C/min under 3 bar He flowing at 100 ml/min. Reflections below 25 (2θ°) were not considered as no representative diffractions were detected.

4.5 Conclusions

As received and mechanically milled MgH_2 for 2, 5, 10h under 2 argon and hydrogen atmospheres were investigated to compare the behavior of the material and the phase changes during the milling process. In total 6 samples were synthesised and characterised through XRD, Raman spectroscopy, DSC, TGA and in-situ X-ray diffraction measurements.

XRD measurements after 2, 5, 10h milling MgH_2 under Ar and 100 bar H_2, showed peaks corresponding to the α–MgH_2 phase which were less intense and broader than those in the as received material. Moreover, peaks corresponding to the γ–MgH_2 phase were also detected on milled samples. The increase in peak widths is an indicative of a reduction in estimate crystallite size from 207nm for as received material to 18nm for the 10h milled MgH_2 which contributes to decreasing the desorption temperatures.

Raman spectroscopy showed that for the milled samples under Ar, only the 2h sample was Raman active. The vibrational modes observed in the material were consistent with previous investigations from the literature (Reed and Book, 2011, Santisteban et al., 2000), showing 3 main modes B_{1g}, E_g and A_{1g} at 318.3, 947.1 and 1264 cm^{-1} respectively. Furthermore, the Raman spectrum of the samples milled under 100 bar H_2 showed that the 2, 5 and 10h milled samples were Raman active given that in all the samples the 3 main vibrational modes located at 317.8 (B_{1g}), 947.6 (E_g) and 1257.9 (A_{1g}) related to MgH_2 phase were observed.

Moreover, according to reported investigations performed by Kuzovnikov et al.(Kuzovnikov et al., 2013) on the γ–MgH_2 showed that in addition to the 3 main modes, intense peaks were detected at 186 and 660 cm^{-1} and some other weak modes at 313 and 509 cm^{-1}. These additional modes corresponding to the γ–MgH_2 were also observed in our work on the 5 and 10h milled samples under 100 bar H_2 at 179.6, 657.3 cm^{-1} and 253.5, 586.9 cm^{-1}. There is a slight difference

with the vibrational modes observed from the literature, this effect can be attributed to the mechanical milling of the samples, due to the given reference reported the study of the as-received MgH_2.

It is important to highlight that to the best of the author's knowledge, reports of Raman spectroscopy on milled MgH_2 were not reported in the literature. Therefore, for the first time in this thesis was experimentally confirmed that ball milled samples were Raman active and results were consistent with previous measurements performed on the as-received MgH_2. However, there was observed a slight difference in the Raman modes between the as-received and milled samples which might be attributed to the mechanical milling process. Nevertheless, further investigations are needed to corroborate this hypothesis.

Thermal decomposition of the as-received and milled products in Ar and H_2 were performed to further understand the material behaviour and decomposition mechanisms. DSC measurements specified that desorption proceeds in one single step reaction for both groups of samples milled in Ar and H_2. A shoulder was evidenced in the DSC curves; this extension is associated with the decomposition of the γ-MgH_2 phase which according to the literature decomposes at lower temperatures than the α- MgH_2.

As for hydrogen storage properties in the samples milled under Ar, onset dehydrogenation temperature was reduced by up to 118 °C from 370 °C for the as-received MgH_2 to 251.8 °C for the 10h milled sample. Although, the hydrogen capacity was also decreased when increasing the milling time, thus, the as received material released 6.8 wt. % of H_2, whereas, the 10h milled sample showed an evolution of 5.7 wt. % H_2, which is 1.1 wt. % H_2 less than the as-received sample and corresponds to only 83.8 wt. % of the total capacity of the same.

The hydrogen desorption temperatures of the samples milled in 100 bar H_2, indicate a decrease in the onset desorption temperature in comparison to the as-received MgH_2 of approximately 120 °C. From 370 °C (as-received) to 249.6 °C (10h milled). This temperature is 2 °C lower than the results obtained in the samples milled under Ar. Although, again a reduction in the hydrogen capacity was detected in the MgH_2 milled in H_2 from 6.8 wt.% for the as-received sample to 6.55 wt.% for the 10h milled sample. This is just 0.25 wt.% less than the experimentally achieved for the as-received MgH_2, which evidences that milling in H_2 has a positive effect in the dehydrogenation of the MgH_2 in comparison to the Ar milled samples.

From these results (Figure 4.18 and 4.19), it is clear that hydrogen sorption properties of MgH_2 can be altered by mechanical milling. Furthermore, it was observed that as the milling increases, the hydrogen desorption temperature is decreased but so is the hydrogen capacity.

Nevertheless, none of the sample experimentally studied in this work, were able to approach to the theoretical hydrogen capacity of 7.6 wt. % H_2 for the MgH_2.

In-situ XRD showed that the milled MgH_2 starts the decomposition process at around 250 °C; where MgH_2 diffraction intensities decrease and Mg peaks become more intense, up to 400 °C. At this temperature reflections of the MgH_2 phase are no longer detected and the only remaining phases observed in the sample corresponded to Mg and MgO. The last is believed to be formed by the oxidation of Mg on the decomposition process due to a small leak in the apparatus used for the measurement. Results from in-situ XRD show a good agreement with the experimental data observed from the DSC and TGA in this thesis.

Although, the desorption temperature was significantly decreased around 120 °C with increasing the milling time (10h), temperatures about 250 °C remain still high for practical on-board applications.

CHAPTER V

5. RESULTS AND DISCUSSION: LITHIUM MAGNESIUM ALLOY

5.1 Introduction

Li-Mg-H hydrides are potential candidates for hydrogen storage due to their high theoretical gravimetric hydrogen density 8.8 and 9.5 wt. % H_2 for $LiMgH_3$ and Li_2MgH_4 respectively (Vajeeston et al., 2008, Li et al., 2011).

Ikeda et al.(Ikeda et al., 2005b) tried to synthesise the hydride experimentally. Unfortunately, attempts were unsuccessful. (Vajeeston et al., 2008), (Pfrommer et al., 1994) and (Li et al., 2011) predicted the structure of $LiMgH_3$ (R3c space group $LiTaO_3$–type) and Li_2MgH_4 (Pbam space group Na_2MgCl_4-type) from computational methods.

Current work performed by Guo S.(Guo, 2015), reported the hydrogenation of Li-Mg ribbon into LiH and $Mg_{(1-x)}Li_xH_2$ (x = ~0.04) using high-pressure milling. Furthermore, decomposition of Li-Mg hydrided samples was described and a hydrogen desorption temperature was lowered from 900 to 470 °C.

Many attempts have been performed to try to synthesise $LiMgH_3$ and Li_2MgH_4 using various methods and techniques (Ikeda et al., 2005b, Vajeeston et al., 2008, Smith et al., 2010, Li et al., 2011, Guo, 2015, Pfrommer et al., 1994). However, to date, none of the experimental studies have been able to synthesise such hydrides.

Therefore, this chapter will investigate the formation ability of Li-Mg-H ternary hydrides from a Li-Mg alloy via high-energy reactive milling under hydrogen at 100 bar pressure, as well as the structural and hydrogen sorption characteristics of the as-milled samples.

The Li-Mg alloy was obtained from Ilika plc in a ribbon form; due to the reactive nature of the alloy, it was always kept inside an argon-filled glove box to prevent oxidation. Before milling, the ribbon was gently polished; to remove any surface defects and/or oxides, using a SiC grinding paper (P800). It is thought that the Li-Mg alloy was synthesised via cold-rolling and induction melting (Shi et al., 2001). However, its composition is related to the material information reported by Shi et al., given that (Ilika plc) was not able to confirm the nature of the material. The conditions employed for the synthesis of the Li-Mg alloy were reproduced from previously reported work performed by (Guo, 2015) with several modifications in the milling conditions and time. Around 1g of as-received Li-Mg ribbon was inertly introduced into a stainless steel high-pressure milling pot with stainless steel 10 mm milling balls (ball to powder ratio was considered as 50:1). The milling vial was degassed and hydrogenated for approximately 5 cycles, then pressurised with 100 bar H_2. The loaded milling pot was then placed into a planetary ball milling apparatus; the conditions for the milling process were set as 100 rpm (bias) rotation speed. The sample was milled for 15, 30 and 60 min with intervals of 10 minutes milling followed by 10 min pause to prevent over-heating.

As-milled samples were characterised by ex-situ/in-situ X-ray diffraction, and DSC-TGA techniques.

5.2 Structural characterisation of as received and as milled Li-Mg alloy (ribbon)

The as received Li-Mg alloy had a flexible and soft ribbon form (about 1mm thickness and 5mm width). Figure 5.1 illustrates the as received and milled Li-Mg ribbon. The ribbon presented a characteristic light-grey colour before treatment (polishing), and after gently removing the oxide layer on the surface a light-silver appearance was evidenced.

Figure 5.1 Li-Mg alloy (ribbon) acquired from Ilika plc with approximate scale bar.

X-ray diffraction patterns of the as-received and as-milled material for 1 hour are shown in Figure 5.3. The XRD pattern on the as-received material shows that the Li-Mg ribbon has a solid solution composition (lm-3m space group). To gain a better understanding of the structure, a Rietveld refinement (Figures 5.4 and 5.5) was carried out and the lattice parameters were obtained. The composition of the Li-Mg alloy (ribbon) is likely to show a stoichiometric composition of 97 at.% Li and 3 at.% of Mg, according to the lattice parameter variation as a function of Li content (Figure 5.2) (Herbstein and Averbach, 1956b, Herbstein and Averbach, 1956a).

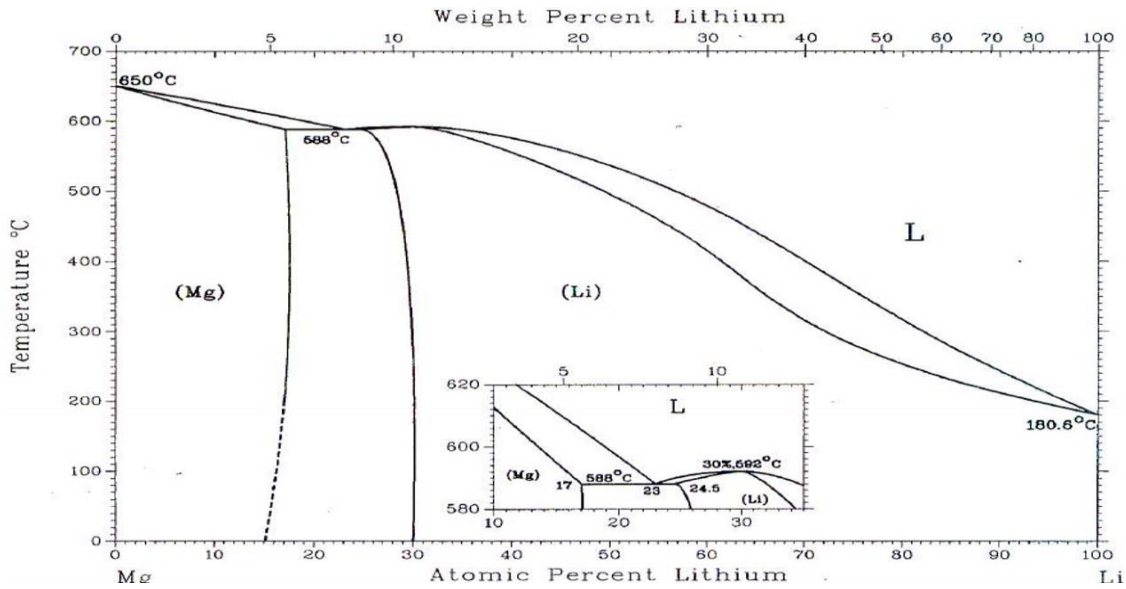

Figure 5.2 Lithium Magnesium Alloy phase diagram (Nayeb-Hashemi et al., 1984)

After milling the sample for 15 and 30 minutes in 100 bar H_2, it was shown that the composition of the sample has not changed, moreover, the material remained in a ribbon form. No further characterisation was performed on these milled samples as our main aim was to form a powder in order to compare the results of this work with those performed by Guo, S.(Guo, 2015) using a less energy intensive milling conditions in an attempt to improve its sorption properties.

When the sample was milled for 1 h, the Li-Mg ribbon changed its composition into a (light grey colour) powder form. Diffractions peaks for the as-milled sample showed the Li-Mg phase was still present after milling, accounting for a 21.33 wt. % of the sample, in addition, hydrogenation of the Li phase was observed and LiH phase showed a total amount of 75.61 wt % of the sample, the remaining 2.99 wt. % related to Mg phase and a tiny amount of MgH_2 was also detected accounting for less than 0.5 wt. %. An unidentified small peak appeared at approximately 26.15 2θ (°). This peak does not correspond to any known oxide, hydroxide related to Li, Mg or Fe nor to the theoretical $LiMgH_3$ and Li_2MgH_4 (Vajeeston et al., 2008, Li et al., 2011). Moreover, this unknown peak was also reported in the study of Li-Mg ribbon via reactive milling under H_2 performed by Guo, S(Guo, 2015).

Fast hydrogenation of Li-Mg alloy was demonstrated even after 1 h milling under 100 bar H_2 using milder milling conditions than previously reported in the literature.

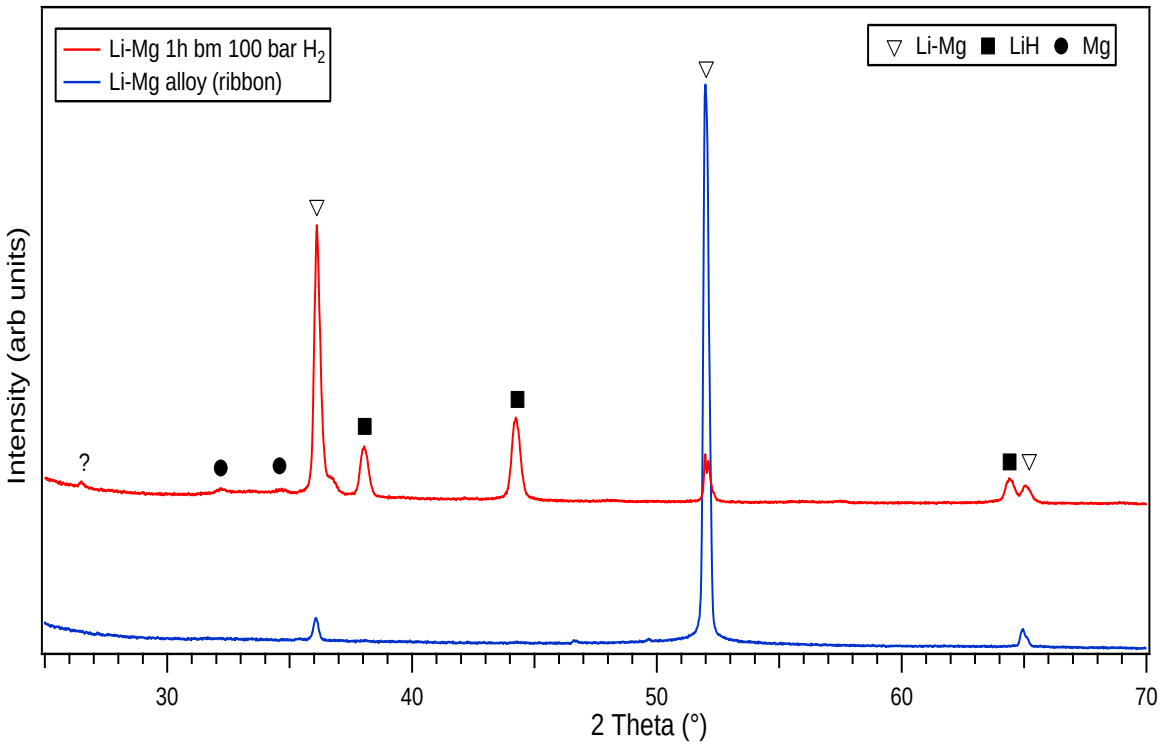

Figure 5.3 XRD pattern of as-received Li-Mg ribbon, and after ball milling for 1 h.

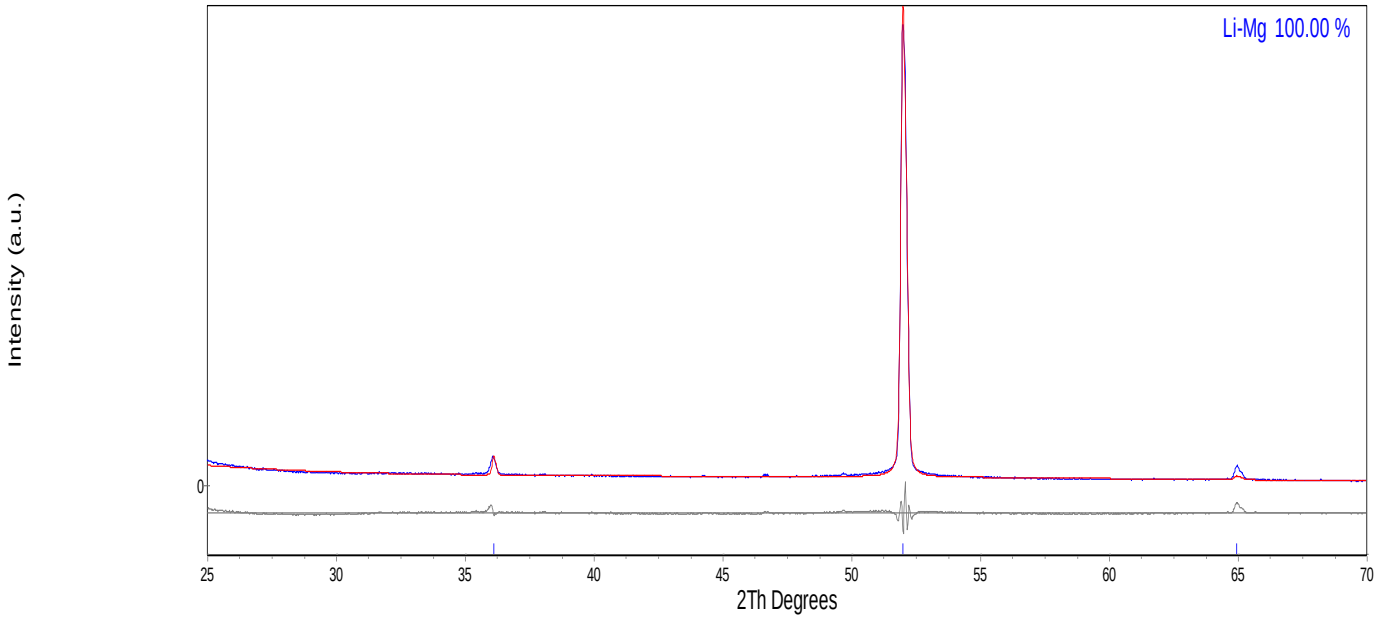

Figure 5.4 Rietveld refinement of as-received Li-Mg ribbon, values before 25 were not considered for the refinement as no representative diffractions were detected. (Observed data is shown by blue lines, calculated data is represented by the red lines and the difference is plotted below in grey). Goodness of fit 2.013

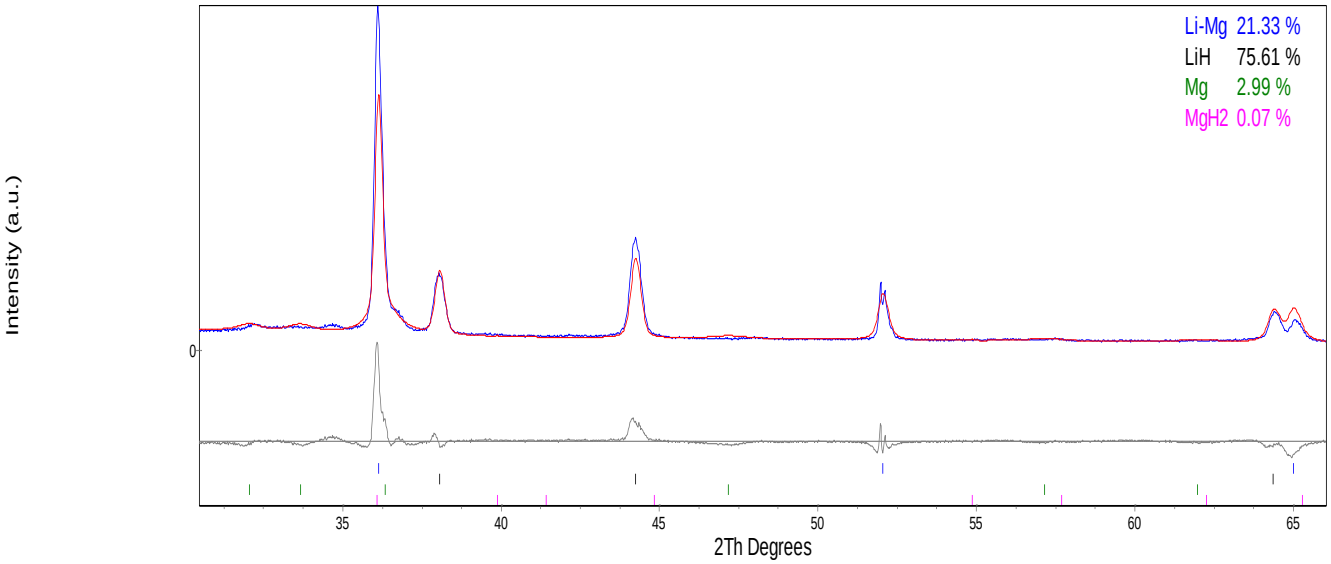

Figure 5.5 Rietveld refinement of 1 h milled in 100 bar H_2 Li-Mg ribbon, values before 25 were not considered for the refinement as no representative diffractions were detected. (Observed data is shown by blue lines, calculated data is represented by the red lines and the difference is plotted below in grey). Goodness of fit 2.137

The lattice parameters obtained from the refinement of the as-received and as-milled material shown in Figure 5.4 and Figure 5.5 respectively, show that Li-Mg as-received material tends to contract when milling for 1 h. Lattice parameters of LiH (Figure 5.13) appear to be slightly larger than the reported in the literature. Furthermore, Mg phase indicates that after milling there is a significant increase in the lattice parameters, resulting in a larger c/a ratio as well as volume in comparison to previous works. This effect can be related to the separation of Li atoms from the alloy to form a hydride, leaving a small amount of Li in solution with the Mg. Refinement for MgH_2 phase was not carried out, as the diffraction peaks were not intense enough to perform a proper fitting. Table 5.1 summarises the lattice parameters of all active phases in the as-received, as well as in the milled sample and show a comparison with literature data.

Table 5.1 Summary of the lattice parameters for the as-received and 1 h milled Li-Mg samples in comparison to literature values.

Milling Time	Li-Mg Ribbon		Mg			LiH	
	a (Å)	V (Å^3)	a (Å)	c (Å)	V (Å^3)	a (Å)	V (Å^3)
As-received	3.52±0.01	43.4±0.1	N/A	N/A	N/A	N/A	N/A
1 h	3.51±0.01	43.3±0.1	3.22±0.01	5.3±0.1	47.8±0.1	4.09±0.01	68.5±0.1
Literature (Guo, 2015)	3.51(6)		3.20(2)	5.20(4)	46.2(1)	4.08(3)	68.0(1)

5.3 Thermal decomposition

5.3.1 DSC-TGA measurements

DSC-TGA measurements were investigated to determine the decomposition temperatures and if any change in the weight of the sample has occurred during the decomposition process. Figure 5.5 illustrates the DSC traces for the decomposition of the as-received Li-Mg and 1h milled material under 100 bar H_2 (a) under Ar and (b) under H_2 atmospheres. Results of weight losses, onset, peak and end temperatures of the samples experimentally gained in this work are summarised in Table 4.2 and compared with previous reports obtained from literature (Guo, 2015).

For both Li-Mg samples, no reactions were observed below 180 °C, thus plots are only focused on the range of temperature where reactions were detected.

DSC peaks for the as-received material heated under Ar show an exothermic reaction detected from188 up to 197 °C, peaking at approximately 192 °C; this exotherm may be linked to the melting of the Li-Mg ribbon (see phase change Figure 5.8) as a result of the heating. Consequently, from 197 to 200 °C follows an endothermic reaction centred at 198 °C. For the

1h milled Li-Mg heated under Ar, a single endothermic reaction is observed starting at 189 °C up to 210 °C, the main inflexion is detected at 194 °C. No exothermic reactions were detected; hence it makes sense to link this reaction to a possible H_2 desorption from the Mg hydride formed during the reactive milling.

DSC traces for the as-received Li-Mg under H_2 present two reactions, one exothermic followed by one endothermic, following the same decomposition tendency as in the decomposition of the material under Ar, although, at lower temperatures. The first exothermic reaction is observed from 187 up to 195 °C deflecting at 190 °C; again, this reaction might be related to the melting of the Li-Mg, followed by an endotherm starting at 195 °C, peaking at 197 °C, up to 199 °C. On the other hand, for the 1h milled (100 bar H_2) sample, there is only one endothermic reaction reflected from the DSC centred at 193 °C. This peak could be linked to the decomposition of MgH_2, although at significantly lower temperature than for the milled magnesium hydride at ~360 °C (Varin et al., 2006).

TGA analysis was executed on the 1h milled Li-Mg to investigate the mass change of the material. Figure 5.7 shows the TGA curve for the as milled material; a total amount of 0.19 wt.% H_2 was evolved from the TGA up to 250 °C. This result is similar to the literature, where hydrogen released accounted for 0.17 wt. % H_2 between 240 and 450 °C. Nevertheless, dehydrogenation proceeds at lower temperatures.

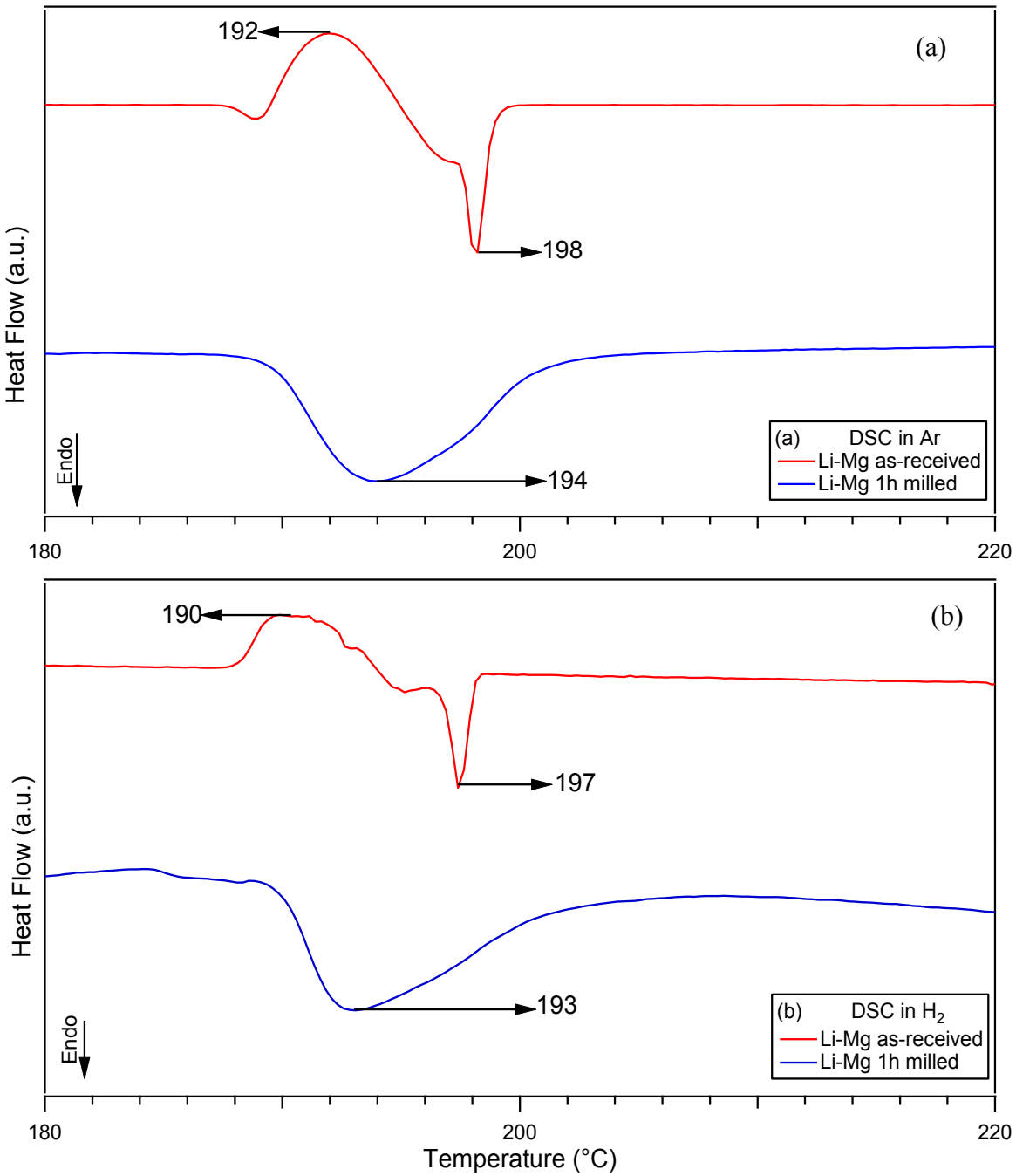

Figure 5.6 DSC measurements of the as received and 1h milled (100 bar H_2) Li-Mg alloy (a) under 3 bar Ar at 100ml/min and 2 °C/min heating rate, (b) under 3 bar H_2 flowing at 100 ml/min and a heating rate of 2 °C/min

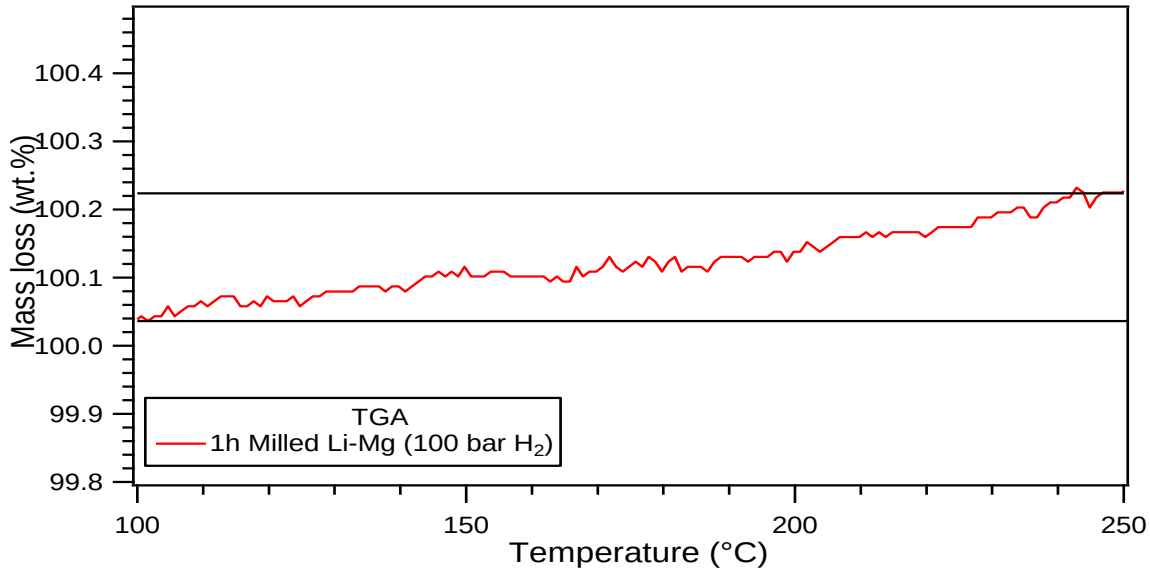

Figure 5.7 TGA of the 1h milled (100 bar H2) Li-Mg sample heated under 3 bar Ar flowing at 40 ml/min, heating rate 2 °C/min.

Table 5.2 Summary of the DSC & TGA desorption temperatures and mass losses for the Li-Mg as-received and 1h milled (100 bar H_2) samples, heated under different atmospheres compared to the literature(Guo, 2015).

Li-Mg Alloy					
	Milling Time (h)	DSC exo/endo			TGA (wt.%) loss
		T_{on}(°C)	T_{pk}(°C)	T_{end}(°C)	
Argon	Li-Mg (exo)	188	192	197	N/A
	Li-Mg (endo)	197	198	200	
	1	189	194	210	0.19
Hydrogen	Li-Mg (exo)	187	190	195	N/A
	Li-Mg (endo)	195	197	199	
	1	189	193	210	N/A
Literature (Guo, 2015)	1		284		0.17

5.3.2 In-Situ XRD

In-Situ X-ray diffraction was performed to investigate the compositional changes of the as-received and 1h milled (100 bar H_2) Li-Mg samples upon heating. The XRD patterns were taken isothermally every 25 °C from 30 (RT) to 250 °C and then cooled to room temperature. The collection time was approximately 30 min per scan, under 3 bar He and 3 bar H_2 flowing at 100ml/min.

5.3.2.1 Li-Mg Ribbon (as-received)

Figure 5.8 illustrates the In-Situ XRD measurements of the as-received Li-Mg under 3 bar He upon heating. At 30 °C diffractions related to Li-Mg are observed with the main peak at 51.74 °. On heating, the same reflections are observed up to 150 °C. From 200 to 250 °C, Li-Mg peaks are no longer detected, however, a bump in the intensity from around 30 to 40 (2θ°) is observed with a small diffraction related to the oxidation of Li (Li_2O); this observed bump can be linked with the melting of the material, this confirms the findings from the DSC measurements.

When cooling down to 30 °C (RT), Li-Mg diffractions were detected, in addition to the Li_2O phase, indicating the reformation of Li-Mg phase after melting.

Consequently, in-situ X-ray diffractions of the Li-Mg ribbon (as-received) heated under 3 bar H_2 were investigated as shown in Figure 5.9; from 30 to 100 °C diffractions linked to the Li-Mg phase were detected with the main diffraction peak located at 36.13 (2θ°). On heating to 200 °C, reflections of Li-Mg disappeared, and peaks related to the LiH phase started to form, showing the hydrogenation of Li from the solid solution. In addition, Li oxide Li_2O peaks are detected; those are probably due to a small leak in the instrument. On further heating to 250 °C,

in addition to the LiH and Li_2O diffractions, a new phase related to the MgH_2 phase is present; the formation of this phase evidences the rapid hydrogenation of the material under acceptable conditions of temperature and pressure. On cooling down to 30 °C, the remaining phases detected correspond to the LiH, MgH_2 and Li_2O that still remain present in the sample.

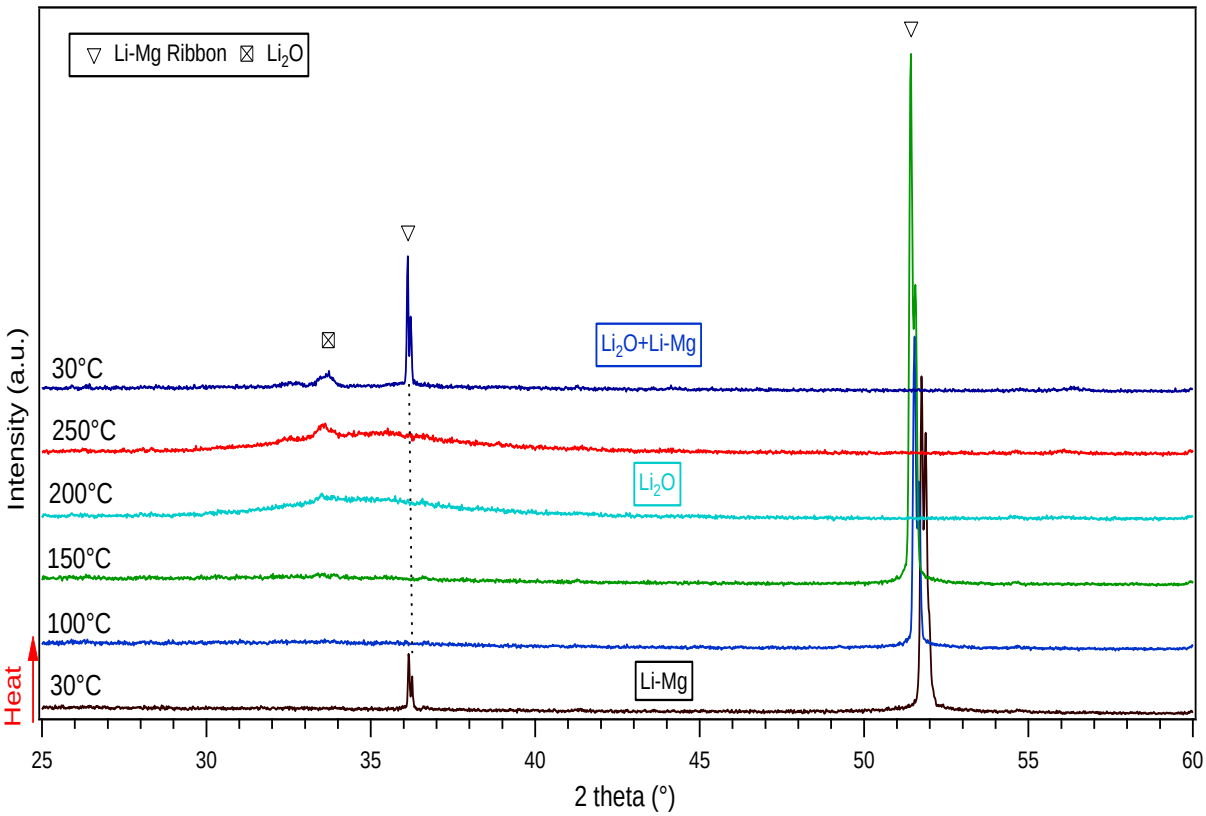

Figure 5.8 In-Situ XRD of as-received Li-Mg ribbon heated and cooled in 3 bar He flowing at100ml/min. No reflections were detected below 25 °C, hence are not shown.

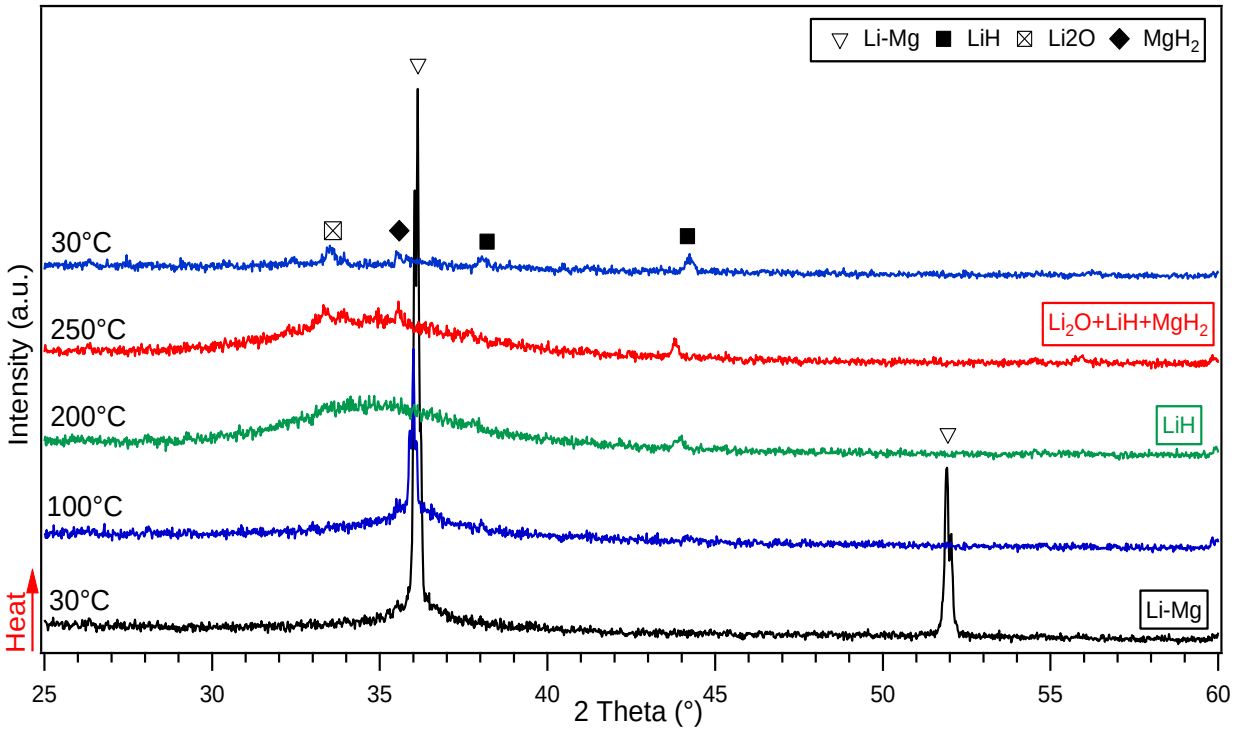

Figure 5.9 In-Situ XRD diffraction patterns for Li-Mg sample heated and cooled down under 3 bar H_2 flowing at 100ml/min. No reflections were detected below 25 °C, therefore, are not presented.

5.3.2.2 Li-Mg 1h milled in 100 bar H_2.

In-Situ XRD measurements of the as-milled Li-Mg sample are illustrated in Figure 5.10. At room temperature, the diffraction peaks for Li-Mg, LiH, MgH_2, and Mg are detected. On heating, Li-Mg, MgH_2 phases show a decreased intensity, while LiH and Mg diffraction intensities increase. The increased intensity can be attributed to the lattice ordering. With increasing temperature to 150 °C, Li-Mg and MgH_2 phases tend to decrease even further and show a shift to higher angles (inset Figure 5.10), whereas, the LiH and Mg peaks appear more intense and sharp. In addition, a new phase is formed due to oxidation of Li and is present until the end of the measurement. This Li_2O phase is attributed to a small leak in the instrument. Between 200 and 250 °C Li-Mg and MgH_2 intensities decrease even further, leading to more intense LiH and Mg peaks. This effect can be attributed to starting of the MgH_2 decomposition into Mg releasing some H_2.

These results agree well with the DSC findings (Figure 5.6(b)). When cooling down to room temperature, same reflections were observed.

With respect to the lattice parameters of the 1h milled Li-Mg sample, it is observed that the cell volumes of the Li-Mg, LiH and MgH_2 phases almost linearly increase up to 250 °C as a result of thermal expansion. On the other hand, the cell volume of MgH_2 from the Li-Mg sample was larger than the as-received MgH_2. This could be an indication that the Mg^{2+} (r_{ionic} = 0.72 Å) was partially substituted by a larger Li^+ (r_{ionic} 0.76 Å) (Shannon, 1976), to form a bct-Mg(Li)H_2 solid solution. A rough estimation of the composition of the observed $Mg_{(1-x)}Li_xH_2$ phase using Vegard's law (Denton and Ashcroft, 1991) was x = ~0.04.

In contrast, the cell volume of the Mg phase presents a different variation as shown in Figure 5.11. There is a linear increase in the lattice parameters (a, c) up to 200 °C due to thermal expansion (Figure 5.12). Parameter c suffers a rapid reduction above 210 °C, while lattice a, remains in the range of ~3.237±0.002 Å. This effect produces a contraction in the cell volume. As $Mg_{(1-x)}Li_xH_2$ (x = ~0.04) completely decomposes, the reaction product Li (r = 1.56 Å) subsequently dissolves into α-Mg (r = 1.60 Å) to form a hcp Mg(Li) solid solution. The degree of substitution increases rapidly on further heating. When the maximum solubility of Li in Mg is reached (~17 atom% Li at 450 °C ((Nayeb-Hashemi *et al.*, 1984), the hcp Mg(Li) transforms to a bcc phase.

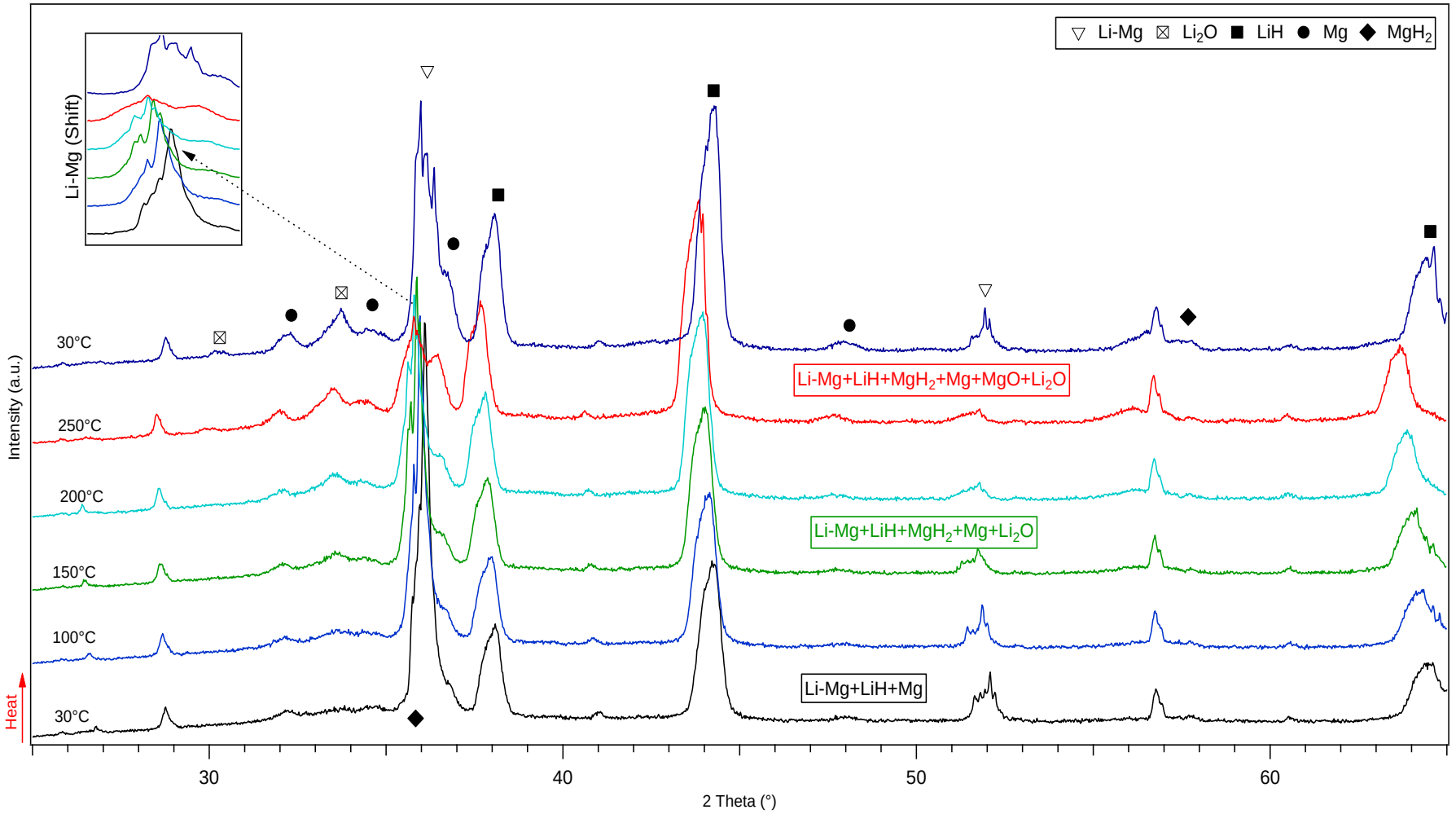

Figure 5.10 In-Situ XRD diffraction patterns for 1h milled (100 bar H_2) Li-Mg sample heated and cooled down under 3 bar H_2 flowing at 100ml/min. No reflections were detected below 25 °C, hence, are not presented.

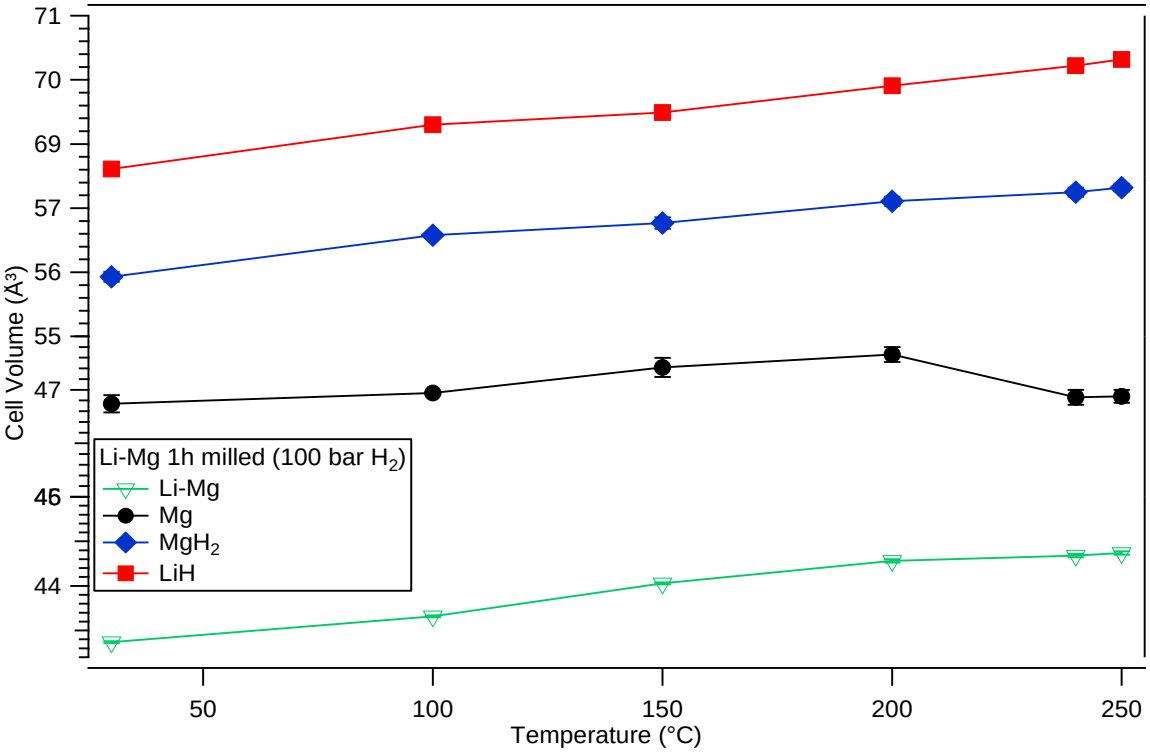

Figure 5.12 Unit cell volumes plotted against temperature for the Li-Mg, LiH, Mg and MgH_2 phases in the Li-Mg alloy milled for 1h in 100 bar H_2. Solid lines are a guide for the eye. Where error bars are not shown, they are smaller than data symbols

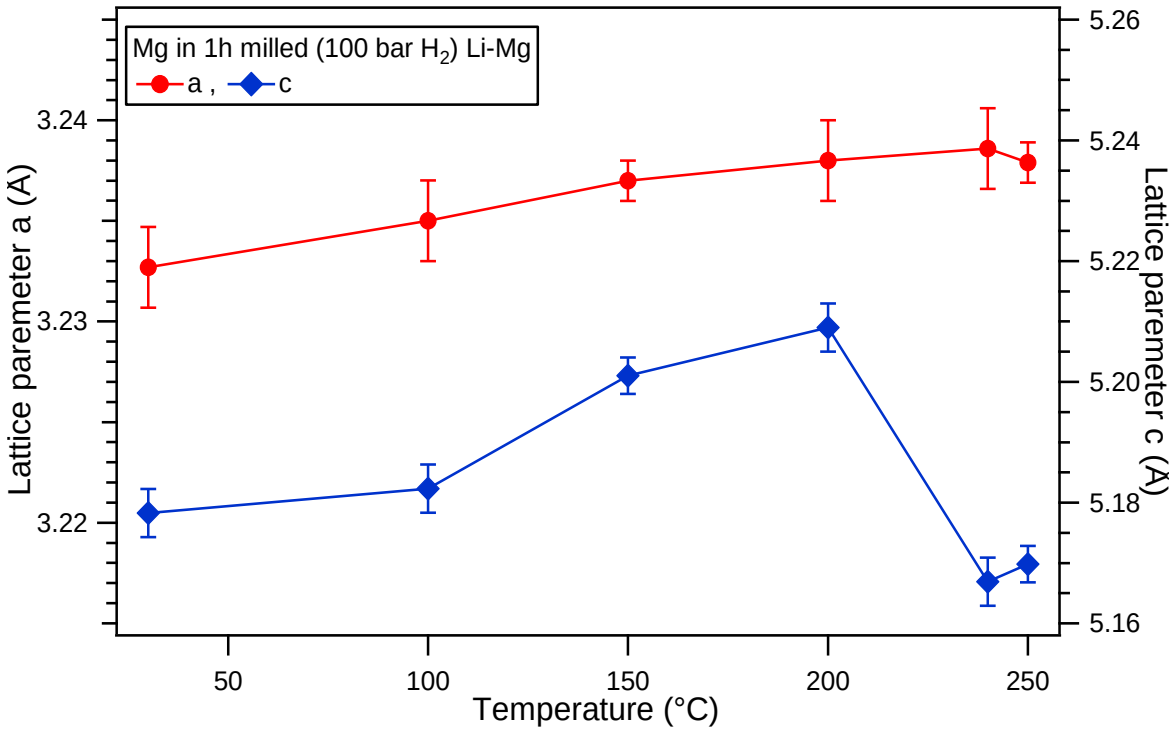

Figure 5.11 Lattice parameters a, c of the Mg phase in the 1h milled Li-Mg alloy milled in 100 bar H2. Solid lines are a guide for the eye.

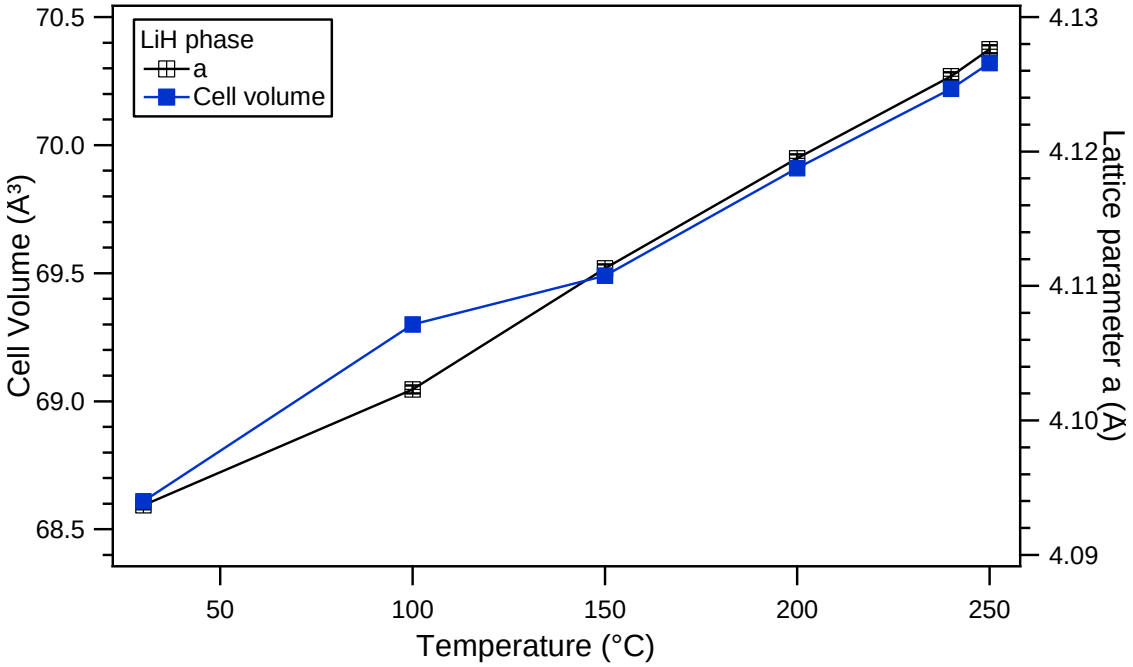

Figure 5.13 Unit cell parameter and volume plotted against temperature for the LiH phase in the Li-Mg alloy milled for 1h in 100 bar H_2. Solid lines are a guide for the eye. Where error bars are not shown, they are smaller than data symbols

5.4 Conclusions

The hydrogenation of a Li-Mg ribbon was investigated via reactive milling the sample in 100 bar H_2 and in-situ XRD measurements. It was found that direct hydrogenation is achieved after only 1h milling the sample, forming a powder containing the Li and Mg hydride phases. Moreover, hydrogenation of the Li-Mg ribbon was also reached exposing the sample to a constant 3 bar H_2 pressure flowing at 100 ml/min. In addition, a minor diffraction located at ~ 26.2 (2θ°) was detected, which was not due to any known oxide, hydroxide, or the theoretical $LiMgH_3$ and Li_2MgH_4 (Li et al., 2011, Vajeeston et al., 2008).

Rietveld refinement of the as received Li-Mg hydride shows one single phase with (002) preferred orientation. When refining the sample milled for 1h, Li-Mg accounting for 21.3 wt. %, LiH (75.6 wt. %), Mg (2.9 wt. %) and MgH_2 (0.1 wt. %) phases are observed.

DSC measurements for the as-received sample under argon show two reactions, one exothermic and one endothermic at 192 and 198 °C. The exothermic curve is attributed to the melting of the sample, and the endothermic reaction is linked to the recrystallization of the LiH, these reactions are confirmed by observing the phase diagram (Figure 5.2). On the other hand, the DSC traces of the 1h milled Li-Mg alloy, show one endothermic reaction peaking at 194 °C, this can be attributed to the desorption of the hydrides formed during the milling.

Consequently, The Li-Mg alloy as-received and the 1h milled were examined via DSC under H_2, showing that for the as-received material there were two reactions (one exothermic and one endothermic) as previously detected in the measurements performed under argon. However, at lower temperatures 190 (exothermic) and 197 °C (endothermic) for the as-received material and 193 °C (endothermic) for the 1h milled sample.

There was achieved a very low weight loss of approximately 0.19 wt. % H_2 in the 1h milled sample obtained from the TGA measurements. This mass loss is slightly higher than the 0.17 wt. % H_2 obtained by Guo S. for the 1h milled Li-Mg sample.

The in-situ XRD patterns of the as-received Li-Mg under 3 bar H_2 indicate the hydrogenation of the material after ~ 5h under 3 bar H_2 and 200 °C. Furthermore, the in-situ X-ray diffractions of the 1h milled sample showed that the sample start to decompose the MgH_2 phase into Mg and H_2 at around 150 °C, which agrees with the decomposition temperature observed from the DSC measurements. Nevertheless, it is believed that at the temperature of 250 °C, not a complete dehydrogenation was achieved, as MgH_2 peaks are detected at this temperature. Therefore, the total amount of hydrogen released (0.19 wt.%) may be increased.

Lattice parameters of the phases present in the 1h milled product show a linear rate of growth when the temperature is increased, although, Mg phase was an exception to the rule showing

that parameter c increases up to 200 °C then rapidly decreases causing a contraction in the cell volume.

It is worthwhile mentioning that results reported in this work for the 1h milled Li-Mg alloy present similar dehydrogenation pathways than previously reported for the same milling time composite; however, the reactions occur at lower temperatures. While, Guo, S(Guo, 2015). reported a decomposition temperature of approximately 284 °C to desorb 0.09 wt. % H_2, and a total amount of 0.17 wt.% H_2 at 425 °C, in this work a similar amount of H_2 (0.19 wt.%) was released up to 250 °C, showing a decrease in the decomposition temperature of about 175 °C.

On the other hand, no phases related to Mg_2FeH_6 were detected during this work, as reported in the literature (Guo, 2015). This may be related to the milder conditions used (60 min milling at 100 rpm) for the synthesis and characterisation of the material.

It is important to highlight, that this work was carried out to investigate the possible formation of Li-Mg-H ternary phases ($LiMgH_3$ and Li_2MgH_4) from the rapid hydrogenation of a Li-Mg alloy. However, no traces of these theoretical ternary phases were observed.

Although, hydrogenation of the Li-Mg alloy was achieved under relatively low temperature and pressure conditions, the amount of hydrogen that can be desorbed it is extremely low for practical applications. Therefore, further investigation of the sorption kinetics and reversibility, using 10, 20 and 50 bar H_2 back pressure, needs to be considered in the future work.

CHAPTER VI

6. RESULTS AND DISCUSSION: SODIUM MAGNESIUM HYDRIDE

6.1 Introduction

Ternary hydride systems have drawn special attention over the last decade; in particular Mg-base ternary hydrides are being investigated as a potential storage material for mobile applications, due to their favourable characteristics such as high gravimetric capacity, abundance and low cost (Bouamrane et al., 2000, Bouhadda et al., 2010, Bouhadda et al., 2013, Rönnebro et al., 2000, Ikeda et al., 2005a, Fornari et al., 2007, Ikeda et al., 2007a, Ikeda et al., 2007b, Komiya et al., 2008, Pottmaier et al., 2011, Reardon et al., 2013, Chaudhary et al., 2015). Extensive studies have demonstrated that reduction of grain size to a nanoscale can play an important role in the kinetic and thermodynamic destabilisation of the samples (Reardon et al., 2013, Chaudhary et al., 2015, Reardon, 2014). However, more information is still need in order to fully understand the reactions and structural changes of these systems to consider them as candidates for on board vehicular energy storage applications.

Perovskite-type hydrides with the structure ABH_3 (where A alkaline, alkali earth metal and B transition metal) are an interesting ternary hydride system; when replacing B for an alkali/alkaline earth metals in ABH_3 system, the gravimetric capacity can be increased (Reardon et al., 2013, Ikeda et al., 2005a, Rönnebro et al., 2000). Therefore, there have been a number of attempts to synthesize such compounds. DFT computational studies reported the possible formation of high capacity hydrides $LiMgH_3$ and Li_2MgH_4 containing approximately 9 and 10

wt. % hydrogen, respectively. Nevertheless, these compounds have not yet been experimentally synthesised (Fornari et al., 2007, Rönnebro et al., 2000, Bouamrane et al., 2000, Li et al., 2011). The formation of ternary $MMgH_3$ (M=Na, K, Rb) has been reported (Fornari et al., 2007). It was found that $KMgH_3$ decomposes in one single step and the total amount of hydrogen released was 3.8 wt. % at 400 °C. No reversible reactions were reported for this ternary hydride. On the other hand, $RbMgH_3$ was observed to decompose in two step reactions releasing a total amount of 3.5 wt. % H_2 at 400 °C. However, reversibility was not reported.

$NaMgH_3$ was the most promising ternary hydride, because it can completely desorb an average of 6 wt. % H_2 at 400 °C and can be partially recombined (approximately 30 %) applying 10 bar pressure and 400 °C, which make it a potential hydrogen storage material (Ikeda et al., 2005a, Ikeda et al., 2007b). $NaMgH_3$ has an orthorhombic perovskite structure (Figure 6.1) analogous to the $GdFeO_3$ type (space group Pnma) (Komiya et al., 2008, Rönnebro et al., 2000, Bouamrane et al., 2000).

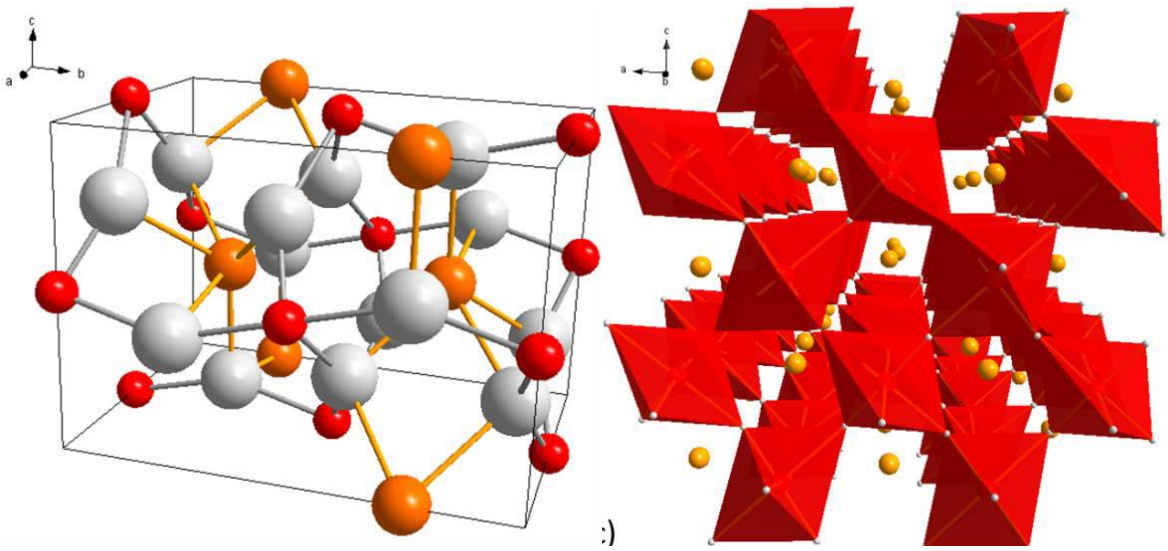

Figure 6.1 $NaMgH_3$ unit cell, light grey, red, and gold spheres represent H, Mg and Na respectively (left); Structure of $NaMgH_3$ as a polyhedral representation viewed along the [010] direction (right).

Investigations performed by Sheppard et al. (Sheppard et al., 2011) showed kinetic and thermodynamic information for the decomposition of $NaMgH_3$ into Mg and NaH. Desorption enthalpy of 86.6 ± 1.0 kJ/(mol H_2) and entropy of 132.2 ± 1.3 kJ/(mol H_2 K) indicate that $NaMgH_3$ is thermodynamically more stable than MgH_2.

It has been investigated the destabilisation of $NaMgH_3$ and was found that thermodynamic properties can be enhanced by catalytic doping or adding new elements (Wang et al., 2016). For example, Chaudhary et al. (Chaudhary et al., 2015) found that $NaMgH_3$ when doped with Si ($2NaMgH_3$+Si), displayed a decomposition temperature of around 250 °C which is lower than the decomposition temperature of $NaMgH_3$.

Ikeda et al.(Ikeda et al., 2005a) reviewed for the first time the formation ability, as well as the reversible hydriding and dehydriding reactions of $NaMgH_3$. It was found that hydrogen desorption followed two steps reactions as shown in equations (2.2 and 2.3). Moreover, hydrogen was partially recombined from decomposed products, showing that $NaMgH_3$ can be reversible under 10 bar H_2 and 400 C°.

Work by Pottmaier et al. and co-workers (Pottmaier et al., 2011), investigated the structure and thermodynamic properties of $NaMgH_3$. Results of the investigation showed the desorption reaction of $NaMgH_3$ into NaH and Mg at 400 °C under 2 bar H_2, Furthermore, evidenced reversibility of NaH and Mg back to $NaMgH_3$ at 400 °C under 5 bar H_2.

More recent works performed by Reardon et al (Reardon et al., 2013) showed the facile synthesis of $NaMgH_3$ via reactive milling under Ar of NaH and MgH_2. Results of the investigation concluded that after 5h milling in Ar, the $NaMgH_3$ phase is formed along with some oxide reflections. Moreover, this study evidenced two-step dehydrogenation and a total amount of 4.7 wt. % of H_2 release up to 400 °C.

This work, continues the investigations performed by Ikeda et al.(Ikeda et al., 2007b), Pottmaier et al.(Pottmaier et al., 2011) and Reardon et al (Reardon et al., 2013). The novelty of this method relies on the synthesis, as no hydrogen atmosphere was used for the sample formation during any stage of the process. Thus, determining changes in kinetics and thermodynamic reactions. Moreover, this work will examine re-hydrogenation ability of the milled samples and results will be compared to previous reported data to validate its functional application.

The investigation will take part in 5 sections. Firstly, as-received materials for NaH and MgH_2 will be characterised through XRD. Secondly, will be evaluated thermal decomposition by DSC & TGA/MS to define onset decomposition temperatures and hydrogen mass loss of samples. Thirdly, as-milled products will be characterised by X-ray diffraction. Next, DSC and TGA/MS equipment will be used to analyse temperature decomposition and release of hydrogen from the milled samples. After, to get a complete understanding of the decomposition mechanism and reactions, decomposed samples will be analysed by in-situ XRD studies. Finally, recombination ability will be checked under 10 bar H_2 to verify whether sodium magnesium hydride is reversible (using the mentioned conditions).

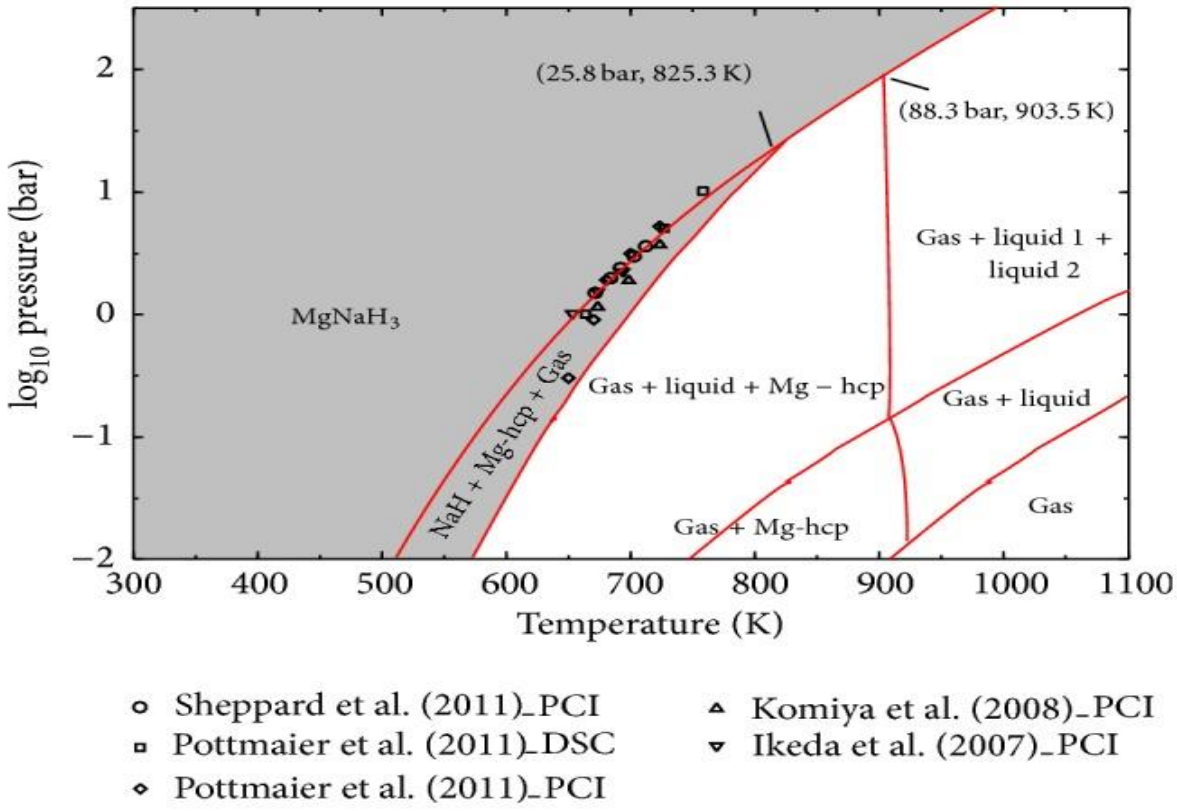

Figure 6.2 Calculated pressure-temperature equilibrium diagram for $NaMgH_3$ in comparison with experimental data from the literature (Abdessameud et al., 2014).

6.2 Characterisation of as-received materials

X-ray measurements were performed on the as received materials. Figure 6.3 shows the XRD patterns for NaH and MgH_2. In the XRD pattern of MgH_2 there are small peaks of Mg. The most intense peak at 27.92 (2θ degrees) corresponds to MgH_2 phase. On the other hand, X-ray diffraction from NaH shows peaks associated to NaH phase with the most intense peak at 31.66 (2θ degrees). Both diffractions present good crystallinity.

Thermal decomposition performed on as received samples was carried out by DSC-TGA-MS measurements (Figure 6.4). Results obtained during this experimental work are lower than theoretical reported in the literature; ~4.0 wt. % H_2 for NaH 6.5 wt. % H_2 for MgH_2, reasonable explanation to that fact can lie in the purity of the powders (95%).

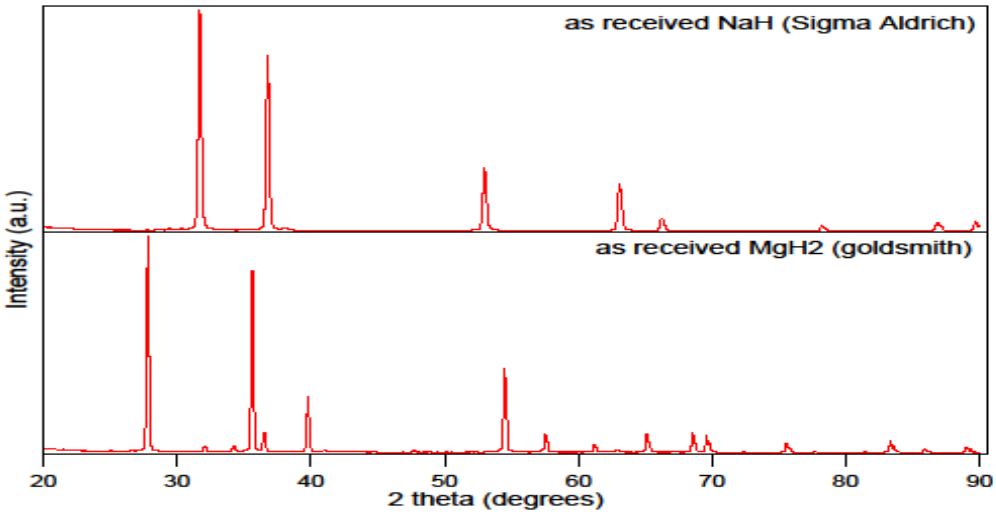

Figure 6.4 XRD patterns for the as-received NaH (top) and MgH_2 (bottom)

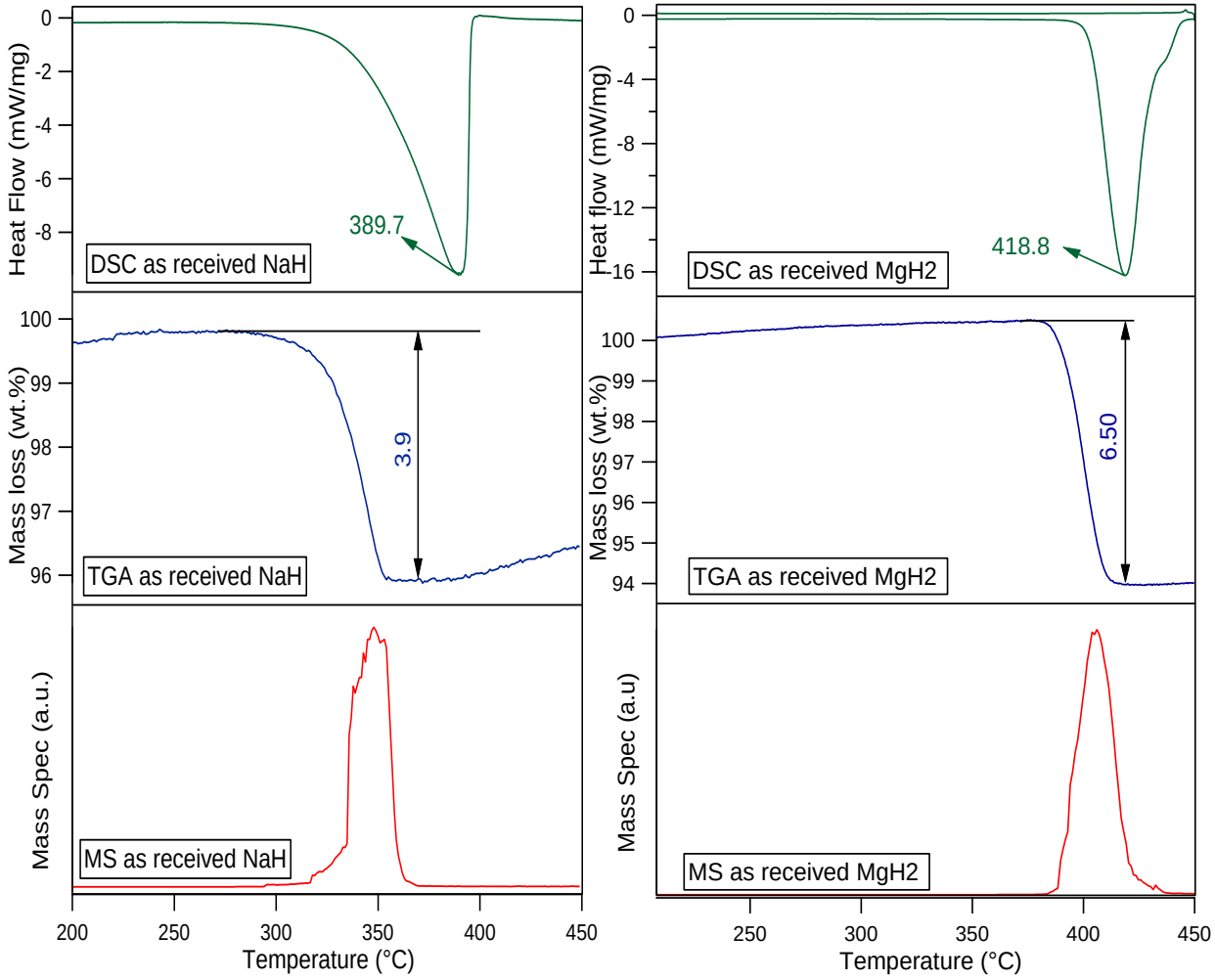

Figure 6.3 DSC-TGA-MS of the as-received (left) NaH and (right) MgH_2 heated at 2 °C/min in 3 bar Ar flowing at 100 ml/min (DSC), and 1 bar Ar flowing at 40 ml/min (TGA). MS shows the hydrogen evolution of the as-received materials.

6.3 Characterisation of as-milled materials

Characterisation of as milled materials has been performed in order to find out which products have been formed during mechanical milling. Figure 6.5 and Figure 6.6 show the XRD patterns from the mechanical-milled products of NaH and MgH_2 under argon and hydrogen atmospheres. The XRD refinement shows that the $NaMgH_3$ has an orthorhombic structure with a Pnma space group. The formation of $NaMgH_3$ phase reported in the literature (Ikeda et al., 2007b) is observed only after 2h ball milling, a small and almost unrecognisable peak related to MgO can be detected at approximately 42.47° 2θ in the 15h milled samples in Ar and H_2, this can be explained because of extremely sensitivity of samples to air. No traces of remaining MgH_2 were detected and it is assumed that this effect was due to the relatively intensive milling conditions (400 rpm; ball to powder ratio 50:1). During the experimental characterisation, extra care was taken to avoid exposure of samples to air, despite our best efforts X-ray diffraction shows contamination has occurred.

Mechanical milled samples of NaH and MgH_2 for 2,5 and 15h in Ar and H_2 showed one single phase related to $NaMgH_3$ structure confirmed by X-ray diffraction with the most intense peak detected at 32.78 2θ°. No evidence of unknown peaks was noticed even after ball milling for 15h. Peak intensities were observed to increase with the milling, thus the sample milled for longer time (15h) shows stronger XRD diffractions than the sample milled for 2h.

This information leads us to infer that $NaMgH_3$ can be easily formed without the use of high pressure techniques which is advantageous for the synthesis (i.e. could be cost-effective).

The lattice parameters and the weight percent of crystalline phases of sodium magnesium hydride were determined through Rietveld refinement as shown in Figure 6.7, using as a structural model based on Ikeda et al. (Ikeda et al., 2005a) data collected from ICSD (ICSD, 2017)

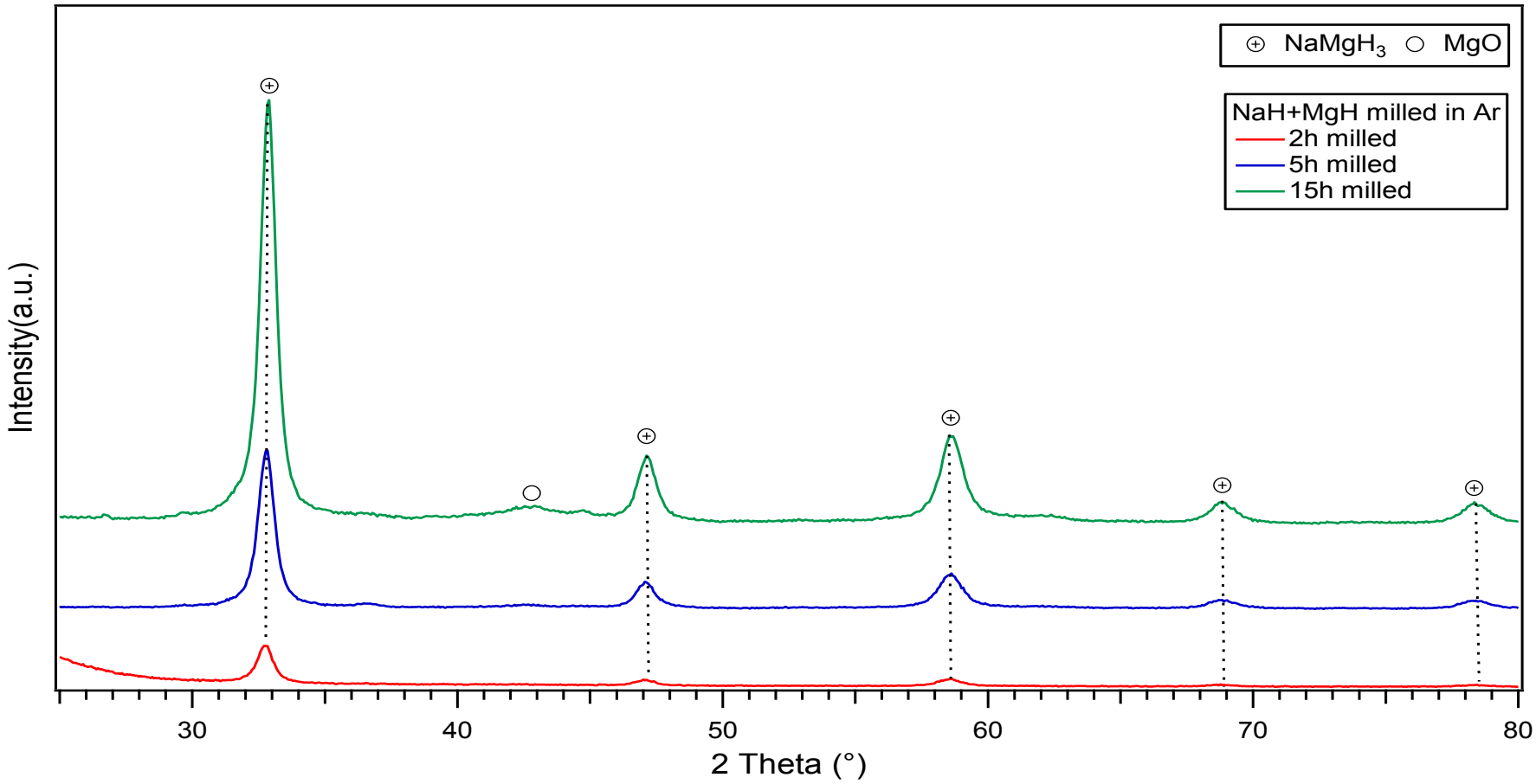

Figure 6.5 RT-XRD patterns of NaH and MgH_2 mechanical milled for 2, 5 and15h in Ar showing $NaMgH_3$ phase.

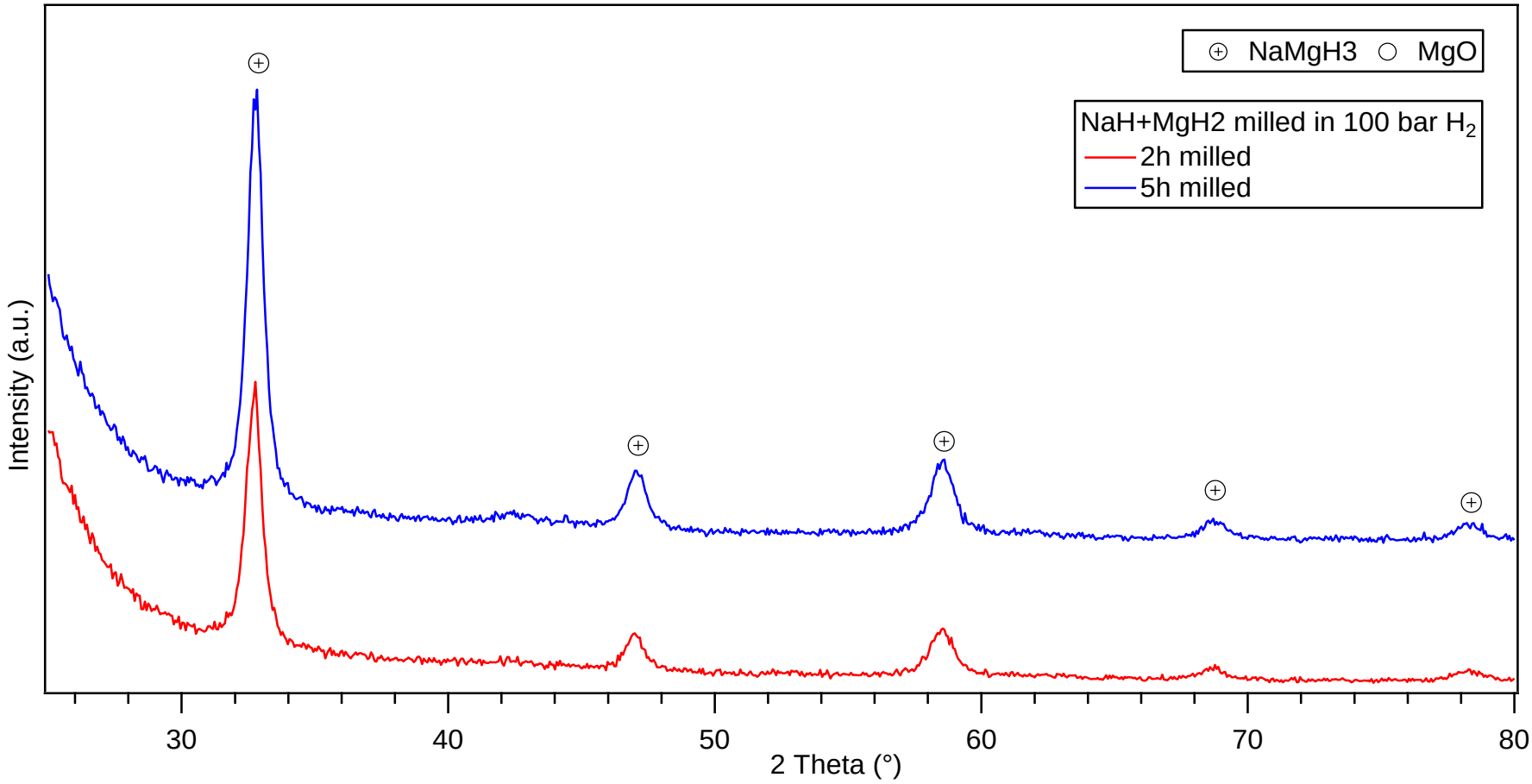

Figure 6.6 RT-XRD patterns of NaH and MgH_2 mechanical milled for 2, 5 and15h in 100 bar H_2 showing $NaMgH_3$ phase formation.

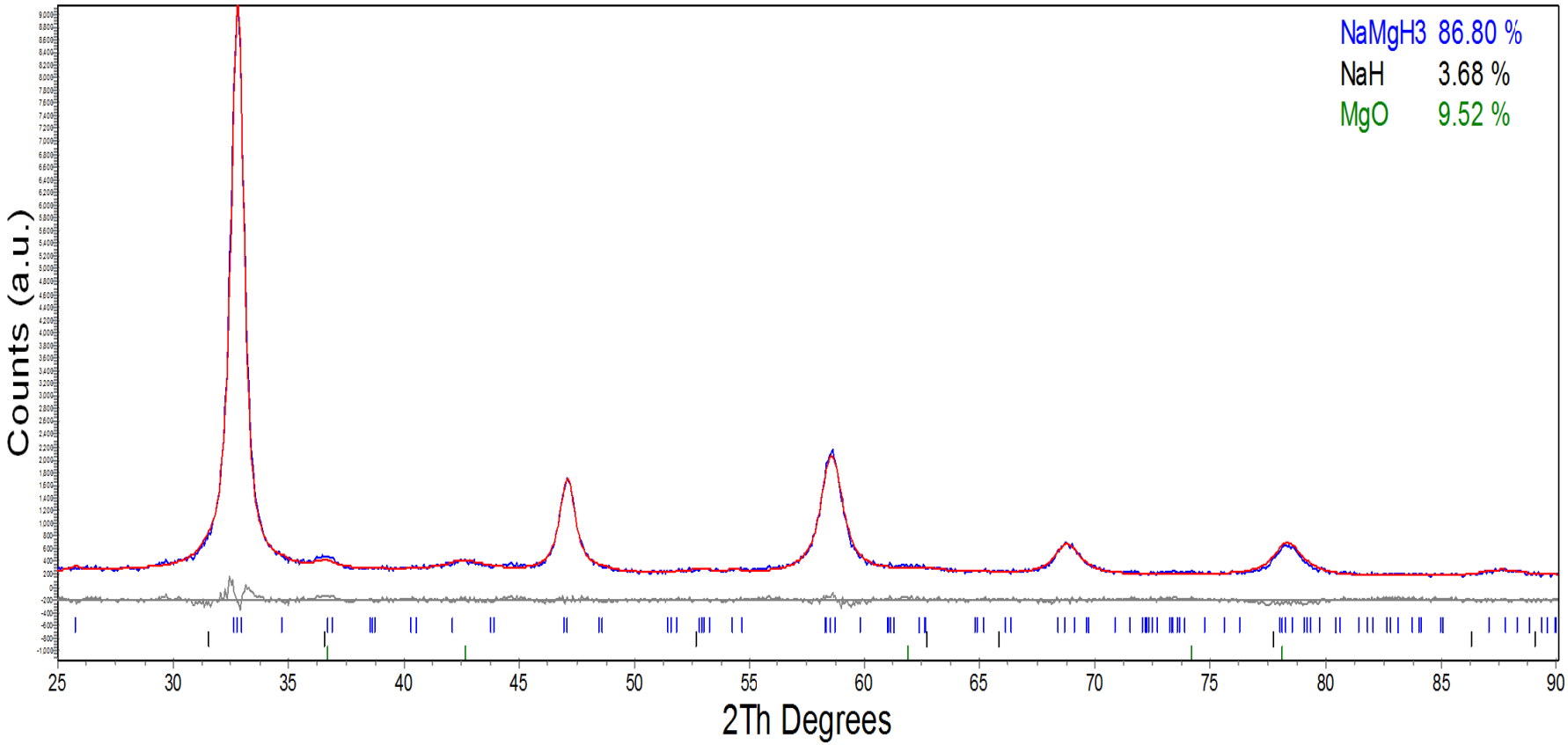

Figure 6.7 TOPAS refinement of NaH+MgH_2 milled for 5h in Ar. 2 theta (°) values before 25 were not considered for the refinement as no representative diffractions were detected. (Observed data is shown by blue lines, calculated data is represented by the red lines and the difference is plotted below in grey). Goodness of fit 1.214

The refinement converged in good agreement with the previously reported orthorhombic structure (perovskite type). From the refinement is clear that lattice parameters tend to expand linearly with increasing milling time, resulting in a larger cell volume for both samples milled in Ar and 100 bar H_2. Figures 6.8 and 6.9 illustrate the change in lattice parameters plotted against the milling time for Ar and H_2 milled samples respectively.

Table 6.1 summarises the lattice parameters of the $NaMgH_3$ phase for the milled samples in Ar and 100 bar H_2 compared to previous literature reported data. The change in lattice parameters can be due to different factors, such as deformation caused by ball-milling or substitution reaction.

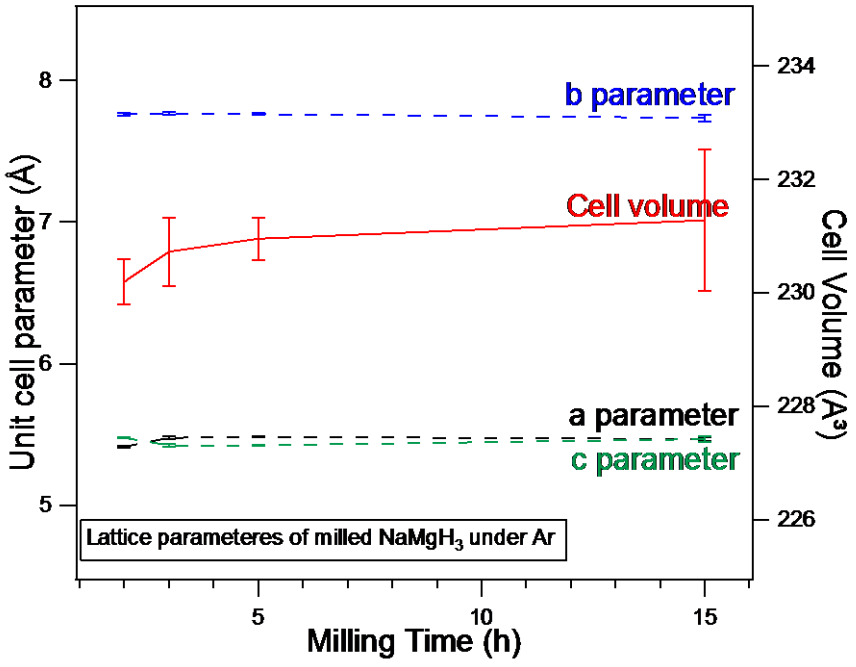

Figure 6.8 Lattice parameters a (black line), b (blue line) c (green line) and cell volume (red line) of the $NaMgH_3$ phases obtained from $NaH+MgH_2$ samples that had been milled in Ar for 2, 5 and 15h. Where error bars are not shown, they are smaller than data points.

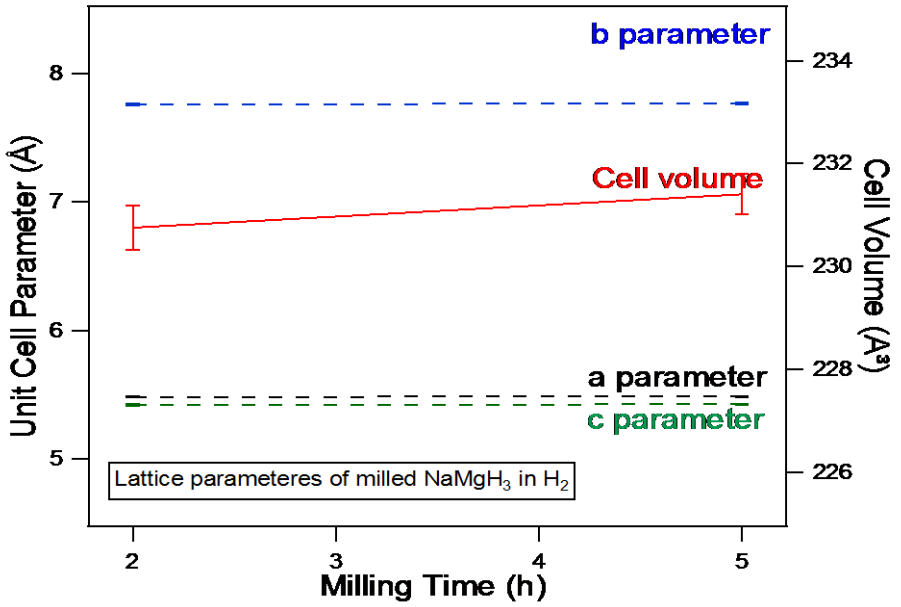

Figure 6.9 Lattice parameters a (black line), b (blue line) c (green line) and cell volume (red line) of the $NaMgH_3$ phases obtained from $NaH+MgH_2$ samples that had been milled in 100 bar H_2 for 2 and 5h. Where error bars are not shown, they are smaller than data points.

Table 6.1 Change in lattice parameters and weight percent of $NaMgH_3$ phases milled for 2, 3, 5 hours under argon and hydrogen atmospheres.

		$NaMgH_3$ (This work)				**(Literature) (Ikeda et al., 2005a)**			
	Mill time (h)	lattice parameters (Å)			Cell Volume (Å^3)	lattice parameters (Å)			Cell Vol. (Å^3)
		a	b	c		a	b	c	
Ar	2	5.42± 0.01	7.76± 0.01	5.4± 0.01	230.19± 0.40	5.46 (2)	7.7 (4)	5.4 (2)	227.32(4)
	5	5.49± 0.01	7.76± 0.01	5.43± 0.01	230.96± 0.60				
	15	5.49± 0.01	7.76± 0.01	5.43± 0.01	231.28± 0.40				
H_2	2	5.49± 0.01	7.76± 0.01	5.42± 0.01	230.75± 0.44				
	5	5.49± 0.01	7.77± 0.01	5.43± 0.01	231.40± 0.39				

6.4 Thermal decomposition

DSC-TGA-MS measurements were performed in order to determine the decomposition temperature, mass loss and which gases were present during the decomposition process of the sample. Figures 6.10 & 6.11 show the DSC-TGA-MS traces of samples milled for 2, 5, and 15h in Ar and H_2 respectively. Results of weight losses, onset, peak and end temperatures of milled samples experimentally gained in this work are summarised in Table 6.2, and compared with previous reports from literature data. (Ikeda et al., 2005a, Pottmaier et al., 2011, Reardon et al., 2013)

DSC traces of the samples milled in Ar for 2h, show that decomposition of the main $NaMgH_3$ phase occurs in two steps. The first decomposition starts at ~287°C (T_{on}), with the maximum inflection peaking at 370 °C (T_{pk}); this curve might be related to the decomposition of $NaMgH_3$, immediately after; a second curve can be observed peaking at 383 °C. The second inflection tends to be more pronounced and broader than the first, and can be linked with the decomposition of NaH up to 408 °C where the reaction is completed. A total amount of 5.8 wt. % of H_2 evolution was detected from the TGA-MS which corresponds to 96.7 wt. % of the theoretical maximum (6 wt. %) for the $NaMgH_3$.

On the 5 h milled sample in Ar, DSC traces show two endothermic reactions starting at 286 °C and peaking at 368.9 and 385 °C for the first and second endotherms respectively, leading to a total mass loss of 4.8 wt.% H_2 up to 405 °C observed from the TGA-MS. Desorption temperature of the sample is reduced about 1 °C in comparison to the 2h milled sample, although, the H_2 capacity is diminished as well.

DSC performed on the 15h milled sample in Ar, the H_2 signal showed dehydrogenation proceeds in two steps: first desorption curve started at 278 °C reaching a maximum at 369 °C,

whereas the second desorption peak was located at 391 °C. Sample desorbed a total of 4.7 wt. % of H_2 up to 400 °C.

For the samples milled in 100 bar H_2, 2 and 5h milled compound dehydrogenation followed two-step reaction starting at 279 and 282°C respectively. Peaks were reached at and 386 °C for the 2h and 369 and 387 °C for the 5h milled materials. Only H_2 gas signal was detected from the MS up to 403 °C accounting for 5.2 wt. % mass loss. On the other hand, the 5h milled sample main inflections were detected at 369 and 387 °C for the first and second endothermic reactions. TGA showed a total of 5.1 wt. % of H_2 release.

DSC-TGA results in this work show a good agreement validating that the dehydrogenation process of the $NaMgH_3$ phase proceeds in two steps, the first release of hydrogen is attributed to the decomposition of $NaMgH_3$ into NaH and Mg releasing hydrogen. The second desorption is related to the decomposition of NaH into Na metal, releasing hydrogen. The reactions are complete at approximately 400 °C when the DSC, TGA and MS signals do not show any changes thereafter. Hydrogen capacity in this investigation (5.8 wt. %) is close to the theoretical maximum (6 wt. %) for the $NaMgH_3$ phase.

Moreover, it was evidenced that increasing milling time positively affect the dehydrogenation properties by reducing the reaction temperatures; this effect is associated with the reduction in the crystallite size of the compounds. Although, milling for longer times causes the hydrogen capacity to be lowered, this decrease can be explained due to MgO formation.

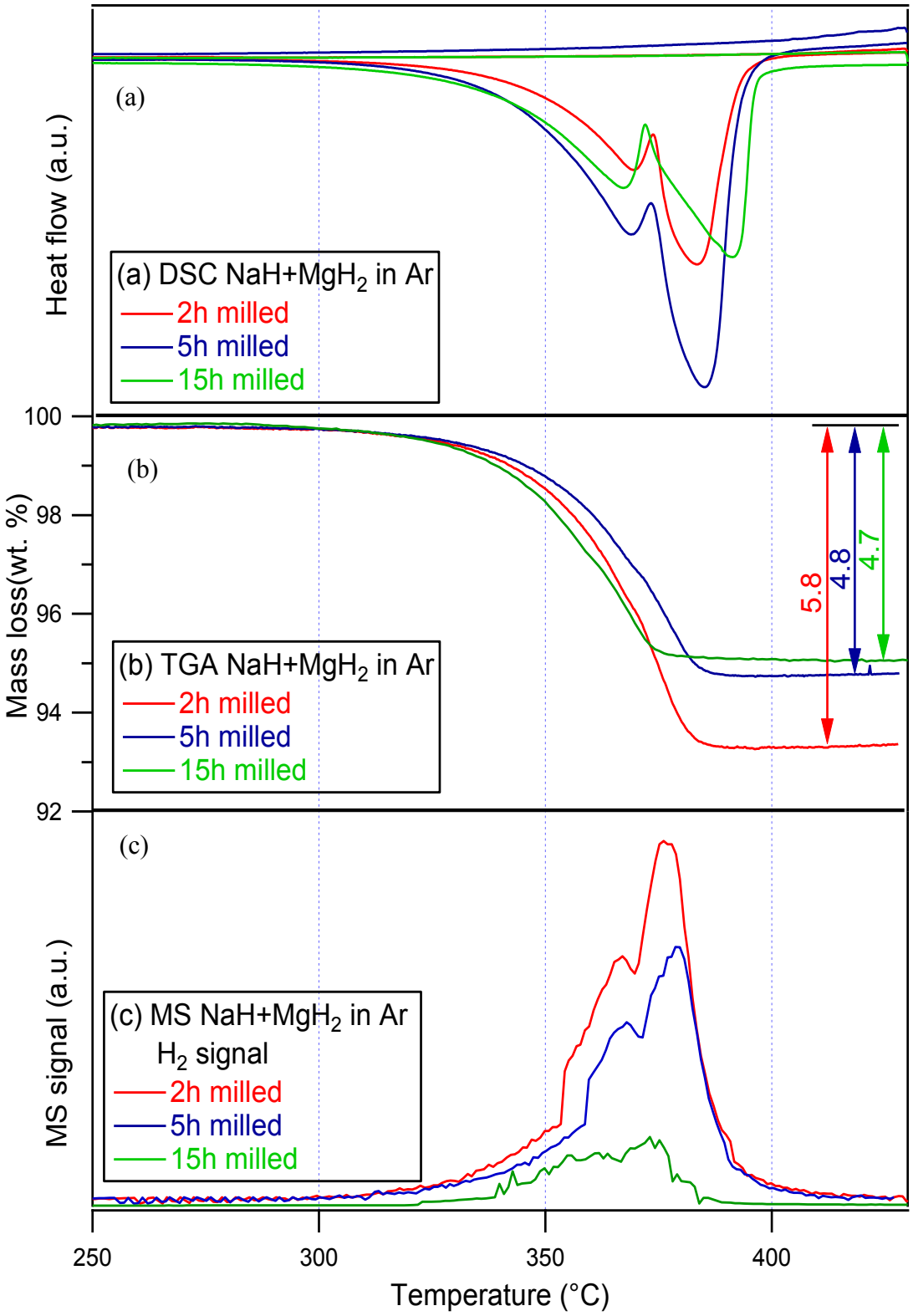

Figure 6.10 (a) DSC, (b) TGA and (c) MS measurements of NaH+MgH_2 which had been milled in Ar for 2, 5, and 15h. All measurements were carried out at a heating rate of 2 °C/min under 3 bar flowing Ar at 100 ml/min (DSC), and 1 bar Ar flowing at 40 ml/min (TGA). Temperatures lower than 250 °C did not show any peaks, hence are not plotted.

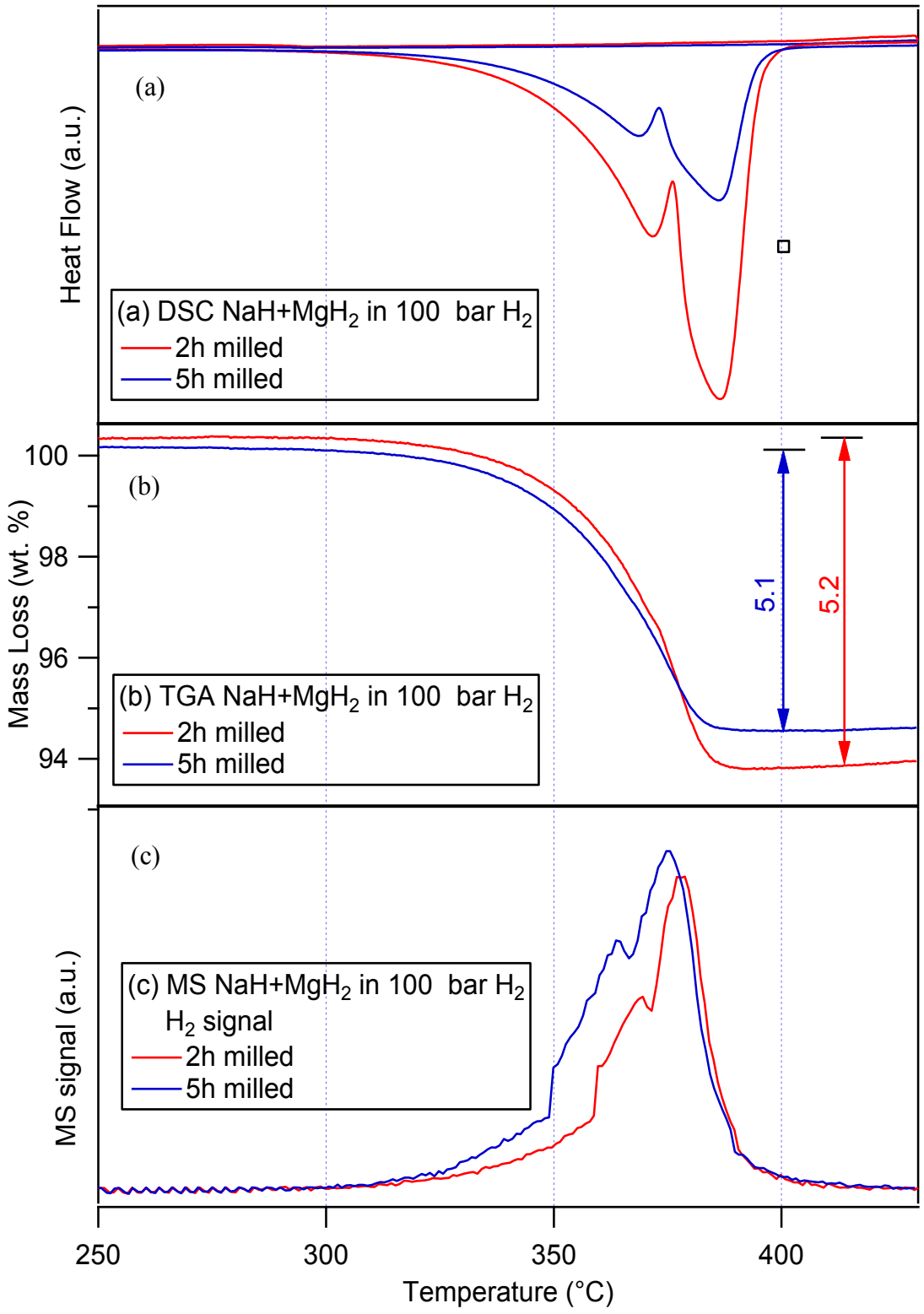

Figure 6.11 (a) DSC, (b) TGA and (c) MS measurements of NaH+MgH_2 which had been milled in 100 bar H_2 for 2 and 5h. All measurements were carried out at a heating rate of 2 °C/min under 3 bar flowing Ar at 100 ml/min (DSC), and 1 bar Ar flowing at 40 ml/min (TGA). Temperatures lower than 250 °C did not show any peaks, hence are not plotted.

Table 6.2 Summary of DSC-TGA measurements of the 2, 5 and 15h milled samples in Ar and 100 bar H_2 compared to previous reported literature. (Ikeda et al., 2005a)

		DSC				TGA
	M. Time (h)	Ton (°C)	Tp1 (°C)	Tp2 (°C)	Tend (°C)	wt (%)
Ar	2	287	370	383	408	6.4
	5	286	369	385	407	5
	15	278	367	391	409	4.7
H_2	2	279	372	387	408	6.5
	5	282	369	386	409	5.6
Literature da et al., 2005a)	20		391	436		5.8

6.5 Analysis of Products after Dehydrogenation

6.5.1 In-situ XRD of milled samples in Ar

Figure 6.12 shows the in-situ XRD of $NaH+MgH_2$ milled for 5h in Ar loaded in a corundum sample holder heated at 2°C/min; with an interval of 25°C for each pattern, in 3 bar He flowing at 100ml/min. At 30 °C, the sample presents peaks related to sodium magnesium hydride ($NaMgH_3$) phase and some peaks of the sample container. On heating, the intensity of the main $NaMgH_3$ phase decreases while the peaks for the sample holder remain unchanged as expected. At 250 °C traces of new phases are observed (sodium hydride NaH, magnesium oxide MgO). These phases correspond to the decomposition of the sodium magnesium hydride $NaMgH_3$ and oxidation of magnesium Mg during the heating. At 300 °C we can still observe the main sodium magnesium hydride ($NaMgH_3$) phase but less intense, in addition, peaks related to sodium hydride NaH, and magnesium oxide MgO phases with increased intensity are present, along

with traces of magnesium Mg metal. Increasing the temperature to 330 °C, the intensity of magnesium Mg, sodium hydride NaH, and magnesium oxide MgO increase, whereas, the intensity of sodium magnesium hydride $NaMgH_3$ decreases even further. At 350 °C sodium magnesium hydride $NaMgH_3$ and sodium hydride NaH phases are no longer present. This suggests their total decomposition. Only magnesium Mg metal, and magnesium oxide MgO patterns are observed at this temperature and the same traces remain up to 400 °C with increased intensity. Reflections from Na are not observed on heating to 400 °C, this effect, according to the phase diagram shown in Figure 6.2, is attributed to a phase transition from solid to liquid (melting) and further evaporation of Na preventing to be detected by the XRD. These measurements confirm the validity of the reactions assigned to the DSC peaks and show the decomposition of the sodium magnesium hydride into magnesium and sodium metal in two steps reaction according to equations (2.2) and (2.3).

Figure 6.13 shows the room temperature XRD pattern of the decomposed material from the in-situ XRD measurement. There are peaks related to magnesium and sodium in addition, to a small trace of magnesium oxide.

Rietveld refinement of Figure 6.13 is shown in Figure 6.14, from this figure is noted that decomposed sample contains 29 wt. % of crystalline magnesium and 42 wt. % of crystalline sodium. The remaining crystalline material 29 wt. % is magnesium oxide formed during the4decomposition presumably due to a leak in the anton-par cell apparatus used for the in-situ measurements.

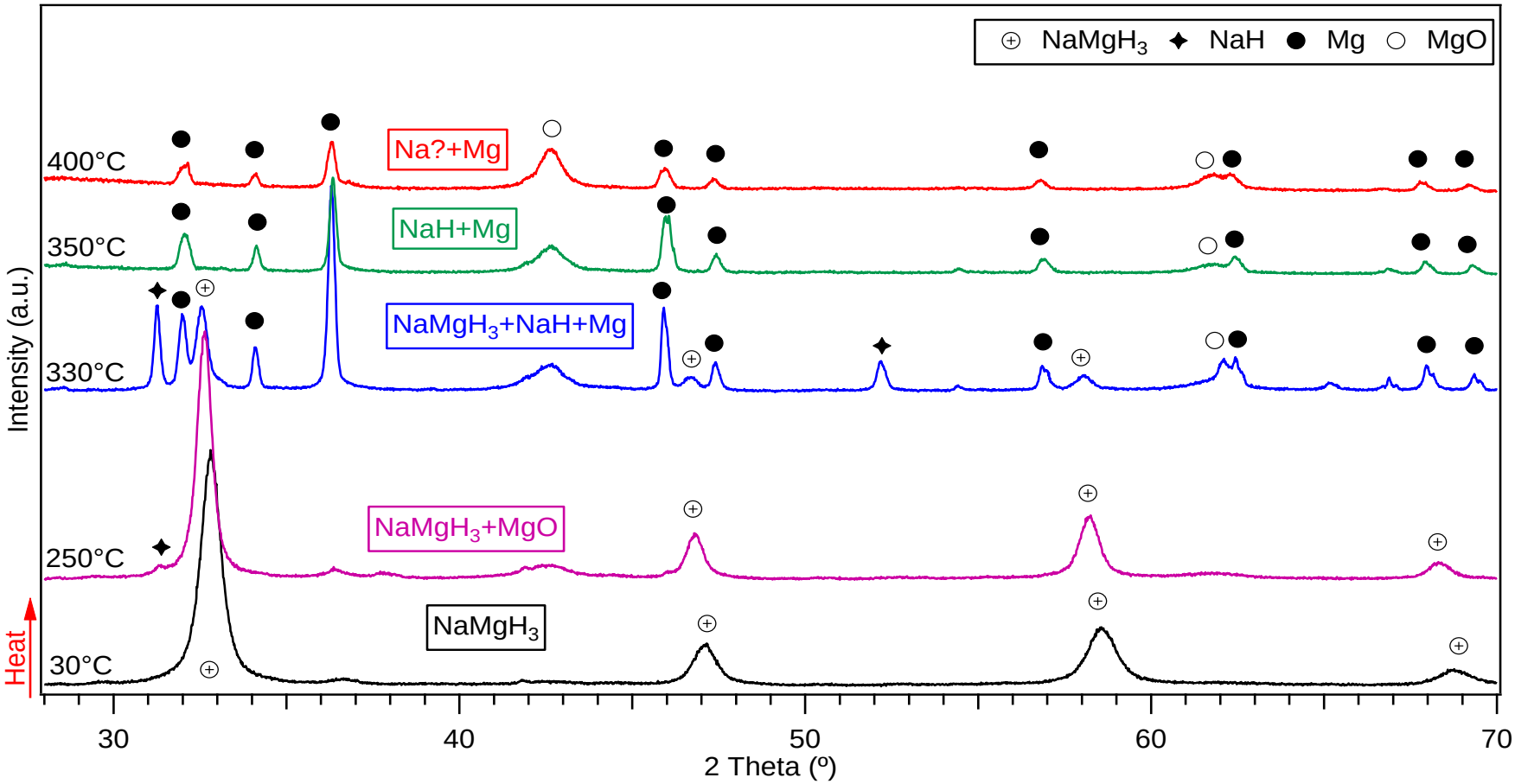

Figure 6.12 In-situ XRD of NaH+ MgH_2 milled for 5h in Ar heated from 30 to 400 °C at 2 °C in 3bar He flowing at 100 ml/min

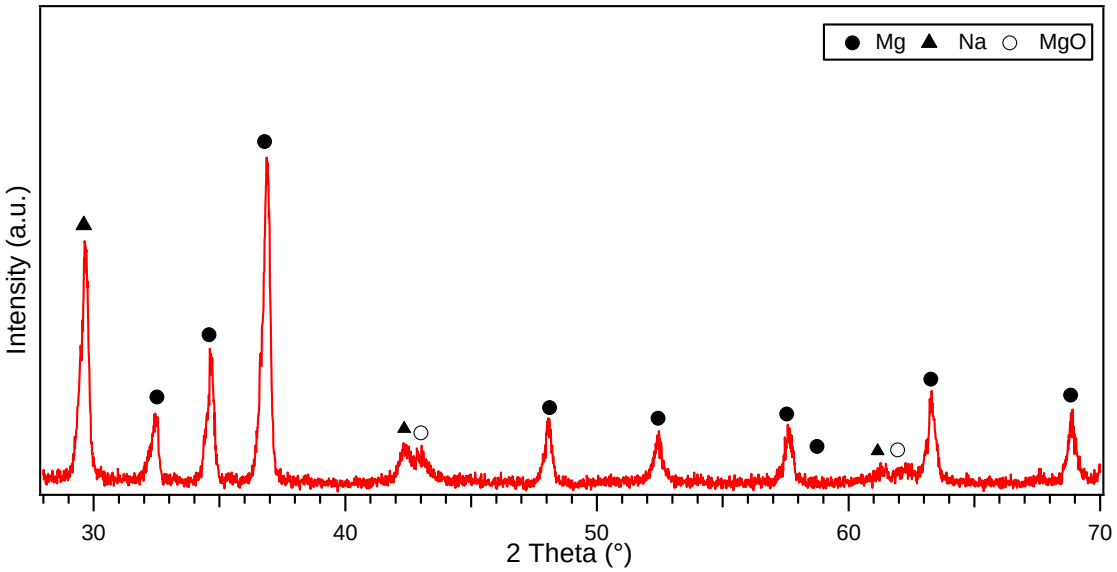

Figure 6.13 RT XRD of the decomposed milled NaH+MgH_2 for 5h in Ar after In-Situ XRD

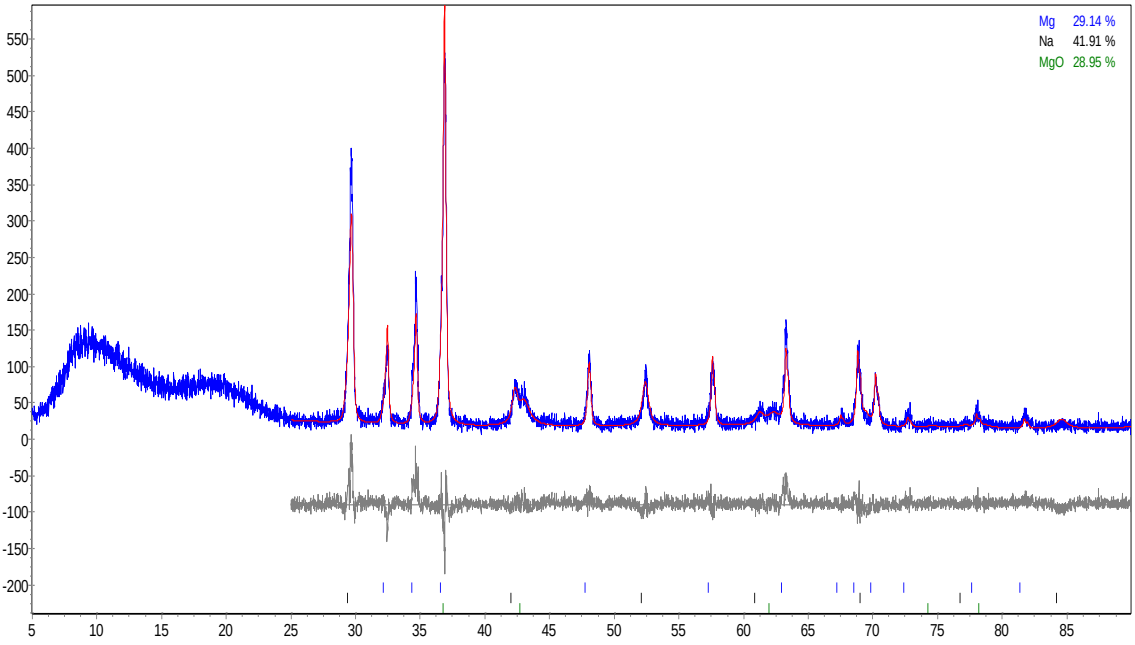

Figure 6.14 Retvield refinement of the decomposed milled NaH+MgH_2 for 5h in Ar after In-Situ XRD. Red line shows the calculated data. Blue line shows the data received from the cif file. Grey line shows the difference between the observed and calculated data. Goodness of fit = 1.212

6.5.2 In-situ XRD of milled samples in 100 bar H_2

Figure 6.15 shows the in-situ XRD of NaH+MgH_2 milled for 5h in 100 bar H_2 loaded in a boron nitride sample holder heated at 2°C/min, in 3 bar He flowing at 100ml/min. Each pattern was collected with an interval of 25 °C. At 30 °C (RT), sample presents diffractions related to $NaMgH_3$ phase and some peaks of the sample container. On heating, the intensity of the main sodium magnesium hydride $NaMgH_3$ phase decreases whereas peaks of the sample holder remain unchanged as expected. At 250 °C traces of new phases associated with NaH, Mg and small diffraction of MgO. These phases correspond to the starting decomposition of the $NaMgH_3$ main phase and oxidation of Mg during the heating attributed to a small leak in the instrument. At 330 °C remaining of $NaMgH_3$ is still detected, however their intensity is significantly lowered. In addition, NaH, Mg, MgO phases show increased intensity.

Increasing the temperature to 350 °C the intensity of Mg, NaH, and MgO increase further, whereas, reflections of $NaMgH_3$ are no longer present demonstrating the total decomposition of the phase. Only Mg metal, and MgO patterns can be observed up to 400 °C. No reflections from Na metal were observed on heating up to 400 °C, as previously mentioned in the milled samples under Ar, this effect is attributed to a phase transition from solid to liquid (melting) and further evaporation of Na preventing to be detected by the XRD as illustrated in Figure 6.2. XRD reflections show a good agreement with the reactions assigned from the DSC. Two steps reaction according to equations (2.2) and (2.3) were obtained in the 5h milled sample in 100 bar H_2.

Figure 6.16 illustrates the surface plot of the milled $NaMgH_3$ highlighting the decomposition reactions and the temperatures of the phase changes.

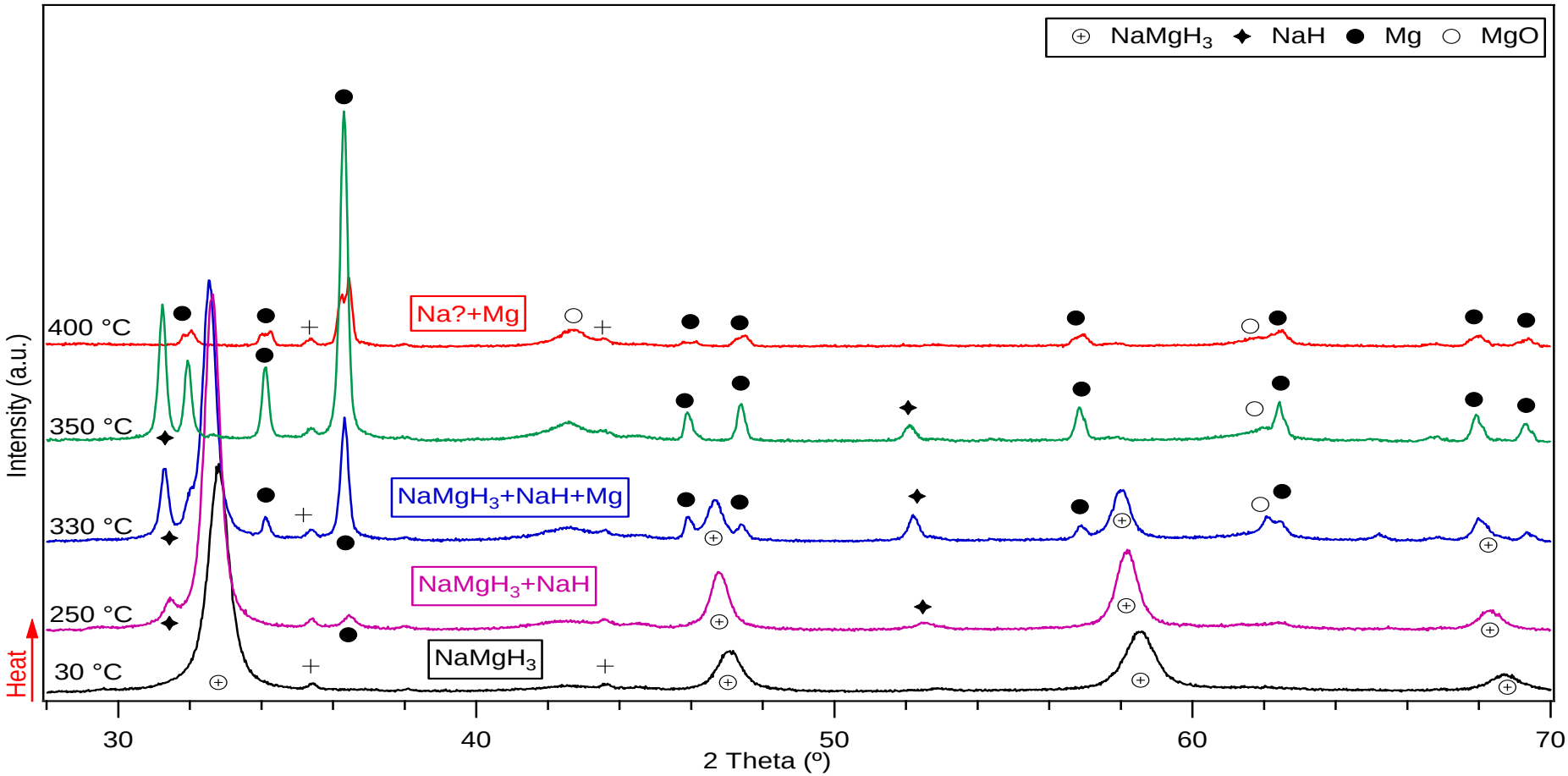

Figure 6.15 In-Situ XRD of NaH+MgH_2 milled for 5h in 100 bar H_2 heated from 30 to 400 °C at 2 °C in 3bar He flowing at 100 ml/min.

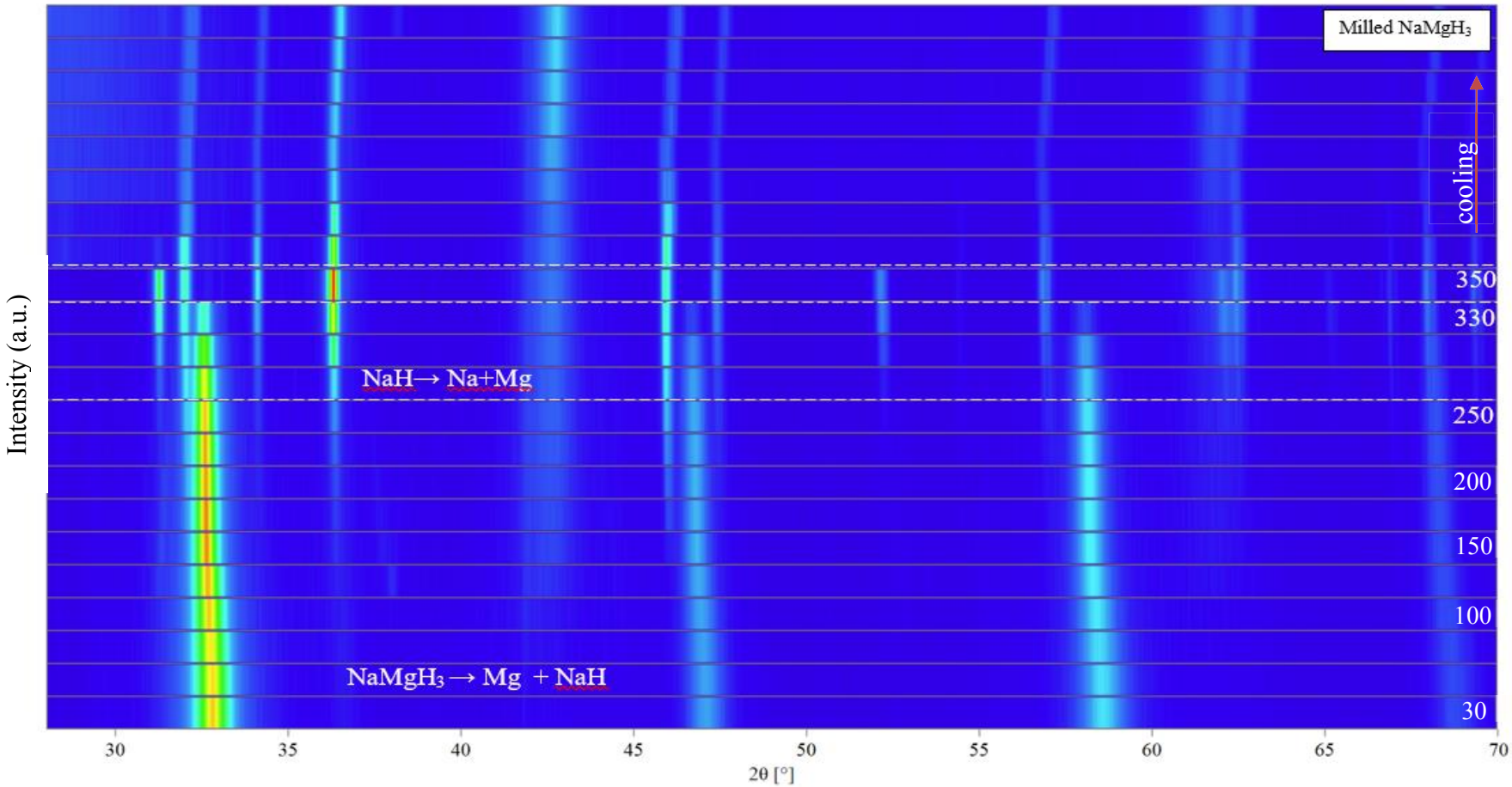

Figure 6.16 Surface plot from in-situ XRD of 5h milled $NaMgH_3$ heated under He (100 ml/min, ~3 bar) between 30 – 450 °C. A brighter colour corresponds to a higher diffraction intensity. The white dashed lines show the phase transition temperature and are given as a guide for the eye.

6.6 Reversibility.

The dehydrogenated $NaH+MgH_2$ milled for 5h in Ar (in-situ XRD), was subsequently heated at 10 bar constant flow of hydrogen gas at 100ml/min in order to study the re-hydrogenation ability of the same after decomposition.

Figure 6.17 shows the re-hydrogenation of Mg and Na products; obtained from the decomposition of the sample under 3bar He, under 10 bar H_2 heated at 2°C/min with patterns taken isothermally at 25 °C from room temperature to 400 °C. Initially, Mg and Na metals are present. On heating to 100 °C, same reflections remain but less intense. At 200°C, the reformation of the $NaMgH_3$ phase is distinguished, this phase is accompanied with traces of NaH and Mg phases. Additionally, extremely intense peaks of MgO can be also observed, these are potentially related to a leak in the anton-par cell apparatus where the experiment was carried out. At 300°C, diffractions of Mg and NaH phases disappeared, leading as to the conclusion that sample has been successfully re-hydrogenated. On heating to 400°C, peaks for the recombined phase have disappeared, and only magnesium oxide patterns can be seen.

To investigate the reason of this unexpected reaction, another measurement had to be performed. Thus, sample was removed from the in-situ XRD cell and transferred to an argon filled glove box. When taking the sample holder out of the cell was noticed that the colour and texture on the surface of the sample has changed from a dark grey homogeneous powder to a light grey, when unloading the sample from the sample holder was detected that this effect was only present on the surface of the sample, underneath, the texture of the same remained unchanged.

Consequently, sample was hand mixed and loaded into a Kapton dome-shaped, vacuum-tight sample holder for ex-situ XRD characterisation. Figure 6.18 shows the ex-situ XRD pattern collected after manually mixing the re-hydrogenated $NaMgH_3$ sample. From this figure, was

seen that MgO peaks are still present but their intensity is decreased in comparison to the in-situ diffractions.

The pattern for the $NaMgH_3$ phase is well defined and the intensity is greater. Therefore, we can conclude that the reason we were not able to observe the $NaMgH_3$ phase after 400°C, was due to the magnesium oxide layer formed on the surface of the sample during heating, preventing accurate XRD characterisation of the whole sample.

To evaluate the amount of each material present in the sample Rietveld refinement was carried out (Figure 6.19) and shows that re-hydrogenated sample contains 27% wt.% of crystalline sodium magnesium hydride, 5.6 wt.% of sodium hydride and the remaining belongs to oxides. The high levels of oxides can be attributed to the highly sensitivity of the sample when is exposed to air during the decomposition due to a small leak in the apparatus.

Figure 6.20 shows the surface plot of the rehydrogenated $NaMgH_3$, indicating the temperature and phase reversibly formed from Na and Mg metals.

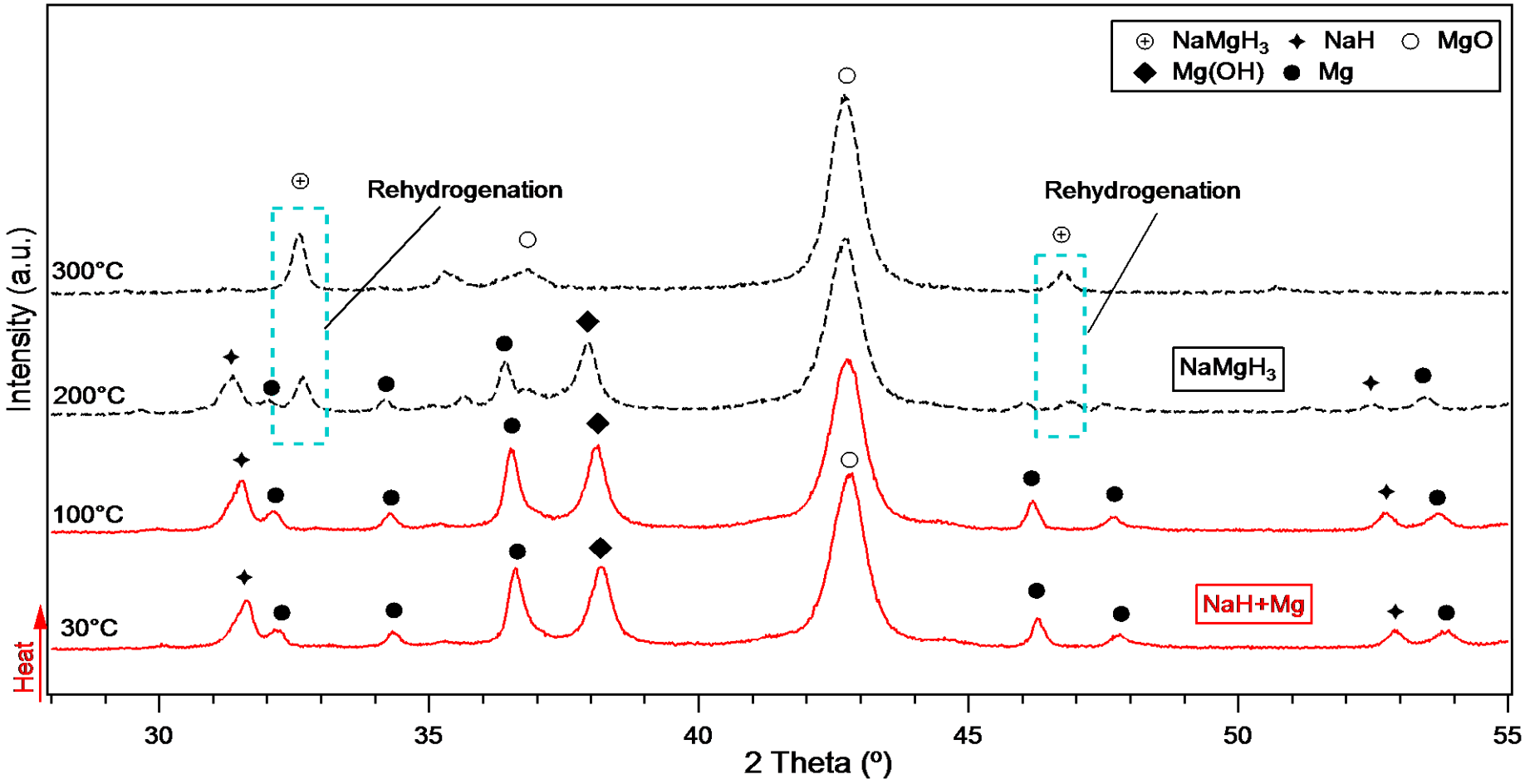

Figure 6.17 In-Situ XRD of the decomposed $NaH+MgH_2$ sample milled for 5h (Ar) in 3 bar He. Heated from RT to 400 °C in 10 bar H_2 flowing at 100 ml/min. Blue dashed lines show the re- hydrogenation of the $NaMgH_3$ phase.

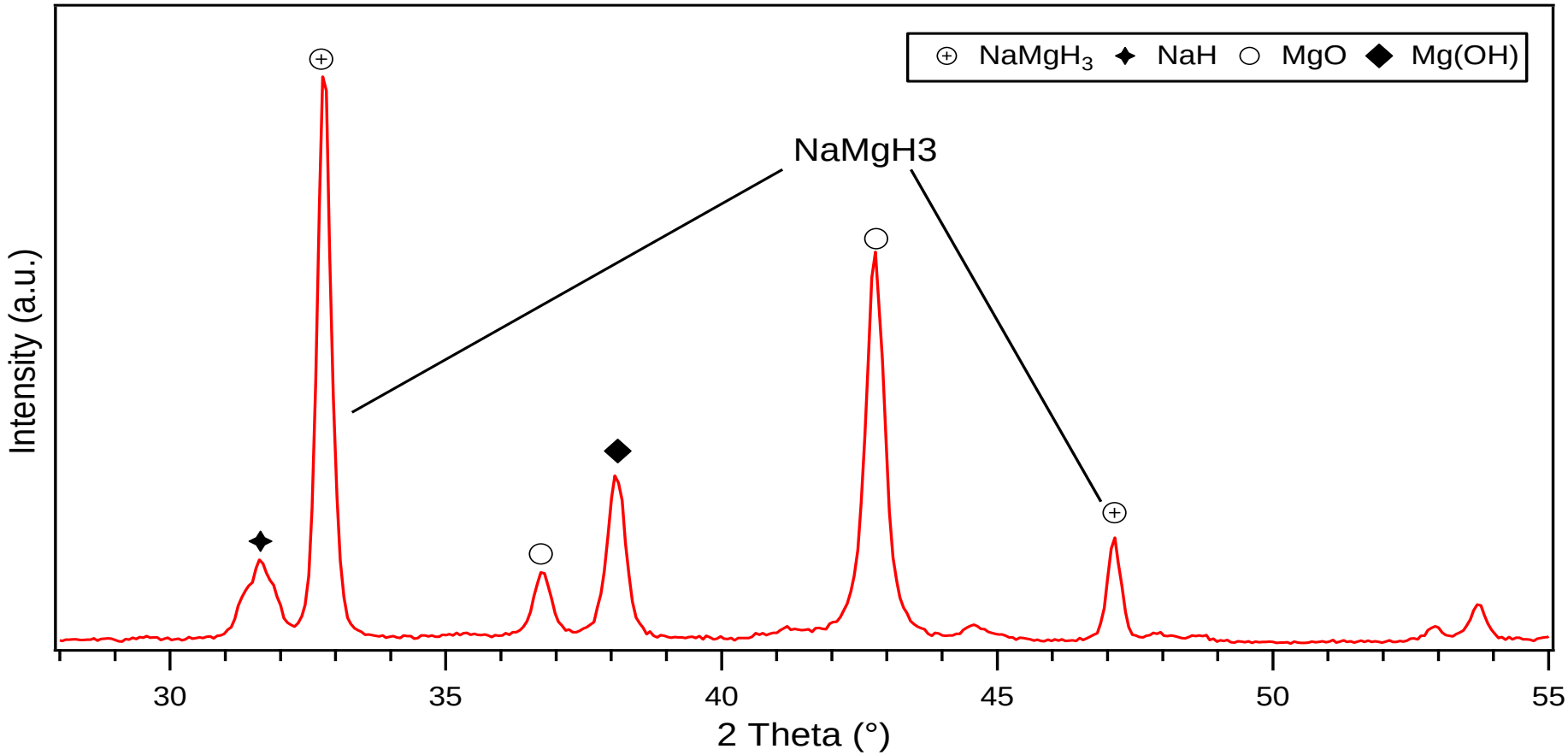

Figure 6.18 Ex-situ XRD of the re-hydrogenated NaH+MgH_2 that has been milled for 5h in Ar.

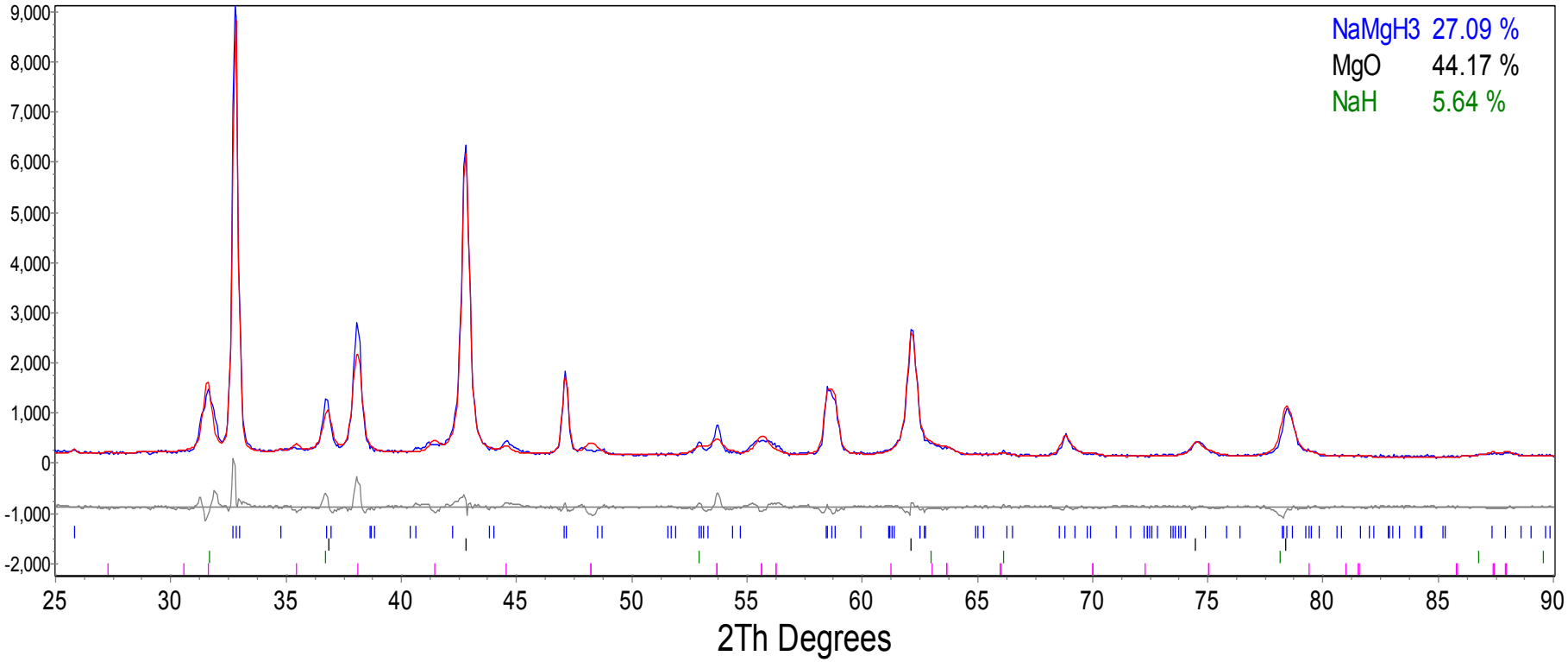

Figure 6.19 TOPAS refinement of the re-hydrogenated NaH+MgH_2 milled for 5h (Ar). 2 theta (°) values before 25 were not considered for the refinement as no representative diffractions were detected. (Observed data is shown by blue line; calculated data is represented by the red line and the difference is plotted below in grey). Goodness of fit 1.321

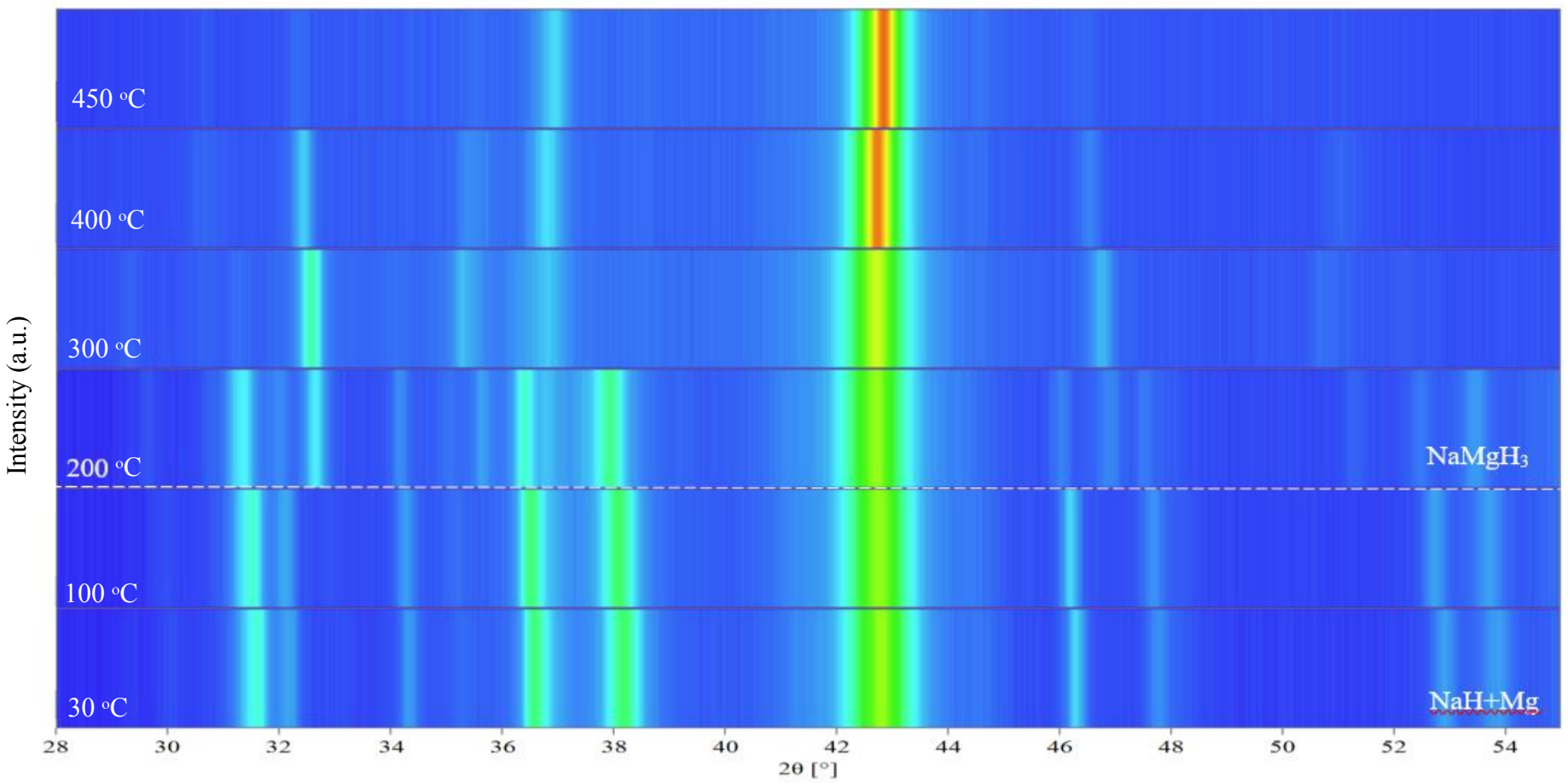

Figure 6.20 Surface plot from in-situ XRD of rehydrogenated $NaMgH_3$ heated under H_2 (100 ml/min, ~10 bar) between 30 – 450 °C. A brighter colour corresponds to a higher diffraction intensity. The white dashed lines show the phase transition temperature and are given as a guide for the eye.

6.7 Conclusions

The aim was to synthesise sodium magnesium hydride via mechanical milling between sodium hydride and magnesium hydride in an argon and hydrogen atmospheres. Analysis of as milled materials confirmed the successful formation of the orthorhombic sodium magnesium hydride only after 2 hours milling.

There is a modification of the sodium magnesium hydride lattice parameters after 2,5,15 hours milling in argon resulting in an increase of parameters a, b and c and hence of unit cell volume. The same characteristics can be observed for the samples milled under hydrogen.

Thermal decomposition of the as milled product was investigated to further understand the material behaviour, and compare to previous reported values and decomposition mechanism. DSC for the argon milled samples, showed 2 endothermic peaks on heating up to 410°C. The first peak at approximately 370°C reduces in temperature as the milling time increases, showing that reduction in crystallite size can have a positive effect in the reaction. This endotherm corresponds to the hydrogen desorption of the $NaMgH_3$ phase. The second endothermic peak at 383 °C increases in temperature with the milling time, this peak corresponds to the decomposition of the NaH phase. Complete dehydrogenation is achieved at approximately 408 °C. Similar DSC information was obtained for samples milled under hydrogen.

Argon milled samples TGA, indicates decomposition with an onset temperature of approximately 290°C completed by 410°C. Moreover, samples milled for 2 hours show a weight loss of approximately 5.8 wt.%, which is in good agreement with the theoretical predicted and previous reported values from the literature (Ikeda et al., 2005a, Pottmaier et al., 2011, Wu et al., 2008, Reardon et al., 2013). Further milling 5 and 15 hours show a decrease in weight loss to 5 and 4.7 wt.% respectively. TGA of samples synthesised in hydrogen show a comparable mass loss with samples milled in argon of around 5.2 and 5.1 wt.% H_2 for 2 and 5h

samples respectively, indicating that increasing the milling time reduces the hydrogen desorption capacity.

Mass spectrometer for samples milled in argon and hydrogen atmospheres show that only hydrogen is released during thermal decomposition. The hydrogen release for the first reaction starts at around 280°C and is complete at approximately 376°C with the main peak at 370°C. The second hydrogen evolution begins at 376°C, with a sharp peak at 383°C and is finished by 410°C temperature at which hydrogen stops being desorbed.

In-situ XRD showed the phase changes of the sample on heating. At room temperature $NaMgH_3$ main phase was reflected. At 250°C, $NaMgH_3$ starts to decompose into NaH and Mg. At 350°C, NaH decomposed into Na releasing H_2. The only products observed upon decomposition were Mg and MgO. No traces of pure sodium were observed during heating, this effect was explained based on the Na-Mg-H phase diagram (Figure 6.2), where it is clear that sodium suffers a phase transition (melts) on heating and vaporises due to the change from solid to liquid form, preventing XRD detection.

Ex-situ XRD on the decomposed products shows the reflections of metallic magnesium and sodium and some remains of magnesium oxide.

Re-hydrogenation of the $NaMgH_3$ phase from the decomposed sample was investigated. In-situ XRD on flowing hydrogen was performed in attempt to re-hydrogenate the decomposed products. Reabsorption was achieved at ~200°C and 10 bar H_2 flowing at 100ml/min. At 400°C intense reflections of MgO peaks and no traces of $NaMgH_3$ where observed, this effect is due to a small leak in the Anton-Paar cell used for the measurement causing the oxidation of the sample in the surface and preventing correct reflection of the sample.

Ex-situ XRD on the recombined product after hand mixing in the glove box showed the $NaMgH_3$ phase was present but due to the oxide layer on the surface of the sample was not detectable, therefore validating our theory from previous observations (Ikeda et al., 2005a, Ikeda et al., 2007b, Pottmaier et al., 2011).

It is therefore proposed that mechanical milling of sodium and magnesium hydrides form a new hydride. This synthesised compound (sodium magnesium hydride) produces enhanced results in comparison to those reported from literature. (Pottmaier et al., 2011, Ikeda et al., 2007b, Reardon et al., 2013, Komiya et al., 2008, Wu et al., 2008)

It is important to highlight that ball milling was carried out in an Ar atmosphere under relatively low pressure, which is advantageous for scaling-up. Nevertheless, the onset decomposition temperature ~270 °C remains too high for on-board hydrogen storage applications.

CHAPTER VII

7. RESULTS AND DISCUSSION: $Li_xNa_{1-x}MgH_3$ HYDRIDE SYSTEM

7.1 Introduction

As mentioned in the previous chapter ternary compounds with perovskite structure (ABH_3) have attracted attention as candidates for solid-state hydrogen storage; particularly, magnesium and alkali elements due to their light weight and relative abundance (Rönnebro et al., 2000, Li et al., 2011, Pottmaier et al., 2011).

From the perovskite ternary hydrides, $NaMgH_3$ has stood out due to its relatively high theoretical volumetric and gravimetric hydrogen storage densities (88 kg/m^3 & 6 wt.%), and the ability to reversibly absorb and desorb H_2 (Bouhadda et al., 2010). In addition, this perovskite structure due to the superior hydrogen mobility, constitutes a promising material for future generations of electronic devices due to its high ionic conductivity (Pottmaier et al., 2011).

Even though, $NaMgH_3$ exhibits a decrease in desorption temperatures (400°C) compared to the starting materials, conditions for mobile hydrogen storage applications are not yet met (Wang et al., 2016). Therefore, there is a need to enhance the sorption kinetics and lower the decomposition temperatures of the ternary hydride.

Furthermore, it has been established that replacing a transition metal (B) with an alkali/alkaline earth metal in the ABH_3 system can enhance the gravimetric capacity, when light metals (Li. Mg, Na) are incorporated (Ikeda et al., 2005b, Ikeda et al., 2005a, Ikeda et al., 2007a, Reardon et al., 2013, Fornari et al., 2007, Komiya et al., 2008). Ikeda et.al reported the formation ability of $Li_xNa_{1-x}MgH_3$ (x=0, 0.5 & 1) after mechanical milling NaH, MgH_2 and LiH for 20 h under a

hydrogen atmosphere. The (x=0) composition resulted in a single phase $NaMgH_3$ compound, while for (x=0.5, 1) the unreacted remains of MgH_2 were detected (Ikeda et al., 2005b).

Xiao et al. (Xiao et al., 2009) performed density functional theory (DFT) calculations on $Li_xNa_{1-x}MgH_3$, predicting that substituting of Li for Na into the system will lead to a decrease in unit-cell parameters, due to the smaller ionic size of Li^+ (compared to Na^+).

Martinez Coronado et.al, and Zhong-min and co-workers (Martínez-Coronado et al., 2012, Wang et al., 2016) synthesised $Na_{1-x}Li_xMgH_3$ (x= 0, 0.25 & 0.5), (x=0, 0.5, 1.0) employing high-pressure technique and mechanical milling respectively, and confirmed these DFT predictions.

The aim of this study is to synthesise $Li_xNa_{1-x}MgH_3$ with nominal compositions (x=0, 0.2, 0.5, 0.8) by mechanical milling under Ar atmosphere, rather than under hydrogen; to the best of the author's knowledge the use of this method to synthesize the $Li_xNa_{1-x}MgH_3$ system has not been reported. In addition, there is a great need to investigate the recombination ability of the $Li_xNa_{1-x}MgH_3$ system.

This chapter describes a study of the phase structure, thermal analysis and recombination ability of the $Li_xNa_{1-x}MgH_3$ (x=0, 0.2, 0.5, 0.8) system.

7.2 Sample Preparation

Powders of MgH_2 (95% pure hydride phase and remainder 5% Mg; Sigma-Aldrich Inc.), NaH (95% pure; Sigma-Aldrich Inc.) and LiH (99.9% pure; Sigma-Aldrich Inc.) were mixed to obtain the following composition: $Li_xNa_{1-x}MgH_3$, (x= 0, 0.2, 0.5, and 0.8). Mixtures were placed in a steel vial with steel balls diameter of 10 mm and then ball milled with a ball to powder ratio of 50:1. The initial mixtures were mechanically milled in a planetary ball mill apparatus (Retsch

Planetary Ball Mill PM400) at 400 rpm for 5 hours with intervals of 5 min milling and 5 minutes rest time to try to avoid excessive over-heating.

The samples thus prepared were characterised by, powder in-situ X-ray diffraction measurement (Anton Paar cell) and ex-situ XRD (Bruker D8 Advance diffractometer using Cu Kα (0.154nm) radiation, thermogravimetric analysis (Netzsch TG 209) heating rate of 2 °C/min, under 40 ml/min flowing argon and differential thermal analysis (Netzsch DSC 204 HP Phoenix) heating rate of 2 °C/min, under 100ml/min flowing argon at 3 bar constant pressure, installed inside of an argon filled glove box. Furthermore, in order to reduce (hydro)-oxidation, the vials employed for the ball milling process and the as-prepared samples were always handled in a glove box filled with purified argon of less than 0.5 ppm oxygen.

7.3 Characterisation of milled material

To determine which reaction products have been formed during mechanical milling process it is necessary to examine the milled material, X-ray diffraction, followed by a thermal decomposition analysis is undertaken.

Figure 7.1 shows the XRD patterns for the as-milled products. Adding x=0 to the system, peaks of $NaMgH_3$ phase can be identified which correspond to the orthorhombic (space group Pnma) perovskite-type structure. There are also unreacted peaks corresponding to NaH and MgO phases, the last can be related to oxidation due to sample processing and handling.

With the Li substitution x=0.2, a slight decrease of peak intensity in the main $NaMgH_3$ phase is observed and the same unreacted NaH phase is present, LiH is not observed, presumably because it reacted with NaH and MgH_2 mixtures on milling, leading to a lattice contraction in the main $NaMgH_3$ phase represented by a shift to a higher diffraction angles due to the smaller

size of the Li cations (inset of Fig. 7.1). Intense peaks of MgH_2 and NaH phases can be observed when adding x=0.5, 0.8 into the system; these leftover peaks appear as a result of unreacted product after the milling process.

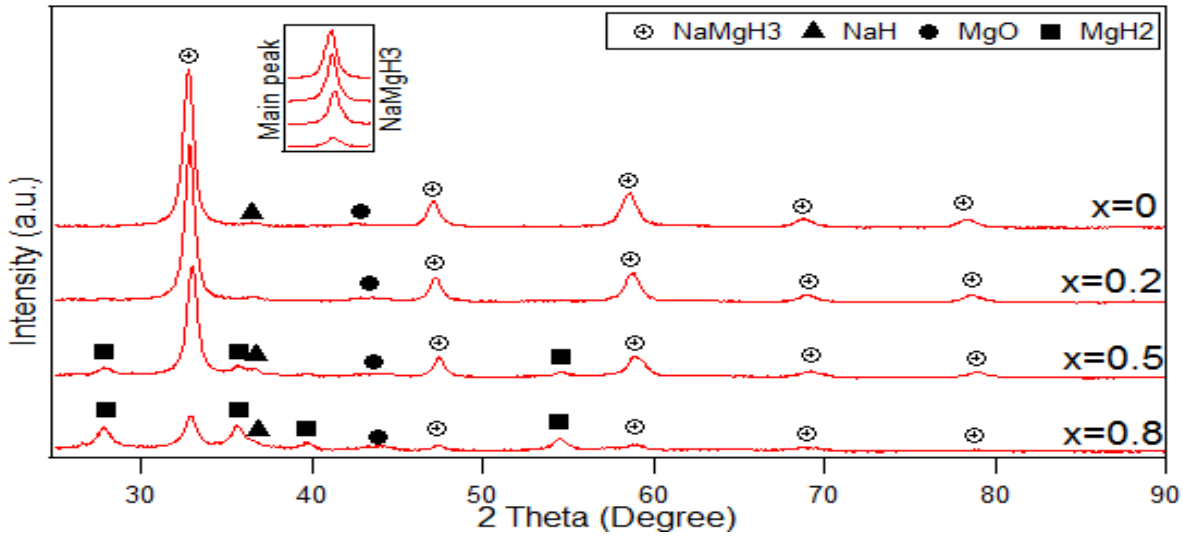

Figure 7.1 XRD patterns of 5h ball milled $Li_xNa_{1-x}MgH_3$ (x = 0, 0.2, 0.5, 0.8) hydride system. Main $NaMgH_3$ peak zoomed in for the different Li x substitutions.

$NaMgH_3$ phases show a decrease in the peak intensity, whereas MgH_2 and NaH peak intensity increases as the amount of Li increases. No LiH peaks were observed presumably because this reacted with the $NaMgH_3$ phase when replacing Na by Li leading to a peak shift due to smaller size of Li cations which confirms the incorporation of Li ions into the $NaMgH_3$ perovskite crystal structure(Martínez-Coronado et al., 2012).

This effect suggests that substitution of Na by Li can be performed up to a certain point; in the case of this research it is experimentally determined to be x = 0.5, when we go beyond that amount (i.e. x = 0.8) the intensity of the main phase is substantially decreased and more intense peaks of unreacted phases can be observed (Ikeda et al., 2005b, Martínez-Coronado et al., 2012, Wang et al., 2016).

These events have been explained by Ikeda et. al. on the basis of the tolerance factor (t) calculations to predict the structure stability of ABX_3 perovskite-type hydrides. Ikeda et.al. reported that perovskite–type hydrides with stable structure are suggested to be within the range of tolerance factor (0.77 to 1.00)(Ikeda et al., 2007b). Therefore, in this investigation, $Li_xNa_{1-x}MgH_3$ substituted samples with nominal composition x = 0, 0.2 and 0.5 lay within this range showing a unit cell decrease tendency (Fig. 7.2), where it is evident that the sample containing Li_x (x=0.8) substitution presents a different pattern, showing an increase in the cell volume since t value does not fall into the limit range.

In order to carry out a more accurate structural study, and to identify and quantify the phases of the $Li_xNa_{1-x}MgH_3$ (x= 0, 0.2, 0.5, & 0.8) hydride samples, Rietveld Refinement has been performed. Results for the lattice parameters and cell volumes are contained in Table 7.1 and compared to previous literature reports.

Table 7.1 Lattice parameters for $Li_xNa_{1-x}MgH_3$ hydride (5h ball milled) compared to the literature data.

Lattice parameters	This work				Martínez C. et al.(Martínez-Coronado et al., 2012)		
$Li_xNa_{1-x}MgH_3$	x=0	x=0.2	x=0.5	x=0.8	x=0	x=0.25	x=0.5
a (Å)	5.48± 0.05	5.45± 0.07	5.45± 0.04	5.44± 0.13	5.46(6)	5.46(5)	5.46(1)
b (Å)	7.74± 0.07	7.69± 0.02	7.68± 0.06	7.69± 0.21	7.70(9)	7.70(8)	7.69(2)
c (Å)	5.43± 0.04	5.44± 0.01	5.39± 0.03	5.43± 0.13	5.41(6)	5.40(6)	5.39(1)
V ($Å^3$)	230.49± 0.37	227.74± 0.74	225.66± 0.29	225.98± 0.24	227.88(4)	227.61(4)	226.96(9)

Lattice parameters of the $Li_xNa_{1-x}MgH_3$ system obtained from the refinement significantly decrease as Li is added; Figure 7.2 (top) presents the lattice parameters in function of the Li substitution into the sample; this reaction can be explained by the smaller Li^+ ionic size in respect to the replaced Na^+ ions. Moreover, this effect can also be observed in the volume decrease of the unit cell plotted in Figure 7.2 (bottom). Nevertheless, when the addition of Li reaches x=0.8 there is a significant increase in the cell volume.

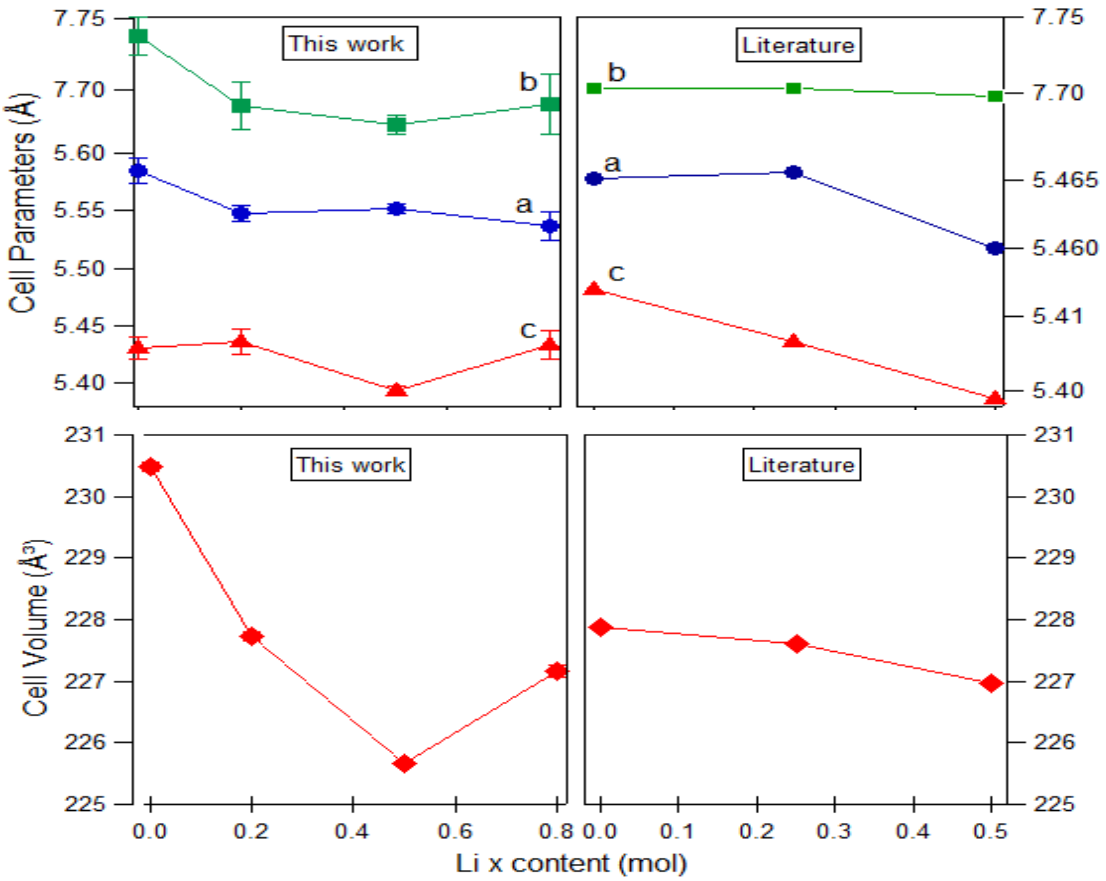

Figure 7.2 Unit cell parameters (top) and Cell Volume parameters (bottom) of $Li_xNa_{1-x}MgH_3$ hydride system in function of Li substituted into the system. This work (left) vs literature (right)[11]. Where error bars are not shown, they are smaller than the data symbols.

7.4 Measurement of hydrogen storage capacity of the $Li_xNa_{1-x}MgH_3$ (x=0, 0.2, 0.5, 0.8) hydrides

7.4.1 Thermal analysis (DSC-TGA-MS)

Thermal analysis was conducted via DSC and TGA measurements in order to study the dehydriding mechanisms, thermal transitions and mass changes of the quaternary $Li_xNa_{1-x}MgH_3$ (x=0, 0.2, 0.5, 0.8) hydride. Figure 7.3, illustrates the DSC-TGA-MS curves of Li substituted (x=0, 0.2, 0.5, 0.8) samples.

For the sample with Li substitution x=0, two overlapped endothermic reactions can be observed from the DSC (Figure 7.3 a) peaking at 369 °C and 390 °C, respectively. The first endotherm is attributed to the decomposition of the main $NaMgH_3$ phase into NaH and Mg, whereas, the second curve is related to the NaH decomposition; this corresponded to a total amount of H_2 released of 4.6 wt. % at around 410 °C (TGA Figure 7.3 b). Decomposition reactions obtained from the measurements performed suggest two steps dehydrogenation for the $Li_xNa_{1-x}MgH_3$ (x=0) as previously shown (Chapter 2) in equations 2.2 and 2.3. Those results agree with previous reported data (Ikeda et al., 2005b)

In the case of Li substitution x=0.2, DSC traces of the sample show two endothermic reactions peaking at 360 °C for the $NaMgH_3$ decomposition and 385 °C for the dehydrogenation of NaH. TGA shows a total amount of 5.1 wt. % H_2 is released, (3.5 wt. %) attributed to the first step reaction at around 360°C and (1.6 wt. %) to the second step up to 380°C. Achieving a peak temperature decrease of around 7 °C in comparison to the sample with Li addition (x=0). Decomposition reactions of the $Li_{0.2}Na_{0.8}MgH_3$ follow the same two-step dehydrogenation as described above (equations 2.2 and 2.3).

For the Li addition x=0.5 DSC-TGA traces (Figure 7.3) show three endothermic peaks at 310, 348, 370 °C for the first, second and third decomposition respectively. No exothermic reactions were observed. The first curve is linked to the MgH_2 decomposition, the decomposition of $NaMgH_3$ phase into NaH and Mg is attributed to the second endotherm, and the final peak is related to the decomposition of NaH into Na along with Mg.

The total amount of H_2 released accounts for 5.1 wt. %, (2.8%) related to the first step dehydrogenation at around 305°C, (1.1%) to the second desorption reaction at approximately 340°C, and (1.2%) for the third reaction at around 365°C. Decomposition reactions obtained from the measurements performed, suggest a three-step dehydrogenation for the $Li_{0.5}Na_{0.5}MgH_3$ as shown in equations 7.1, 7.2 and 7.3:

$$NaMgH_3+MgH_2 \rightarrow NaMgH_3+Mg+H_2 \quad (7.1)$$

$$NaMgH_3+Mg+H_2 \rightarrow NaH+2Mg+2H_2 \quad (7.2)$$

$$NaH+2Mg+2H_2 \rightarrow Na+2Mg+5/2H_2 \quad (7.3)$$

DSC and TGA for the $Li_{0.8}Na_{0.2}MgH_3$ exhibit a three-stage desorption: the first desorption peak is at 314 °C, the second desorption peak is located at 332 °C, whereas the third desorption peak was centred at 350 °C. A total amount of 5.2 wt. % H_2 was released, (3.1%) of the weight loss corresponded to the first step dehydrogenation at around 310°C, (1.1%) to the second hydrogen decomposition at about 330°C and the last reaction step released (1%) of H_2 up to 350 °C.

The decomposition reactions of the $Li_{0.8}Na_{0.2}MgH_3$ follow the same three- step dehydrogenation as described above (equations 7.1, 7.2 and 7.3).

Mass spectrometer was connected to the TGA to assess the evolution of gases during the decomposition process. 7.3 (c) shows that hydrogen was the only gas evolution detected throughout the thermal decomposition of the $Li_xNa_{1-x}MgH_3$ hydride system.

Two dehydrogenation steps can be perceived for the $Li_0Na_1MgH_3$ and $Li_{0.2}Na_{0.8}MgH_3$ hydrides and three desorption steps have been detected for the $Li_{0.5}Na_{0.5}MgH_3$ and $Li_{0.8}Na_{0.2}MgH_3$ hydrides respectively. These results are in good agreement with the TGA traces obtained in this work. Table 7.2 summarises the results experimentally gathered in this work for the DSC and TGA measurements.

Table 7.2 Desorption temperatures and amount of H_2 released from $Li_xNa_{1-x}MgH_3$

Nominal composition	H_2 (wt%)	T_{ons} (°C)	T_{peak} 1,2 & 3 (°C)	T_{end} (°C)
x=0	4.6	275	368 389	386
x=0.2	5.1	258	364 389	397
x=0.5	5.1	254	310 348 369	411
x=0.8	5.2	252	314 330 350	408

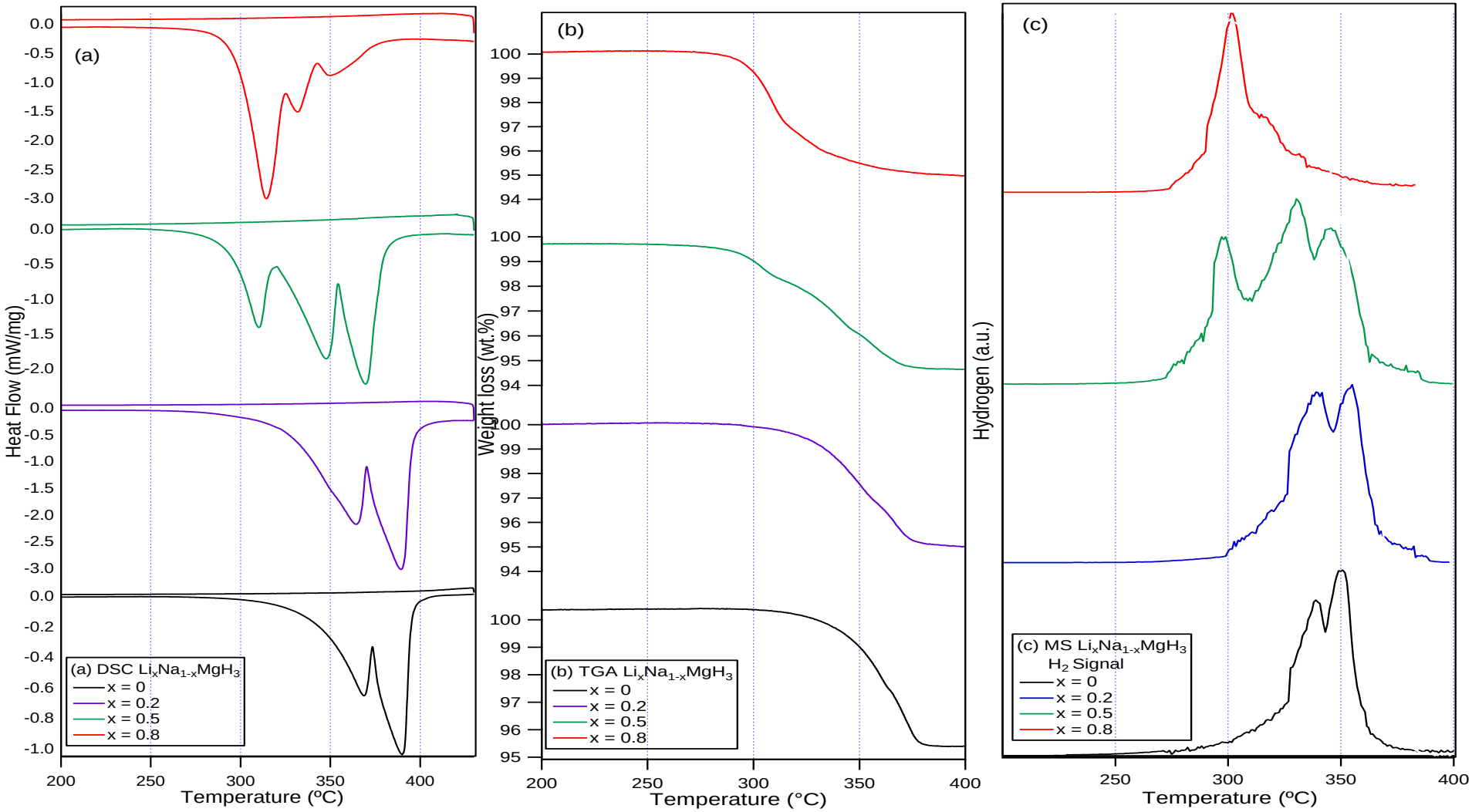

Figure 7.3 (a) DSC, (b) TGA and (c) MS curves of nominal composition $Li_xNa_{1-x}MgH_3$ hydride system (x=0, 0.2, 0.5 and 0.8). All measurements were performed at a heating rate of 2 °C/min from 30 to 400 °C in flowing 3 bar Ar at a rate of (100 ml/min) (DSC) and 1 bar Ar flowing 40 ml/min (TGA). Data below 200 °C are not plotted as no exo/endothermic reactions were detected.

7.4.2 Analysis of Decomposition Products (in-situ XRD)

In-situ XRD measurements were performed to give a better understanding of the decomposition reactions and phase changes. Patterns were collected every 25 °C from room temperature to 400 °C in a flowing He atmosphere at 100ml/min and 3 bar constant pressure.

Figure 7.4 shows the reflections of the $Li_xNa_{1-x}MgH_3$ hydride system for x=0. Initially, reflections of $NaMgH_3$ can be observed as one single phase. With increasing temperature from 30°C to 225 °C, the diffraction peaks of $NaMgH_3$ gradually shift to higher angles, followed by a decrease in intensity. On heating to 250 °C, small peaks of Mg can be observed due to the decomposition of $NaMgH_3$. At 300 °C intensity of Mg peaks increased, and a new phase arise. This new phase corresponded to the decomposition of NaH phase and was present until 330 °C. In addition to those phases, MgO patterns were present in the sample and become more intense on heating. At 350 °C was observed reflections of Mg with increased intensity, no traces of Na were detected, however, patterns of Mg oxide were present. On heating to 400 °C same reflections were noticed, the intensity of Mg peaks decreased considerably, while in oxide peaks increased.

No traces of Na metal were observed as would have been expected from the decomposition of NaH. However, we assume that Na reflections were present in the sample but were not observed in the XRD due to the phase transition (melting see Fig. 6.2) that Na suffers on heating, causing evaporation of the sample and therefore preventing the detection of the same.

To confirm this assumption ex-situ XRD was carried out the decomposed sample after In-situ measurements. Figure 7.5 reflects the patterns of the room temperature measurements of the decomposed $Li_xNa_{1-x}MgH_3$ hydride (x=0). There are patterns related to Na and Mg metal phases and some traces of MgO. Therefore, we can infer that the system fully decomposed after heating to 400°C.

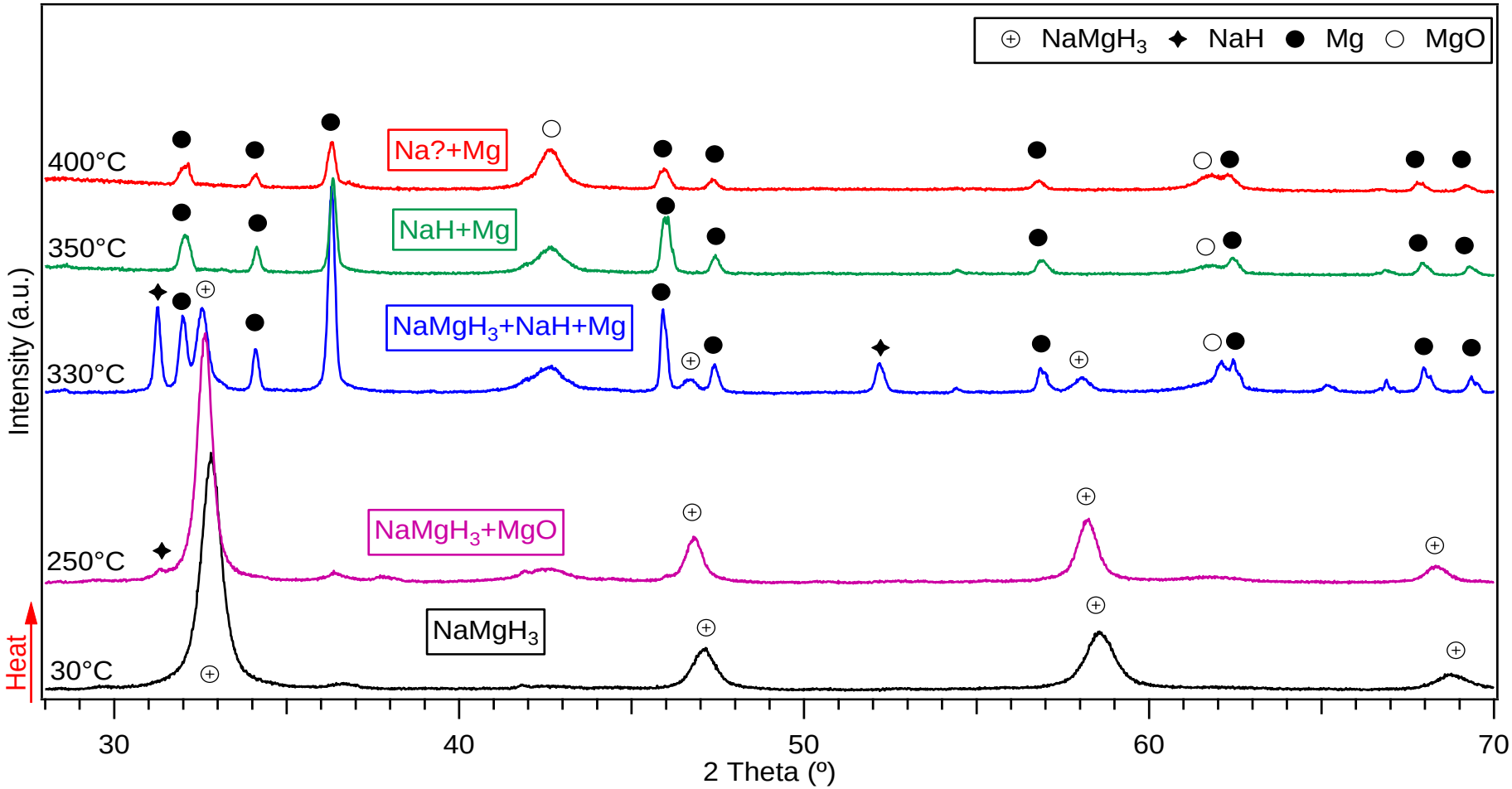

Figure 7.4 In-situ XRD of 5h ball milled $Li_xNa_{1-x}MgH_3$ (x=0) showing the decomposition reactions of the sample under 3 bar flowing He atmosphere. Measurements were taken from 30°C to 400°C at a rate of 2°C/min. values before 28 were not considered as no representative diffractions were detected.

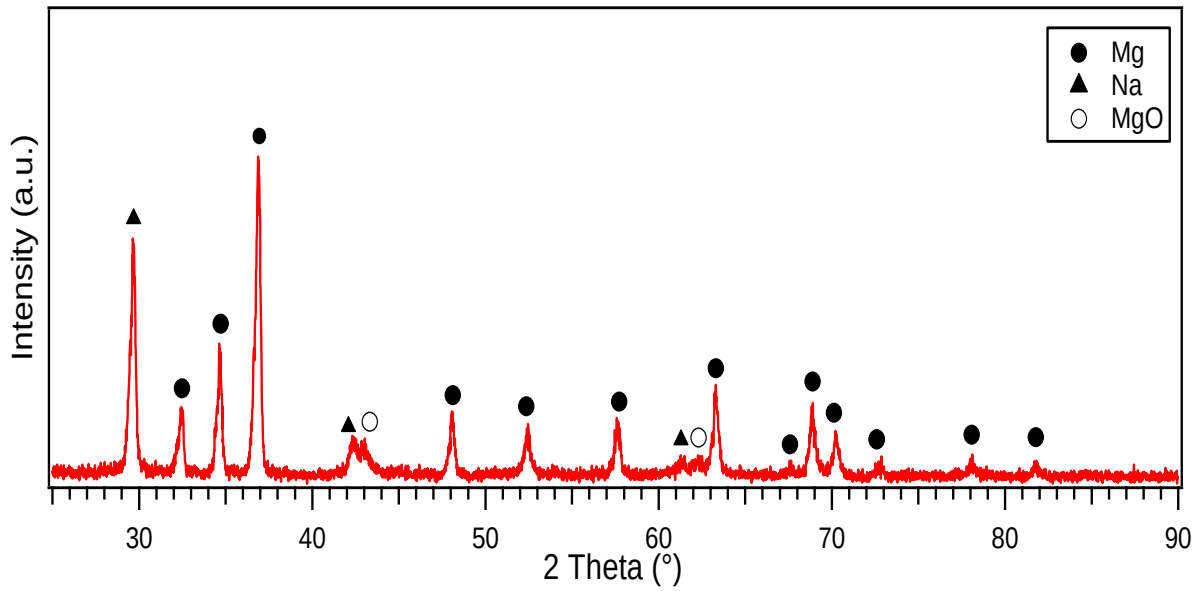

Figure 7.5 RT XRD of the 5 h milled $Li_xNa_{1-x}MgH_3$ (x=0) after dehydrogenation under 3 bar He flowing at 100 ml/min. 2 theta (°) values before 25 were not considered as no representative diffractions were detected.

Figure 7.6 shows the Rietveld Refinement of the ex-situ XRD measurement, showing that the dehydrogenated sample contains around 29.14 wt. % of crystalline Mg, 41.91 wt. % of Na and the remaining crystalline material belongs to MgO. The oxidation might be as a result of impurities in the gas stream, besides, a leak in the Anton-Parr cell apparatus used to perform the measurement.

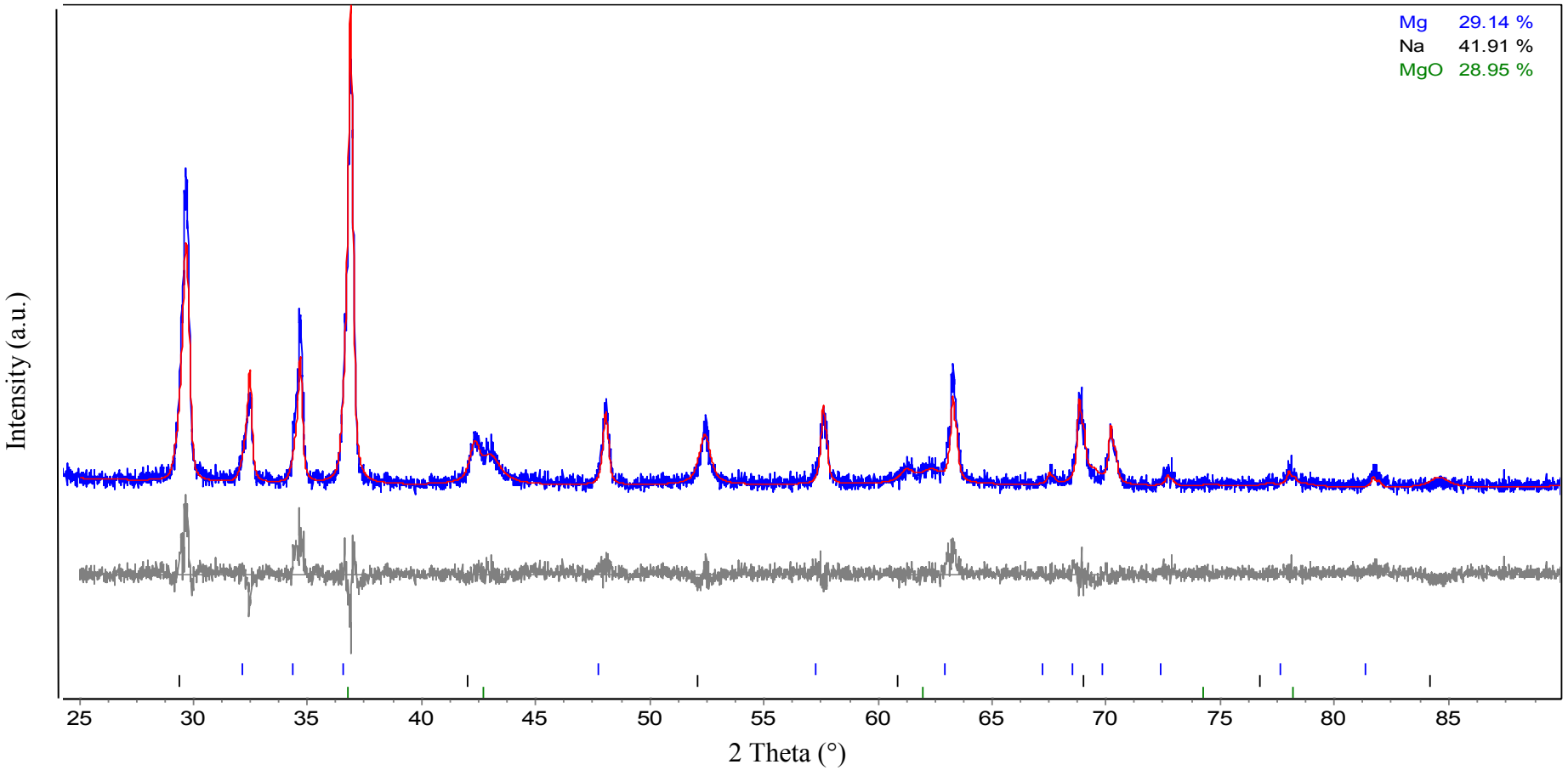

Figure 7.6 TOPAS refinement of $Li_xNa_{1-x}MgH_3$ (x=0), 2 theta (°) values before 25 were not considered for the refinement as no representative diffractions were detected. (Observed data is shown by blue line, calculated data is represented by the red lines and the difference is plotted below in grey). Goodness of fit 1.212

Figure 7.7 shows the in-situ XRD patterns for the $Li_xNa_{1-x}MgH_3$ hydride with nominal composition (x=0.2). On heating, from 30 to 300°C, the only phase detected agrees with the $NaMgH_3$ pattern. At 330 °C, decomposition of $NaMgH_3$ is started, and new phases attributed to NaH, and crystalline Mg starts to form. When heating to 350 °C, reflections of NaH and Mg become more intense, and no traces of $NaMgH_3$ was observed, leading us to the conclusion that decomposition has occurred. At 400 °C, the remaining phases observed correspond to Mg metal and MgO. No traces of crystalline Na were detected as would be expected from the dehydrogenation of NaH phase after 350 °C.

To investigate further these outcomes, ex-situ XRD was carried out on the decomposed sample. Figure 7.8 illustrates the RT-XRD patterns for the decomposed $Li_{0.2}Na_{0.8}MgH_3$ after In-situ measurements. To carry out the measurement sample was transferred to an Ar filled glove box, consequently, removed from the Anton Parr cell, hand mixed and placed in a sealed Kapton dome sample holder.

The evidence of Na, Mg and MgO confirmed by the diffraction peaks, support the decomposition hypothesis. However, no sign of lithium was observed in the sample even after ex-situ XRD. This could probably be either because is eventually present as an amorphous phase (Martínez-Coronado et al., 2012), or due to the small size of lithium cations, causing the reflections to shift to higher diffraction angles (Xiao et al., 2009).

The decomposition reactions and temperatures of the $Li_{0.2}Na_{0.8}MgH_3$ are illustrated in Figure 7.9 showing the surface plot of the ternary hydride.

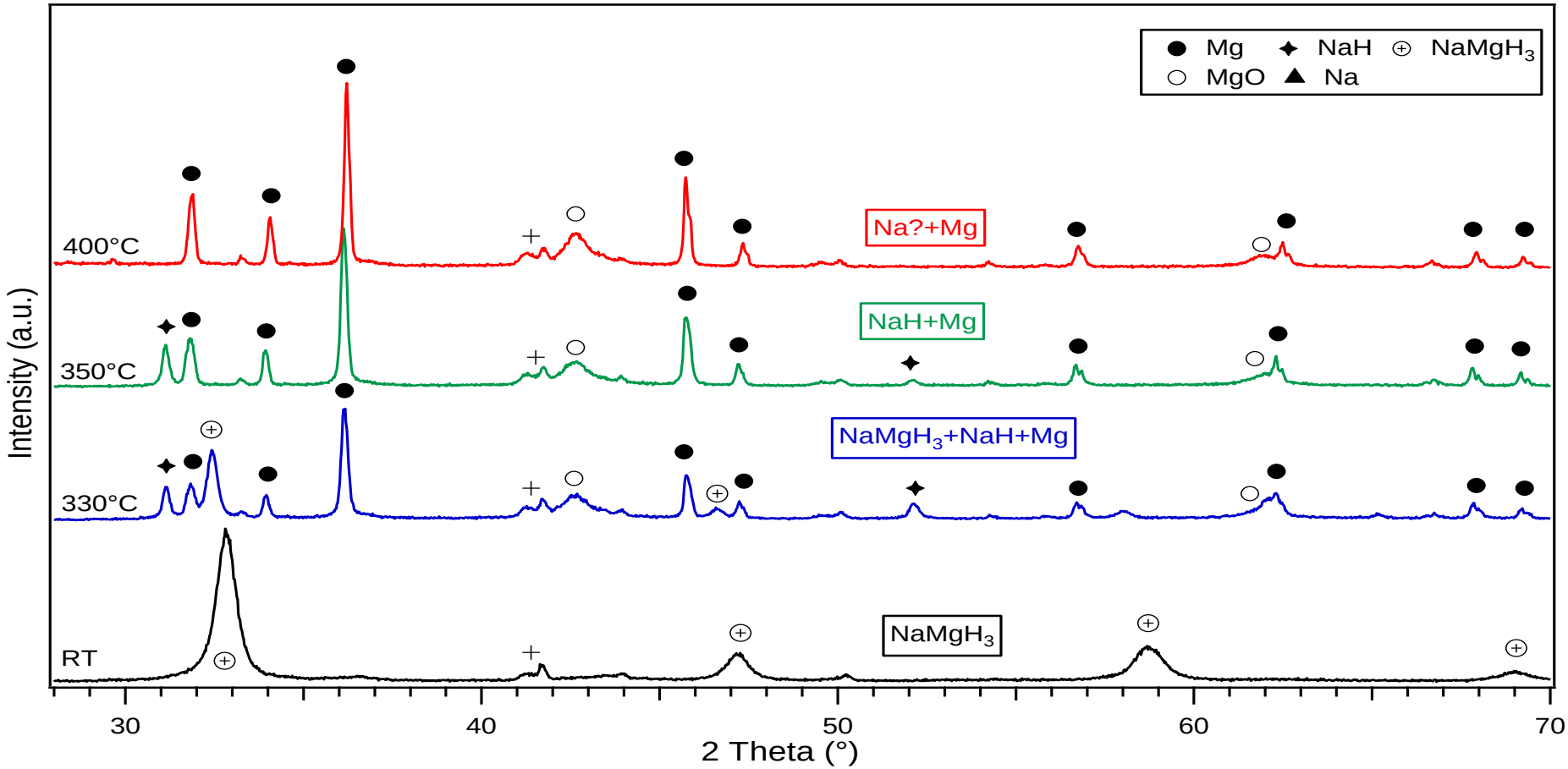

Figure 7.7 In-situ XRD of 5h ball milled $Li_{0.2}Na_{0.8}MgH_3$ showing the decomposition reactions of the sample under 3 bar flowing He atmosphere. Measurements were taken from 30°C to 400°C at a rate of 2°C/min. values before 28 were not considered as no representative diffractions were detected.

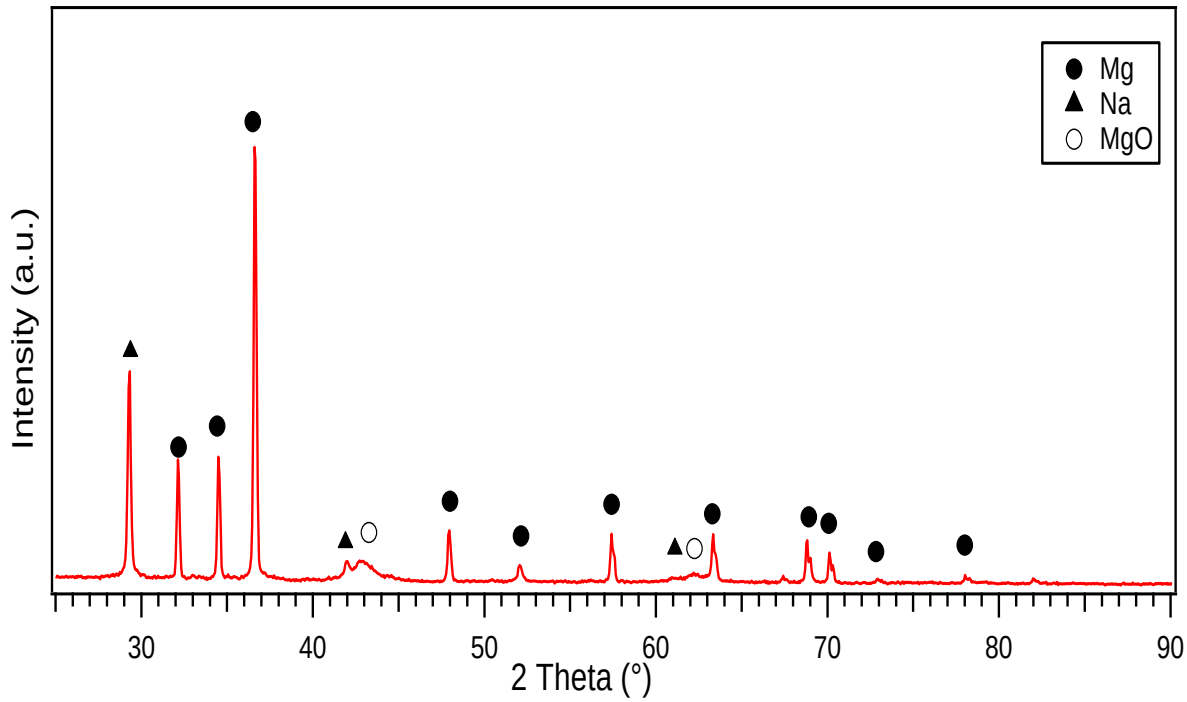

Figure 7.8 RT XRD of the 5 h milled $Li_xNa_{1-x}MgH_3$ (x=0.2) after dehydrogenation under 3 bar He flowing at 100 ml/min. 2 theta (°) values before 25 were not considered as no representative diffractions were detected.

Figure 7.9 shows the Rietveld Refinement of the ex-situ XRD measurement, showing that the dehydrogenated sample contains around 29 wt. % of crystalline Mg, 28 wt. % of Na and the remaining crystalline material belongs to MgO. The oxidation might be due to impurities in the gas stream, and leak in the apparatus used to perform the measurement.

Figure 7.11 illustrates the reflections for the in-situ patterns of the $Li_{0.5}Na_{0.5}MgH_3$. At 30°C, peaks corresponding to $NaMgH_3$ main phase, in addition to MgH_2 peaks, are detected. These reflections remain until 250 °C; a deflection towards the left has been confirmed from the patterns with decreased intensity. At 250 °C MgH_2 starts to decompose, therefore, small traces of Mg peaks are perceived at this temperature range. At 330 °C, in addition to the sodium magnesium hydride, a new phase is formed, reflections attributed to NaH are detected corresponding to the decomposition of $NaMgH_3$. MgH_2 patterns are no longer present showing decomposition of the extra magnesium present in the system.

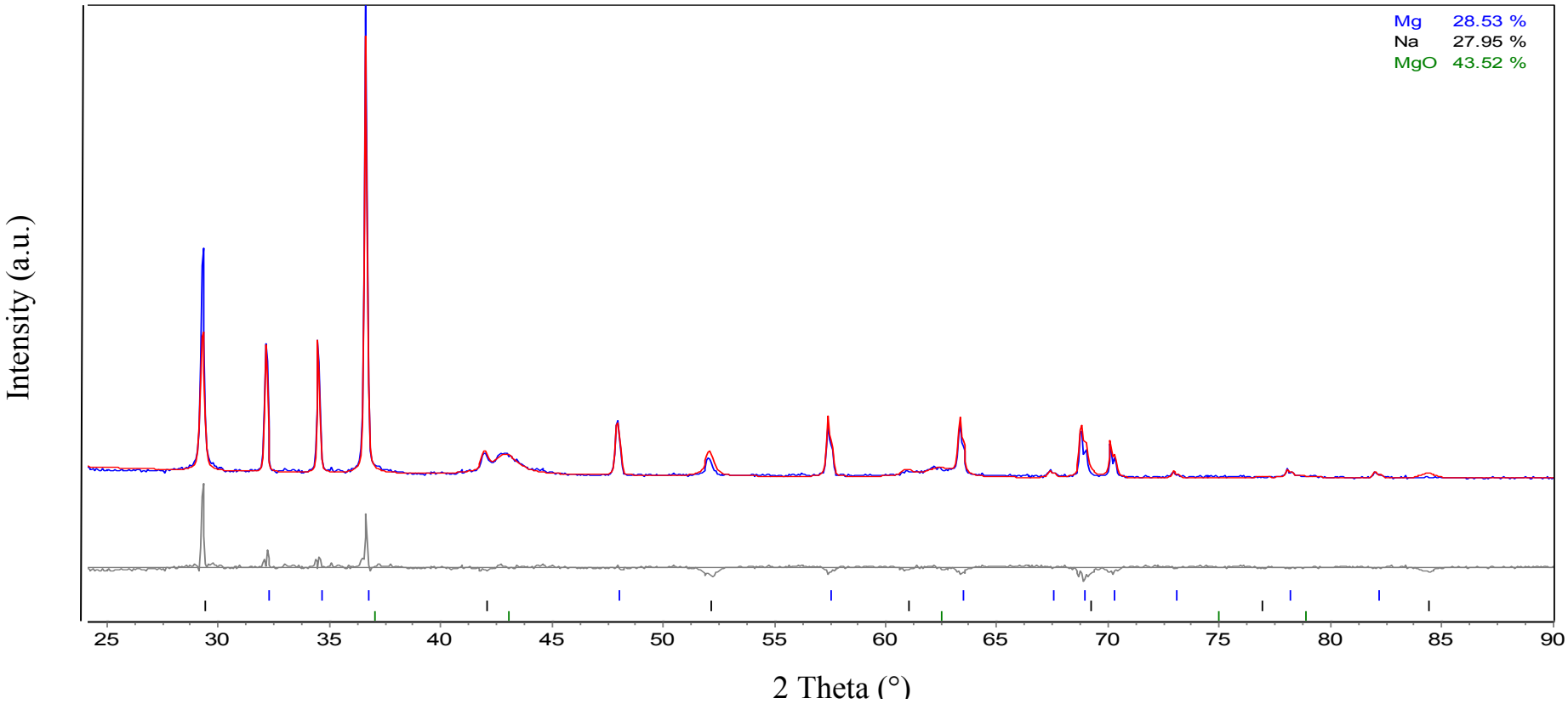

Figure 7.9 TOPAS refinement of $Li_xNa_{1-x}MgH_3$ (x=0.2), 2 theta (°) values before 25 were not considered for the refinement as no representative diffractions were detected. (Observed data is shown by blue line, calculated data is represented by the red lines and the difference is plotted below in grey). Goodness of fit 1.677

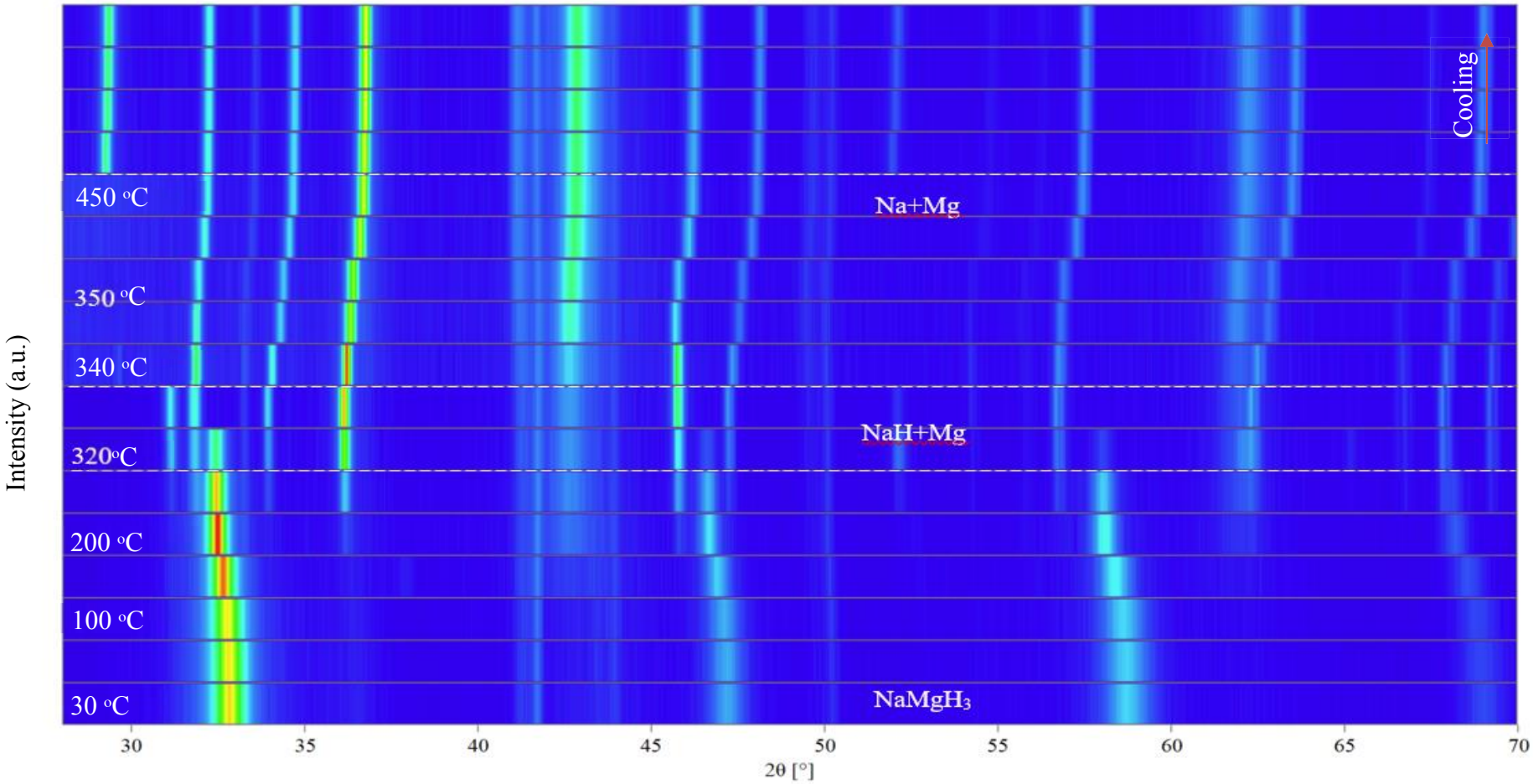

Figure 7.10 Surface plot from in-situ XRD of $Li_xNa_{1-x}MgH_3$ (x=0.2) heated under H_e (100 ml/min, ~3 bar) between 30 – 450 °C. A brighter colour corresponds to a higher diffraction intensity. The white dashed lines show the phase transition temperature and are given as a guide for the eye.

Some reflections related to magnesium and lithium oxides are also evident at this temperature range. On heating to 350 °C, sodium magnesium hydride has fully decomposed, hence no peaks can be observed. Reflections of Mg and NaH show increased intensity and oxides (Li, Mg, Na) patterns become more evident. At 400 °C, only magnesium phase remains present, in addition to oxide peaks.

No trace of sodium hydride or sodium metal are present, lithium and magnesium oxide peaks become more intense and sharp. The absence of Na peaks after decomposition of the NaH phase might be explained by the increased intensity of the oxides upon heating. Furthermore, no traces of lithium hydride or metal were evidenced. However, it is inferred they are reacting into the sample due to the patterns shift detected during the heating process.

Room temperature X-ray diffractions have been taken from the decomposed product and are shown in Figure 7.12. There are peaks due to sodium and magnesium metal, as expected from decomposition reactions via equations (2.2-2.3), in addition to small diffraction peaks associated with magnesium oxidation.

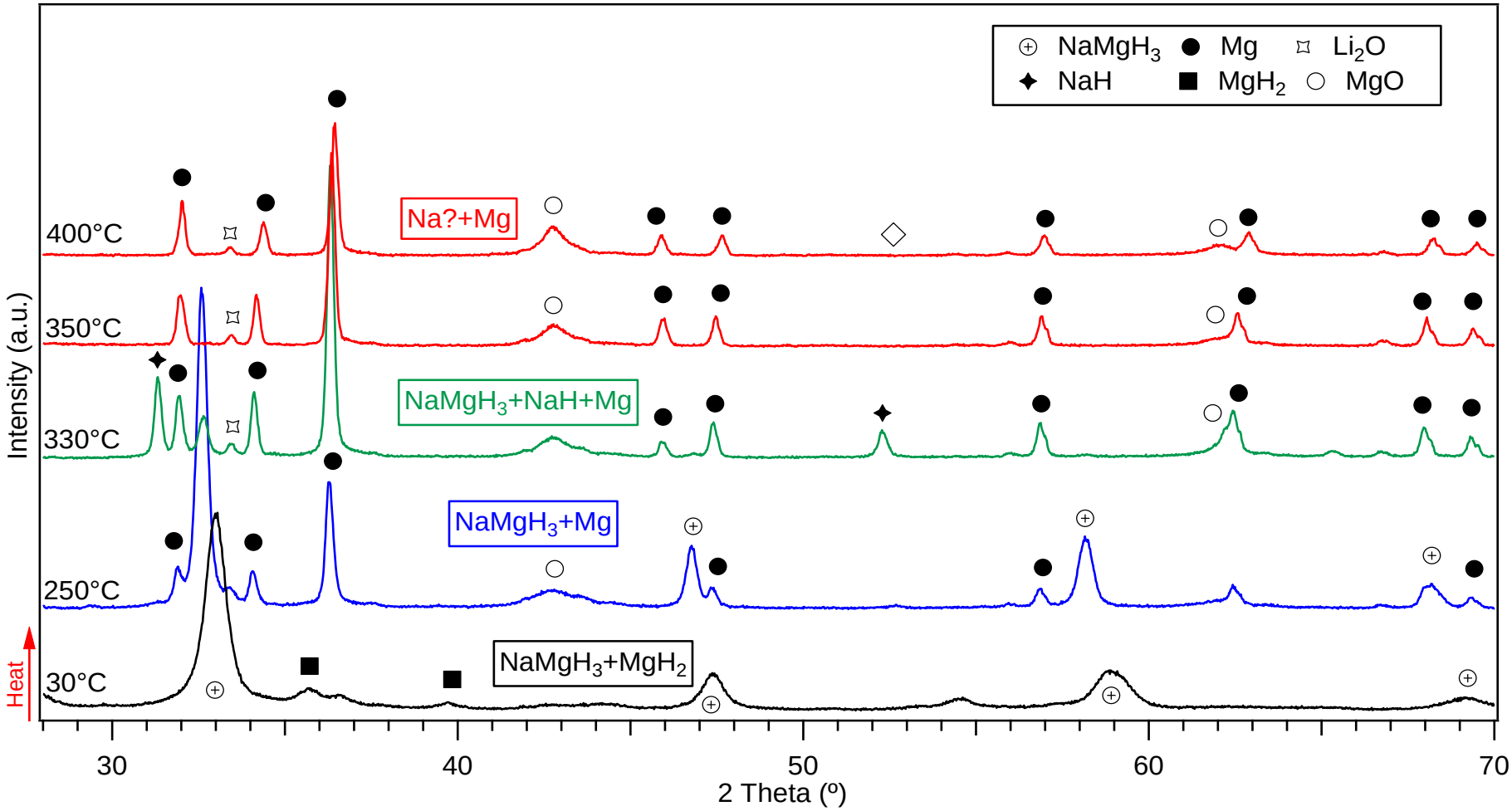

Figure 7.11 In-situ XRD of 5h ball milled $Li_{0.5}Na_{0.5}MgH_3$ showing the decomposition reactions of the sample under 3 bar flowing He atmosphere. Measurements were taken from 30°C to 400°C at a rate of 2°C/min. values before 28 were not considered as no representative diffractions were detected.

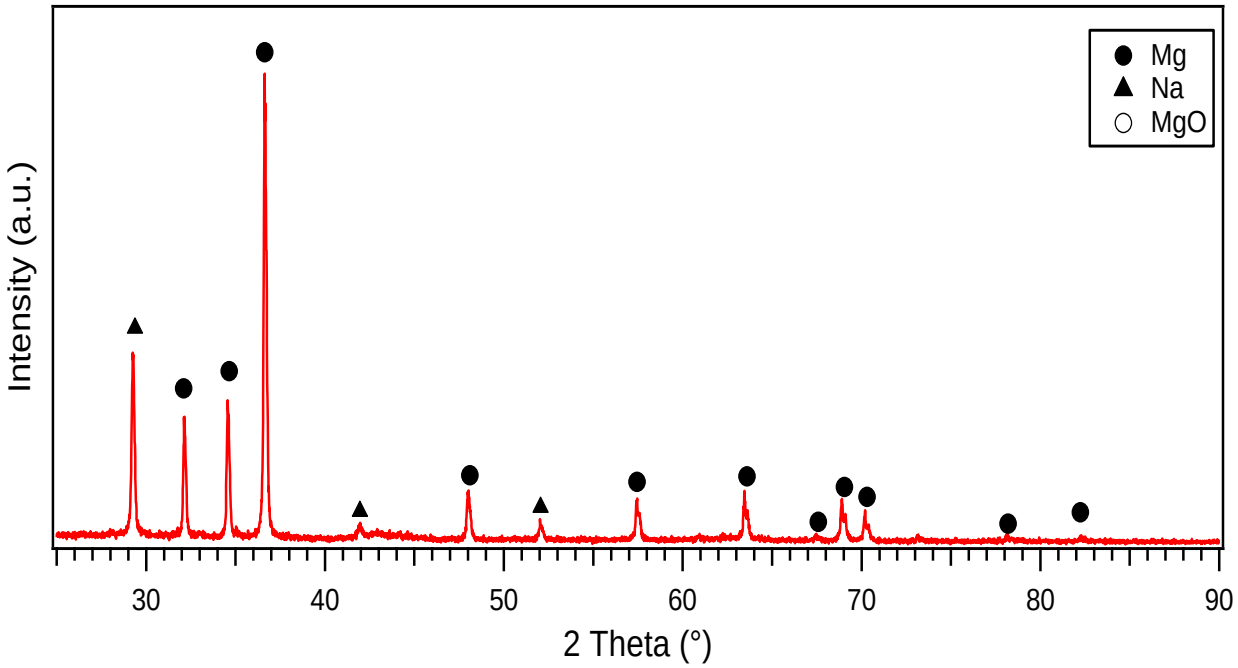

Figure 7.12 RT XRD of the 5 h milled $Li_xNa_{1-x}MgH_3$ (x=0.5) after dehydrogenation under 3 bar He flowing at 100 ml/min. 2 theta (°) values before 25 were not considered as no representative diffractions were detected.

Refinement of the decomposed product was executed to discern, the amount of crystalline material into the system. Rietveld analysis showed that there is around 33 wt.% of crystalline sodium, 42 wt.% of magnesium, and the remaining corresponds to magnesium oxide crystalline material. Figure 7.13 illustrates the Rietveld refinement of the room temperature XRD after the In-situ decomposition of $Li_{0.5}Na_{0.5}MgH_3$ hydride system.

Figure 7.14 illustrates the surface plot of the $Li_{0.5}Na_{0.5}MgH_3$ hydride, highlighting the temperatures and phase changes on heating.

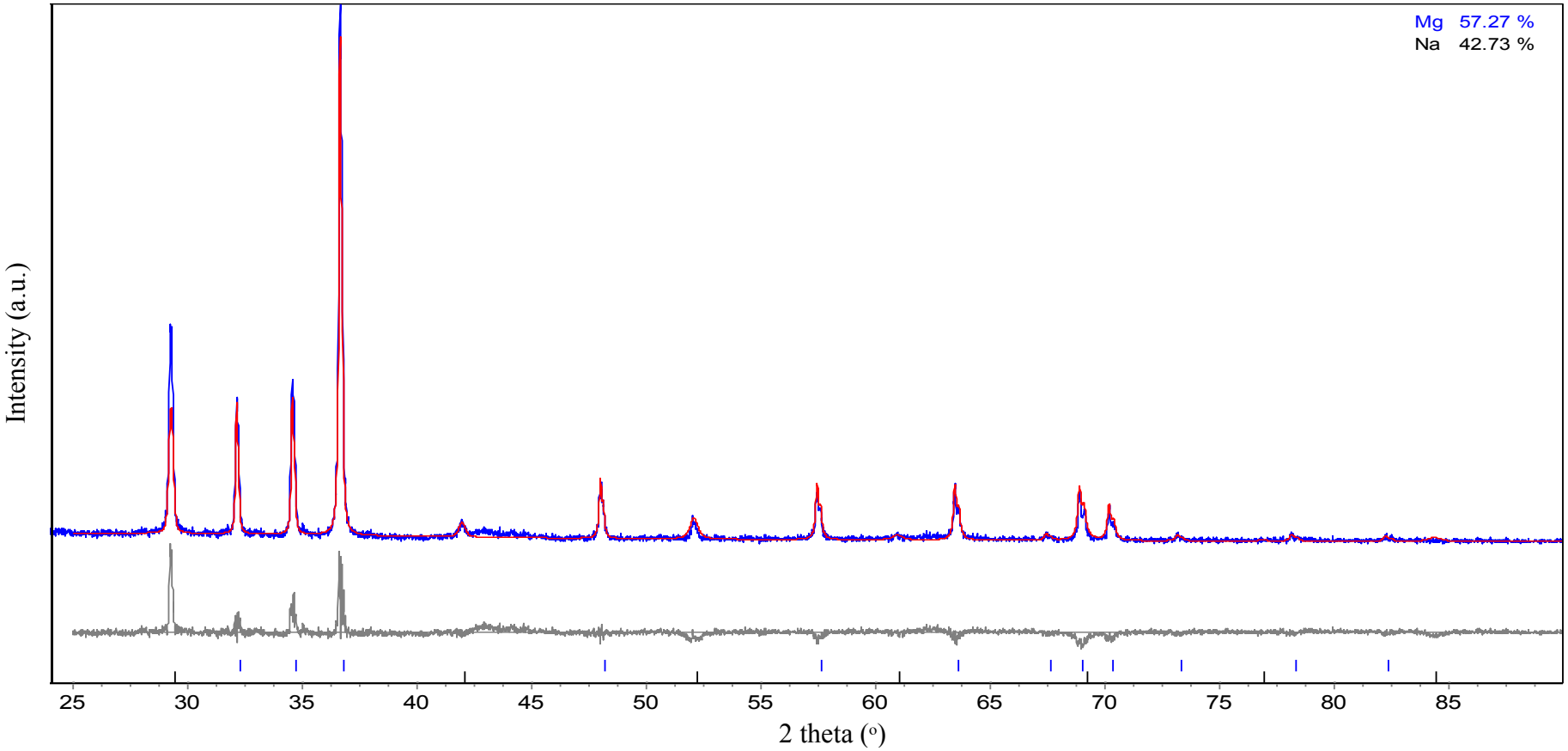

Figure 7.13 TOPAS refinement of $Li_xNa_{1-x}MgH_3$ (x=0.5), 2 theta (°) values before 25 were not considered for the refinement as no representative diffractions were detected. (Observed data is shown by blue line, calculated data is represented by the red lines and the difference is plotted below in grey). Goodness of fit 1.529

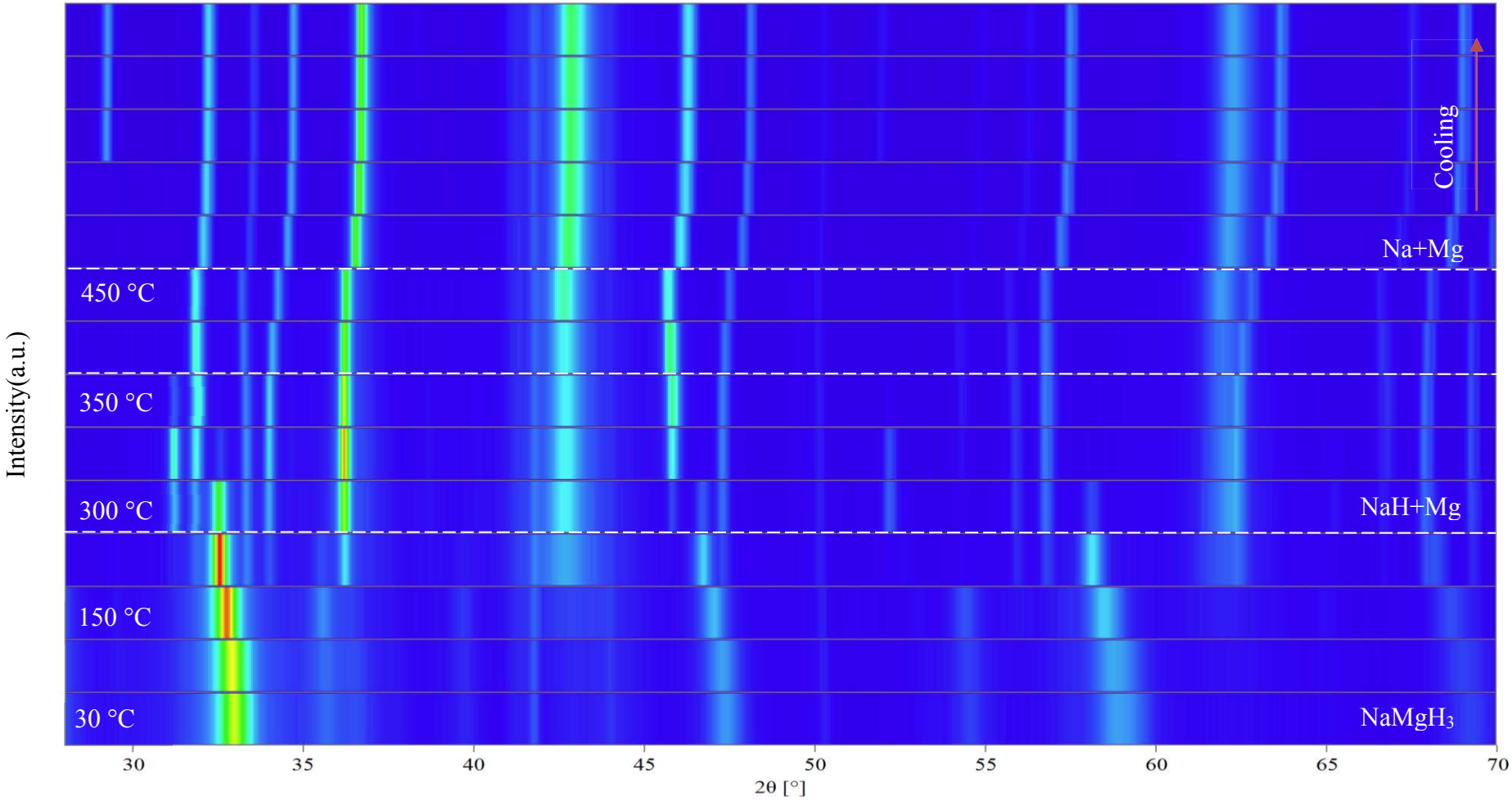

Figure 7.14 Surface plot from in-situ XRD of $Li_xNa_{1-x}MgH_3$ (x=0.5) heated under H_e (100 ml/min, ~3 bar) between 30 – 450 °C. A brighter colour corresponds to a higher diffraction intensity. The white dashed lines show the phase transition temperature and are given as a guide for the eye.

In-situ XRD measurements for the $Li_{0.8}Na_{0.2}MgH_3$ hydride sample are presented in Figure 7.15 show similar structural changes as in the $Li_{0.5}Na_{0.5}MgH_3$ previously studied, but at diverse temperatures: $NaMgH_3$ and MgH_2 peaks shift to higher 2 theta values on heating up from 30 to 250 °C. Increasing the temperature to 250 °C, we observe that the formation of Mg phase, result of the decomposition of MgH_2, in addition, there are more intense reflections of $NaMgH_3$, and formation of (Mg and Li) oxides. At 330 °C, no traces of MgH_2 phase can be detected indicating complete hydrogen desorption. This is confirmed by the grown intensity of magnesium peaks in the sample. Moreover, intensity of $NaMgH_3$ is reduced and the evidence of NaH reflections is attributed to the decomposition of the sodium magnesium hydride, also at this temperature the presence of (Li, Mg) oxides were detected.

On heating to 350°C, sodium magnesium hydride reflections are no longer visible, showing complete dehydrogenation. No Na or Li peaks can be detected, only Mg and oxides reflections are observed. As previously discussed this effect is probably related to the oxidation of the sample during the heating preventing to detect sodium peaks after decomposition of sodium hydride in the case of sodium, for the lithium it was assumed that is present besides the lithium oxide peaks, because of the peak shift reaction.

Figure 7.16 shows the room temperature XRD pattern of the decomposed material from the In-situ XRD. This shows intense peaks linked to magnesium, and small reflections of sodium and magnesium oxides patterns.

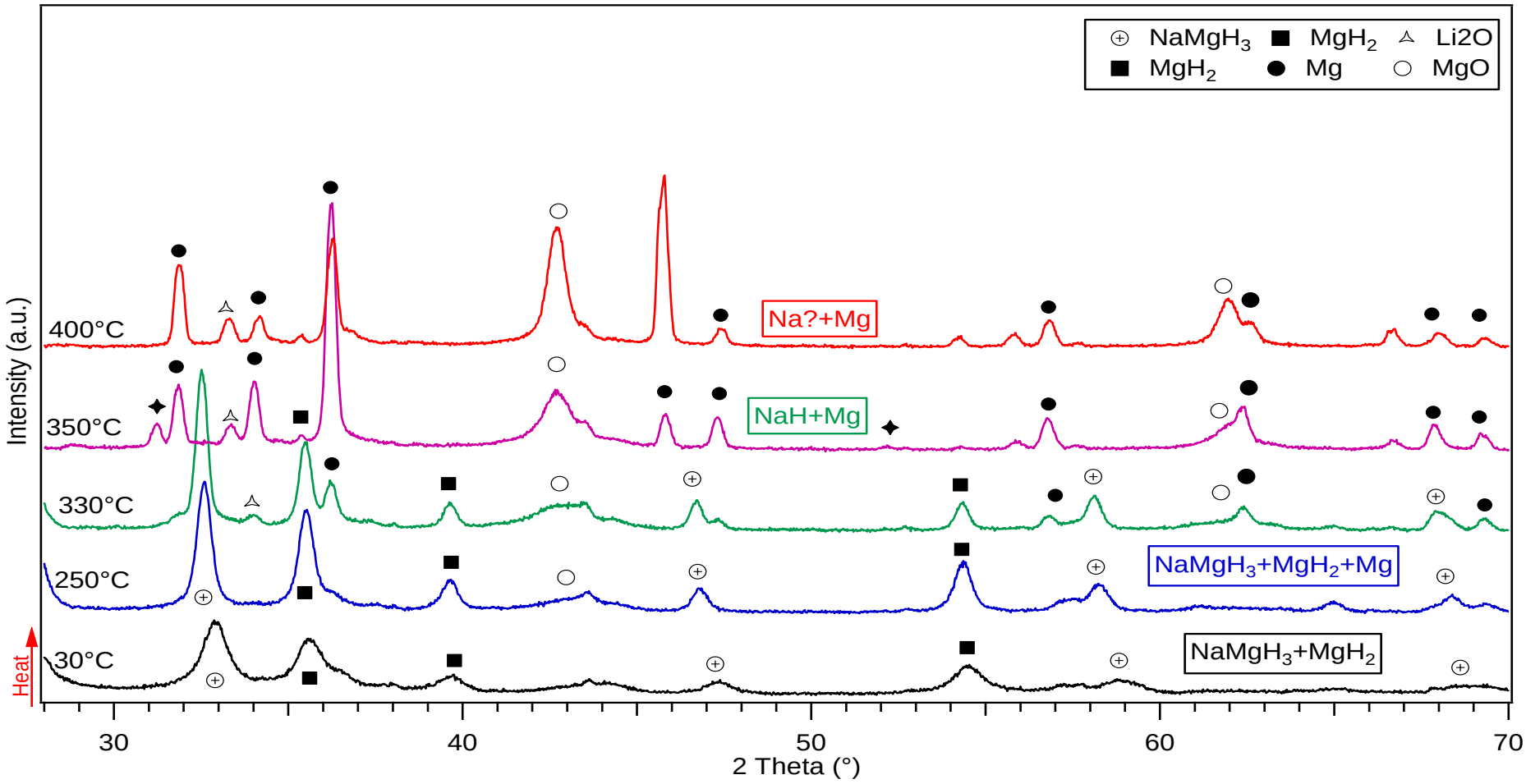

Figure 7.15 In-Situ XRD of 5h ball milled $Li_{0.8}Na_{0.2}MgH_3$ showing the decomposition reactions of the sample under 3 bar flowing He atmosphere. Measurements were taken from 30°C to 400°C at a rate of 2°C/min. values before 28 were not considered as no representative diffractions were detected.

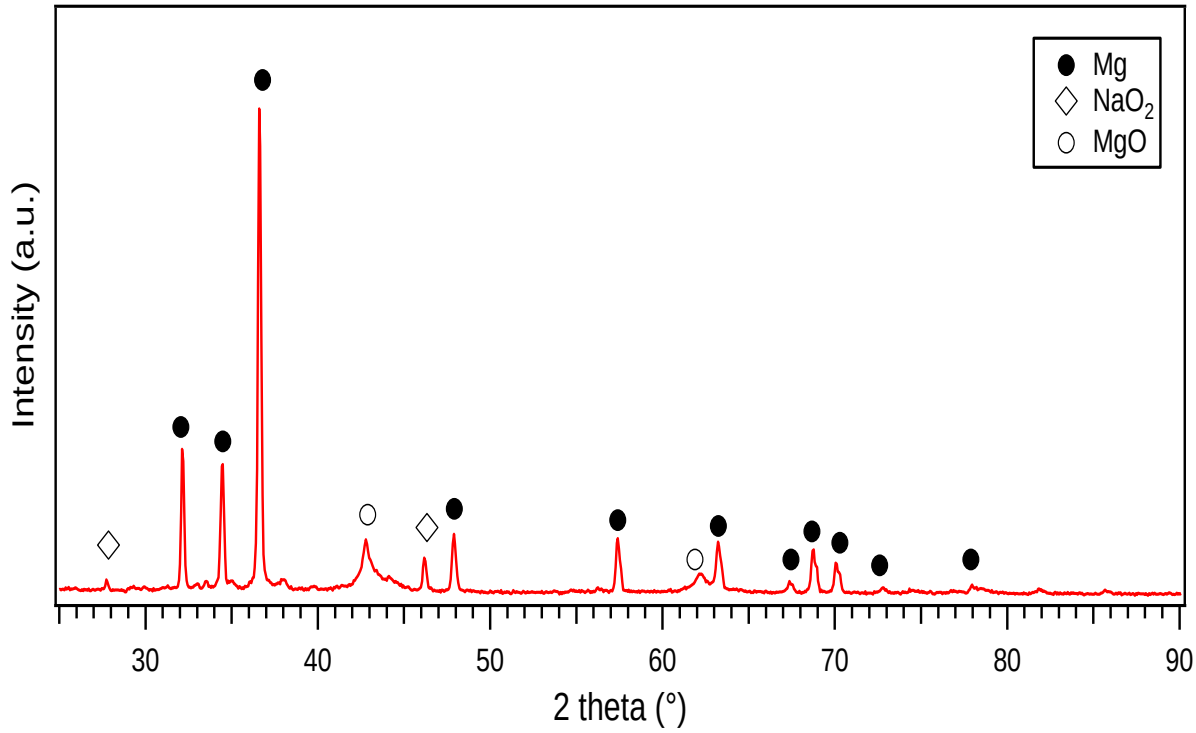

Figure 7.16 RT XRD of the 5 h milled $Li_xNa_{1-x}MgH_3$ (x=0.8) after dehydrogenation under 3 bar He flowing at 100 ml/min. 2 theta (°) values before 25 were not considered as no representative diffractions were detected.

Rietveld refinement on the decomposed sample shows that 32 wt.% of the material belongs to crystalline Mg, 58 wt.% to MgO. No peaks of sodium metal were detected as would expect according to reaction equations (7.1-7.3). This effect can be related to the small amount of Na used for the synthesis of the sample.

Temperatures of dehydrogenation reactions and phase changes are illustrated in Figure 7.17, showing the surface plot of the sample,

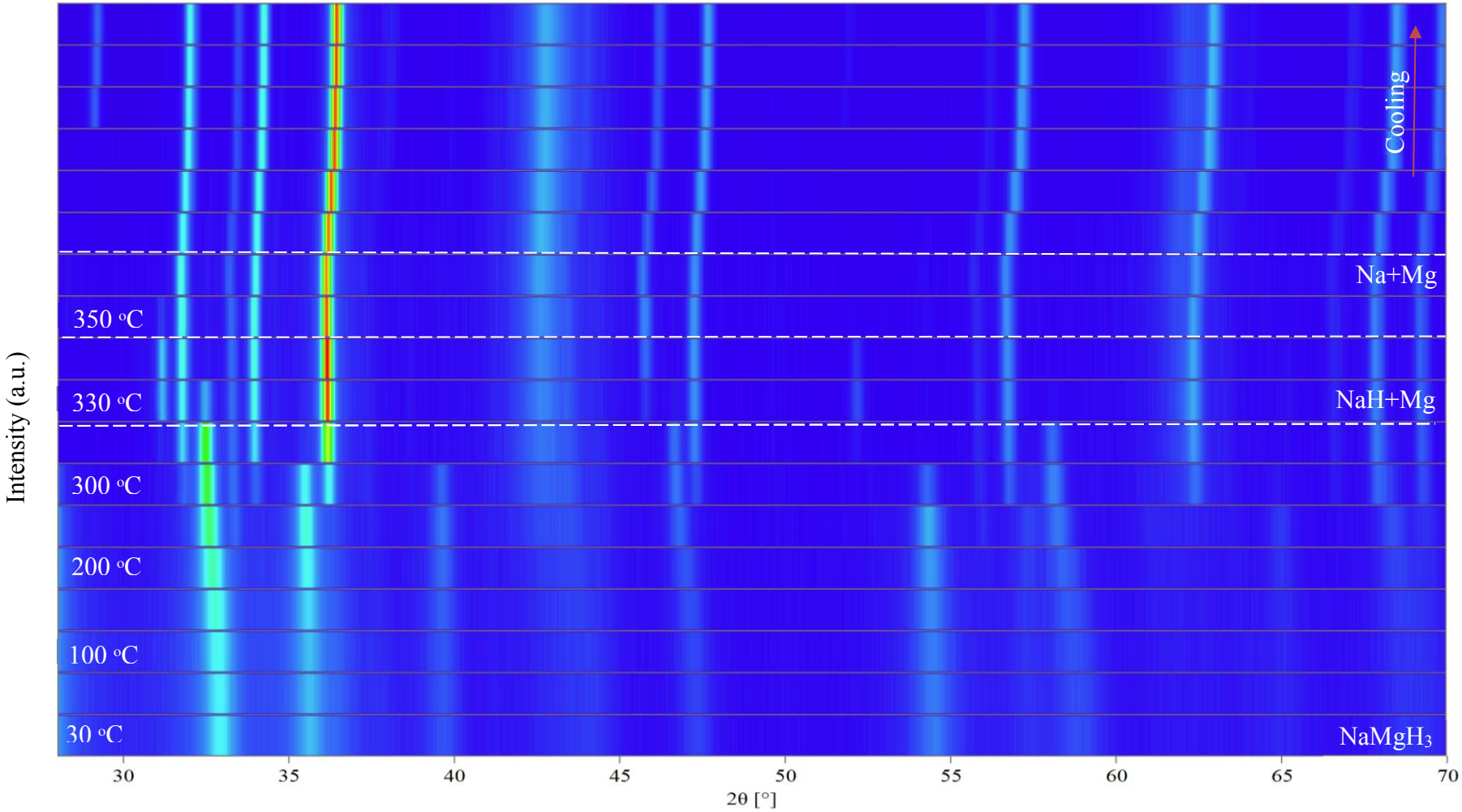

Figure 7.17 Surface plot from in-situ XRD of $Li_xNa_{1-x}MgH_3$ (x=0.8) heated under H_e (100 ml/min, ~3 bar) between 30 – 450 °C. A brighter colour corresponds to a higher diffraction intensity. The white dashed lines show the phase transition temperature and are given as a guide for the eye.

7.5 Recombination ability

After dehydrogenation of the Li substituted hydrides with nominal compositions (x= 0, 0.2, 0.5, 0.8) into Na and Mg metals, samples were heated up to 400 °C under a 10 bar hydrogen atmosphere to investigate if $NaMgH_3$ phase can be reversibly formed.

7.5.1 In-situ XRD

Figure 7.18 shows the reflections for the re-hydrogenated $Li_xNa_{1-x}MgH_3$ (x=0) mixture. On heating from 30 to 100 °C traces of Mg, NaH and (Na and Mg) oxides are detected. On further heating to 200 °C was noticed that the phase associated with $NaMgH_3$ was present, therefore, has successfully recombined after its decomposition. There are still some remains of sodium hydride, magnesium and sodium and magnesium oxides at this temperature. At 300 °C, more intense reflections of sodium magnesium hydride phase were observed, at the same time patterns for NaH and Mg were less intense. Peaks for MgO grew in intensity, leading to a decrease in $NaMgH_3$ phase intensity at 400 °C.

Ex-situ XRD was performed to investigate the products after complete decomposition in Figure 7.19 is shown the patterns of the re-hydrogenated material from In-situ XRD. There are reflections related to $NaMgH_3$, NaH, Mg, and Mg oxide. To evaluate the amount of each material in the sample Rietveld refinement was carried out (Figure 7.20) and shows that re-hydrogenated sample contains 27% wt.% of crystalline sodium magnesium hydride, 5.6 wt.% of sodium hydride and the remaining belongs to oxides. The high levels of oxides can be attributed to the highly sensitivity of the sample when is exposed to air.

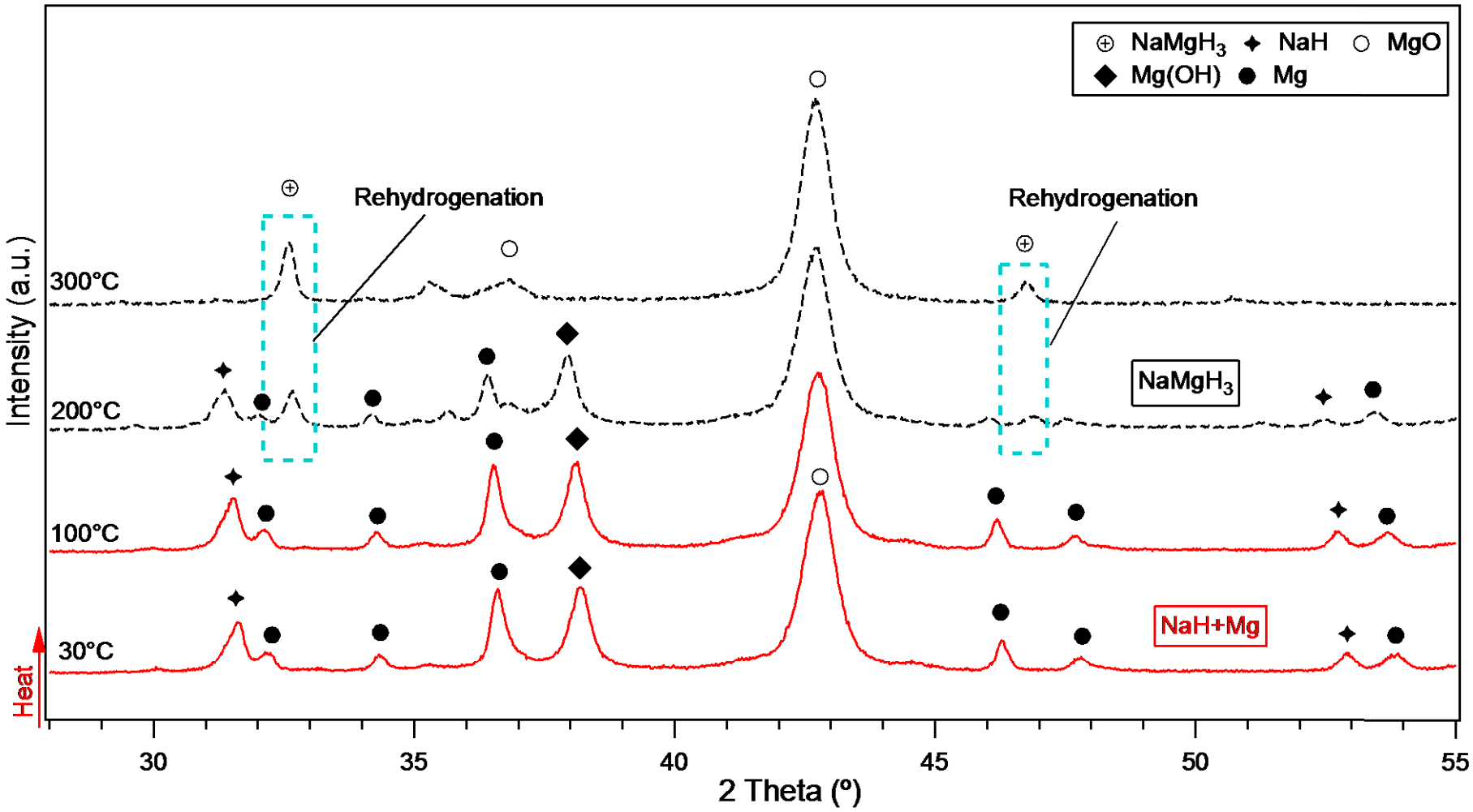

Figure 7.18 In-situ XRD of the 5 h milled $Li_xNa_{1-x}MgH_3$ (x=0) rehydrogenated sample under 10 bar H_2 flowing at (100 ml/min) after decomposition. Data was collected isothermally in 50 °C intervals. Dashed (black line) indicates the patterns where rehydrogenation is detected.

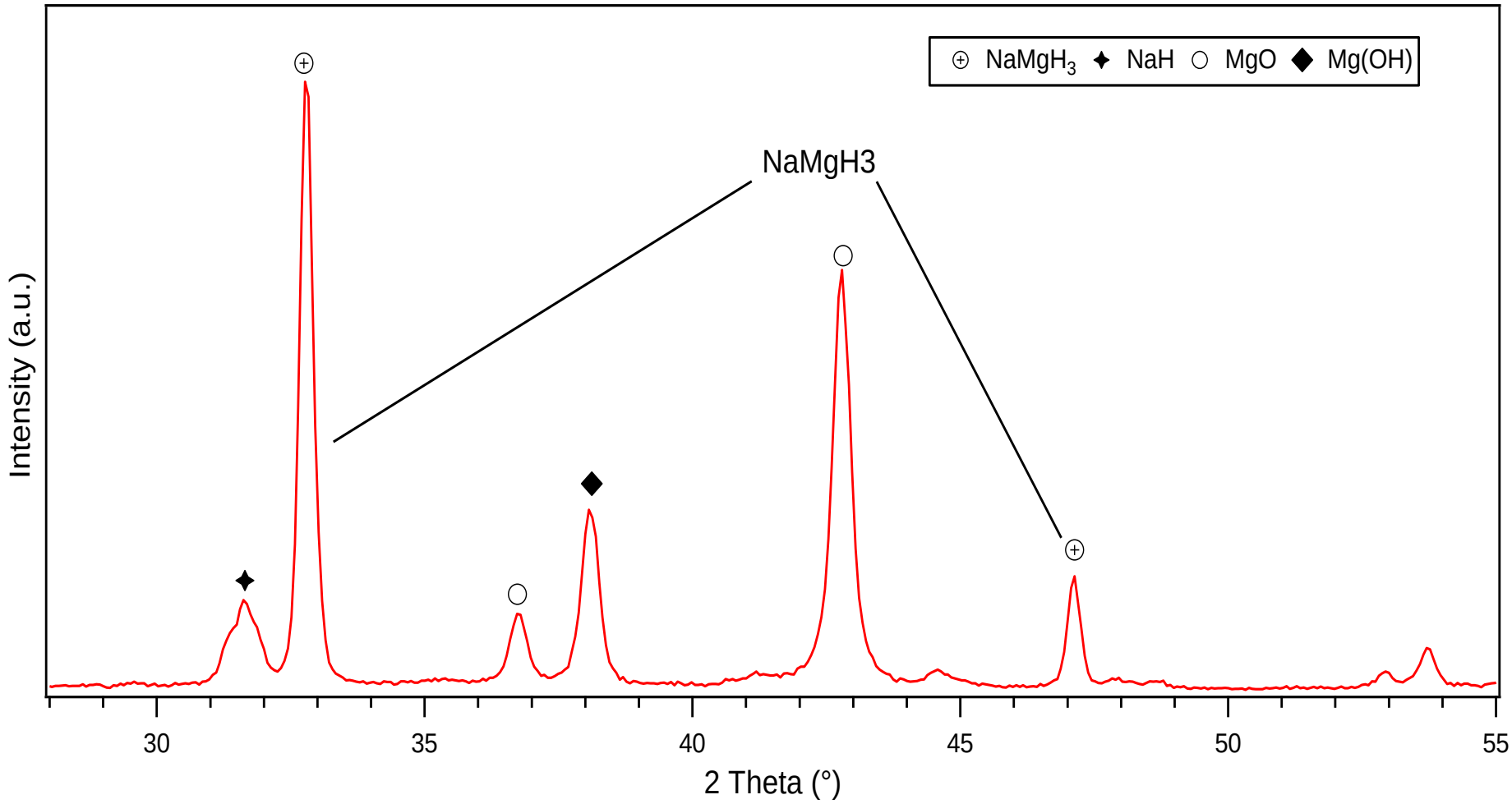

Figure 7.19 RT XRD of the 5 h mi lled $Li_xNa_{1-x}MgH_3$ (x=0) after re-hydrogenation in 10 bar H_2 flowing at 100 ml/min. 2 theta (°) values before 25 were not considered as no representative diffractions were detected.

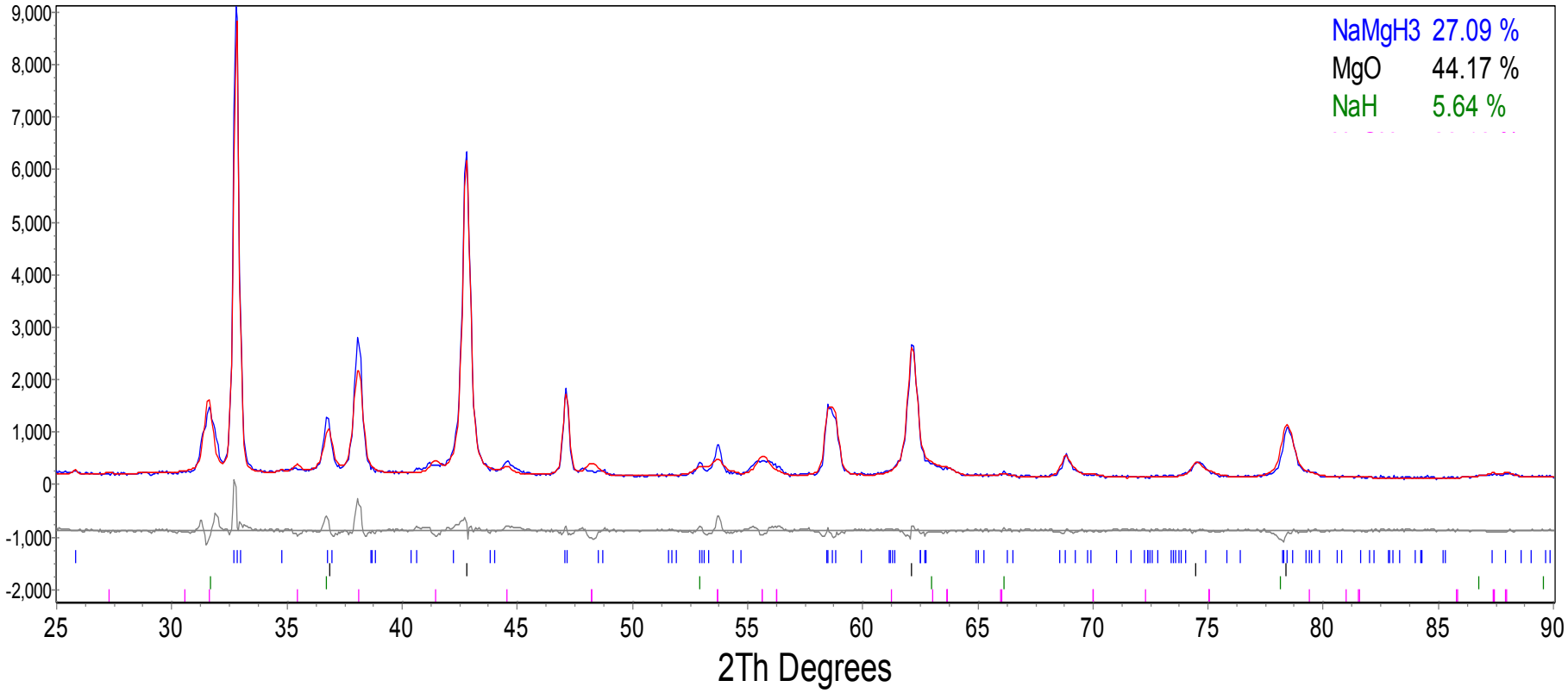

Figure 7.20 TOPAS refinement of $Li_xNa_{1-x}MgH_3$ (x=0), 2 theta (°) values before 25 were not considered for the refinement as no representative diffractions were detected. (Observed data is shown by blue line, calculated data is represented by the red lines and the difference is plotted below in grey). Goodness of fit 1.468

For $Li_xNa_{1-x}MgH_3$ (x=0.2), In-situ reflexions show the hydrogenation of the sample, present similar structural changes than the (x=0), but at different temperatures. At 30°C magnesium, sodium and its oxides were detected. On heating to 200°C the formation of NaH and MgH_2 phases were noticed, and the reformation into $NaMgH_3$ was achieved at 300°C, these reflections become more intense and are present up to 400 °C.

Figure 7.21 illustrates the re-hydrogenation of the $NaMgH_3$ phase in the $Li_{0.2}Na_{0.8}MgH_3$ from In-Situ measurements. Ex-situ XRD and Rietveld refinement (Figures 7.22, 7.23) show the products after In-situ XRD re-hydrogenation. There are peaks consistent with crystalline sodium magnesium hydride accounting for approximately 43 wt. %, sodium hydride 3 wt.%, magnesium 6 wt.% and the residual crystalline material corresponds to magnesium oxide and sodium hydroxide, probably formed during the heating process of the reabsorbed sample.

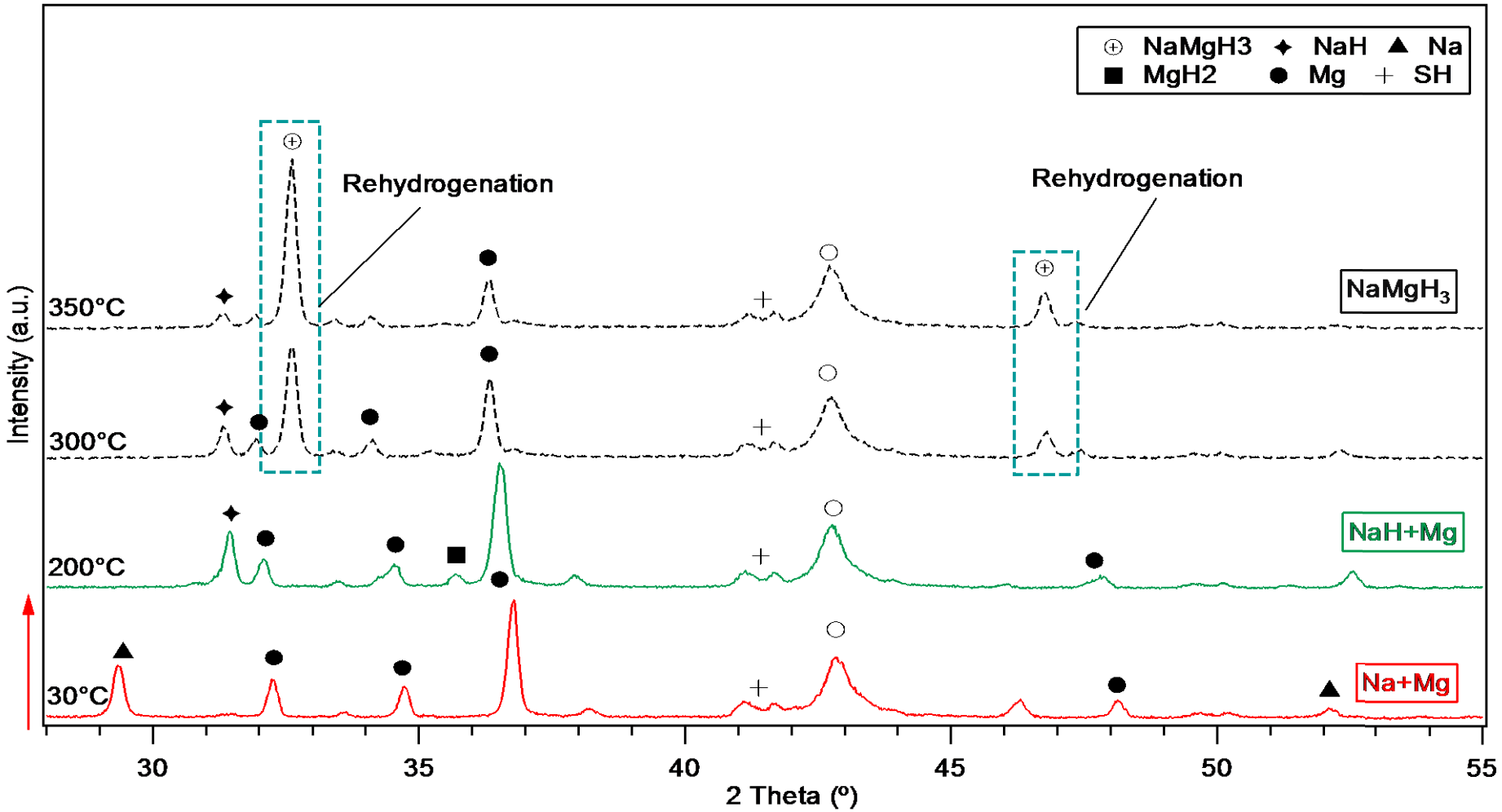

Figure 7.21 In-situ XRD of the 5 h milled LixNa1-xMgH3 (x=0.2) rehydrogenated sample under 10 bar H2 flowing at (100 ml/min) after decomposition. Data was collected isothermally in 50 °C intervals. Dashed (black line) indicates the patterns where rehydrogenation is detected.

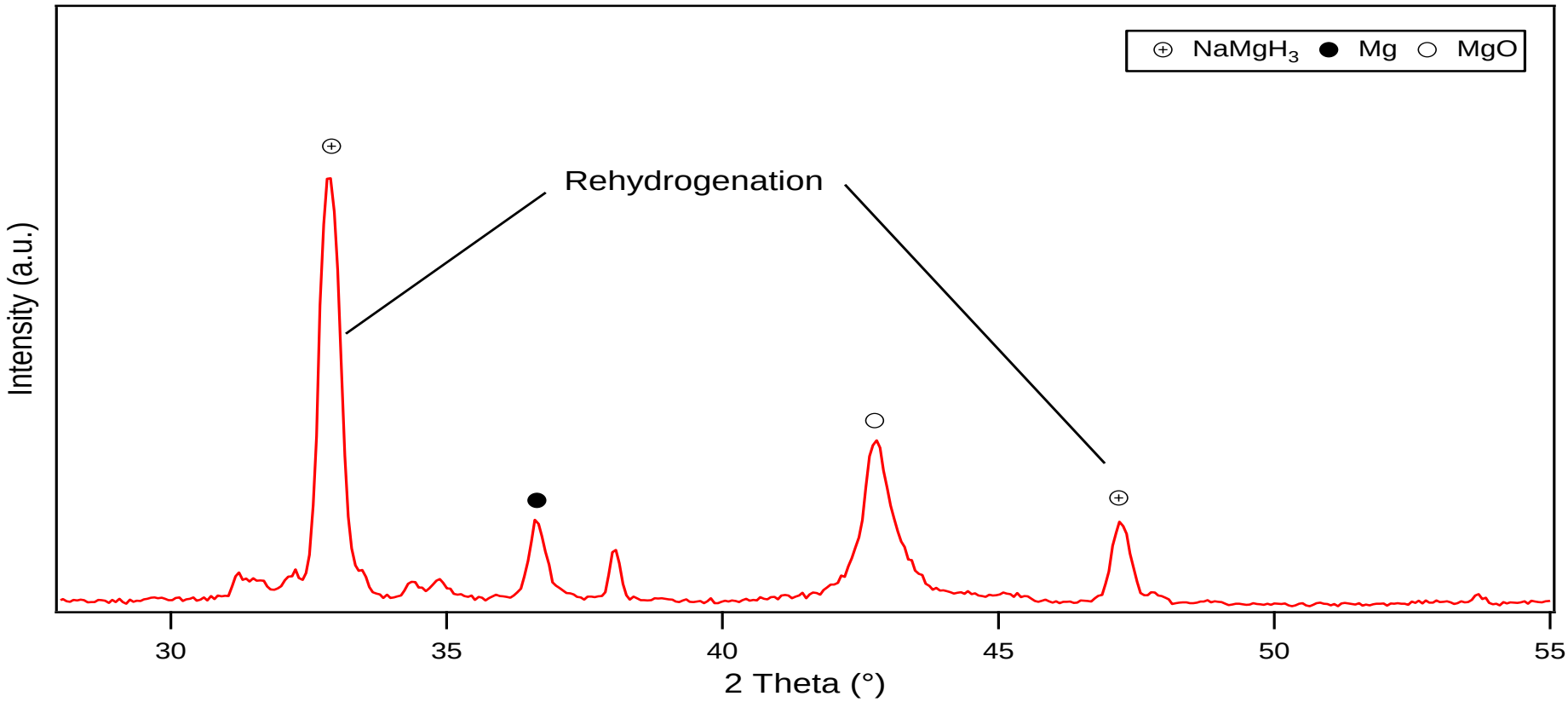

Figure 7.22 RT XRD of the 5 h milled $Li_xNa_{1-x}MgH_3$ (x=0.2) after re-hydrogenation in 10 bar H_2 flowing at 100 ml/min. 2 theta (°) values before 25 were not considered as no representative diffractions were detected.

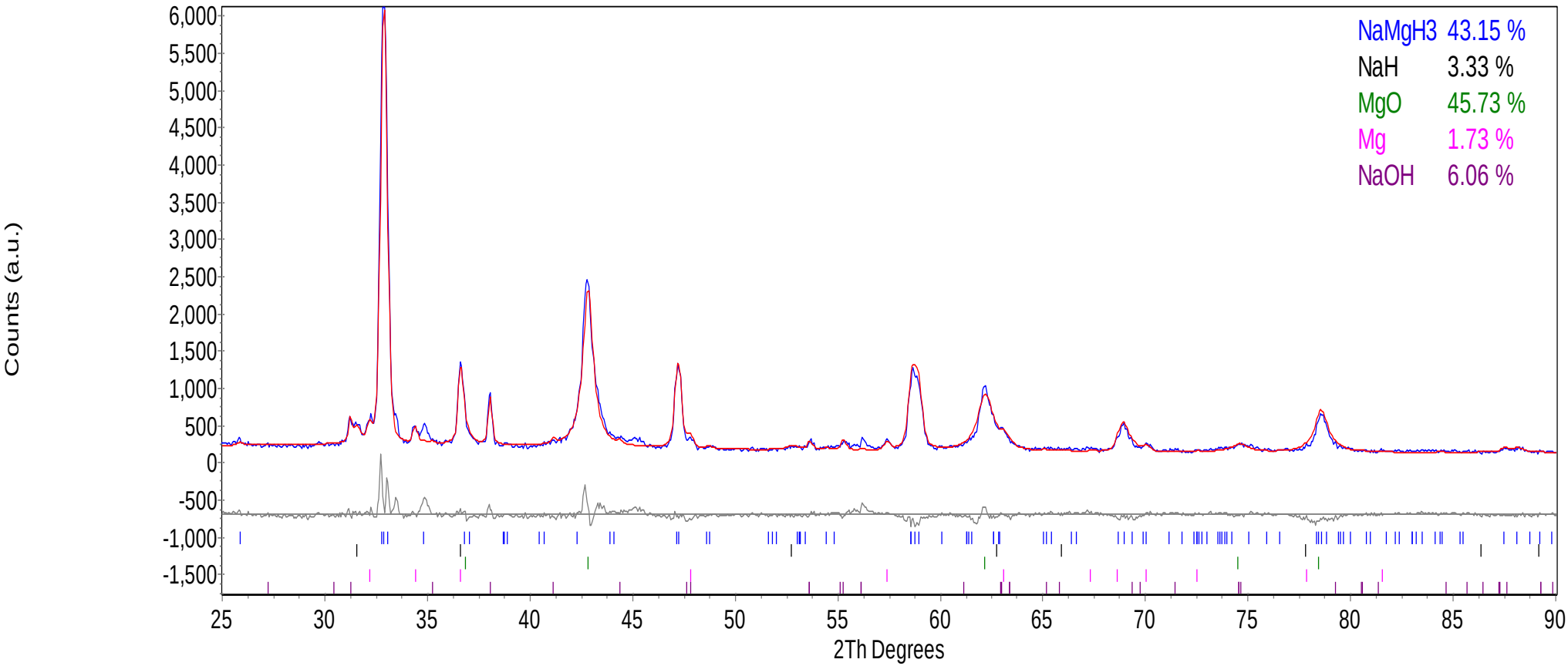

Figure 7.23 TOPAS refinement of $Li_xNa_{1-x}MgH_3$ (x=0.2), 2 theta (°) values before 25 were not considered for the refinement as no representative diffractions were detected. (Observed data is shown by blue line, calculated data is represented by the red lines and the difference is plotted below in grey). Goodness of fit 1.523

In-situ XRD of $Li_{0.5}Na_{0.5}MgH_3$ hydride (Figure 7.24) illustrates the re-hydrogenation of $NaMgH_3$ from the decomposed material. Reabsorption was achieved at 300°C, relatively similar structural changes as in $Li_{0.2}Na_{0.8}MgH_3$ took place. Sodium and magnesium recombine to form sodium magnesium hydride and its reflections can be detected up to 400 °C. The main difference with the x=0.2 sample, lay on the appearance of lithium oxide peaks probably as a result of the increased amount of Li inputted into the hydride. Moreover, Mg patterns shifted to higher 2 theta angles with lower intensity as the temperature increased. Other reflections such as oxides of Mg are also observed during the heating process.

Figure 7.25 shows the Ex-Situ XRD of the recombined $Li_{0.5}Na_{0.5}MgH_3$. Reflections related to sodium magnesium hydride, sodium hydride, magnesium and oxides are present in the sample. There are no lithium or lithium hydride peaks, however, there are diffractions of lithium oxide, therefore, evidencing that lithium is present, but cannot be detected by X-ray diffraction due to its small ionic size.

Figure 7.26 illustrates the Rietveld refinement of the ex-situ $Li_{0.5}Na_{0.5}MgH_3$ in order to determine the amount of each crystalline material in the sample. Results, show that sample contains 22.6 wt.% of crystalline sodium magnesium hydride, 4.7 wt. % of magnesium, 1.6 wt.% of sodium hydride and 0.84 wt.% of magnesium hydride. The remaining products correspond to oxides and hydroxides formed during the hydrogenation process.

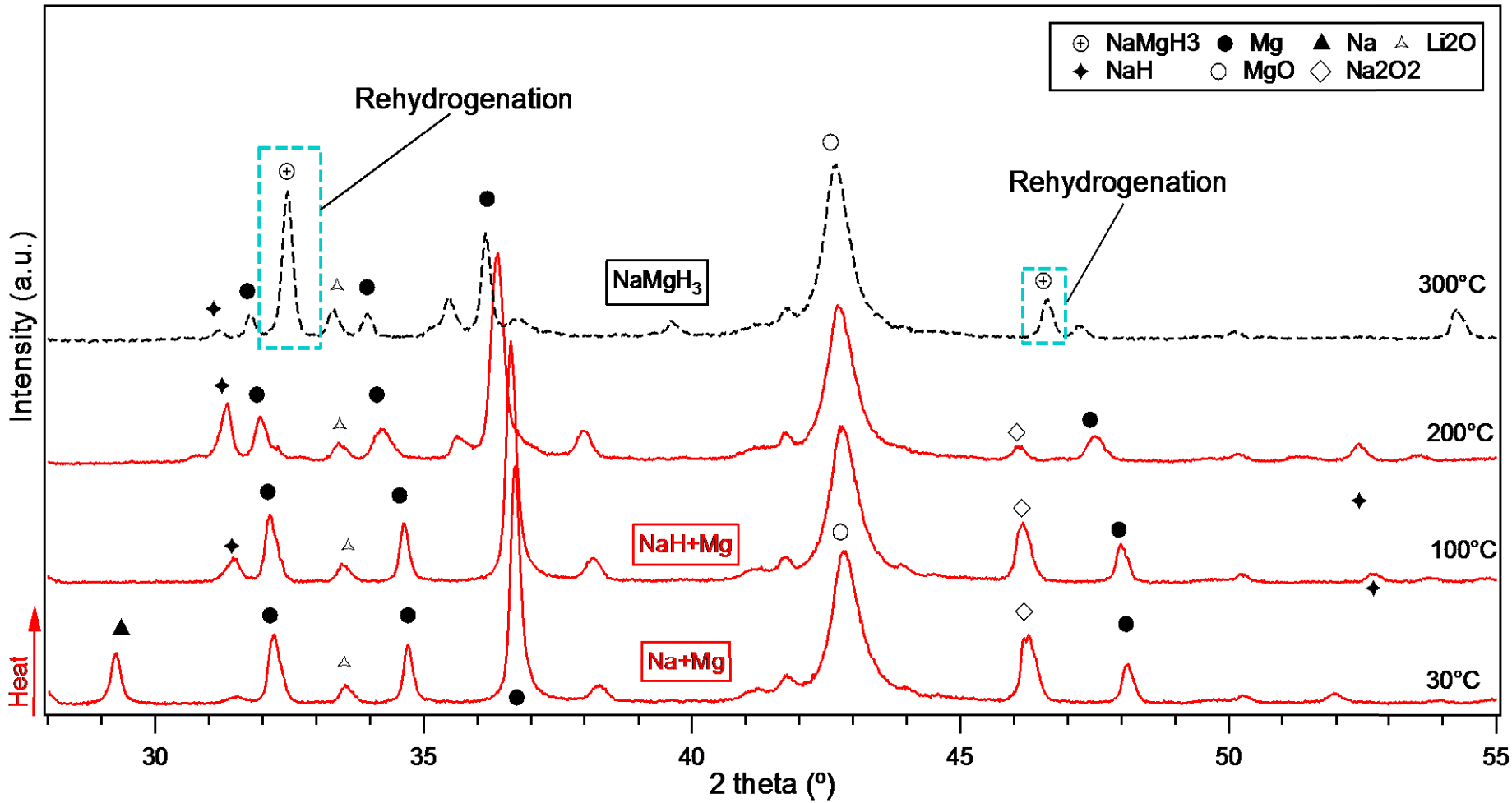

Figure 7.24 In-situ XRD of the 5 h milled $Li_xNa_{1-x}MgH_3$ (x=0.5) rehydrogenated sample under 10 bar H_2 flowing at (100 ml/min) after decomposition. Data was collected isothermally in 50 °C intervals. Dashed (black line) indicates the patterns where rehydrogenation is detected.

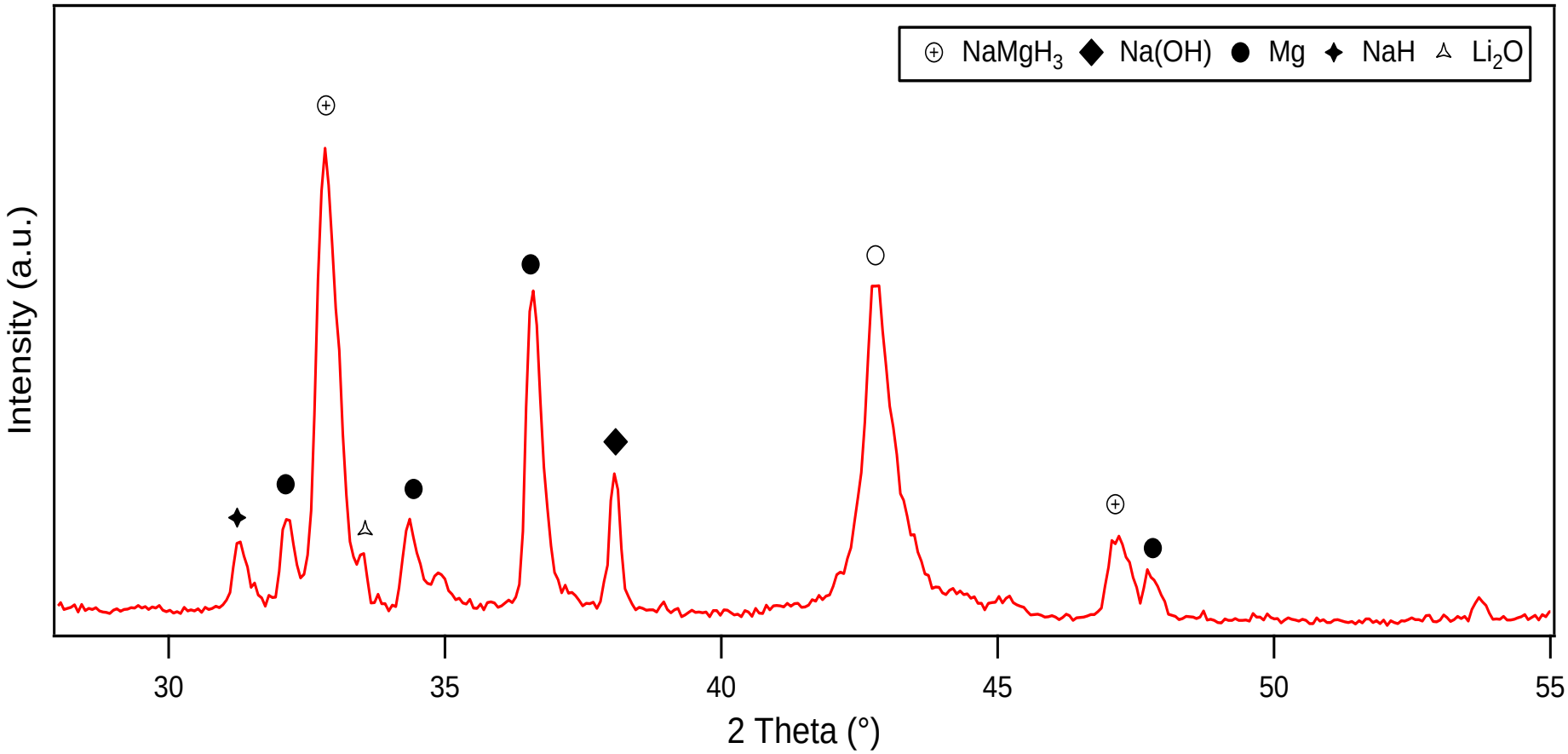

Figure 7.25 RT XRD of the 5 h milled $Li_xNa_{1-x}MgH_3$ (x=0.5) after re-hydrogenation in 10 bar H_2 flowing at 100 ml/min. 2 theta (°) values before 25 were not considered as no representative diffractions were detected.

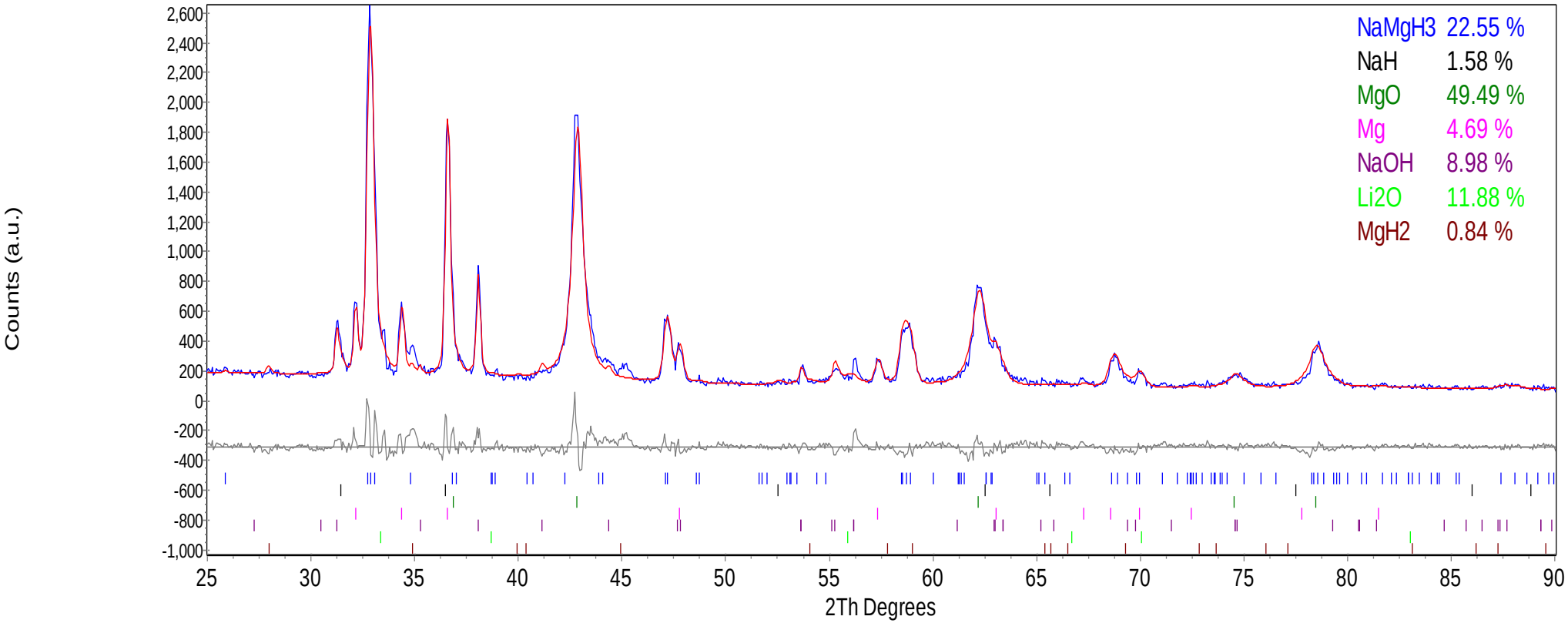

Figure 7.26 TOPAS refinement of $Li_xNa_{1-x}MgH_3$ (x=0.5), 2 theta (°) values before 25 were not considered for the refinement as no representative diffractions were detected. (Observed data is shown by blue line, calculated data is represented by the red lines and the difference is plotted below in grey). Goodness of fit 1.523

Reversibility of $Li_{0.8}Na_{0.2}MgH_3$ compound is shown in Figure 7.27 via In-Situ XRD measurements. The $NaMgH_3$ phase of this sample reforms from the decomposed Na and Mg metals at approximately 250°C on heating at 10 bar H_2 flowing at 100ml/min. Structural changes proceeded similarly than in previous Li (x=0, 0.2, 0.5) hydrides, but at different temperatures. At 200 °C, peaks from hydrogenated Mg and Na were detected increasing with increased intensity on heating. At 250 °C, the main $NaMgH_3$ phase was re-hydrogenated. Additionally, there are also oxide patterns of lithium and magnesium.

To investigate the products after re-hydrogenation of $Li_{0.8}Na_{0.2}MgH_3$ hydride, ex-situ XRD has been performed on the re-hydrogenated sample as shown in Figure 7.28. It shows reflections from sodium magnesium hydride, magnesium hydride, magnesium and some oxides.

Refinement of sample after reabsorbing H_2 (Figure 7.29) shows that sample contains 18 wt.% of crystalline $NaMgH_3$ phase, 25.6 wt.% of magnesium hydride, 14.3 wt% of magnesium, and the remaining crystalline material correspond to magnesium and lithium oxides formed during the re-hydrogenation process.

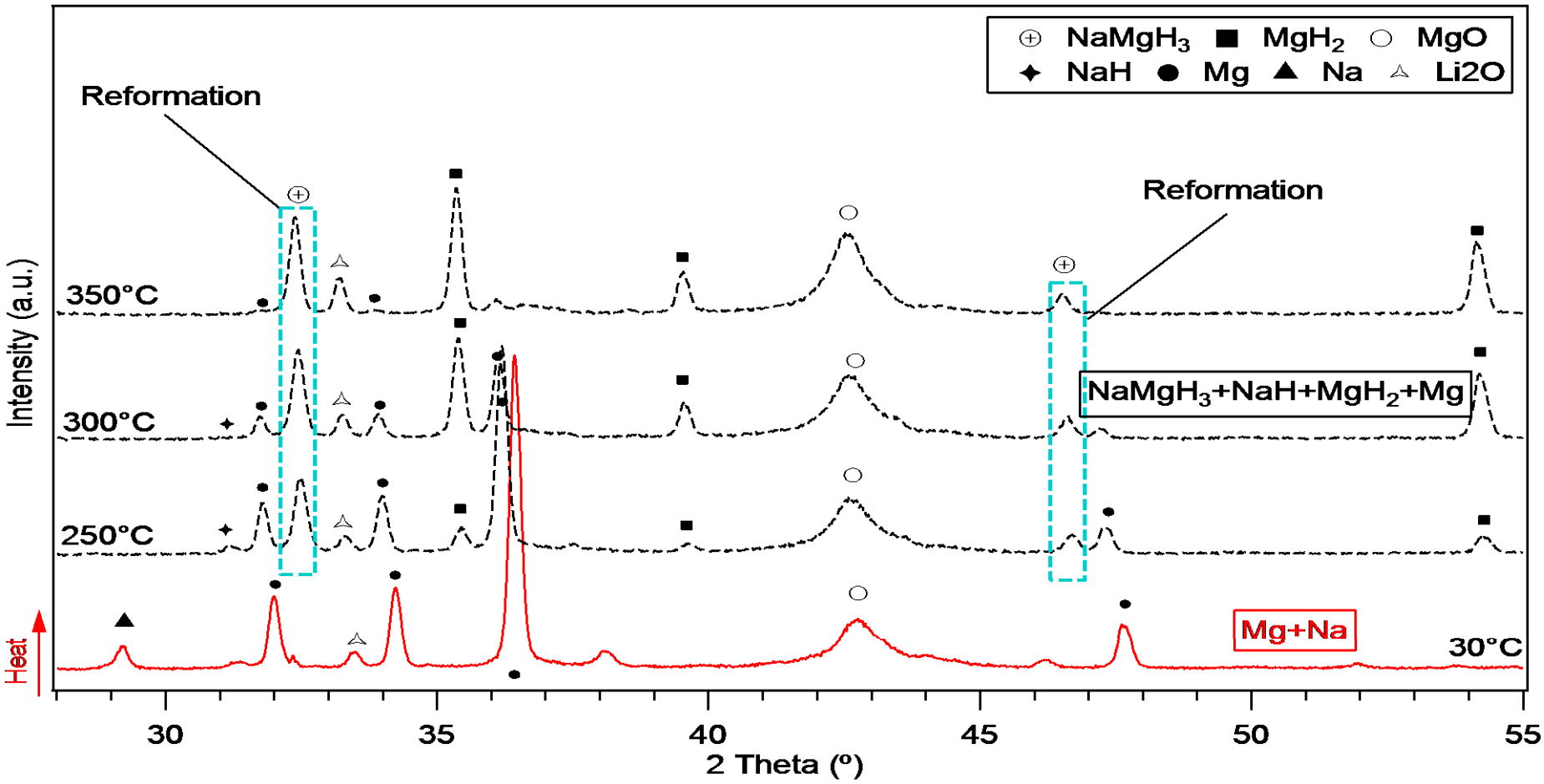

Figure 7.27 In-situ XRD of the 5 h milled $Li_xNa_{1-x}MgH_3$ (x=0.8) rehydrogenated sample under 10 bar H_2 flowing at (100 ml/min) after decomposition. Data was collected isothermally in 50 °C intervals. Dashed (black line) indicates the patterns where rehydrogenation is detected.

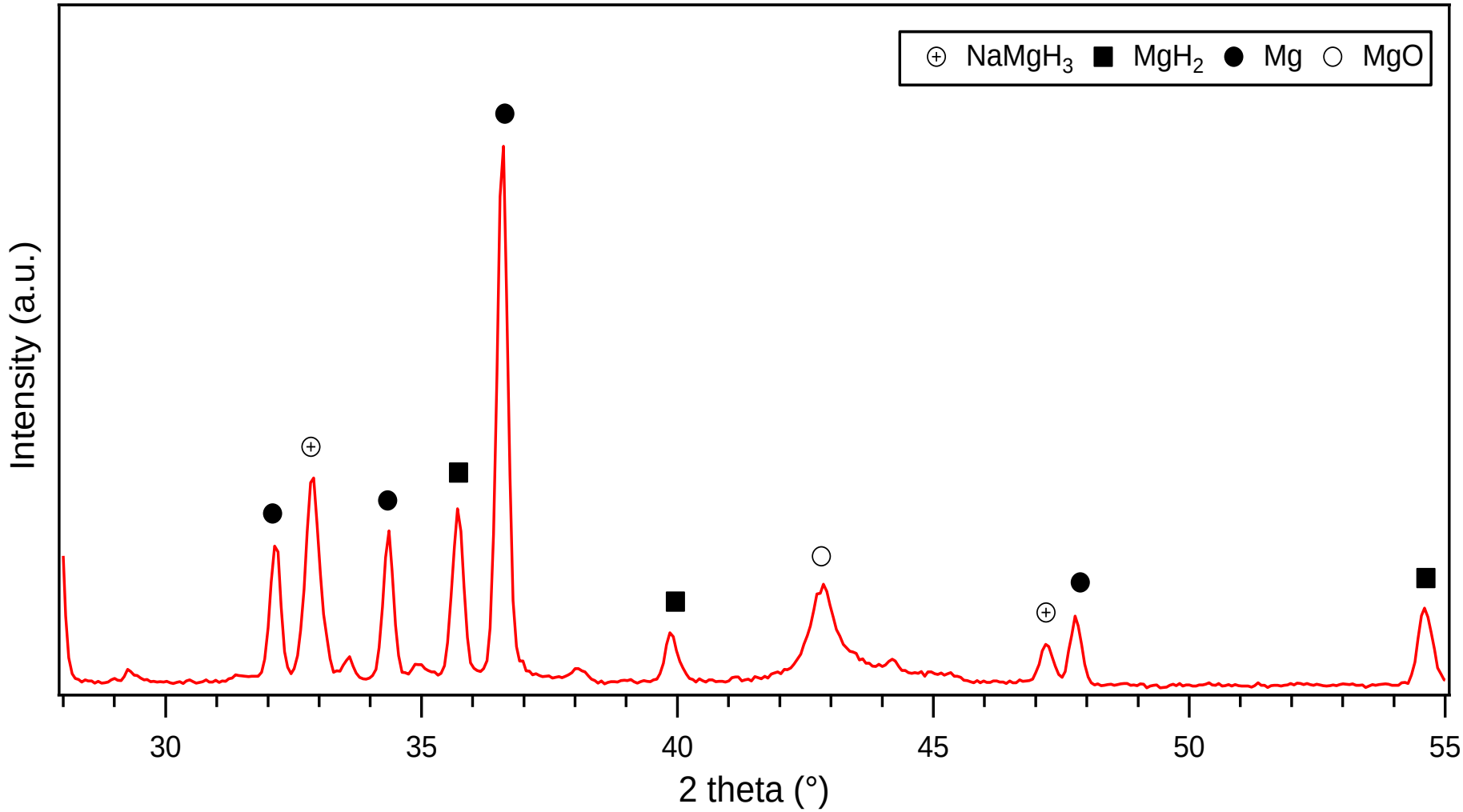

Figure 7.28 RT XRD of the 5 h milled $Li_xNa_{1-x}MgH_3$ (x=0.8) after re-hydrogenation in 10 bar H_2 flowing at 100 ml/min. 2 theta (°) values before 25 were not considered as no representative diffractions were detected.

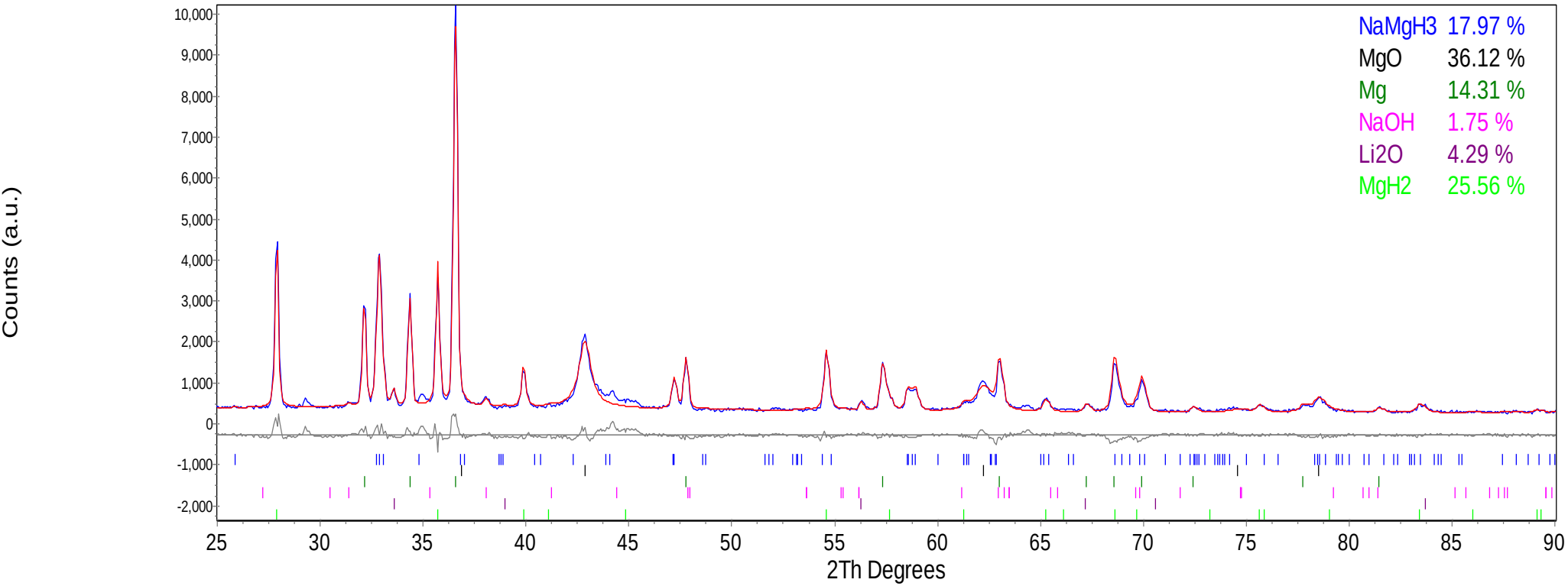

Figure 7.29 TOPAS refinement of $Li_xNa_{1-x}MgH_3$ (x=0.8), 2 theta (°) values before 25 were not considered for the refinement as no representative diffractions were detected. (Observed data is shown by blue line, calculated data is represented by the red lines and the difference is plotted below in grey). Goodness of fit 1.294

7.6 Conclusions

Following the reports of an interesting composition obtained by ball-milling in hydrogen and sintering techniques reported by (Ikeda, Martinez Coronado, Zhong-min Wang), this work investigated the synthesis, characterisation and recombination ability of $Li_xNa_{1-x}MgH_3$ system substituting sodium by lithium hydrides in molar ratios of (x=0, 0.2, 0.5, 0.8). Attempts to obtain these systems were successfully achieved, by mechanical milling mixtures of LiH, NaH, and MgH_2 in an argon atmosphere avoiding the use of high-pressure hydrogen incorporation for synthesis.

Lattice parameters change as the amount of lithium substitute sodium; the more lithium is introduced into the system, the more their lattice parameters decreased. This effect can be observed by the reduction of the cell volume from 230.5 $Å^3$ (x=0) to 225.9 $Å^3$ (x=0.8).

X-ray diffraction for the as milled materials show the formation of sodium magnesium hydride as main phase for the Li x=0 and 0.2 systems. Whereas for the Li x=0.5, 0.8, although the sodium magnesium hydride phase is present, some traces of magnesium hydride are detected. Consequently, there is a decrease in intensity of the main phase, and is more pronounced as the amount of lithium is added to the system.

Thermodynamic characteristics have been investigated and compared with previous studies (Ikeda, Martinez Coronado, Zhong-min Wang). Thermogravimetric analysis for the Li substituted samples showed the mass loss of hydrogen when heating the samples. For $Li_xNa_{1-x}MgH_3$ (x=0) hydride, decomposition started at around 305 °C, and was completed at approximately 390 °C with a total hydrogen loss of 4.7 wt.% When adding Li x=0.2 into the system onset temperature decreases to 300 °C and totally desorbed 5 wt.% of hydrogen until around 380 °C when the reaction is complete. For the Li x=0.5 hydride, a further decrease in the onset temperature is observed, decomposition starts at approximately 280 °C with a weight

loss of nearly 5.1 wt.% and is finished by 385 °C. On Li x=0.8 addition, the hydrogen mass loss was 5 wt. % with an onset temperature of 265 °C and the dehydrogenation is completed at 390 °C. These results indicate that when adding more lithium into the system, there is a notorious reduction in the onset decomposition temperature.

Mass spectrometry for Li substituted samples show the evolution of gases during the thermogravimetric analysis. Hydrogen is the only gas evolved during decomposition. For Li x=0, there are two peaks showing hydrogen release at 365 and 378 °C, when adding Li x=0.2, again hydrogen evolution occurs in two steps peaking at 370 and 385 °C, respectively. The first peak is attributed to the sodium magnesium hydride dehydrogenation, whereas the second evolution corresponds to the hydrogen released from sodium hydride decomposition. For Li x=0.5, there are 3 hydrogen peaks, the first at 315 °C, 356 °C for the second and 375 °C for the third. When Li x =0.8 is added, 3 hydrogen releases are detected at 325, 340 and 358 °C for the first second and third peaks respectively. Decomposition of magnesium hydride is attributed to the first hydrogen evolution, and sodium magnesium hydride and sodium hydride to the second and third hydrogen peaks, respectively. Traces of hydrogen are no longer evident at approximately 410 °C, meaning that hydrogen desorption stops at that temperature.

DSC indicates 2 and 3 endothermic reactions on heating to 430 °C. For the Li x=0, 2 endothermic reactions take place, the first endotherm peaking at approximately 369 °C, correspond to the sodium magnesium hydride decomposition. Thus, the second curve, peaking at 390 °C is due to the sodium hydride decomposition into sodium and magnesium metals. For Li x=0.2, same step reactions are followed but at different temperatures. First peak decomposition (sodium magnesium hydride) can be seen at 365 °C and second decomposition peak (sodium hydride) at 389 °C. Decomposition is completed in both hydride systems at 410 °C. Decomposition of Li x=0.5 sample present 3 endothermic peaks at 310, 348 and 379 °C for

the first, second and third reactions. The first endotherm is due to magnesium hydride decomposition, followed by the sodium magnesium hydride (second) and to complete the process, the dehydrogenation of sodium hydride (third), complete decomposition of the sample is finished at about 400 °C. When adding Li x=0.8 the same 3 decomposition steps are followed, and same dehydrogenation reactions occurred, nevertheless, at different temperatures. The first DSC curve peaks at 315°C, followed by the second endotherm at 332 °C and the last decomposition occurs at 351 °C. Dehydrogenation is completed by 385 °C.

Results from in-situ X-ray diffraction showed the compositional changes in the samples upon heating. Li x=0 diffractions, showed the reflections of sodium magnesium hydride as a single phase from 30 °C until 330 °C, sodium hydride and magnesium phases were detected at around 300 °C indicating the sample decomposition process, in addition magnesium oxides were present from 250°C to 400°C. By 400 °C only traces of magnesium and magnesium oxide are observed. No peaks related to sodium phase were detected, however it is supposed that this may have reacted with oxygen to form sodium oxide and therefore they are not observed by XRD.

In-situ reflections for Li x=0.2 sample show the same decomposition pathway, although at different temperatures. One single sodium magnesium hydride phase is observed from 30 °C to 330 °C, magnesium phase reflections are observed from 320 °C to 400°C, third phase observed between 330 and 350 °C is attributed to sodium hydride. Upon decomposition, there are only reflections associated with magnesium and magnesium oxides remaining. No peaks due to sodium or lithium were observed. It is believed that sodium phase is present, but due to the oxidation of the material during the heating, it cannot be detected by the XRD. On the other hand, the absence of lithium phase might be explained either by the small ionic size of the same; making it difficult to detect, or due to its interaction with another material (i.e. magnesium hydride).

For Li x=0.5 addition, sample decomposition was observed in three steps. Main sodium magnesium hydride phase, in addition to magnesium hydride phase are present from 30 to 320 °C and 280 °C respectively, magnesium phase is observed at 280 °C and is present until 400 °C. Sodium hydride phase is formed at 310 °C and is no longer detected at 350°C, magnesium, and lithium oxides phases formed upon heating are observed from 310 to 400 °C. Only magnesium oxides reflections are noticed on decomposition to 400 °C, sodium and lithium remains are not detected as would be expected, possibly due to the oxidation of the materials on the process.

When Li x=0.8 is added, the same three decomposition steps can be observed as is the Li x=0.5, however at different temperatures. Sodium magnesium hydride, magnesium hydride are detected from 30 to 300 °C. On heating to 320 °C complete decomposition of sodium magnesium hydride is observed. Magnesium hydride decomposes into magnesium from 300 °C and its reflections are perceived upon decomposition. Whereas sodium hydride phase appears at 310 °C and is no longer visible at 330 °C. Oxide phases, such as for lithium, magnesium and sodium, start to form at 250 °C; they remain present upon decomposition with increased intensity. Sodium or lithium peaks are not evident upon decomposition. However, due to the presence of lithium and sodium oxide peaks it is thought that they have reacted with air and oxidised. Moreover, it is believed that lithium could have reacted with another material; therefore, no reflections of this are detected by X-ray diffraction.

Recombination ability had been tested by means of in-situ XRD for the different proposed $Li_xNa_{1-x}MgH_3$ hydride systems, where (x=0, 0.2, 0.5, 0.8). It was found that all systems can be reversible hydride after complete decomposition, upon heating in 10 bar hydrogen flowing at 100 ml/min. Reformation of the main sodium magnesium hydride phase was observed at around 200 °C in all cases. The main disadvantage observed in the rehydrogenation process is the

intense reflections of oxide peaks, which may have led to a decrease in the amount of crystalline material being reformed.

To the best of the author's knowledge there are no studies on the recombination ability of the $Li_xNa_{1-x}MgH_3$ (x=0, 0.2, 0.5, 0.8) hydride systems. Desorption temperatures and decomposition reactions are in good agreement with values obtained from the DSC, in-situ XRD and TGA experiments.

Furthermore, it was established that the lithium-substituted samples x=0.5, 0.8 present 5 and 5.1 wt. % of hydrogen desorption, which is higher than values obtained when introducing less amount of lithium into the system in this work and compared to previous reports from the literature (Martínez-Coronado et al., 2012, Wang et al., 2016, Ikeda et al., 2007a). Enhanced results in decomposition temperatures and higher hydrogen content might be due to; the crystallite size reduction through mechanical milling, the lower structural stability of lithium perovskites and/or the smaller size of lithium in comparison with sodium.

CHAPTER VIII

8. RESULTS AND DISCUSSION: CALCIUM MAGNESIUM HYDRIDE

8.1 Introduction

Ternary hydrides have been investigated as candidates for hydrogen storage systems. Particular interest has been in hydrides that contain magnesium, given the low cost, high volumetric and gravimetric capacity and abundance(Cheng et al., 2012). Yvon et al. reported a list of 28 ternary hydrides between magnesium and alkali (A) or alkaline-earth (Ae) elements(Yvon and Bertheville, 2006). Typically, high-pressure techniques of the metal hydrides or alloys were required for the synthesis of these compounds.

Nevertheless, grain size reduction to a nanoscale was proven to enhance the thermodynamics and kinetics of hydrogen absorption and desorption, although there is limited information in the literature about this particular method of synthesis (Zaluska et al., 1999, Huot et al., 2001).

Significant interest has attracted the synthesis of ternary/quaternary hydrides by substitution of transition metals by light-weight materials. Ternary hydrides compromising Ca have been investigated (e.g. $LiCaH_3$, $NaCaH_3$, $KCaH_3$)(Gingla et al., 1999, Bouamrane et al., 2001, Vajeeston et al., 2010).

First report on Ca-Mg hydrides was on 1970s using high pressure sintering methods under H_2 to synthesise the hydrides(Nomura et al., 1978). More recent investigations show the structures of different alkali metal hydrides $MCaH_x$, where (M=Li, Na, K, Rb, Cs)(Vajeeston et al., 2010, Matar et al., 2011).

Studies of the $Ca_4Mg_3H(D)_{14}$ have been described by Gingl et al., where synthesis of the ternary phase in a high temperature (683 K), and pressure (53 bar) took 6 days in a sealed autoclave.

The product was found in a mixture of MgH_2, CaH_2, and Mg impurities(Gingl et al., 1992a). The structure of a new Ca-Mg-H ternary hydride was described by Bertheville and Yvon, $Ca_{19}Mg_8H(D)_{54}$ was synthesised using a combination of MgH_2 and CaH_2 in a ratio of 2:1 in a high pressure cell for 3 hours, and was found to be iso-structural to $Yb_{19}Mg_8D_{54}$(Bertheville and Yvon, 1999).

Santori et al. employed mechanical milling in their work on mixed hydrides systems compromising Mg-Al-Ca-H and reported the formation of $Ca_{19}Mg_8H_{54}$ and $Ca_4Mg_3H_{14}$ phases, although they were not present as a single phase(Sartori et al., 2009).

Reardon H., studied the mechanochemical synthesis of ternary hydrides compromising alkali metal alkaline earth metals without H_2 during the milling process for the first time using different stoichiometries. Furthermore, this study compromises the investigation of the decomposition mechanisms of the as milled samples(Reardon, 2014).

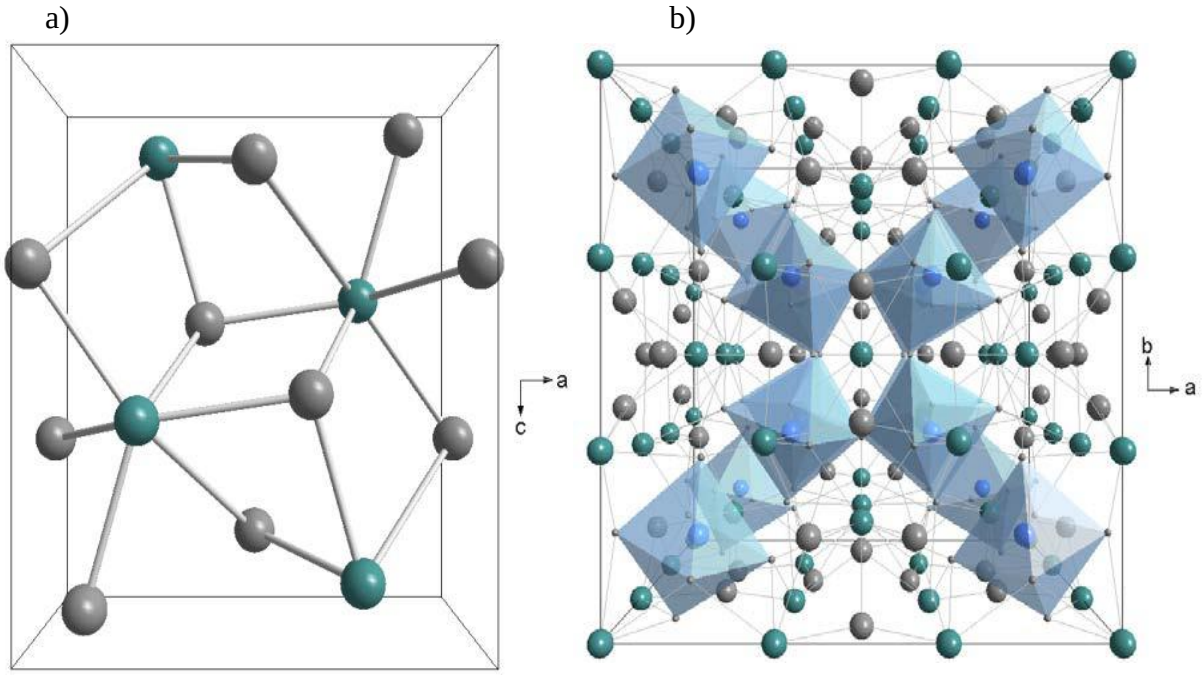

c)

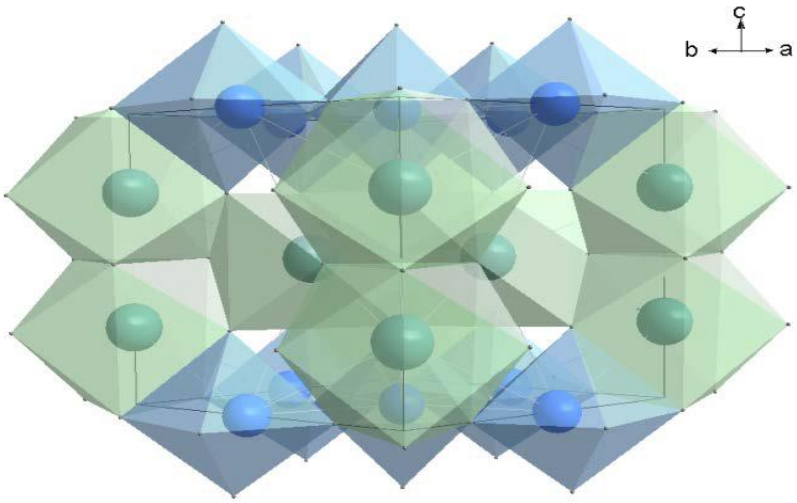

Figure 8.1 a) Schematic unit cells of CaH_2 and the ternary phases b) $Ca_{19}Mg_8D_{54}$ and c) $Ca_4Mg_3D_{14}$. (Green, grey and blue spheres represent Ca, H and Mg, respectively.)

There have been other investigations regarding mixtures of CaH_2 and MgH_2 reporting the hydrolytic properties of the samples prepared by ball milling which showed high hydrogen yields i.e. Mg-MgH_2-CaH_2 >80 % (Tessier et al., 2004), CaH_2 mechanically milled with $Mg_{17}Al_{12}$ alloy 94.8 %(Xiao et al., 2011), and over 99 % yield of H_2 from CaH_2 on a scale laboratory set up in micro- PEM fuel cells(Zhu et al., 2008). Furthermore, thermal decomposition of systems including MgH_2 and CaH_2 and complex hydrides as borohydrides has been extensively reported in the literature. However, these compounds will not be discussed in this work.(Yuan et al., 2011, Pinkerton and Meyer, 2008)

Despite studies describing synthesis and decomposition mechanisms of Ca-Mg-H ternary hydrides were performed previously, there are no reports regarding rehydrogenation properties of the Ca-Mg-H compound. Hence, this information needs to be assessed before considering this material as a suitable candidate for hydrogen storage and its further commercialization.

This chapter explores the synthesis, thermal analysis and rehydrogenation ability of CaH_2 and MgH_2 mixtures milled for 5 hours in argon alone, using a combination of characterisation

techniques. Moreover, samples were synthesised using 2 different stoichiometries to study the effect of modifying the composition of the hydrides.

8.2 Structural characterisation of milled material

Powders of MgH_2 (95% pure hydride phase and remainder 5% Mg; Sigma-Aldrich) and CaH_2 (95%; Sigma-Aldrich) were ball milled in attempt to obtain one single phase mixture (Ca-Mg-H), two molar ratios were investigated MgH_2 : CaH_2 (1:1) and (2:1) by room temperature X-ray diffraction to investigate the phases present in the samples, followed by a thermal decomposition through DSC and TGA measurements to study the reactions and evolution of gases upon temperature changes. Moreover, to deeply examine the reaction changes on heating, In-situ XRD was performed, the same technique was carried on, to determine the re-hydrogenation ability of the decomposed samples.

Figure 8.2 shows the XRD patterns of the as milled CaH_2 and MgH_2 products for the different molar compositions. In the first case for (1:1) composition, one single phase was observed; this corresponds to the cubic $Ca_{19}Mg_8H_{54}$ (space group Im-3) iso-structural to $Yb_{19}Mg_8D_{54}$, previously reported by (Bertheville, Sartori)(Bertheville and Yvon, 1999, Sartori et al., 2009). For the (2:1) composition, again phase related to the cubic $Ca_{19}Mg_8H_{54}$ was observed, in addition to small traces of MgO probably due to the rapid oxidation of the sample when in contact with air. The most intense reflection appears at 31.2 (2θ°).

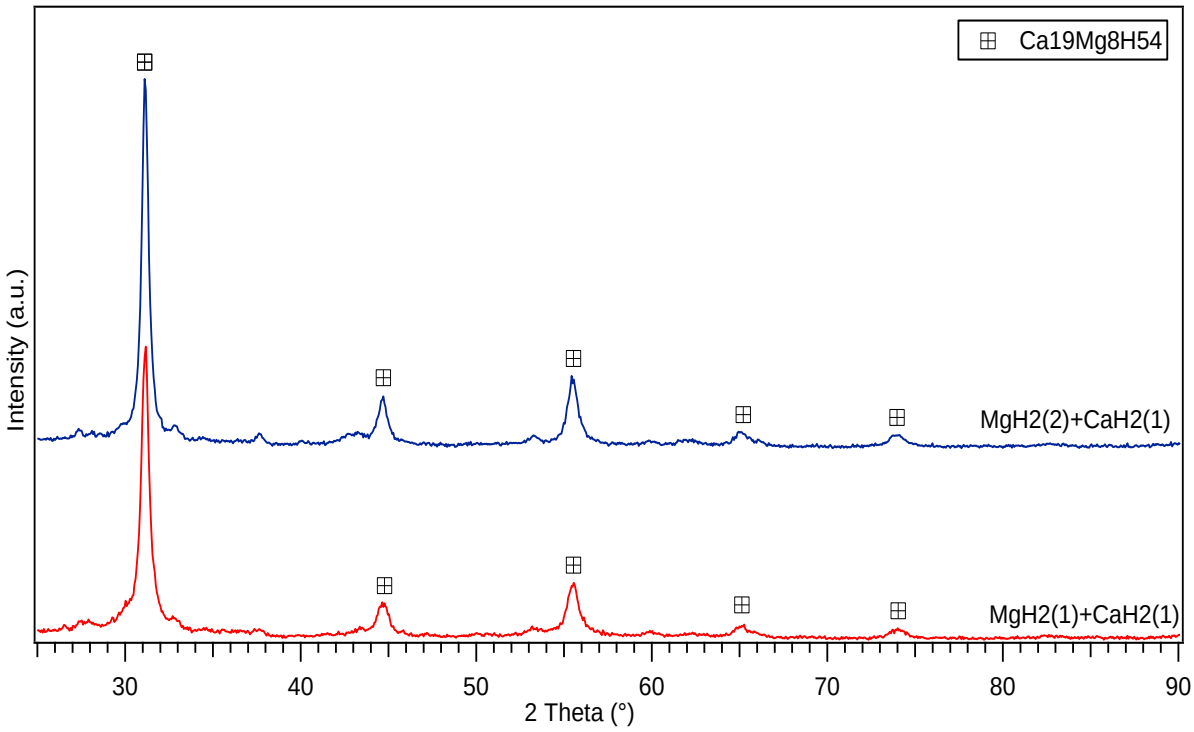

Figure 8.2 XRD patterns of the 5 hours milled MgH_2 + CaH_2. Red line accounts for the (1:1) molar composition, Blue line represents the (2:1) molar ratio.

Rietveld refinement was performed for both compositions (1:1), and (2:1) respectively. From this refinement, the lattice parameters and weight percent of the crystalline phases were obtained and are summarised in Table 8.1. From this interpretation, it can be noticed that the unit cell parameters of the samples are affected by the ratio of the starting hydrides.

Figure 8.3 illustrates the unit cell parameters of the MgH_2 + CaH_2 (1:1), (2:1) and literature values (ref 127). The (2:1) ratio has the closest meaning to that of the (a) cell parameter and volume reported by Bertheville et al.,(Bertheville and Yvon, 1999) for the ternary hydride. Whereas, for the MgH_2 + CaH_2 (1:1) sample, smaller (a) unit cell values and volume are observed.

Table 8.1 Lattice parameters and unit cell volume of MgH_2 + CaH_2 mixtures with different molar compositions compared with known values from literature.

Sample MgH_2 + CaH_2	Lattice parameters (a) (Å)	Cell volume (A^3)
1:1	12.13±0.04	1788.21±0.12
2:1	12.15±0.02	1792.07±0.09
Literature **(Bertheville and Yvon, 1999)**	12.1457 (5)	1791.71(4)

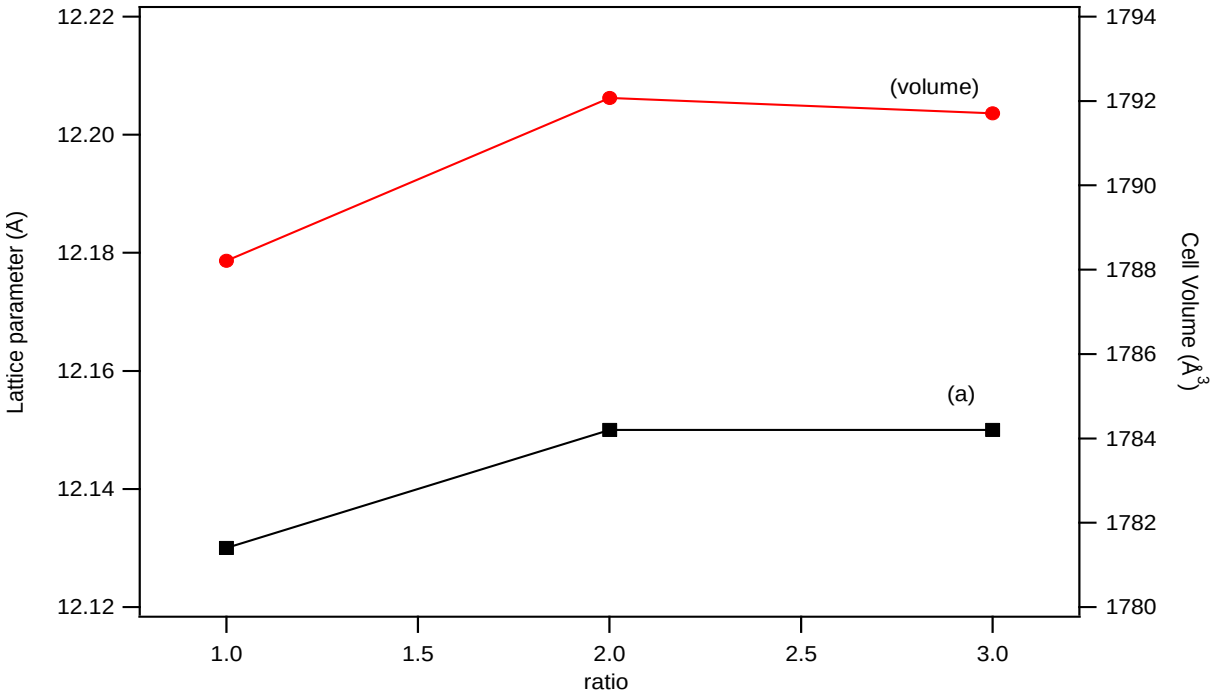

Figure 8.3 Unit cell parameters vs ratio (1:1, 2:1 and Literature) of MgH_2 + CaH_2 mixtures. (Bertheville and Yvon, 1999)

8.2.1 Thermal decomposition

Thermal analysis was conducted in order to examine the temperature reactions and hydrogen release properties of the hydrides. DSC measurements were taken from room temperature (30 °C) to 500 °C in a 100 ml/min constant flowing Ar atmosphere under 3 bar pressure, to

avoid air-water contamination all samples were prepared, loaded and run inside an Argon filled glove box < 5 % ppm oxygen. Figure 8.4 (a) shows the DSC curves of the MgH_2 + CaH_2 (1:1) and (2:1) samples. For the (1:1) molar ratio, two overlapped endotherms are observed peaking at 383 and 405 °C. The first peak is related to the decomposition of the ternary hydride $Ca_{19}Mg_8H_{54}$ into $Ca_4Mg_3H_{14}$ and Mg with hydrogen release, the second endotherm is followed by the decomposition of $Ca_4Mg_3H_{14}$ into CaH_2 and Mg.

For the second molar composition (2:1), two overlapped endothermic peaks are present at 373 °C for the first peak and 400 °C for the second endotherm. These decomposition reactions are attributed to the decomposition of $Ca_{19}Mg_8H_{54}$ into $Ca_4Mg_3H_{14}$ and Mg and the subsequent decomposition of $Ca_4Mg_3H_{14}$ into CaH_2 and Mg. However, at this ratio (2:1), reactions occur at lower temperatures.

These results agree with previous reported data. Nevertheless, show lower decomposition temperature of approximately 20 °C for the $Ca_{19}Mg_8H_{54}$ ternary hydride phase (Bertheville and Yvon, 1999, Yvon and Bertheville, 2006, Reardon, 2014). Consequently, it can be suggested that the decomposition reactions for both compositions MgH_2 + CaH_2 (1:1) and (2:1) follow two steps as proposed in equation (8.1) and (8.2):

$$Ca_{19}Mg_8H_{54} \rightarrow Ca_4Mg_3H_{14} + Mg \quad (8.1)$$

$$Ca_4Mg_3H_{14} \rightarrow CaH_2 + Mg \quad (8.2)$$

Thermogravimetric analysis (TGA) performed showed the mass loss profiles of the samples. Figure 8.4 (b) shows the TGA traces for the (1:1) and (2:1) 5 hours milled MgH_2 + CaH_2 samples. In the first case; for the (1:1) molar ratio, a total mass loss of (2.24 wt.%) of hydrogen was achieved from 315 °C (T_{onset}) to 415 °C (T_{end}). When the molar ratio was (2:1), the sample weight loss was (2.1 wt. %) from 315 °C to 410 °C temperature range.

In order to measure the evolution of gases during the decomposition process, a mass spectrometer was connected to the TGA. Figure 8.4 (c) indicates the hydrogen evolution as the only product (gas) released during the decomposition of the samples. The obtained results from MS are in good agreement with temperatures achieved from the DSC and TGA measurements.

Table 8.2 and Figure 8.5 sumarise the results gathered during the thermal analysis of the samples and show a comparative with previous reported data form the literature for the mixture with same nominal compositions(Reardon, 2014).

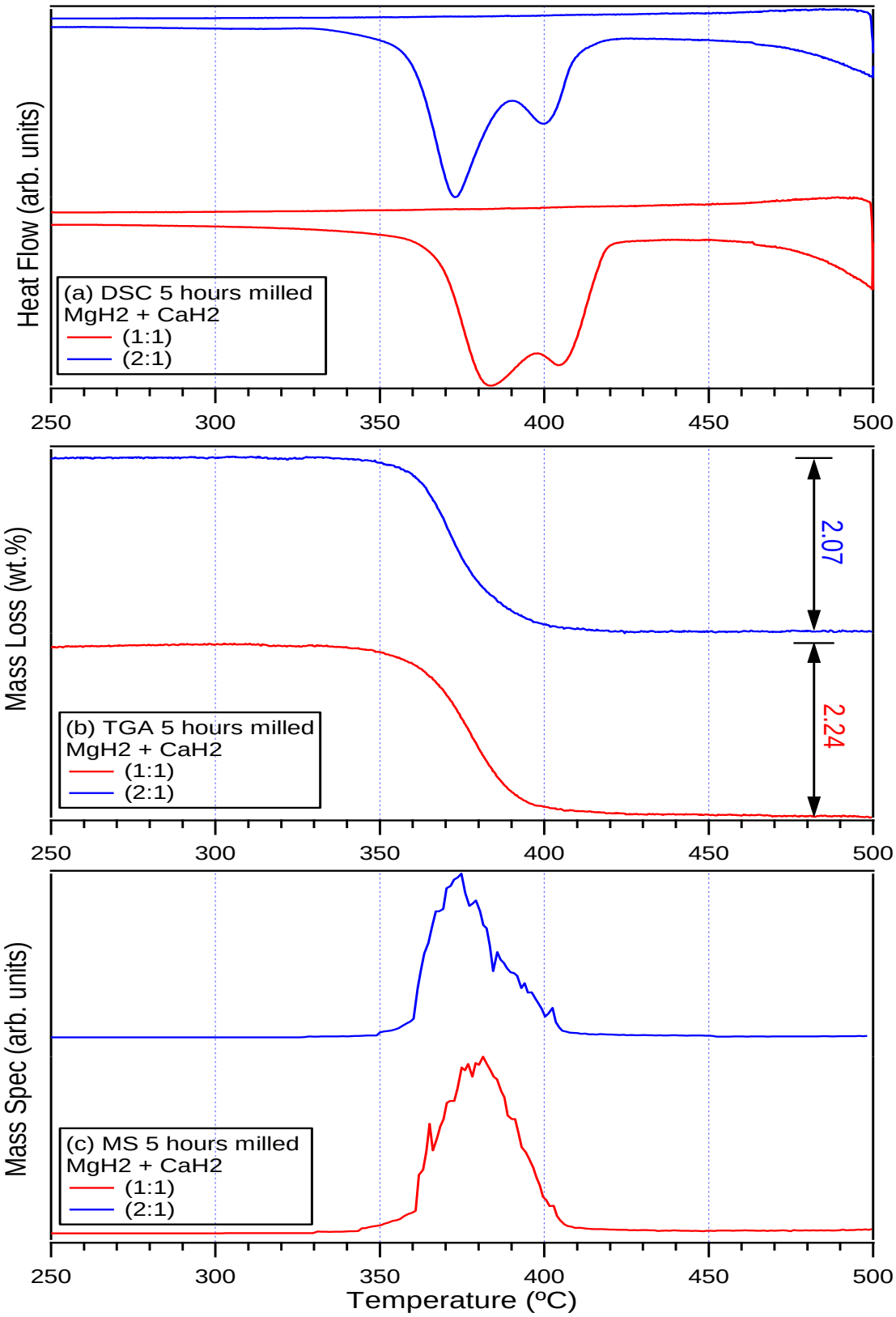

Figure 8.4 DSC-TGA-MS traces of the 5 h ball milled MgH_2 + CaH_2 samples. Red line indicates the (1:1) molar composition. Blue line stands for the (2:1) molar ratio. Heating rate 2 °C/min in 3 bar argon at 100 ml/min (DSC), and 1 bar argon at 40 ml/min (TGA/MS)

Table 8.2 Summary of decomposition temperatures and mass loss of 5 h milled MgH_2 + CaH_2 compared to literature values.(Reardon, 2014)

	DSC				TGA		
Sample MgH_2 +CaH_2	$T_{(onset)}$ (°C)	$T1_{(peak)}$ (°C)	$T2_{(peak)}$ (°C)	$T_{(end)}$ (°C)	$TG_{(onset)}$ (°C)	$TG_{(end)}$ (°C)	Mass loss (wt%)
1:1	347.2	383	405	426.2	338.9	424.6	2.24
2:1	332.7	373	400	419.9	340.2	419.7	2.07
Readon H(Reardon, 2014) (1:1)	359.9	382.2	-	-	368.1	-	2.29
Readon H(Reardon, 2014) (2:1)	350.9	377.4	-	-	358.4	-	3.49

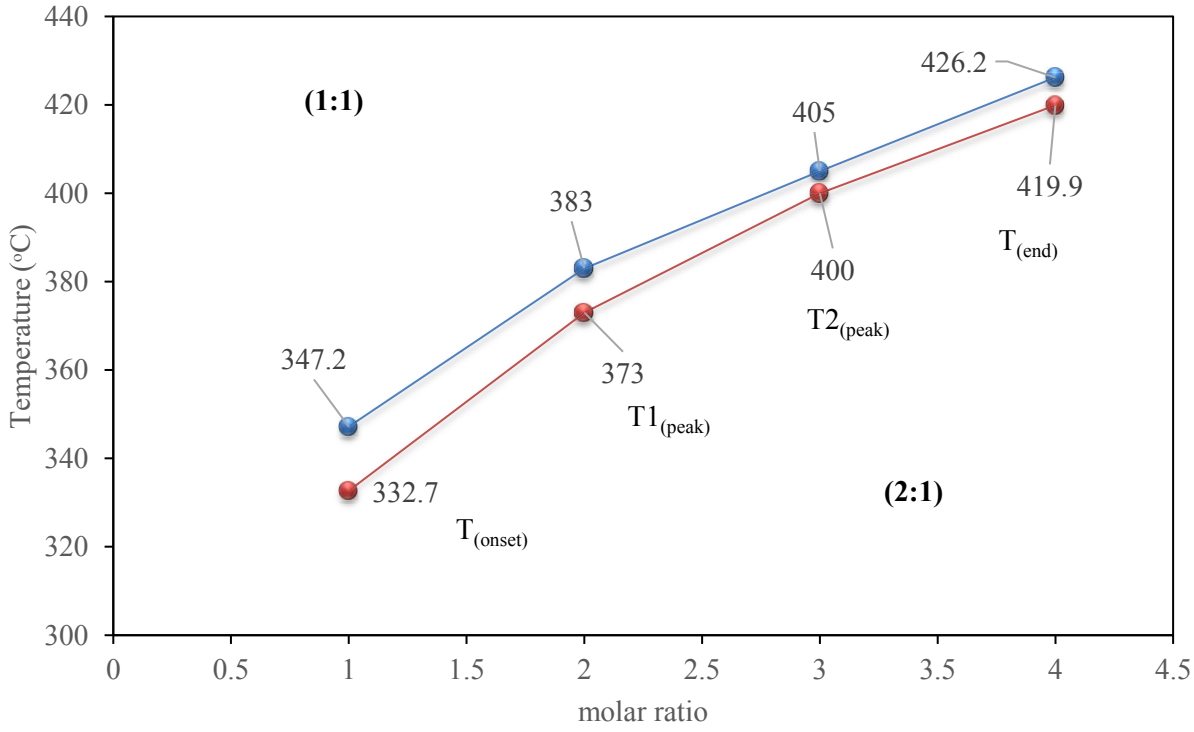

Figure 8.5 DSC temperatures of hydrogen desorption of MgH_2 + CaH_2 observed from the DSC plotted against two different molar ratios. Blue line stands for (1:1), Red line represents (2:1) molar ratio

8.2.2 Analysis of Decomposition Products

The decomposition products of the 5 hours milled samples were investigated by In-Situ X-ray diffraction. Patterns were collected every 25 °C isothermally from 30 °C to 500 °C at a heating rate of 2 °C/min in a flowing helium atmosphere at 100 ml/min and 3 bar pressure. In-situ XRD reflections from MgH_2 + CaH_2 samples with molar ratios (1:1) and (2:1) are presented in Figures 8.6, 8.7 (surface plot), 8.8 and 8.9 (surface plot) respectively.

MgH_2 + CaH_2 (1:1)

For the MgH_2 + CaH_2 (1:1) sample, at room temperature shows a $Ca_{19}Mg_8H_{54}$ phase, and some peaks related to the sample holder. The same patterns are recorded on heating up to 350 °C with increased intensity. Between 325 and 375 °C, evolution of the $Ca_4Mg_3H_{14}$ phase is observed, this corresponds to the decomposition of $Ca_{19}Mg_8H_{54}$, along with this phase traces of CaH_2 are detected, indicating the further decomposition of $Ca_4Mg_3H_{14}$ into CaH_2 and Mg when heating up to 400 °C. From 400 °C onwards, the only phases detected are CaH_2 and Mg and Ca oxides. The presence of these phases indicates that the $Ca_{19}Mg_8H_{54}$ has fully decomposed into CaH_2 and Mg. However, no traces of pure Mg where detected on heating; it is believed that due to impurities in the gas stream or a small leak in the Anton-par cell used for the In-situ XRD measurements, Mg become oxidised, formed MgO and therefore, cannot be detected as pure crystalline material. These observations are in good agreement with the decomposition reactions obtained from DSC measurements previously performed in this work.

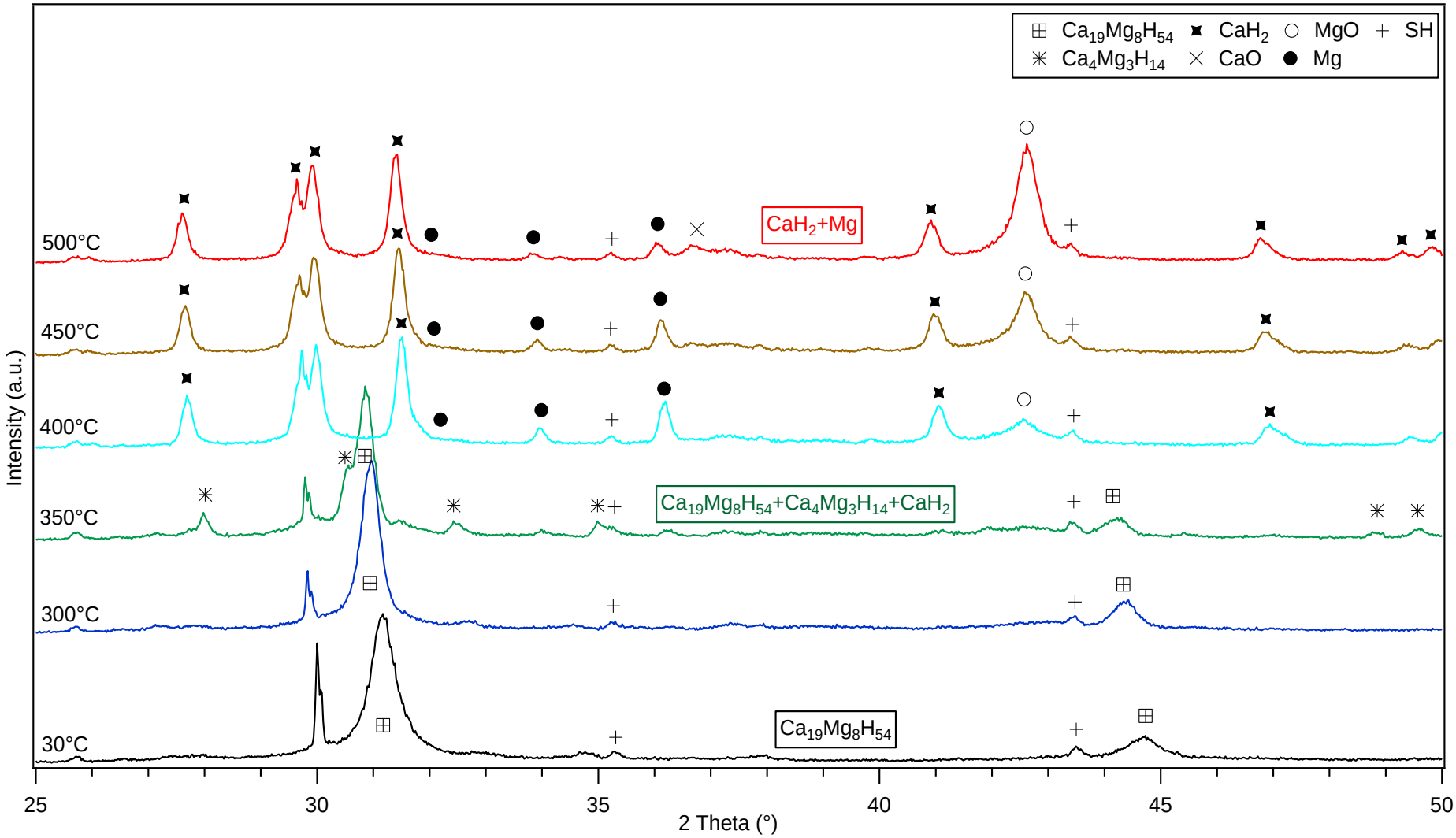

Figure 8.6 In-situ XRD patterns of the 5 h milled MgH_2 + CaH_2 (1:1) heated under He (100 ml/min, ~3 bar) between 30 – 500 °C.

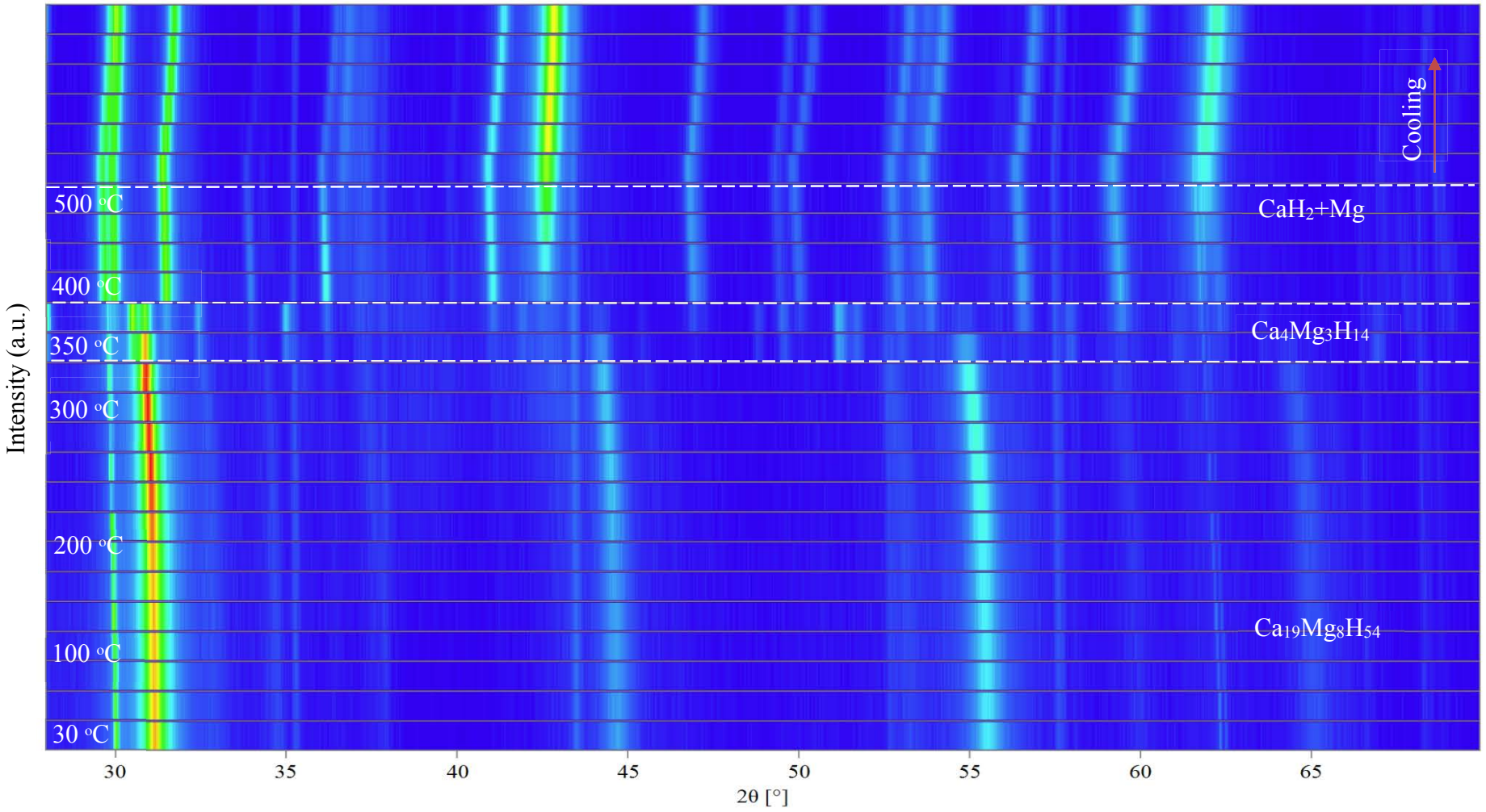

Figure 8.7 Surface plot of In-situ XRD patterns of 5 h milled MgH_2 + CaH_2 (1:1) heated under He (100 ml/min, ~3 bar) between 30 – 500 °C. A brighter colour corresponds to a higher diffraction intensity. The white dashed lines show the phase transition temperature and are given as a guide for the eye.

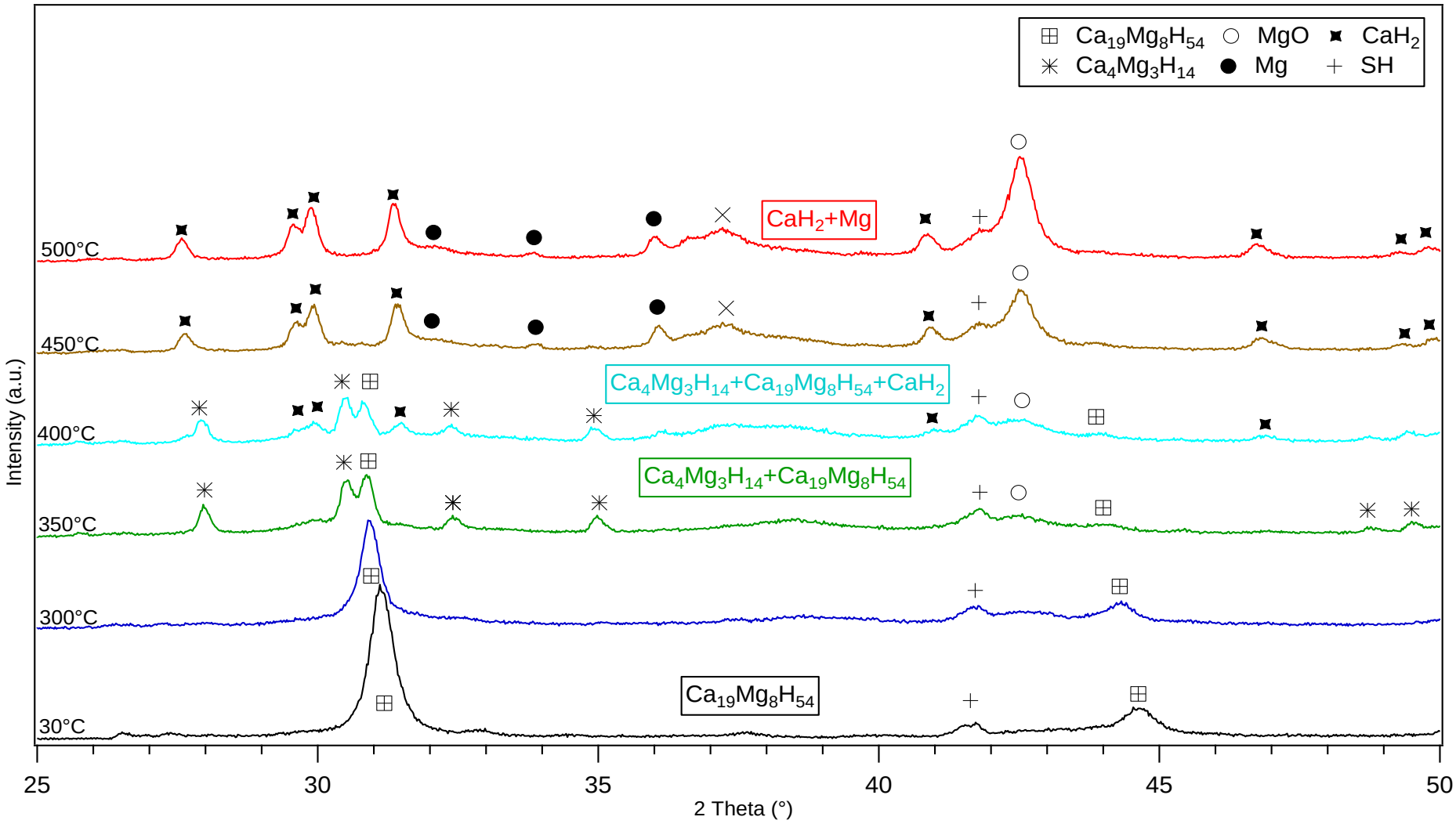

Figure 8.8 In-situ XRD patterns of the 5 h milled MgH_2 + CaH_2 (2:1) heated under He (100 ml/min, ~3 bar) between 30 – 500 °C.

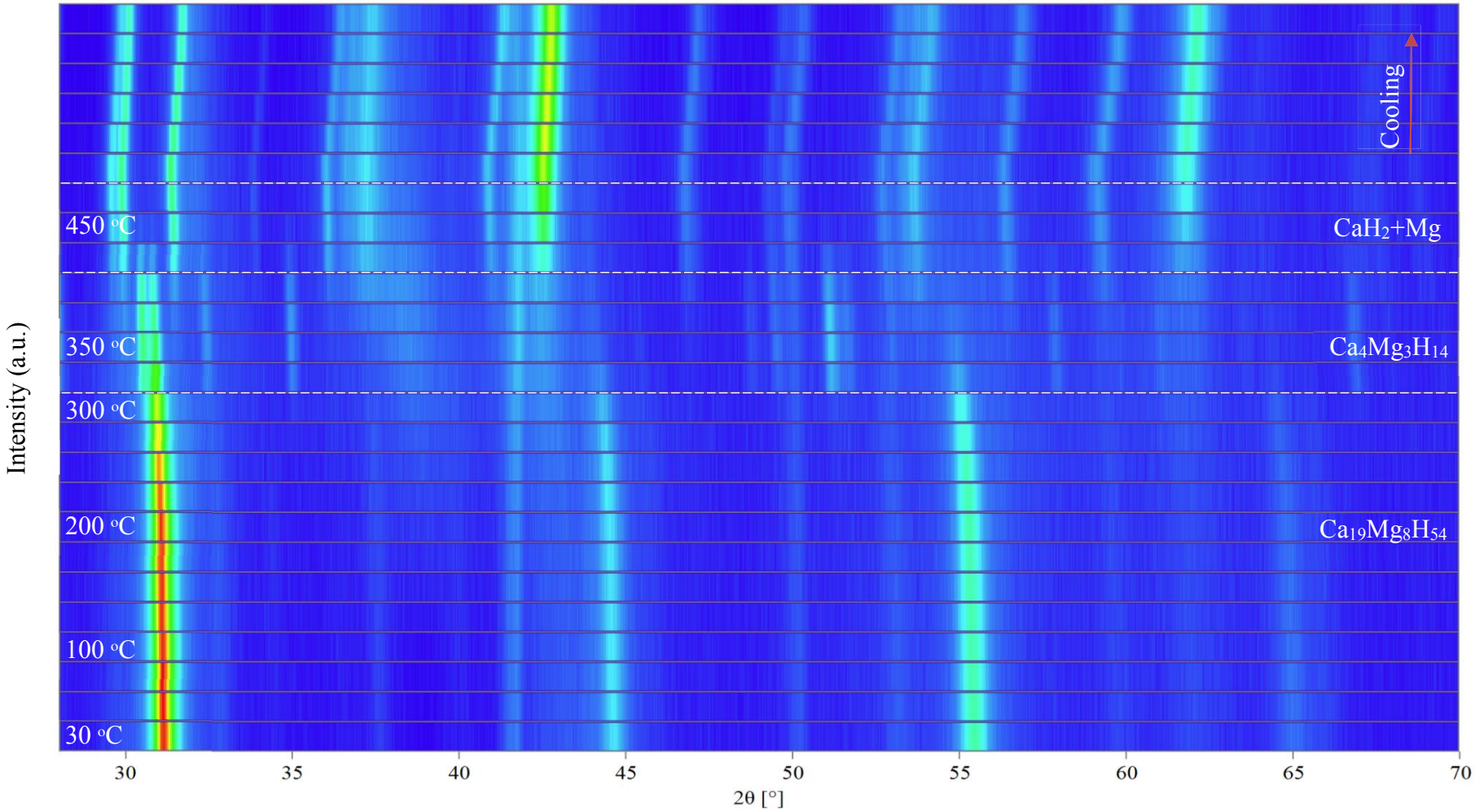

Figure 8.9 Surface plot from In-situ XRD patterns of 5 h milled MgH_2 + CaH_2 (2:1) heated under He (100 ml/min, ~3 bar) between 30 – 500 °C. A brighter colour corresponds to a higher diffraction intensity. The white dashed lines show the phase transition temperature and are given as a guide for the eye.

In order to analyse the decomposed products after In-situ XRD, room temperature X-ray diffraction was performed on the dehydrogenated samples. Figure 8.10 shows the XRD patterns of the decomposed 5 hours milled MgH_2 + CaH_2 (1:1). There are reflections due to CaH_2, Mg and MgO as expected from the decomposition reactions equation (8.1) and (8.2).

Figure 8.10 shows the refined spectra of the decomposed MgH_2 + CaH_2 (1:1) sample, it contains 73 (wt. %) of crystalline CaH_2, 9 (wt.%) of crystalline Mg and the remaining 19 (wt. %) correspond to the crystalline MgO.

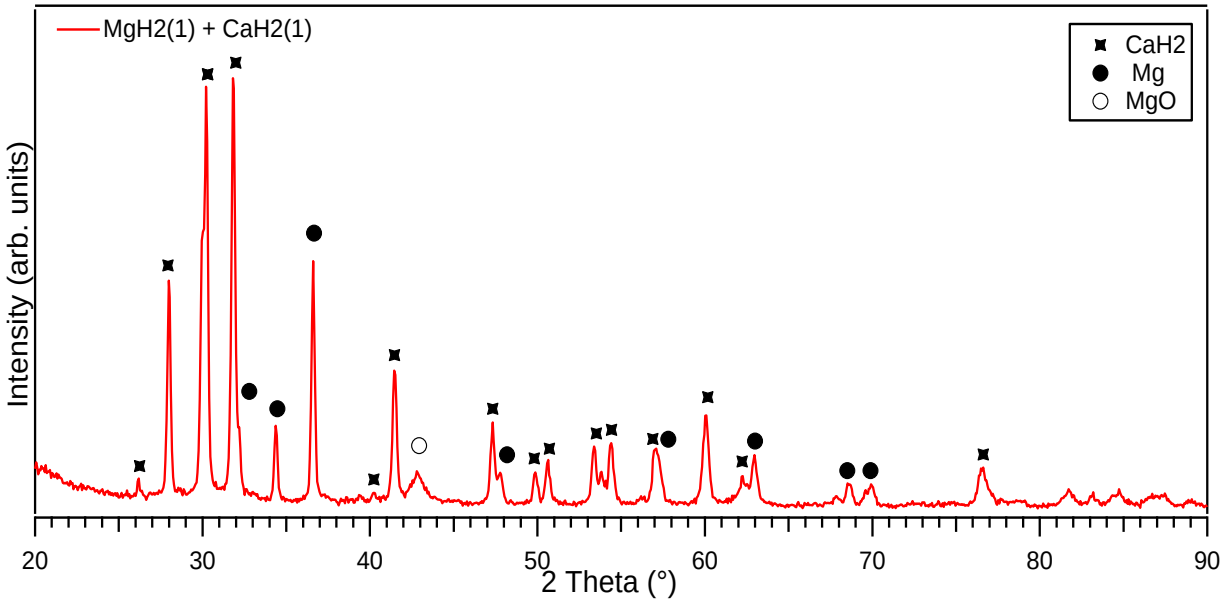

Figure 8.10 Ex-situ XRD of the decomposed MgH_2 + CaH_2 (1:1) after heating to 500 °C

MgH_2 + CaH_2 (2:1)

For the MgH_2 + CaH_2 (2:1) sample at room temperature (30 °C) the only phase detected corresponds to the $Ca_{19}Mg_8H_{54}$. On heating to 300 °C the same reflections of calcium magnesium hydride are observed, gradually shifting to higher angles with intensity decrease.

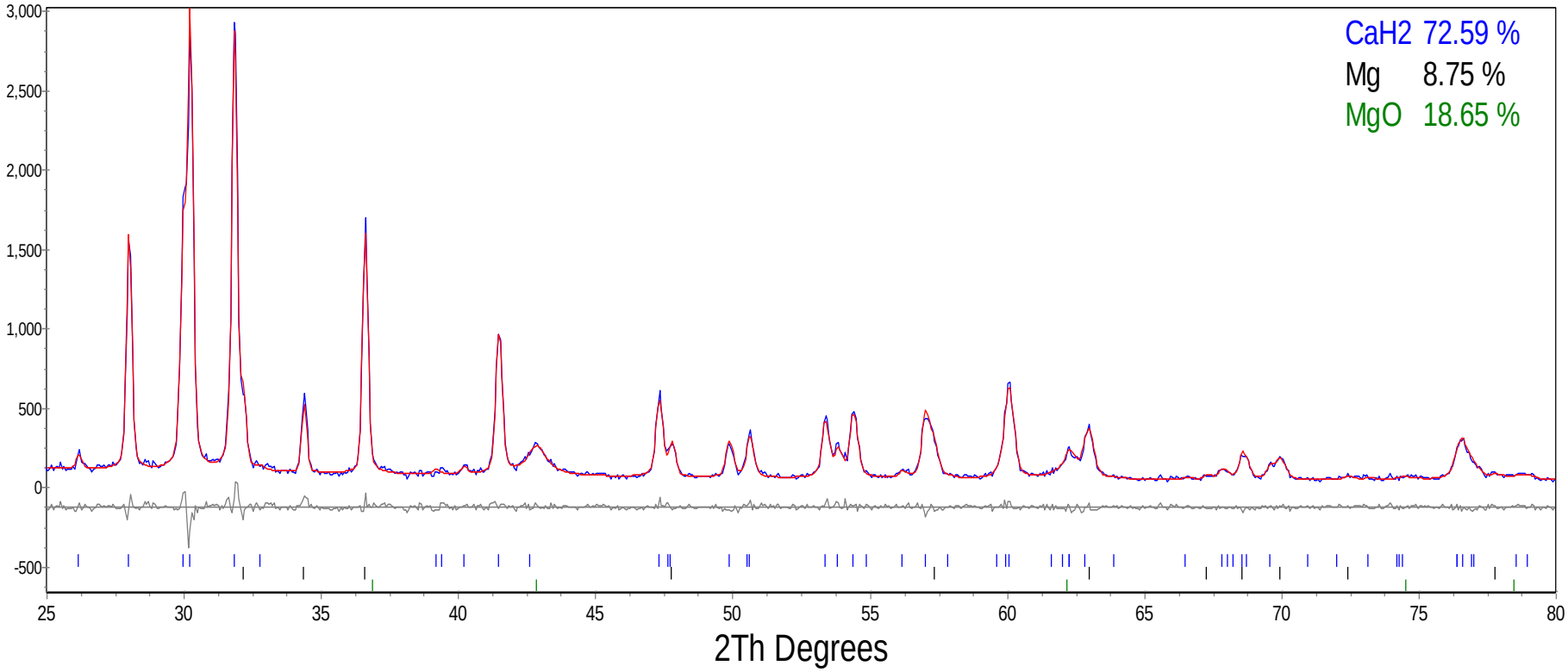

Figure 8.11 Rietveld Refinement of the decomposed 5h milled MgH_2 + CaH_2 (1:1) after heating In-situ to 500 °C. Blue marks represent the CaH_2 phase, Black lines stand for the Mg phase, and Green marks show the MgO phase. Red continued line represents the experimental fitted data from CIF files. Blue continued line is the diffraction pattern obtained from the XRD. Grey line is the difference between the experimental fitted data and the diffraction pattern.

Increasing the temperature to 325 °C the main $Ca_{19}Mg_8H_{54}$ phase starts to decompose and a new phase attributed to the $Ca_4Mg_3H_{14}$ phase is observed along with the main phase. At 350 °C, besides the main phase and $Ca_4Mg_3H_{14}$ phase with increased intensity, another phase starts to develop, this new phase has been matched with CaH_2, demonstrating the further decomposition of calcium magnesium hydride.

In addition to these phases there are some traces of Ca and Mg oxides growing in intensity with the temperature. The same reflections are observed up to 375 °C where the main $Ca_{19}Mg_8H_{54}$ phase disappears and the only evident phases are related to $Ca_4Mg_3H_{14}$, CaO and MgO. On heating to 400 °C, $Ca_4Mg_3H_{14}$ is no longer detected, leading to the conclusion that calcium magnesium hydride has fully decomposed. The remaining CaH_2 phase and Mg and Ca oxides increase their intensity with the temperature until the maximum heating point set at 500 °C.

No peaks of Mg phase were detected during the heating process as would be expected for the decomposition of calcium magnesium hydride; it is assumed that the Mg from the decomposition process was present, however become oxidised due to a leak in the Anton-Paar cell used for the experiment or as a result of impurities in the gas stream, forming an oxide layer on the surface of the sample, consequently precluding the Mg identification by the X-rays.

In order to investigate further this hypothesis, ex-situ measurements were carried out on the decomposed material. Samples were unload inside an argon filled glove box to avoid the contamination of the same, hand mixed with a mortar and pestle to obtain a homogeneous powder and placed in a sealed Kapton dome sample holder for analysis in the XRD.

Figure 8.12 shows the ex-situ reflections of the decomposed $MgH_2 + CaH_2$ with composition (2:1). From this graph, we can confirm our hypothesis as pure Mg reflections are shown in the XRD pattern along with CaH_2 and MgO peaks.

Refinement of the decomposed material after in-situ XRD was performed to determine the amount of each crystalline phase in the sample. Figure 8.13 illustrates the Rietveld refinement of the Ex-situ XRD after decomposition for the 5 hours milled MgH_2 + CaH_2 (2:1).

The refined spectra show that the decomposed sample encloses (67 wt. %) of crystalline CaH_2, (10 wt. %) of crystalline Mg and the remaining (24 wt. %) accounts for MgO.

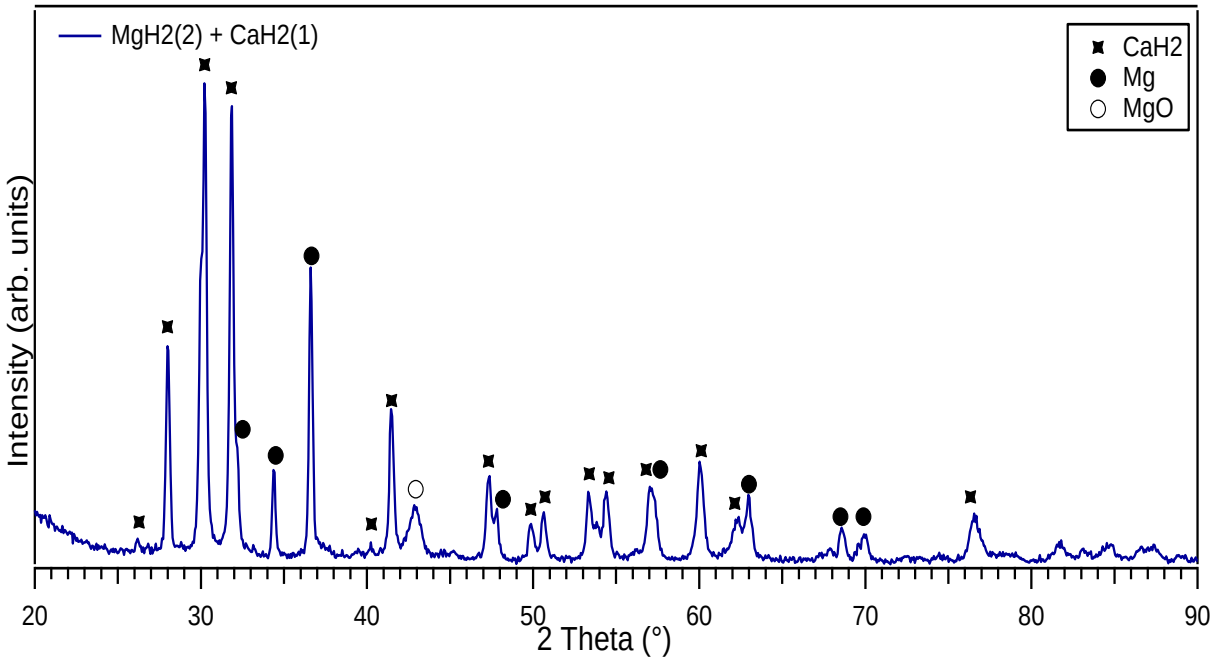

Figure 8.12 Ex-situ XRD of 5 h decomposed MgH_2 + CaH_2 (2:1) after heating to 500 °C

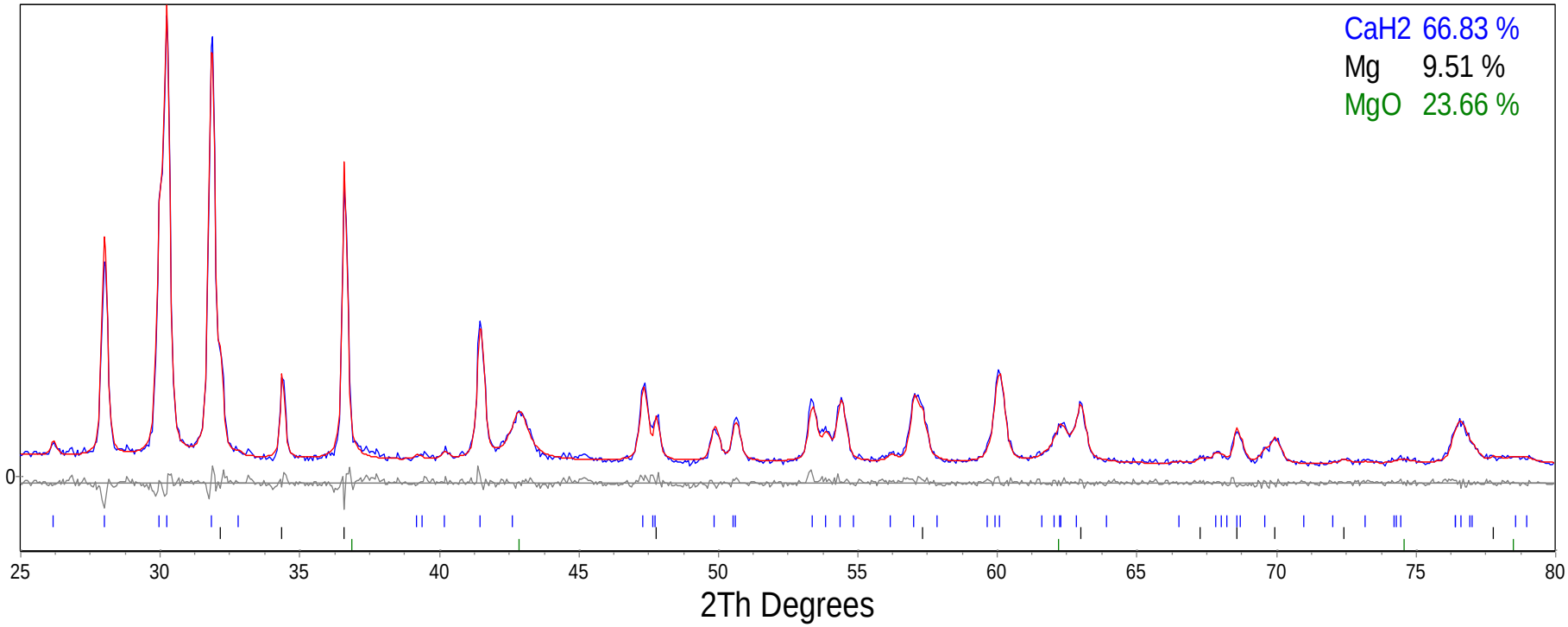

Figure 8.13 Rietveld Refinement of the decomposed 5h milled MgH_2 + CaH_2 (2:1) after heating in-situ to 500 °C. Blue marks represent the CaH_2 phase, Black lines stand for the Mg phase, and Green marks show the MgO phase. Red continued line represents the experimentally fitted data from CIF files. Blue continued line is the diffraction pattern obtained from the XRD. Grey line is the difference between the experimentally fitted data and the diffraction pattern.

8.2.3 Rehydrogenation Ability

To investigate the recycling ability of the decomposed MgH_2 + CaH_2 (1:1) and (2:1), DSC measurements have been employed under 100 ml/min flowing hydrogen at 10 bar pressure. Previously decomposed samples under argon were heated from 30 to 500 °C in a Netzsch HP DSC.

MgH_2 + CaH_2 (1:1)

Figure 8.14 shows the DSC curves for the decomposition of the sample and the second cycle after hydrogenation under 10 bar hydrogen.

From this figure, it is observed that on decomposition there are two endothermic peaks related to the dehydrogenation of the milled material, previously in this Chapter (8.2.2) there is a discussion about these reactions, therefore we are not going to deeply refer to the decomposition of the material, instead this discussion will be focused on the second cycle curves obtained after the second decomposition of the sample that had been rehydrogenated under 10 bar hydrogen. No noticeable reactions are detected below 200 °C. The first curve is observed from 210 °C (T_{onset}) to 373 °C (T_{end}), peaking at around 366 °C. Following this endotherm, there is a wider deflection starting from 373 °C (T_{onset}), and continues up to 413 °C (T_{end}), peaking at around 397 °C. This second decomposition (2^{nd} cycle) process follows the same steps reaction as the first decomposition (1^{st} cycle), although, at different temperatures.

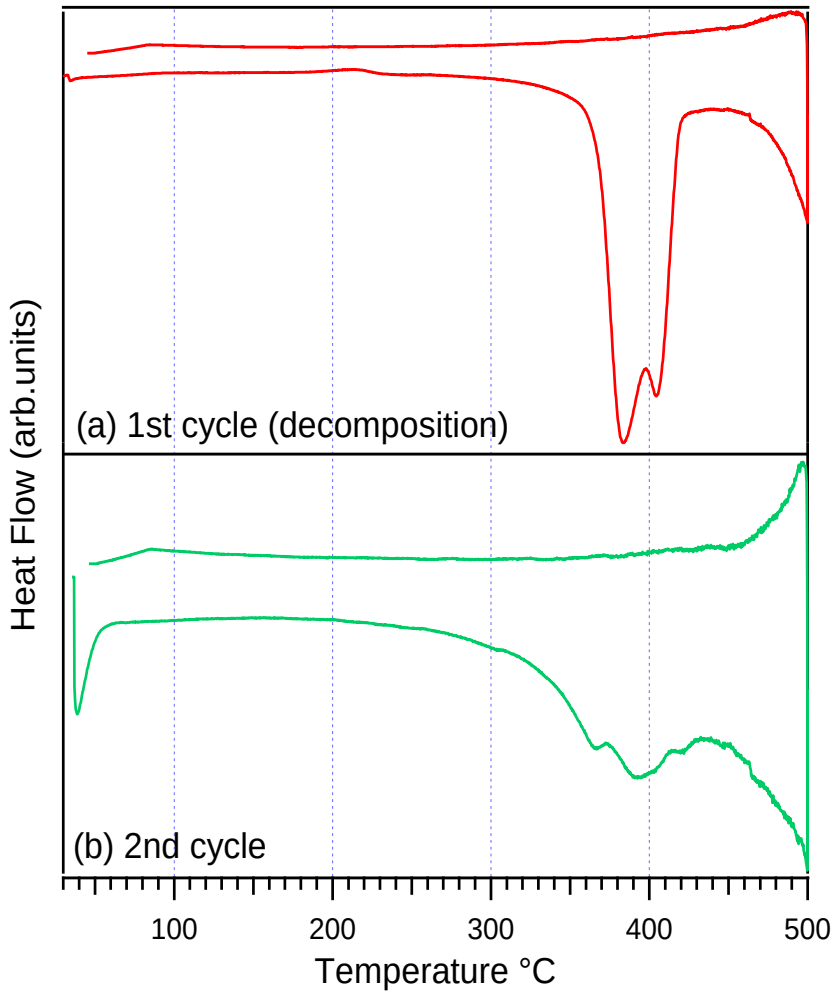

Figure 8.14 DSC of the 5h milled MgH_2 + CaH_2 (1:1) under 100 ml/min flowing argon at 3 bar pressure for both measurements. (a) Red line shows the 1st decomposition traces. (b) Green line shows the second decomposition curves, after rehydrogenation of the first decomposed sample under 10 bar hydrogen.

MgH_2 + CaH_2 (2:1)

Recombination ability of sample with composition (2:1) has been investigated by DSC and is shown in Figure 8.15. From the plot, it is seen that the 1st cycle decomposition follows two-step reactions confirmed by two endothermic curves. Once again, complete discussion about decomposition reactions and temperatures for the first cycle of this specific mixture has been previously discussed in this work (Chapter 8 section 8.2.2); hence, the main focus of this discussion will concentrate on the second (dehydrogenation) cycle.

Second (dehydrogenation) cycle shows two-step decomposition, therefore shows a good agreement with the first (dehydrogenation) cycle, however, at different temperatures. For the first endotherm, it is observed that sample starts to decompose at 210 °C (Tonset), peaking at 367 °C (Tpeak) and is complete at 396 °C (T end). The second endothermic peak starts to decompose at 408 °C, peaking at 415 °C and the reaction is complete at 428 °C. Nevertheless, it has been shown from the DSC measurements that Ca-Mg-H mixtures can be reversibly formed, there is still the need to investigate further the hydrogen release properties of the material after second (decomposition) cycle, and test the behaviour of the samples after several cycles. Unfortunately, due to time restrictions, those measurements cannot be included in this thesis.

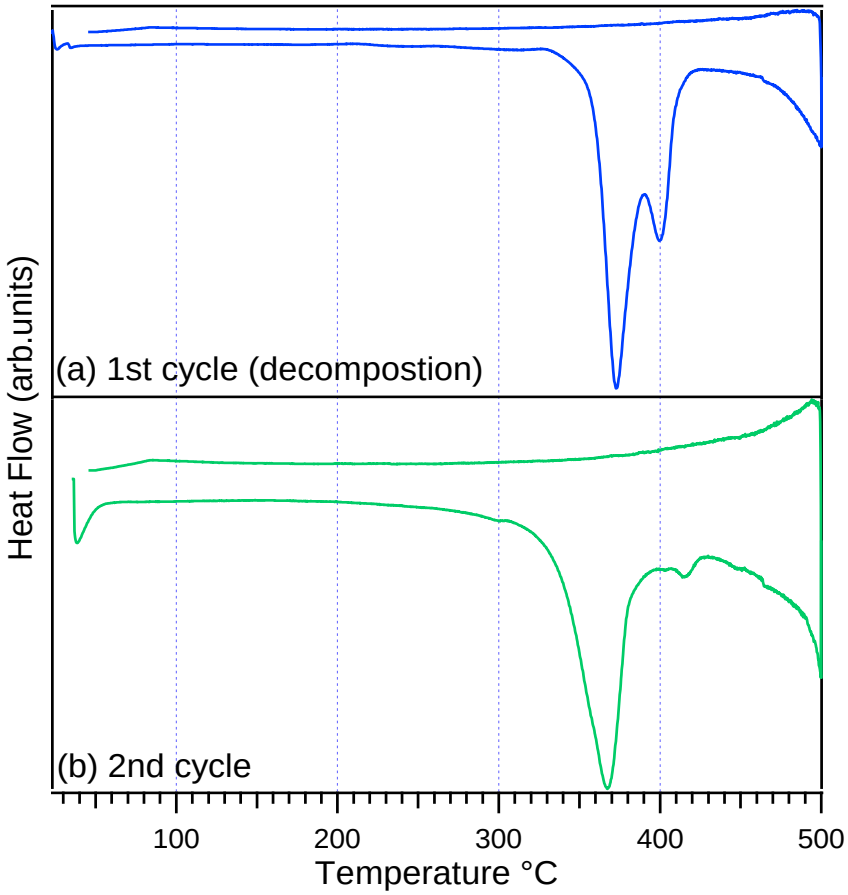

Figure 8.15 DSC of the 5h milled MgH_2 + CaH_2 (2:1) under 100 ml/min flowing argon at 3 bar pressure for both measurements. (a) Blue line shows the 1st decomposition traces. (b) Green line shows the second decomposition curves, after rehydrogenation of the first decomposed sample under 10 bar hydrogen.

8.3 Novel quaternary hydrides ($M_xCa_{1-x}MgH_4$), (M=Li, Na)

This section investigates whether Li or Na hydrides can be incorporated/substituted into the Ca-Mg-H ternary hydride, to form a quaternary mixture by mechanical milling. To the best of our knowledge, such compounds have not yet been investigated. Thus, for the first time ($M_xCa_{1-x}MgH_4$) where (M=Li, Na), will be synthesised.

8.3.1 Quaternary Hydride ($Li_xCa_{1-x}MgH_4$)

The incorporation of Li atoms into the Ca-Mg-H hydride might have a destabilising effect. Previous studies have been reported about Ca-Mg-TM and $CaLi_xAl_{2-x}$ alloys; however no quaternary phases had been observed (Nobuki et al., 2007) (Zhang and Zhao, 2007, Nesper and Miller, 1993). Other studies reported alloys such as Li-Mg-Ca_x (x=0.15 wt.%), but hydrogenation of the same was not described(Song and Kral, 2005). Moreover, $CaLi_{2-x}Mg_x$ ($0<x<2$) alloys have been studied within the last few years, although there were no reports about the formation of ternary or quaternary hydride phases (Asano et al., 2009). Therefore, in this work, an attempt to synthesise for the first time, quaternary hydrides incorporating lightweight metals; such as Li, to the ternary hydrides compromising (Ca-Mg-H) previously described in this Chapter (8.1), would be investigated.

8.3.1.1 Structural characterisation of as milled material

Powders of CaH_2 (95%; Sigma-Aldrich), MgH_2 (95% pure hydride phase and remainder 5% Mg; Sigma-Aldrich) and LiH (99.9% pure; Sigma-Aldrich Inc.) were ball milled for 5, 10 and 15 hours in an attempt to synthesise (Li-Ca-Mg-H) quaternary hydride. LiH was substituted into the sample following $Li_xCa_{1-x}MgH_4$ composition, where x= (0.2) molar ratio.

Characterisation of the as-milled products was performed by ex-situ X-ray diffraction (XRD) to investigate the phases present in the samples. Additionally, to examine the compositional changes upon heating, and to determine the re-hydrogenation ability of the decomposed samples In-situ XRD measurements were taken. Moreover, to study the reactions and evolution of gases upon temperature changes DSC and TGA measurements were performed. Ex-situ XRD patterns of the as-milled materials for 5, 10 and 15 hours are presented in Figure 8.16.

For the 5 hours milled $Li_{0.2}Ca_{0.8}MgH_4$, it can be observed the reflections of the $Ca_{19}Mg_8H_{54}$, with the most intense peak detected at 31.17 (2θ°) and reflections of $Ca_4Mg_3H_{14}$ phase are also detected. In addition, some traces of MgO are observed, probably formed during the milling process. After 10 hours milling, the intensity of the $Ca_{19}Mg_8H_{54}$ main phase increases and more sharp peaks are noticed, $Ca_4Mg_3H_{14}$ phase is no longer detected and MgO peaks become more intense. At 15 hours milling, the intensity of the main phase increases even further and sharper peaks linked with the $Ca_{19}Mg_8H_{54}$ are observed. The lattice parameters of the main phase were refined with the help of TOPAS software; Table 8.3 shows the Rietveld refinement of the 5, 10, and 15 hours milled samples.

Table 8.3 Lattice parameters and cell volume for the 5, 10 and 15 hours milled $Li_{0.2}Ca_{0.8}MgH_4$

	$Ca_{19}Mg_8H_{54}$	Lattice parameters (a)	Cell volume (A^3)
Milling Time	**5**	12.17±0.02	1800.99±0.10
	10	12.16±0.04	1801.07±0.12
	15	12.15±0.03	1797.50±0.09

It is observed that the lattice parameters present a rather small change in the structure for the different milling times. However, the cell volume of the samples decreases as the milling increases.

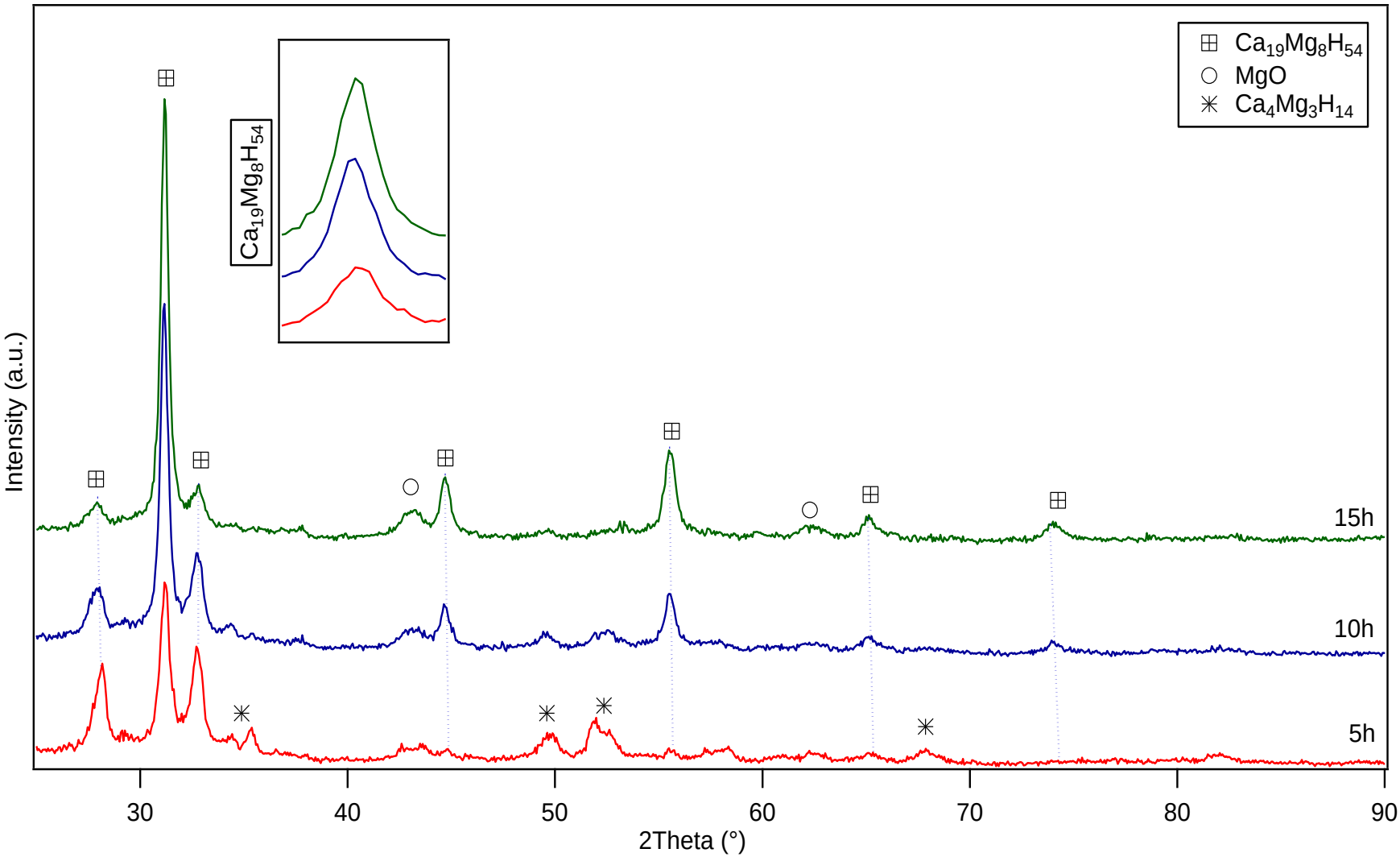

Figure 8.16 Ex-situ XRD for the 5, 10 and 15 h ball milled $Li_{0.2}Ca_{0.8}MgH_4$.

8.3.1.2 Thermal decomposition

Thermal analysis was performed in order to examine the temperature reactions and hydrogen release properties of the quaternary hydride $Li_{0.2}Ca_{0.8}MgH_4$ milled for 5, 10 and 15 hours in an argon atmosphere. DSC measurements were taken from 30 °C to 500 °C in a 100 ml/min constant flowing Ar atmosphere under 3 bar pressure, to avoid air-water contamination all samples were prepared, loaded and run inside an Argon filled glove box < 5 % ppm oxygen. The DSC (a), TGA (b), MS (c) traces for the $Li_{0.2}Ca_{0.8}MgH_4$ samples milled for 5, 10 and 15 h are presented in Figure 8.17. The dehydrogenation of $Li_{0.2}Ca_{0.8}MgH_4$ (5 h) starts at around 325 °C and reaches a maximum peak at 356 °C up to 400 °C, the total release of H_2 accounts for 2.76 wt. % measured up to 500 °C, 1.47 wt.% corresponds to the first release from 325 to 365 °C and 1.29 wt. % is attributed to the second release between 365-400 °C.

With increasing milling time to 10 hours, desorption temperature is slightly decreased from 325 to 321 °C, with a maximum peak observed at 353 °C up to 382 °C. A total amount of 2.56 wt.% of hydrogen is released in one single-step suggesting faster sorption kinetics.

Sample milled for 15 hours exhibits two-stage desorption; the first peaking at 348 °C with a release of (0.54 wt. %) hydrogen. Whereas, the second desorption peak at 359 °C, leads to a 1.86 wt. % mass loss. A total amount of 2.40 wt.% hydrogen is released up to 500 °C.

The 10 h milled $Li_{0.2}Ca_{0.8}MgH_4$ shows the lowest decomposition temperature at 336 °C, while the 5 h milled sample releases the maximum amount of hydrogen (2.76 wt. %) up to 500 °C.

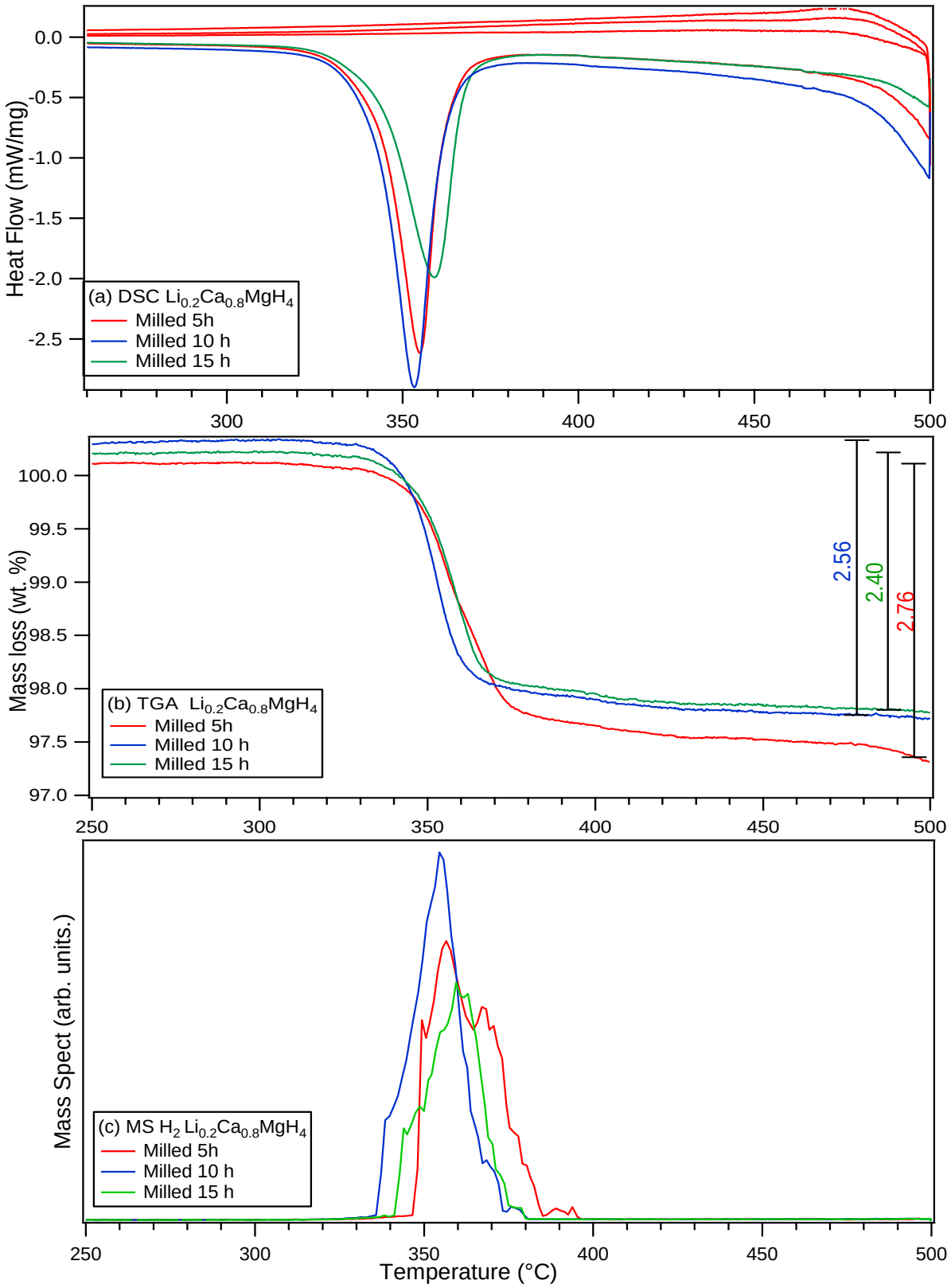

Figure 8.17 DSC-TGA-MS traces of the 5, 10 and 15 hours milled $Li_{0.2}Ca_{0.8}MgH_4$ samples. Measurements were performed at a heating rate of 2 °C/min under 3 bar argon at 100 ml/min (DSC), and 1 bar argon at 40 ml/min (TGA/MS)

8.3.1.3 In-situ XRD

The decomposition products of 5, 10 and 15 h milled $Li_{0.2}Ca_{0.8}MgH_4$, were investigated by In-situ XRD, where samples were heated from 30 to 500 °C at 2 °C/min in He flowing at 100 ml/min.

For the 5 hours milled $Li_{0.2}Ca_{0.8}MgH_4$ (Figure 8.18), reflections of $Ca_4Mg_3H_{14}$ are detected from 30 °C up to 400 °C when they are no longer observed. At 325 °C, small diffractions attributed to the CaH_2 phase are detected and are seen on heating up to 500 °C with increased intensity proportional to the temperature, additionally small traces of MgH_2 phase are observed and decrease in intensity up to 400 °C when they are no longer detected.

The evolution of these peaks indicates the decomposition of the main $Ca_4Mg_3H_{14}$ phase releasing hydrogen, showing good agreement with TGA and DSC results previously described in this chapter.

On heating to 400 °C, only a small fraction of the $Ca_4Mg_3H_{14}$ phase is detected leading to the conclusion that this phase has practically decomposed, besides, more intense diffractions of CaH_2, in addition, a new phase (Mg) shows up and is attributed to the decomposition of the MgH_2. Furthermore, intense oxide peaks (Mg and Ca) are observed at this temperature and can be attributed to a leak in the system.

On further heating from 425 to 500 °C $Ca_4Mg_3H_{14}$ peaks are no longer observed, and the only remaining phases correspond to CaH_2 and Mg, in addition to (Mg and Ca) oxide peaks, agreeing with the previously formulated statement.

These outcomes agree well with the decomposition process suggested by Bertheville and Reardon (Bertheville and Yvon, 1999, Reardon et al., 2013) for the $Ca_{19}Mg_8H_{54}$ phase.

However, in this special case, the main phase formed after 5 hours milling corresponds to the $Ca_4Mg_3H_{14}$ ternary hydride, not to the $Ca_{19}Mg_8H_{54}$ as suggested in the literature. This effect can be attributed to the Li – Ca substitution into the milled sample.

Figure 8.19 shows the surface plot of the 5h milled $Li_{0.2}Ca_{0.8}MgH_4$, illustrating the phase changes during heating and the desorption reactions temperatures.

For the 10 h milled $Li_{0.2}Ca_{0.8}MgH_4$ (Figure 8.19) illustrates the In-situ X-ray diffraction patterns related to the $Ca_{19}Mg_8H_{54}$ arise as the main phase in the sample and are detected from 30 to 300 °C when diffractions are no longer observed. In addition, reflections of $Ca_4Mg_3H_{14}$, and MgO are detected at this temperature, the last is probably formed during the milling process. On heating to 325 °C, $Ca_4Mg_3H_{14}$ is detected and decreases in intensity with the temperature up to 450 °C when reflection disappears.

Intense (Mg and Ca) oxide peaks are also observed, it is believed they are formed on heating due to a system leak. At 375 °C, the diffractions linked to CaH_2 phase are observed and they become more intense on each heating, this effect demonstrates that the Ca-Mg-H phases decompose into CaH_2 and Mg. However, the last does not appear as a visible reflection during the refinement. It is assumed that the Mg reflections due to the decomposition of the ternary phase become oxidised and therefore are present in the sample as MgO. On further heating, up to 500 °C, only reflections of CaH_2, and oxides (Mg and Ca) are detected.

Surface plot of the in-situ XRD for 10 h milled $Li_{0.2}Ca_{0.8}MgH_4$ is illustrated in Figure 8.20, decomposition reactions showing the phase changes and desorption temperatures are described in function of the intensity vs 2 theta degrees.

Figure 8.21 shows the In-situ XRD of the 15h milled $Li_{0.2}Ca_{0.8}MgH_4$. On heating from 30 to 275 °C, the diffractions of $Ca_{19}Mg_8H_{54}$ shows as the main phase, in addition to MgO patterns

probably formed during the milling process. The intensity of $Ca_{19}Mg_8H_{54}$ phase in this range of temperature decreases as the heating increases. At 300 °C new phases form consistent with the ternary $Ca_4Mg_3H_{14}$ and CaH_2.

There are no evident traces of the $Ca_{19}Mg_8H_{54}$ phase, which means it decomposed leading to the formation of new phases previously described. From 300 to 475 °C, phases consistent with $Ca_4Mg_3H_{14}$ are observed with decreased intensity on heating. Furthermore, phases associated to CaH_2 become more intense on hating and these reflections are present up to 500 °C. In addition, between 300 and 500 °C, intense oxide (Mg and Ca) peaks are detected; it is assumed the formation of these oxides is related to a small leak in the equipment used to take the in-situ measurements. The only phases observed upon heating to 500 °C correspond to CaH_2 and (Ca and Mg) oxides. No traces of the crystalline Mg are detected as it would be expected from the decomposition reactions. However, due to the intense MgO diffractions; it is assumed that Mg is present in the sample, but become oxidised.

Figure 8.22 shows the surface plot of the 15 h milled $Li_{0.2}Ca_{0.8}MgH_4$ illustrating the decomposition reactions and temperatures of the hydride on heating.

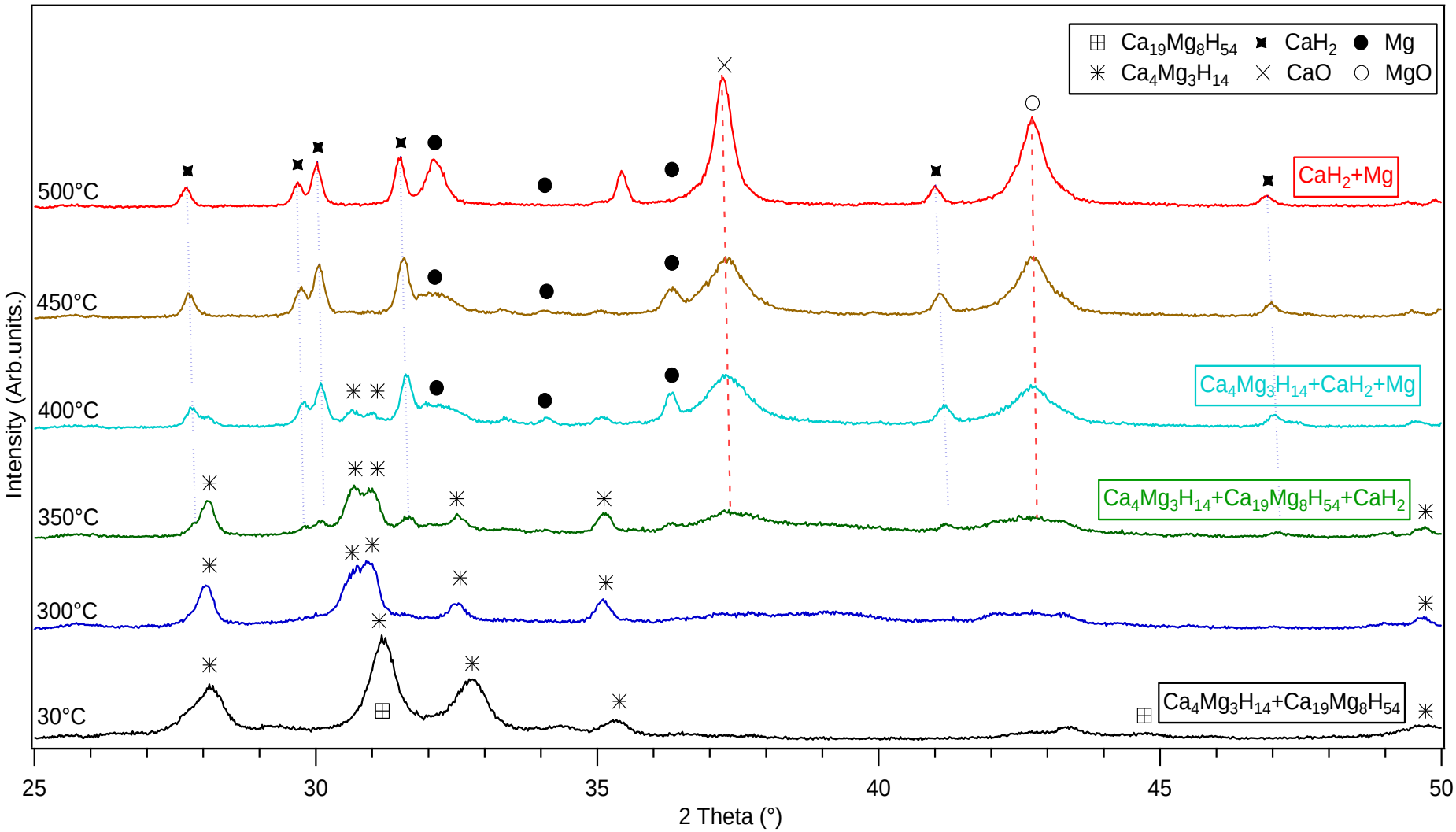

Figure 8.18 In-situ XRD patterns of 5 h milled $Li_{0.2}Ca_{0.8}MgH_4$, heated under He (100 ml/min, ~3 bar) between 30 – 500 °C.

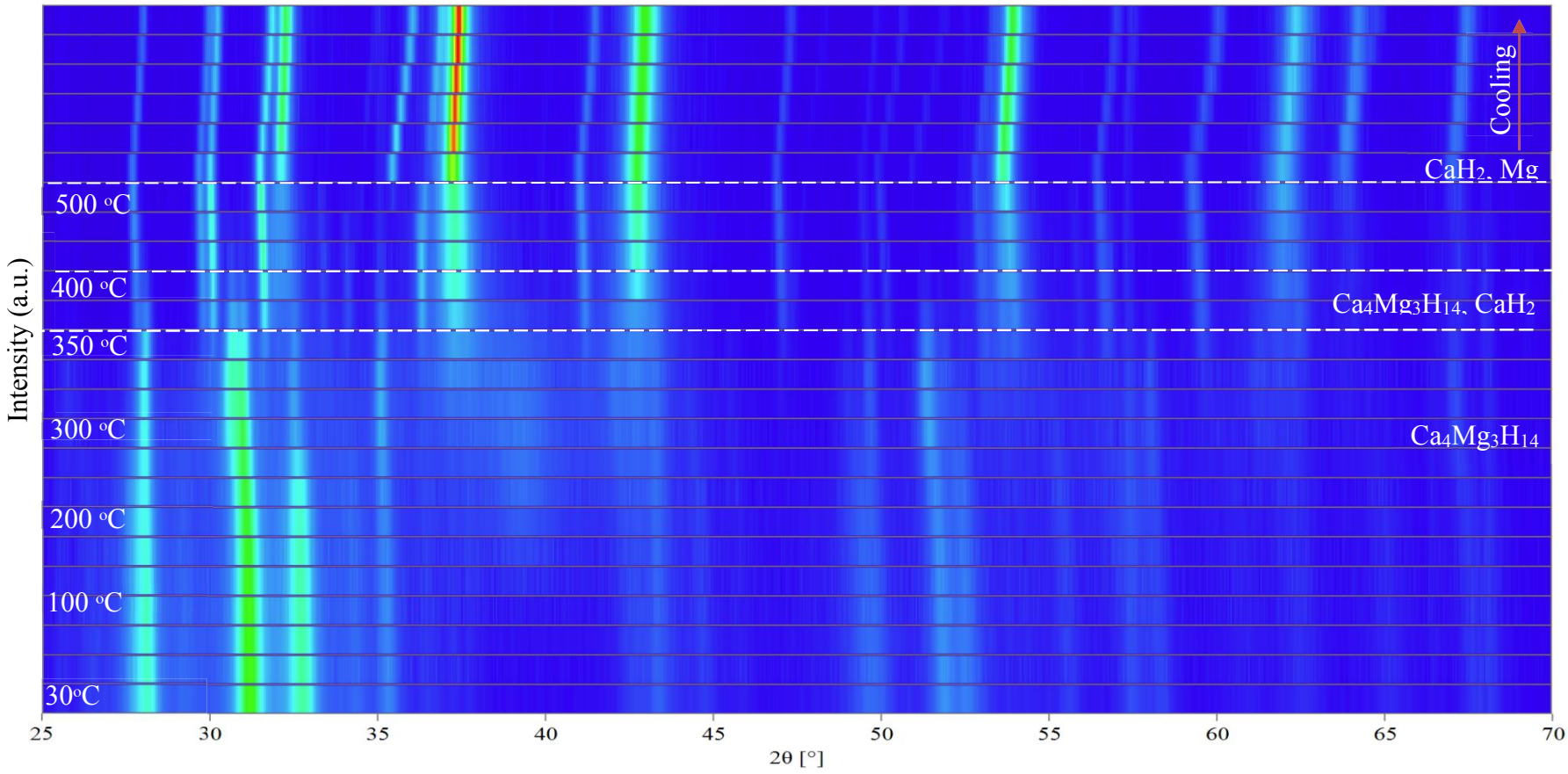

Figure 8.20 Surface plot from in-situ XRD patterns of 5 h milled $Li_{0.2}Ca_{0.8}MgH_4$, heated under He (100 ml/min, ~3 bar) between 30 – 500 °C. A brighter colour corresponds to a higher diffraction intensity. The white dashed lines show the phase transition temperature and are given as a guide for the eye.

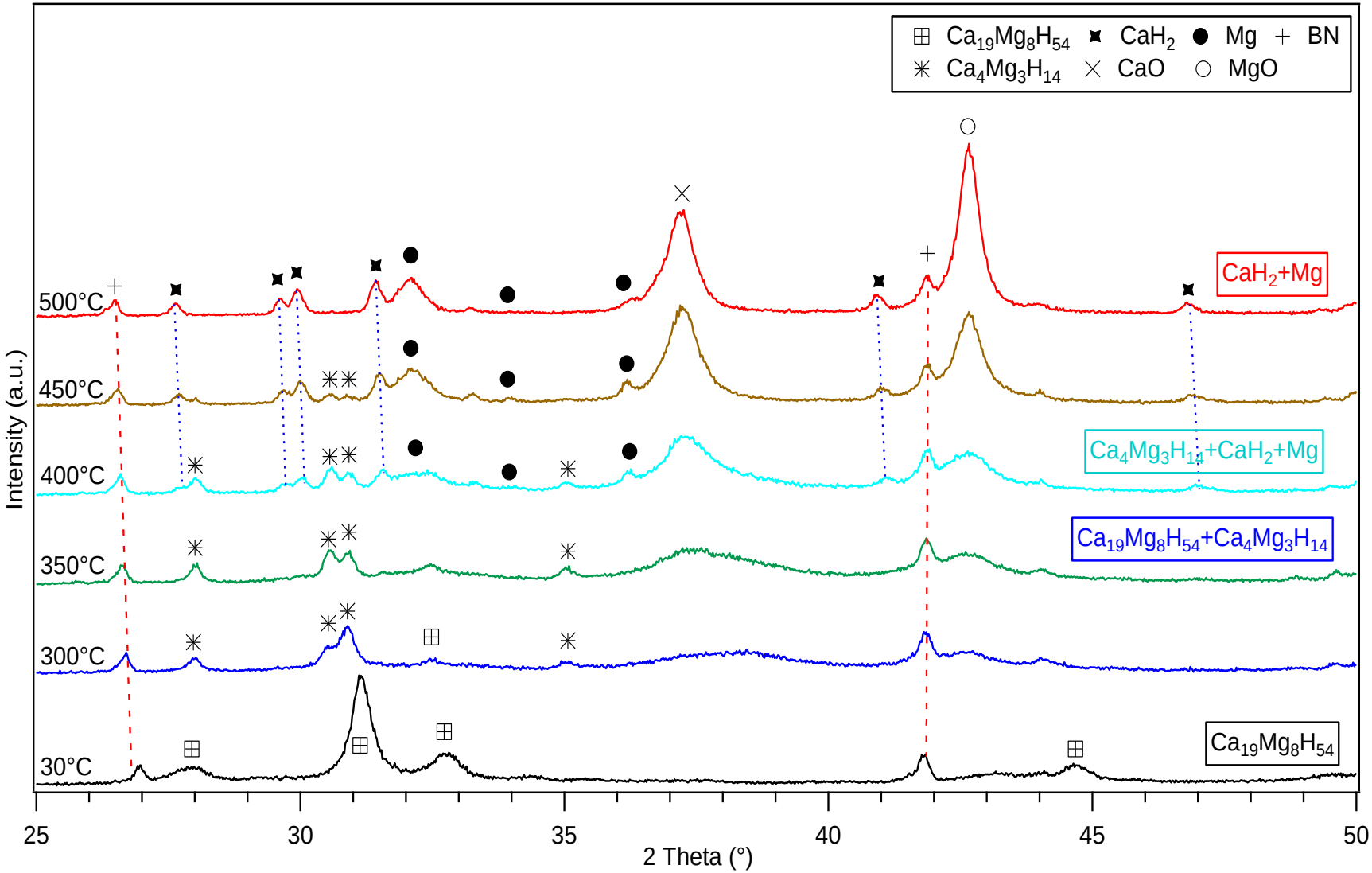

Figure 8.21 In-situ XRD patterns of 10 h milled $Li_{0.2}Ca_{0.8}MgH_4$, heated under He (100 ml/min, ~3 bar) from 30 to 500 °C.

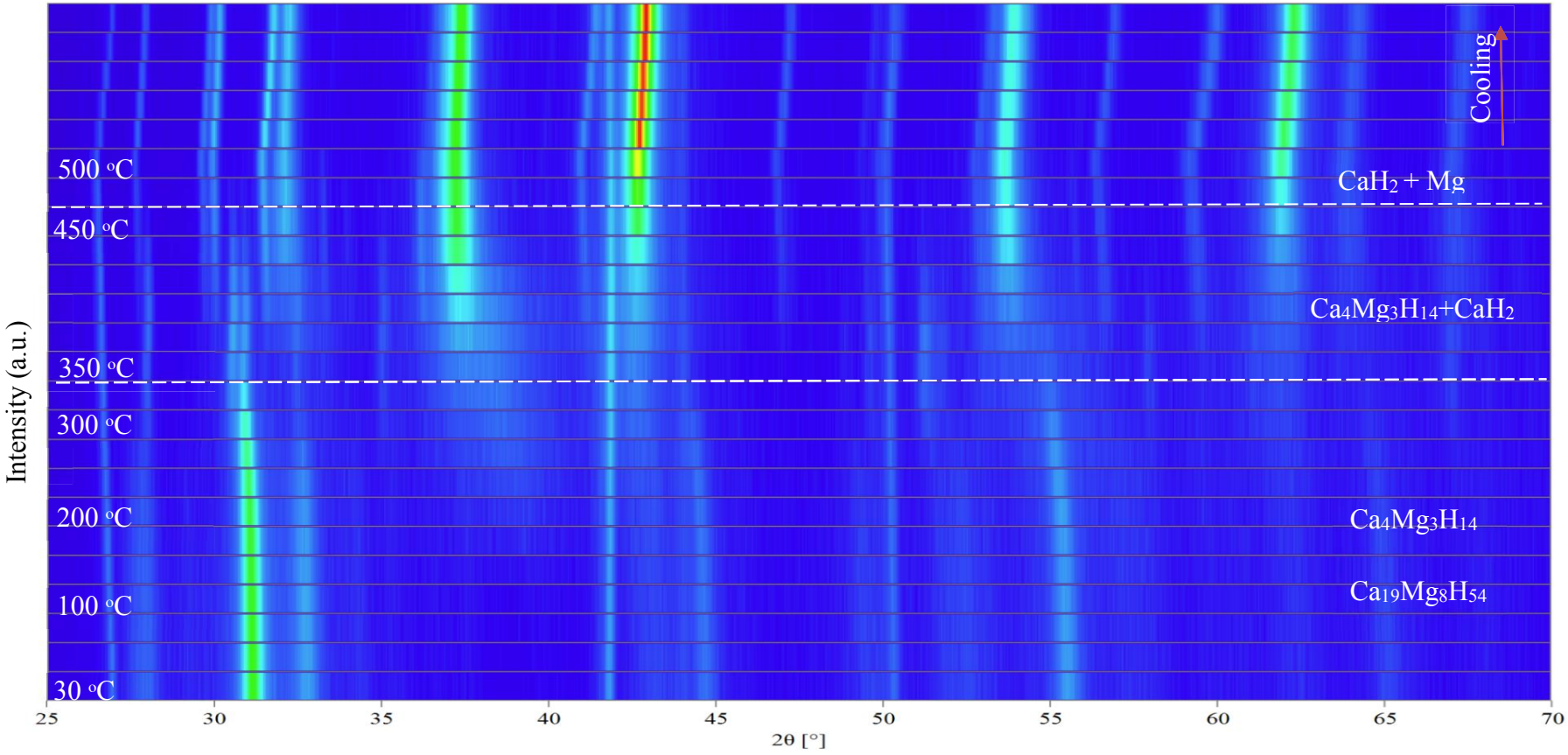

Figure 8.22 Surface plot from in-situ XRD patterns of 10 h milled $Li_{0.2}Ca_{0.8}MgH_4$, heated under He (100 ml/min, ~3 bar) from 30 to 500 °C. A brighter colour corresponds to a higher diffraction intensity. The white dashed lines show the phase transition temperature and are given as a guide for the eye.

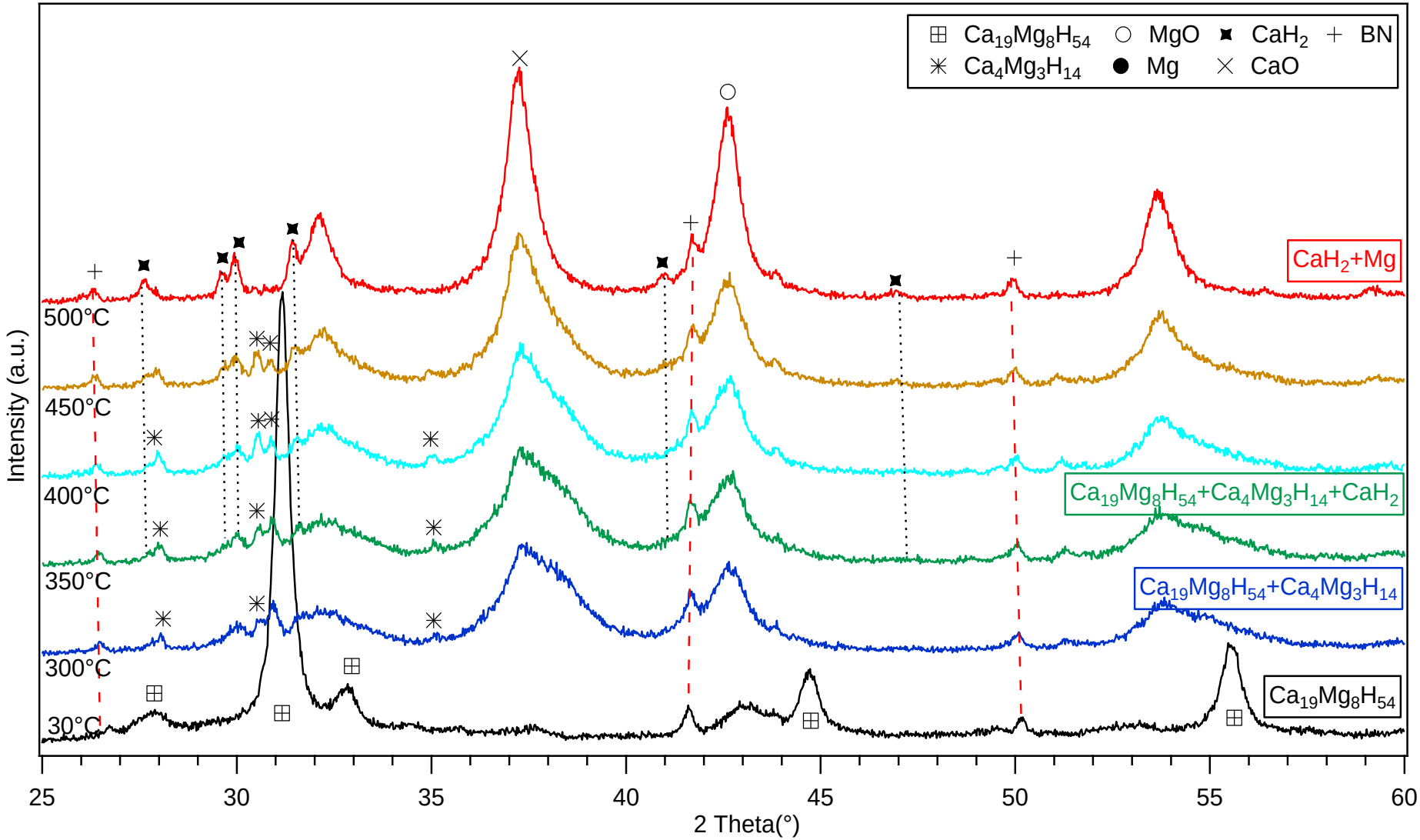

Figure 8.23 In-situ XRD patterns of 15 h milled $Li_{0.2}Ca_{0.8}MgH_4$, heated under He (100 ml/min, ~3 bar) from 30 to 500 °C

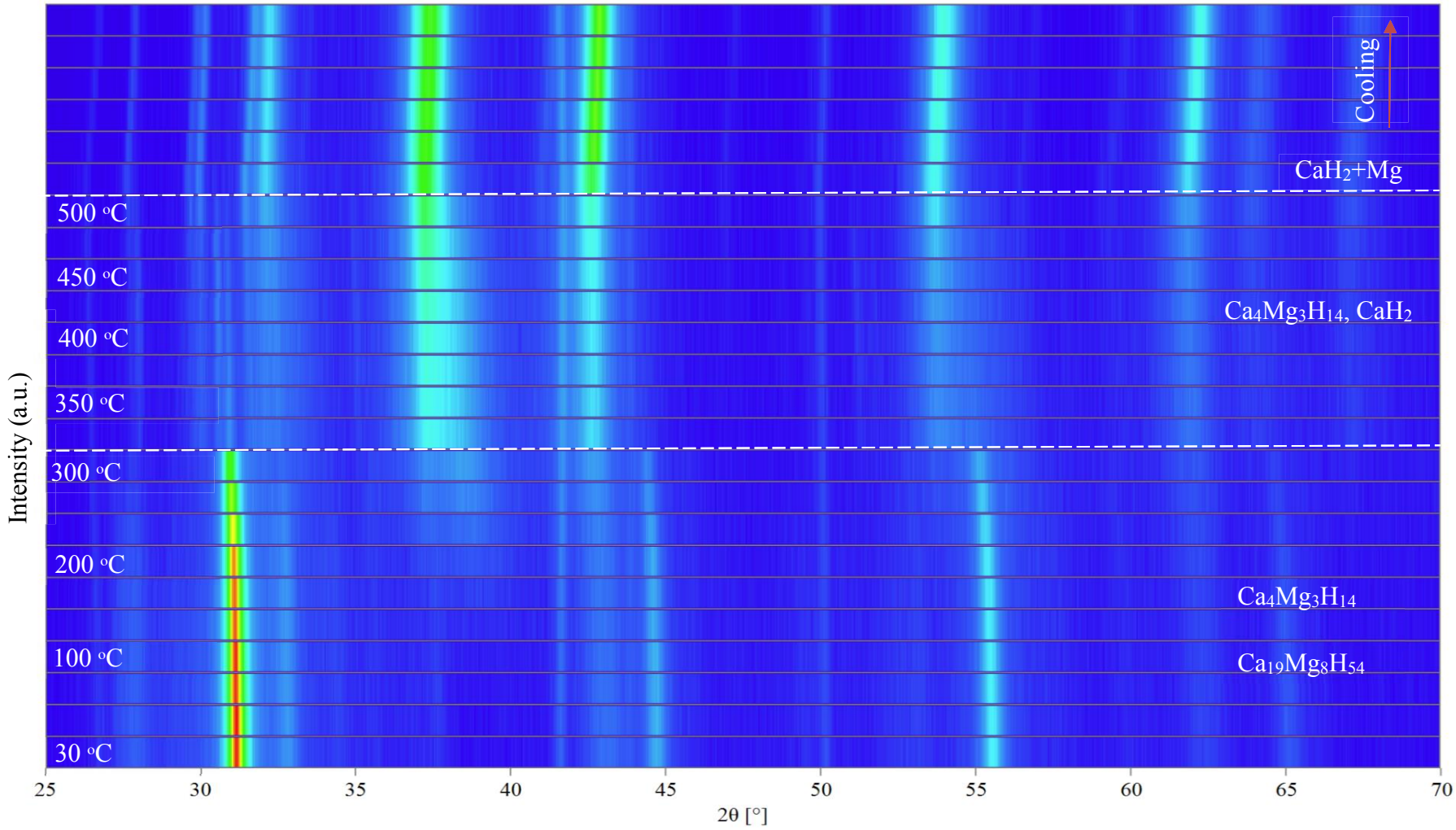

Figure 8.24 Surface plot from in-situ XRD patterns of 15 h milled $Li_{0.2}Ca_{0.8}MgH_4$, heated under He (100 ml/min, ~3 bar) from 30 to 500 °C. A brighter colour corresponds to a higher diffraction intensity. The white dashed lines show the phase transition temperature and are given as a guide for the eye.

8.3.2 Quaternary Hydride ($Na_xCa_{1-x}MgH_4$)

Na substitution into the Ca-Mg-H ternary hydride might have a destabilising effect, due to the smaller ionic size of the Na^+. To the best of our knowledge, there were not previous studies; neither theoretical calculations (DFT) nor experimental investigations, reported in the literature comprising Na-Mg-Ca-H hydrides. However, quaternary hydrides such as and $Na_2Mg_2RuH_8$ were synthesised by Humphries et al.(Humphries et al., 2015a, Humphries et al., 2015b) revealing that the incorporation of transition metals allow the thermodynamic destabilisation or hydrogen storage capacities of the hydrides. Moreover, quaternary hydrides comprising MMg_2FeH_8 (M^{2+} $2Mg^{2+}$ $2H^-$ $[TH_6]^{4-}$) (M = Ba, Ca, Sr; T = Fe, Ru, Os) (Huang et al., 1995a, Huang et al., 1997, Huang et al., 1992a) and $M_4Mg_4Fe_3H_{22}$ ($4Ca^{2+}$ $4Mg^{2+}$ $4H^-$ $3[FeH_6]^{4-}$) (M = Ca, Yb)(Huang et al., 1992a, Huang et al., 1993) have been explored, although, thermodynamic information for these mixtures are limited, some experimental and DFT values have been determined although some experimental(Huang et al., 1995b, Parker et al., 1997, Huang et al., 1992a) and DFT calculated(Takagi et al., 2014) values have been determined i.e. $Ca_4Mg_4Fe_3H_{22}$ decompose at 420 °C(Huang et al., 1992a, Huang et al., 1992b). Nevertheless, the dehydrogenation temperatures offered by these compounds remain high and there is a need to find different ways to destabilise the ternary Ca-Mg-H hydride to meet the criteria for potential hydrogen storage materials. Therefore, in this section, an attempt to synthesise for the first-time quaternary hydrides incorporating lightweight metals; such as Na, to the ternary (Ca-Mg-H) hydrides will be investigated.

8.3.2.1 Structural characterisation of as milled material

Powders of CaH_2 (95%; Sigma-Aldrich), MgH_2 (95% pure hydride phase and remainder 5% Mg; Sigma-Aldrich) and NaH (95% pure; Sigma-Aldrich Inc.) were ball milled for 5, 10 and

15 hours in an attempt to synthesise (Na-Ca-Mg-H) quaternary hydride. Na was substituted into the sample following $Na_xCa_{1-x}MgH_4$ composition, where x= (0.2) nominal composition. Characterisation of the as-milled products was performed by ex-situ X-ray diffraction (XRD) to investigate the phases present in the samples. Additionally, to determine the compositional changes upon heating, and to describe the re-hydrogenation properties of the decomposed samples in-situ XRD measurements were performed. Moreover, to study the decomposition reactions and evolution of gases upon temperature changes DSC and TGA-MS measurements were executed.

Ex-situ XRD diffractions of the as-milled materials for 5, 10 and 15 hours are shown in Figure 8.25. When ball milling the $Na_{0.2}Ca_{0.8}MgH_4$ for 5 hours, reflections of the $Ca_{19}Mg_8H_{54}$ ternary phase were detected with the most intense peak at 31.17 (2θ°), in addition, reflections of $NaMgH_3$ phase were observed along with small traces of MgO. After 10 hours milling, the intensity of the $Ca_{19}Mg_8H_{54}$ and $NaMgH_3$ phase's decrease and broader peaks were noticed. On further milling, to 15 h intensity of the phases decreases even further and peaks become broader.

Reflections of MgO are more intense; this effect might be due to impurities in the milling process, as with increasing the milling time, oxide peaks become more prominent. Table 8.4 shows the refined XRD data for 5, 10, 15 h ball milled $Na_xCa_{1-x}MgH_4$, where x= (0.2) nominal composition.

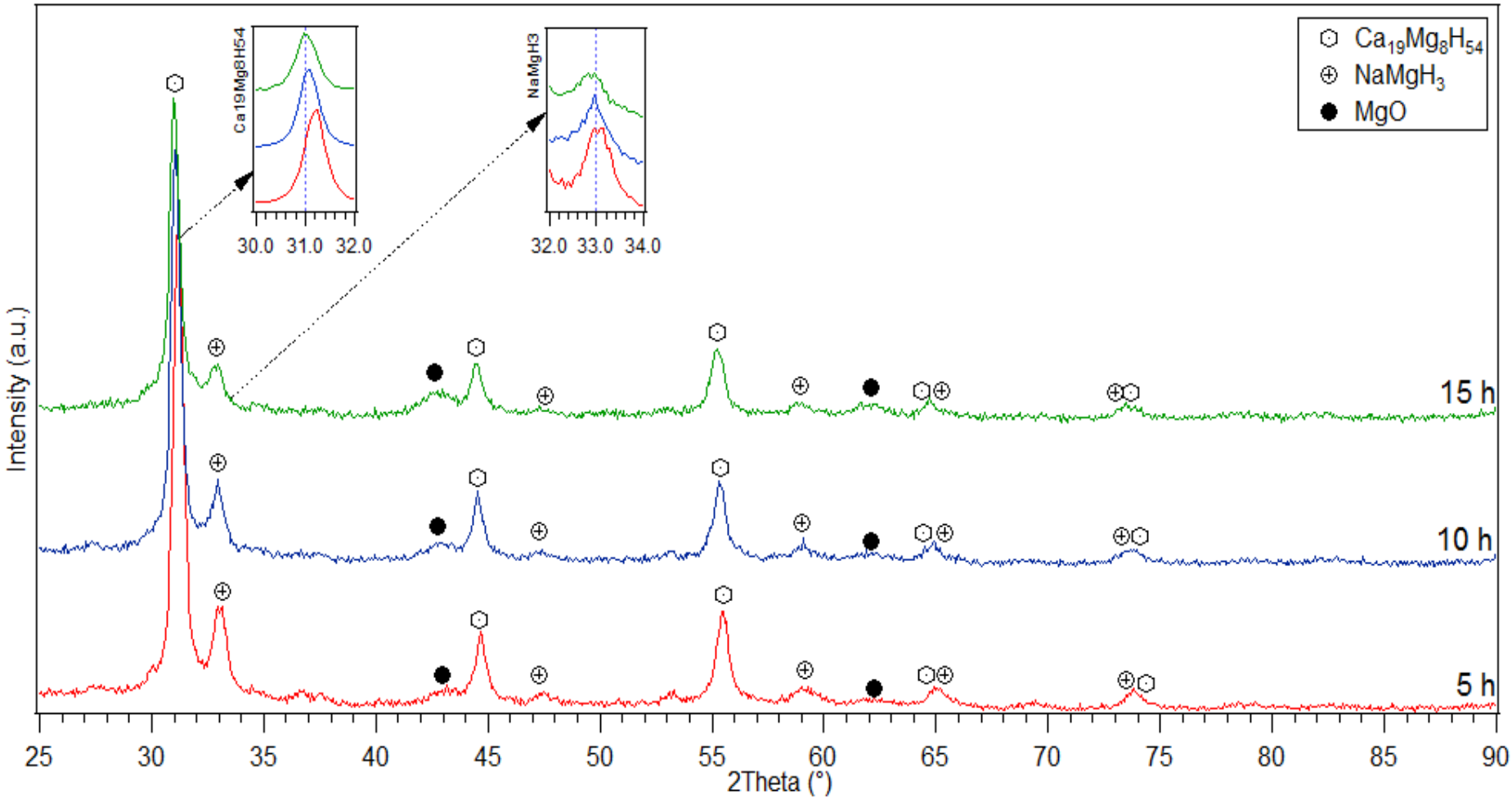

Figure 8.25 Ex-Situ XRD for the 5, 10 and 15 h ball milled $Na_{0.2}Ca_{0.8}MgH_4$ hydride. $Ca_{19}Mg_8H_{54}$ and $NaMgH_3$ main peak diffractions are detailed in the inset upright plots.

Table 8.4 Lattice parameters and cell volumes for the 5, 10 and 15 hours milled $Na_{0.2}Ca_{0.8}MgH_4$

		Lattice parameters a (Å)			Cell Volume (Å^3)
$Ca_{19}Mg_8H_{54}$ (cubic)					
	5	12.17±0.01			1802.17±0.77
	10	12.20±0.01			1815.37±0.81
	15	12.22±0.02			1823.74±0.93
$NaMgH_3$ (Orthorhombic)		**a (Å)**	**b (Å)**	**c (Å)**	
	5	5.42±0.11	7.67±0.12	5.42±0.08	225.07±6.62
	10	5.43±0.19	7.68±0.23	5.43±0.17	226.26±12.81
	15	5.44±0.29	7.69±0.52	5.44±0.26	227.79±22.56

At room temperature for the 5 h milled $Na_{0.2}Ca_{0.8}MgH_4$, (Figure 8.26) reflections of cubic $Ca_{19}Mg_8H_{54}$ (67 wt. %), orthorhombic $NaMgH_3$ (24 wt. %) and cubic MgO (9 wt. %) were identified.

After 10 h milling (Figure 8.27), same structures were observed and quantified as: cubic $Ca_{19}Mg_8H_{54}$ (65 wt. %), orthorhombic $NaMgH_3$ (20 wt. %) and cubic MgO (15 wt. %).

When further milling for 15 h (Figure 8.28), cubic $Ca_{19}Mg_8H_{54}$ (59 wt. %), orthorhombic $NaMgH_3$ (17 wt. %) and cubic MgO (24 wt. %). It is observed from the refinement that unit cell parameters from $Ca_{19}Mg_8H_{54}$ and $NaMgH_3$ increase with the milling time. Moreover, the cell volumes follow the same increase pattern.

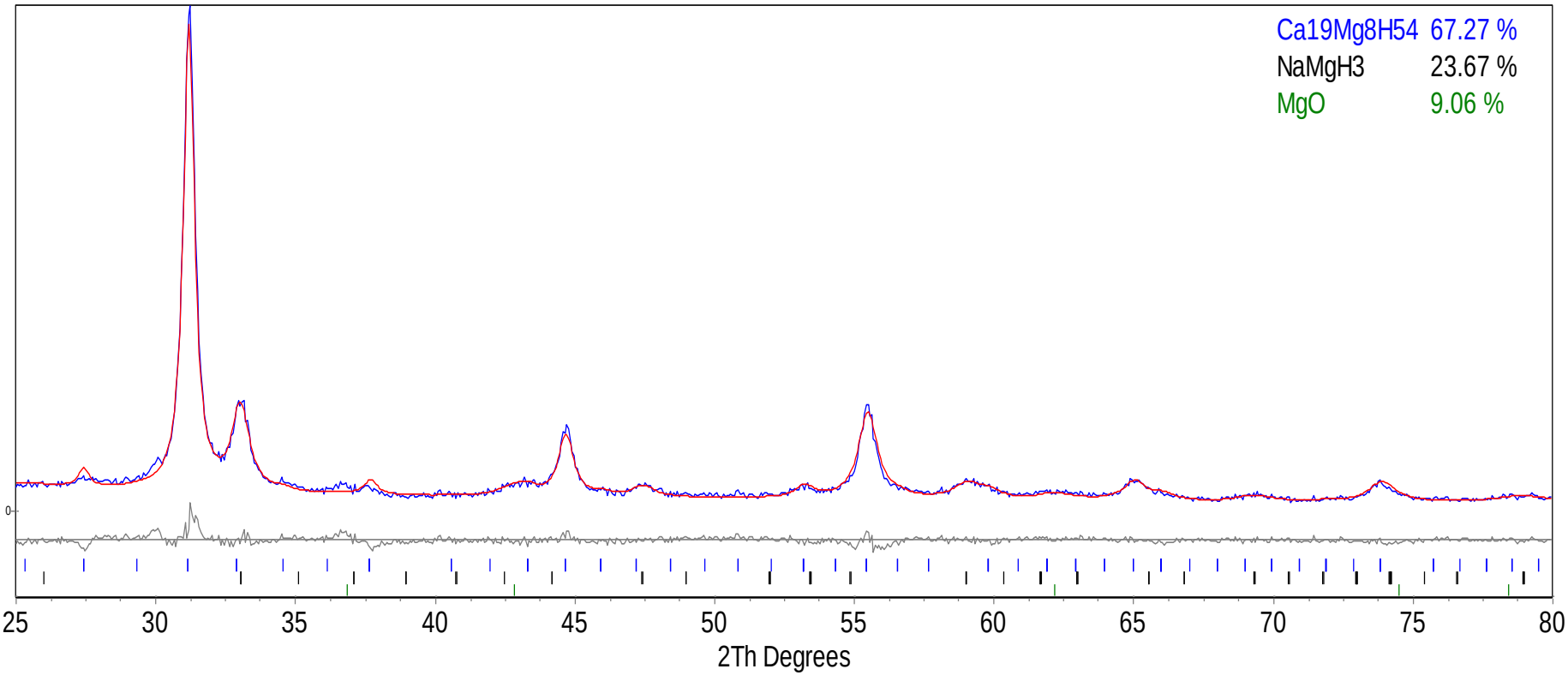

Figure 8.26 Rietveld refinement profile of XRD data for the 5 h milled $Na_{0.2}Ca_{0.8}MgH_4$, showing the observed data (black line), the calculated fitting to the data (red line) and the difference (grey line). Goodness of fit=1.366

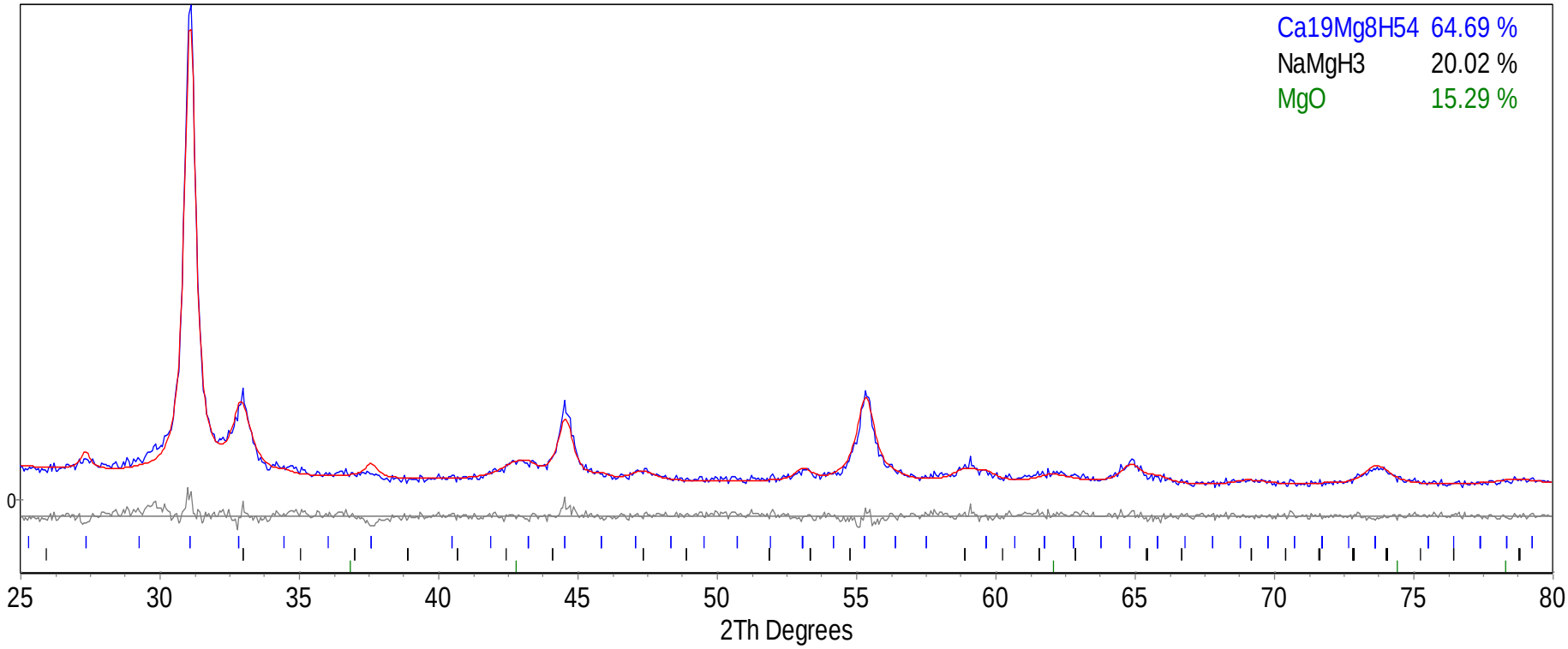

Figure 8.27 Rietveld refinement profile of XRD data for the 10 h milled $Na_{0.2}Ca_{0.8}MgH_4$, showing the observed data (black line), the calculated fitting to the data (red line) and the difference (grey line). Goodness of fit=1.287

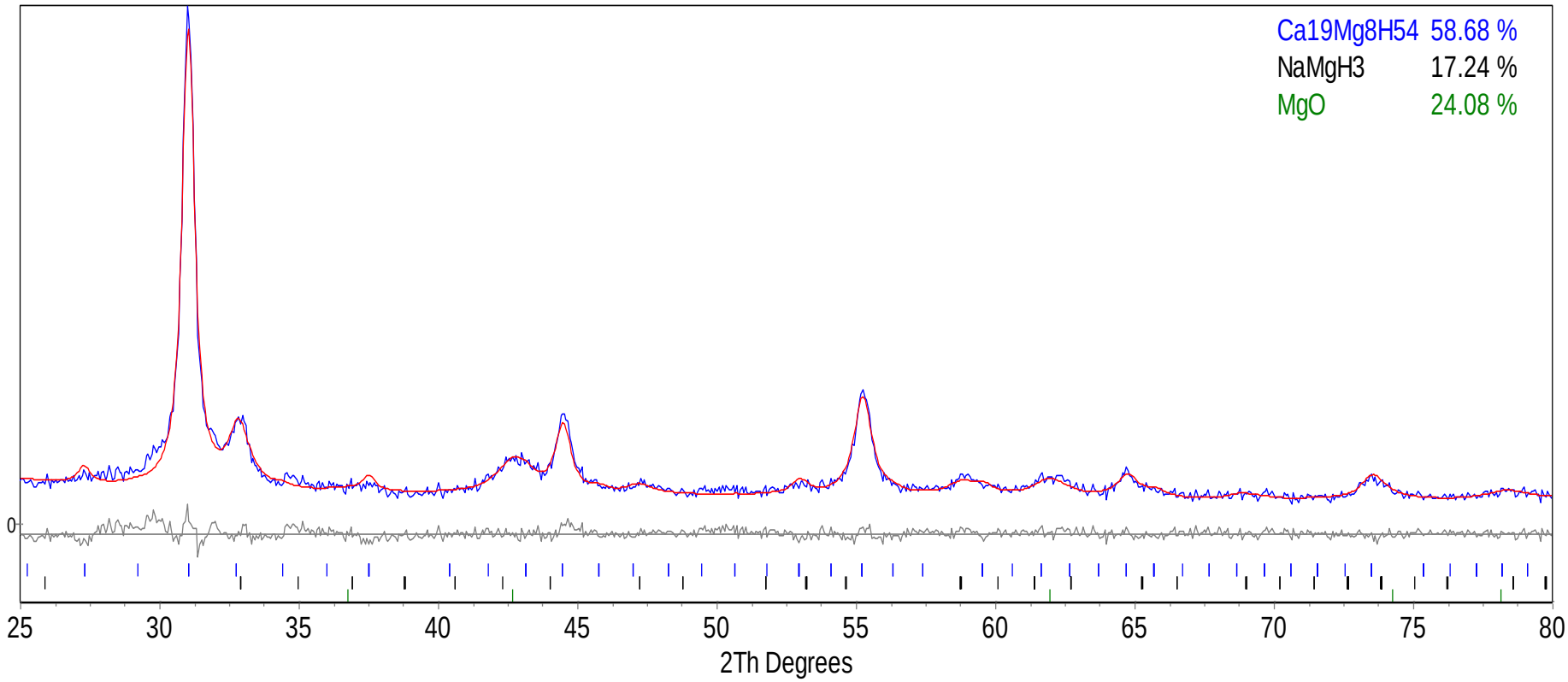

Figure 8.28 Rietveld refinement profile of XRD data for the 10 h milled $Na_{0.2}Ca_{0.8}MgH_4$, showing the observed data (black line), the calculated fitting to the data (red line) and the difference (grey line). Goodness of fit=1.273

8.3.2.2 Thermal decomposition

The temperature reactions and hydrogen evolution of the 5, 10, 15 hours milled $Na_{0.2}Ca_{0.8}MgH_4$ were investigated using DSC and TGA-MS at a heating rate of 2 °C/min under flowing Ar (100 ml/min) for the DSC measurements and (40 ml/min) for the TGA. Measurements were performed inside an argon filled glove box <5% ppm oxygen; to avoid air-water contamination, from 30 °C to 500 °C. Figure 8.29 illustrates the (a) DSC, (b) TGA, (c) MS traces of the 5, 10, 15 hours milled $Na_{0.2}Ca_{0.8}MgH_4$.

The DSC data of the 5 hours milled $Na_{0.2}Ca_{0.8}MgH_4$ show that dehydrogenation proceeds in 3 steps between 298 °C and 386 °C. The first desorption peak at 328.8 °C is determined as the decomposition of the $NaMgH_3$ leading to a 1.55 wt. % mass loss, followed by the second peak at 339.04 °C accounting for 0.44 wt. % mass loss up to 348.8 °C. The third endotherm peaking at 354.54 °C corresponded to the MgH_2 decomposition with a 1.47 wt.% weight loss and is still observed up to 385.8 °C. TGA-MS indicate that a total amount of 3.47 wt.% of H_2 was released up to 385.88 °C.

After milling for 10 hours $Na_{0.2}Ca_{0.8}MgH_4$ the same three-step dehydrogenation reactions were detected. The first dehydrogenation was observed peaking at 336.21 °C with a 1.63 wt. % weight loss, followed by the second endotherm peaking at 347.21 °C leading to 0.29 wt. % mass loss up to 350.46 °C, and the third desorption peak centred at 353.71 °C with a weight loss of 1.41 wt.%. A total amount of 3.32 wt. % of H_2 was released up to 389.89 °C and is shown by the TGA-MS.

Further milling $Na_{0.2}Ca_{0.8}MgH_4$ for 15 hours, shows dehydrogenation follows three step reaction: the first desorption peak is at 341.01 °C with a 1.13 wt.% mass loss, subsequently the second desorption is observed peaking at 351.26 °C leading to 0.36 wt. % weight loss, whereas, the third desorption peak is centred at 361.01 showing a 1.27 wt.% mass loss. The total amount of H_2 released from 314.84 °C and 392.88 °C accounts for 2.76 wt. % of H_2.

To sum up, there is no evidence of any other gas evolutions besides H_2 from the mass spectrometer during the heating process. Moreover, it is observed that the sample milled for 5 hours release 3.47 wt. % of H_2 from 297.83 to 385.88 °C. However, that amount of H_2 evolution accounts for only 56.42 wt. % of the total (6.15 wt. %) H_2 evolution expected for the mixture.

Therefore, it can be inferred that complete dehydrogenation was not achieved at the investigated temperature range. When further milling the sample for 10 and 15 hours no enhancement neither in the desorption temperature nor in the H_2 release was detected. Hence, reducing the crystallite size of the samples seems to not have a destabilizing effect in this particular mixture.

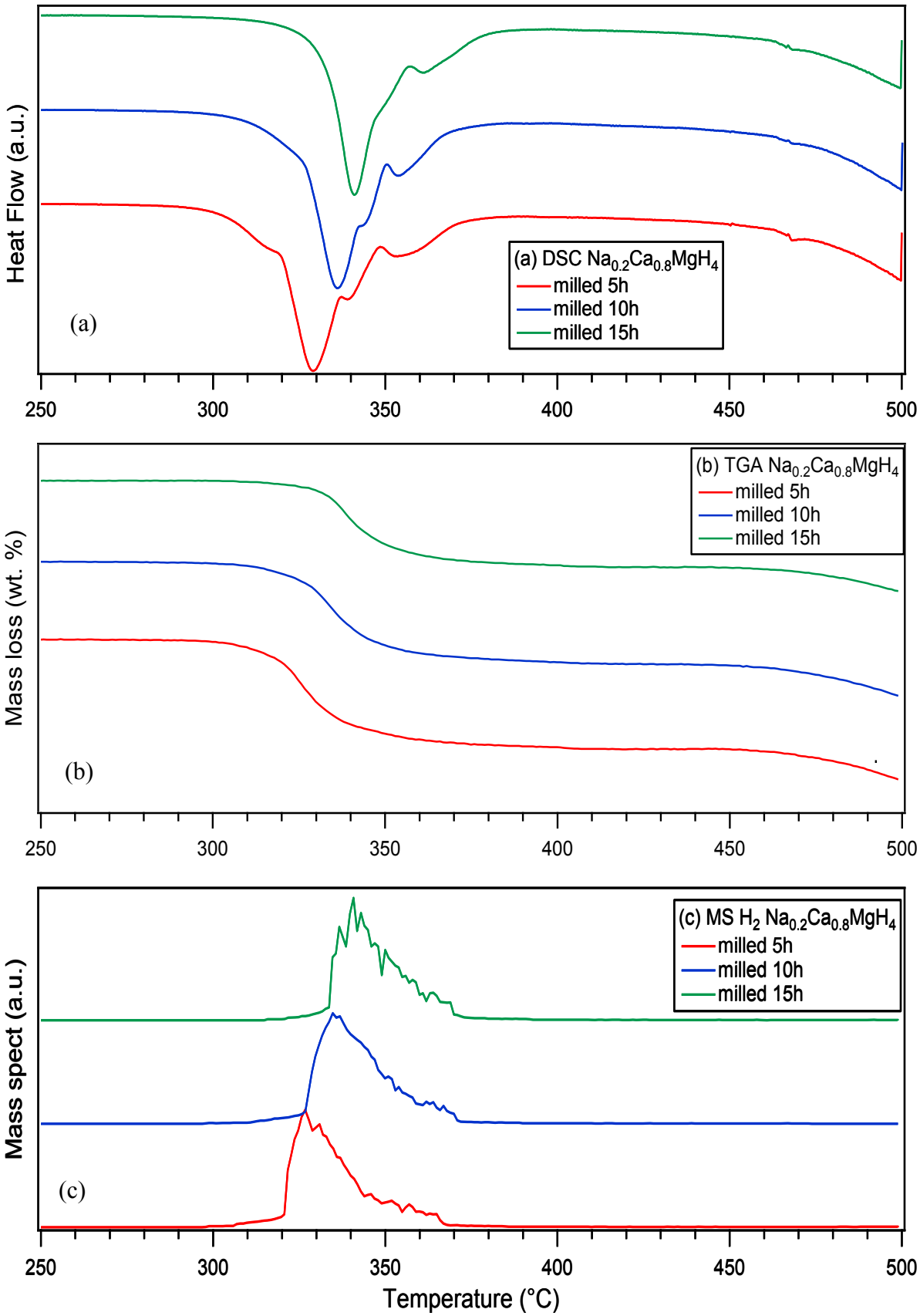

Figure 8.29 DSC-TGA-MS traces of the 5, 10 and 15 hours milled $Na_{0.2}Ca_{0.8}MgH_4$ samples. Measurements were performed at a heating rate of 2 °C/min under 3 bar argon at 100 ml/min (DSC), and 1 bar argon at 40 ml/min (TGA/MS) from 30 °C to 500 °C.

8.3.2.3 In-situ XRD

In order to investigate further and to corroborate the decomposition mechanisms of the 5, 10, 15 milled $Na_{0.2}Ca_{0.8}MgH_4$ obtained from the DSC measurements, in-situ measurements were performed. Ball milled samples were heated from 30 to 500 °C at 2 °C/min in He flowing at 100 ml/min. Loading and handling of the samples was performed inside an argon-filled glove box <5% ppm O_2 to avoid air-water contamination.

Figure 8.30 illustrates the in-situ reflections of the 5 hours milled sample. When $Na_{0.2}Ca_{0.8}MgH_4$ is heated from 30 °C to 325 °C, X-ray diffraction peaks for $Ca_{19}Mg_8H_{54}$ and $NaMgH_3$ are observed. At 325 °C, diffractions of $Ca_{19}Mg_8H_{54}$ and $NaMgH_3$ phases show a decreased intensity and a slight shift to higher 2θ angles due to a contraction in the cell parameters on heating. Additionally, two new phases are detected consistent with CaH_2 and Mg diffractions, indicating that $Ca_{19}Mg_8H_{54}$ started to decompose. Moreover, some traces of (Ca and Mg) oxides are also evidenced at this temperature. On heating to 350 °C, reflections of $Ca_{19}Mg_8H_{54}$ and $NaMgH_3$ were no longer detected showing that the mixtures have decomposed into CaH_2, NaH and Mg phases. In addition, more intense reflections of (Ca and Mg) oxides were observed. On further heating from 350 °C to 500 °C, only reflections for CaH_2 and Mg were observed. No evidence of Na phase was detected as would be expected from the decomposition of NaH. This effect can be attributed to the oxidation of Na on heating, which prevents the X-rays to detect the metal. Nevertheless, to carry out a more extensive investigation into this hypothesis, ex-situ XRD measurements were performed after sample was decomposed in-situ. Figure 8.31 shows the refinement of the ex-situ diffractions from the decomposed $Na_{0.2}Ca_{0.8}MgH_4$. It is evident from the refinement that, 5 hours milled sample contains 63 wt. % of crystalline CaH_2, 12 wt. % of Mg and the remaining crystalline material corresponds to (Mg and Ca) oxides.

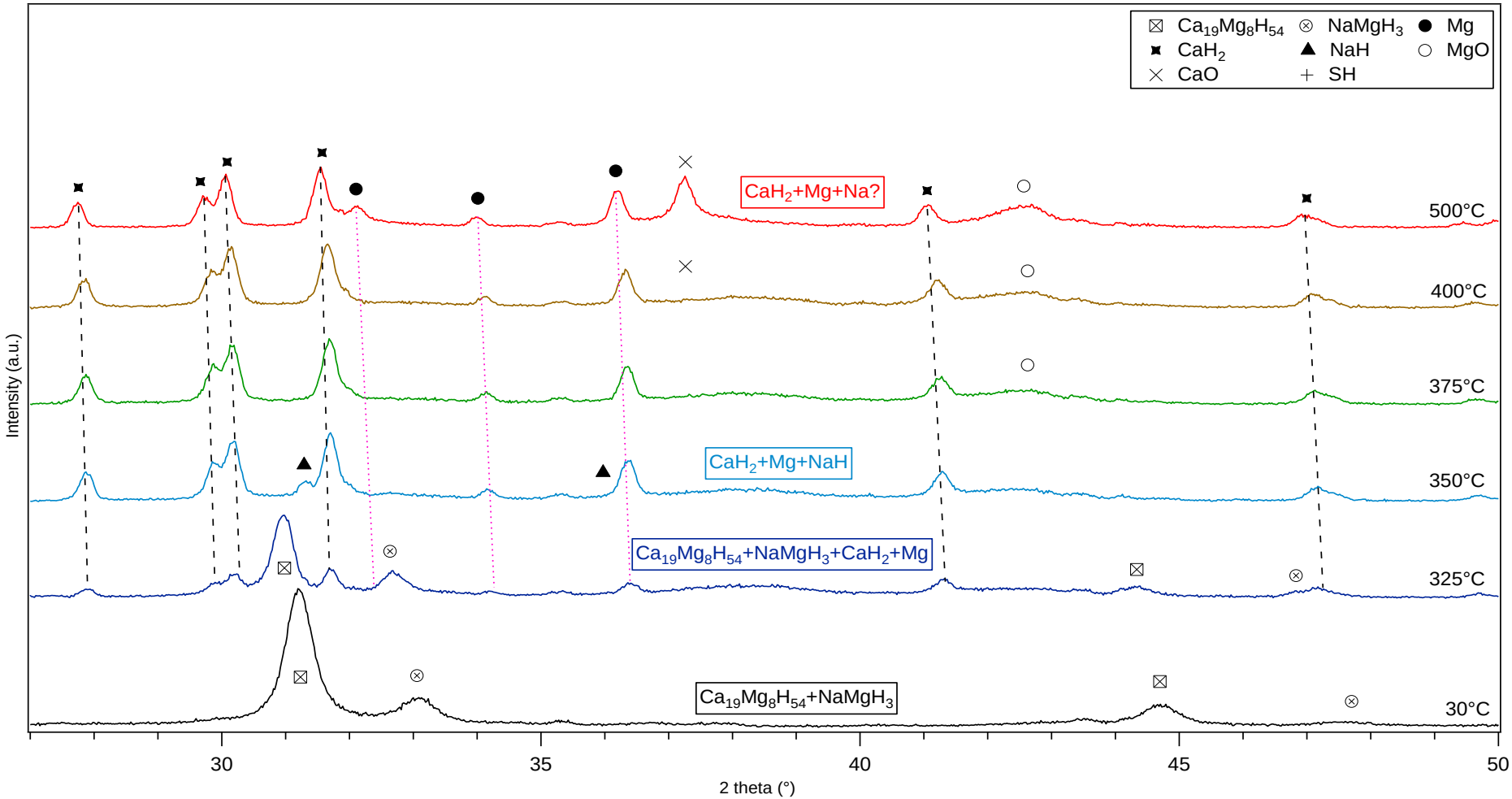

Figure 8.30 In-Situ XRD reflections of the 5 h milled $Na_{0.2}Ca_{0.8}MgH_4$ heated under He (100 ml/min, ~3 bar) between 30 – 500 °C

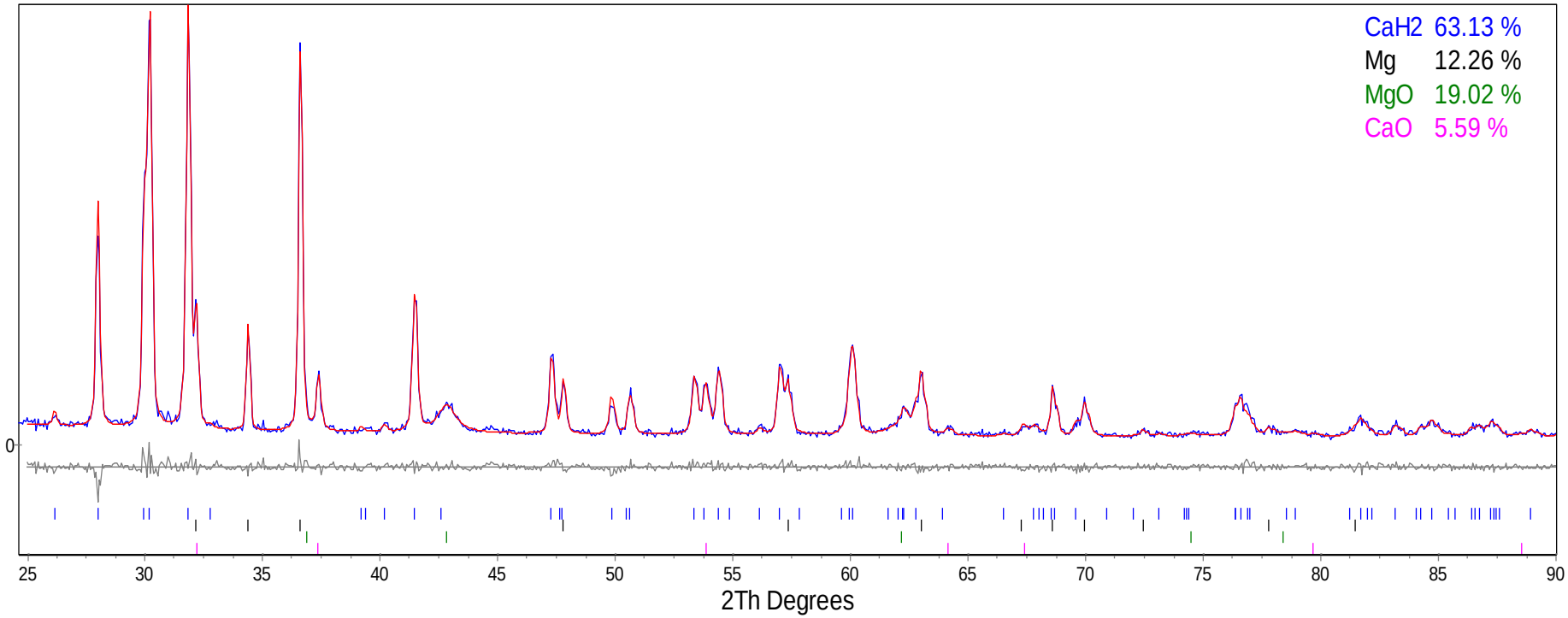

Figure 8.31 Rietveld refinement profile of XRD data for the 10 h milled Na0.2Ca0.8MgH4, showing the observed data (blue line), the calculated fitting to the data (red line) and the difference (grey line). Goodness of fit=1.315

On the other hand, no traces of Na metal or NaH were detected on the refinement of the decomposed sample as would be expected from the decomposition of the $NaMgH_3$. Hence, it is assumed that Na has reacted with the CaH_2 after decomposition producing a peak shift to higher diffraction angles.

Figure 8.32 shows the in-situ reflections of the 10 hours milled $Na_{0.2}Ca_{0.8}MgH_4$ sample. On heating from 30 °C to 300 °C, XRD peaks for $Ca_{19}Mg_8H_{54}$ and $NaMgH_3$ are detected. At 325 °C, diffractions of $Ca_{19}Mg_8H_{54}$ and $NaMgH_3$ phases show a significant decreased intensity and they are shifted to higher 2θ angles due to a contraction in the cell parameters on heating. Furthermore, a new phase is detected consistent with NaH, indicating the decomposition of $NaMgH_3$. Additionally, some traces of (Ca and Mg) oxides are also revealed at this temperature. On heating to 350 °C, reflections of $Ca_{19}Mg_8H_{54}$ and $NaMgH_3$ were no longer identified showing that the mixtures have decomposed into CaH_2 and Mg phases. Besides, more intense reflections of (Ca and Mg) oxides were observed, along with Na_2O diffractions. On further heating from 350 °C to 500 °C, only reflections for CaH_2 and Mg were observed. No evidence of Na phase was detected as would be expected from the decomposition of NaH. However, due to the Na_2O diffractions, it is assumed that Na is present but might become oxidised during the decomposition process. Ex-Situ XRD measurements were performed after sample was decomposed In-situ. Figure 8.33 illustrates the refinement of the ex-situ diffractions from the decomposed $Na_{0.2}Ca_{0.8}MgH_4$. It is evident from the refinement that, 10 hours milled sample contains 56 wt. % of crystalline CaH_2, 9.5 wt. % of Mg and 0.7 wt. % of Na. The remaining crystalline material corresponds to (Mg, Ca, and Na) oxides.

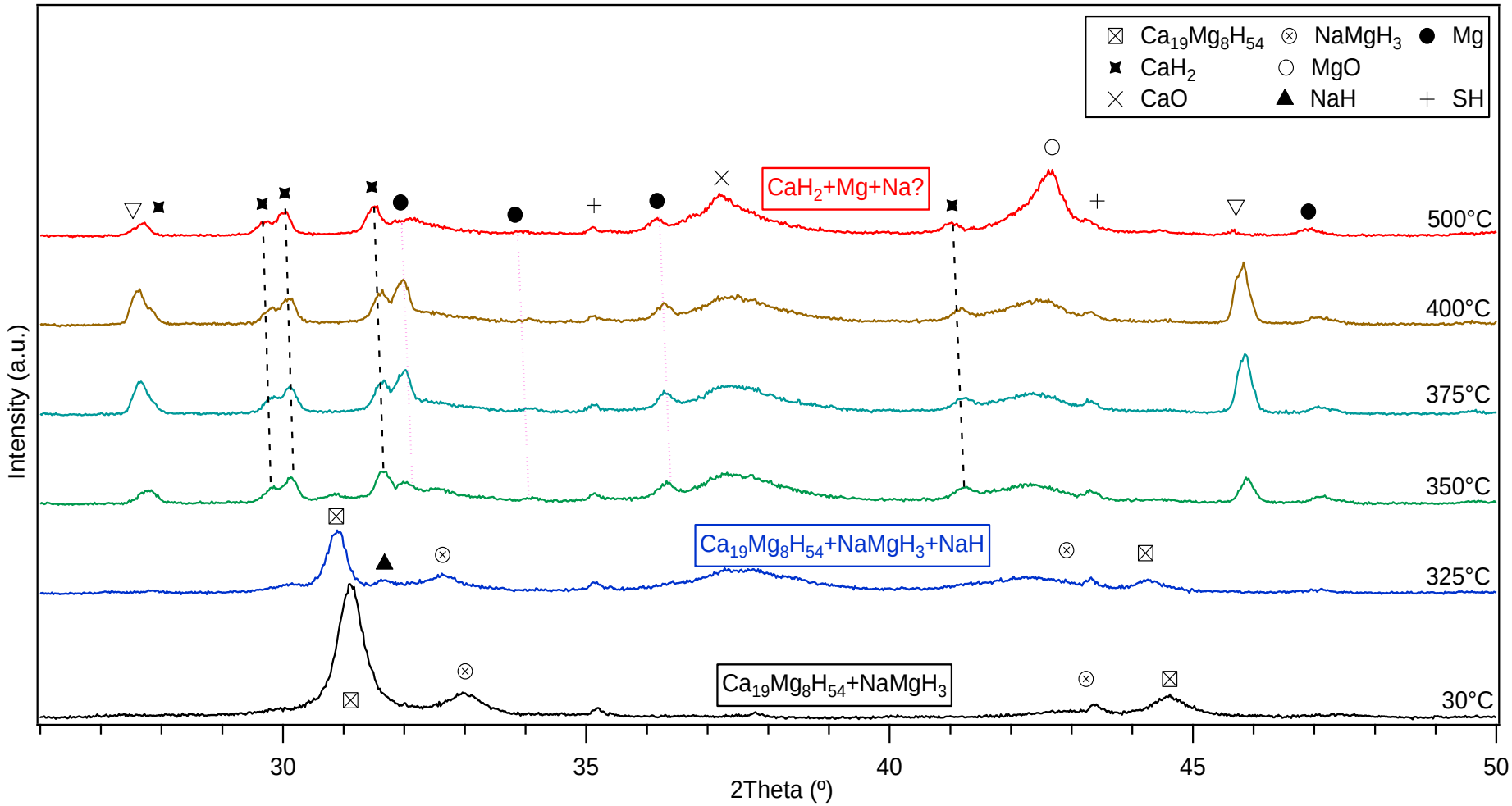

Figure 8.32 In-Situ XRD reflections of the 10 h milled $Na_{0.2}Ca_{0.8}MgH_4$ heated under He (100 ml/min, ~3 bar) between 30 – 500 °C

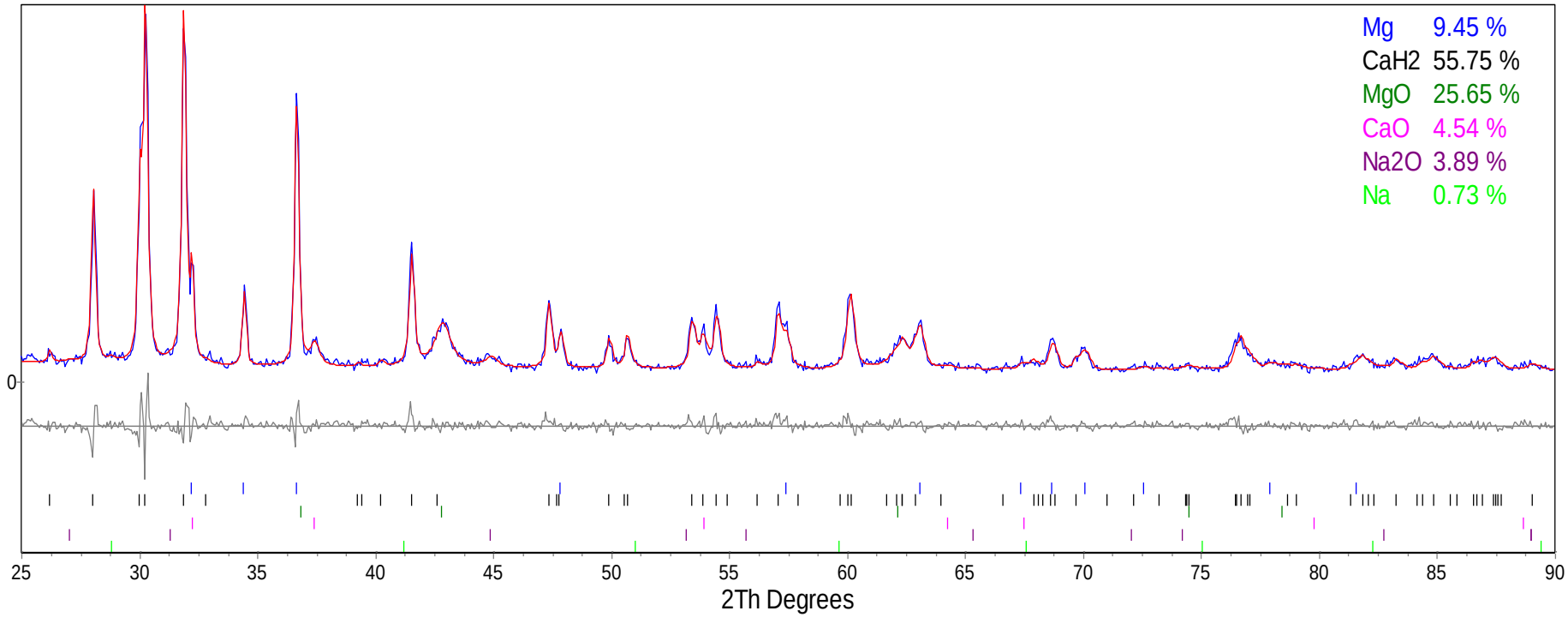

Figure 8.33 Rietveld refinement profile of XRD data for the 10 h milled $Na_{0.2}Ca_{0.8}MgH_4$, showing the observed data (blue line), the calculated fitting to the data (red line) and the difference (grey line). Goodness of fit=1.315

In-situ XRD performed on the $Na_{0.2}Ca_{0.8}MgH_4$ milled for 15 hours is shown in Figure 8.34. Initially, reflections of $Ca_{19}Mg_8H_{54}$ and $NaMgH_3$ are present and these diffractions are observed on heating up to 325 °C with decreased intensity. At 325 °C, a new phase equivalent to the diffractions of CaH_2 is detected, indicating the decomposition of the $Ca_{19}Mg_8H_{54}$ phase. On heating to 350 °C, $Ca_{19}Mg_8H_{54}$ phase is no longer observed leading to the conclusion that the same has decomposed into CaH_2 and Mg. Moreover, NaH phase is also detected at this temperature, and is attributed to the decomposition of the ternary $NaMgH_3$ into NaH and Mg. Additionally, small traces of MgO and CaO are noticed. From 375 to 500 °C diffractions of CaH_2 and Mg are the only remaining phases.

No evidence of Na was detected in this heating range, nevertheless, it is inferred that due to the low vapour pressure of Na at elevated temperatures the x-rays were not able to detect the metal during the heating.

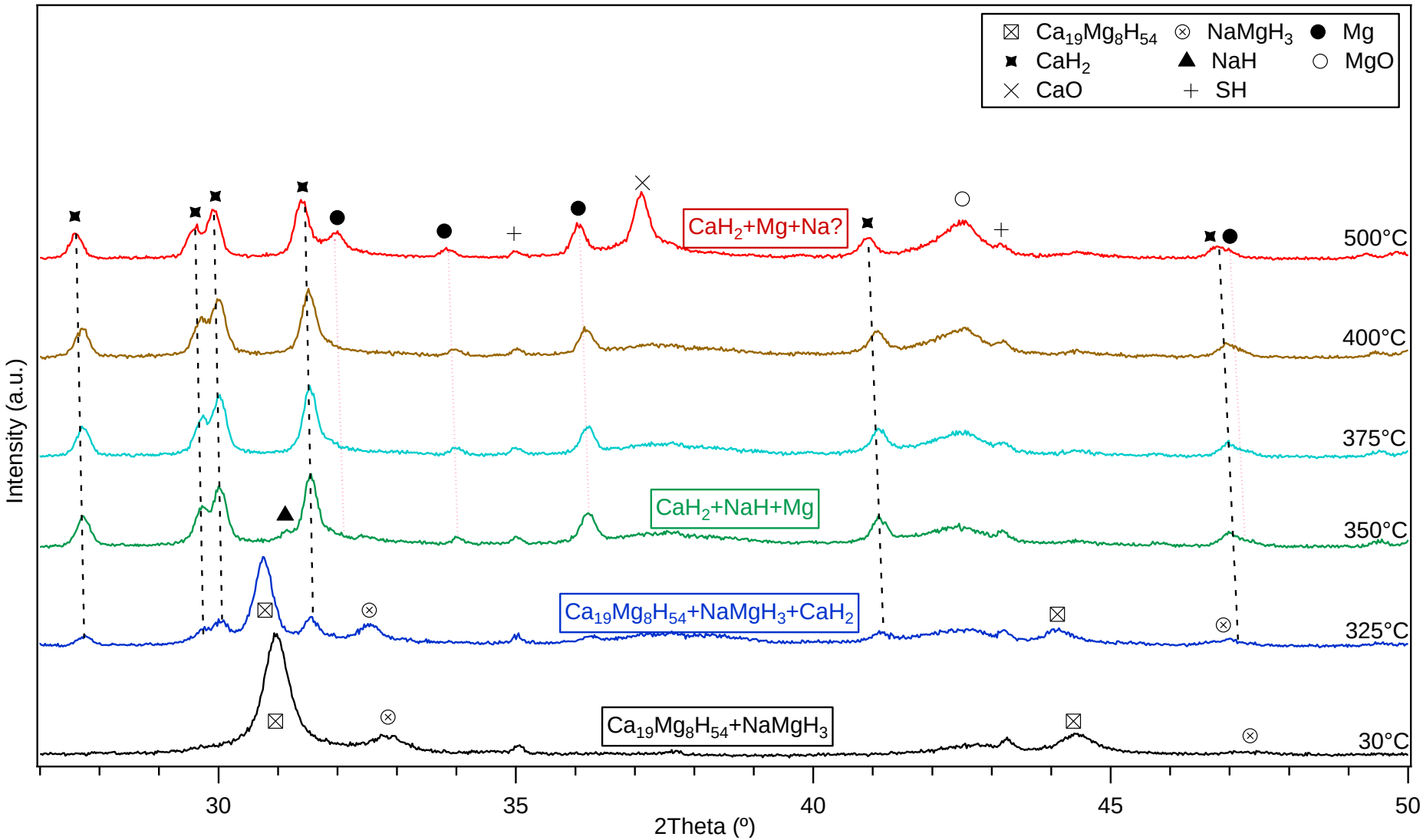

Figure 8.34 In-situ XRD patterns of the 15 h milled $Na_{0.2}Ca_{0.8}MgH_4$ heated under He (100 ml/min, ~3 bar) between 30 – 500 °C

8.4 Conclusions

8.4.1 Ca-Mg-H ternary hydride

The aim of this work was to synthesise Ca-Mg-H ternary hydride mechanically milling in argon alone using as a starting materials CaH_2 and MgH_2. Analysis of the as-milled product shows the synthesis of $Ca_{19}Mg_8H_{54}$ phase after only 5h milling. Two molar compositions were studied MgH_2 : CaH_2 (1:1) and (2:1). From the structural point of view was noticed that the unit cell parameters of the samples are affected by the ratio of the starting hydrides. The MgH_2 + CaH_2 (2:1) sample has the closest meaning to that of the (a) cell parameter and volume reported by Bertheville et al.,(Bertheville and Yvon, 1999) for the ternary hydride in previous reported literature.

Thermal decomposition was carried out in the as-milled samples to understand and compare the desorption reactions, change in weight due to the dehydrogenation and the evolution of gases upon heating. DSC of the (1:1) and (2:1) mixtures show two endothermic reactions and no exothermic curves on heating up to 500 °C. The first endothermic reaction is associated with the decomposition of $Ca_{19}Mg_8H_{54}$ into $Ca_4Mg_3H_{14}$ and this decomposes further into CaH_2 and Mg giving place to the second endothermic reaction for both molar compositions. Diffractions of CaH_2 remain present in the sample even after 500 °C indicating that sample was not totally dehydrogenated. Peak temperatures at around 380, 373 °C for the first endothermic reactions, and 405 and 400 °C for the second reaction respectively, determine that sample containing (2:1) molar composition shows enhanced dehydrogenation temperatures of about 20 °C. Suggested dehydrogenation reactions were determined as: $Ca_{19}Mg_8H_{54} \rightarrow Ca_4Mg_3H_{14} + Mg + H_2$ followed by $Ca_4Mg_3H_{14} \rightarrow CaH_2 + Mg + H_2$.

TGA measurements showed a total amount of 2.24 wt.% of H_2 was released on heating up to 415 °C for the (1:1) compound and a total of 2.1 wt. % of H_2 desorbed from 315 to 410 °C for

the (2:1) ratio. MS attached to the TGA analyser indicated that the only gas evolved during the heating process was hydrogen. This represents ~45% of the theoretical maximum for the $Ca_{19}Mg_8H_{54}$ (5.40 wt.%). The evidence suggested that not complete decomposition of the CaH_2 phase was achieved up to 500 °C. Therefore, it is proposed that higher temperatures are needed for the complete dehydrogenation of the ternary $Ca_{19}Mg_8H_{54}$ hydride and a higher H_2 yield.

In-Situ XRD for the MgH_2 + CaH_2 (1:1) sample, indicate the decomposition mechanisms of the sample undergoes a transition from $Ca_{19}Mg_8H_{54}$ to $Ca_4Mg_3H_{14}$ up to 325 °C, $Ca_4Mg_3H_{14}$ decomposed into CaH_2 and Mg releasing hydrogen. Complete decomposition of the ternary phases is observed up to 400 °C. CaH_2 diffractions are still present even after 500 °C, indicating that this binary hydride needs higher temperatures to decompose.

The In-Situ reflections for the (2:1) sample show the same decomposition pathway as in the previous (1:1) molar composition with a slightly variation in the temperatures. These observations are in good agreement with the decomposition reactions obtained from DSC measurements previously performed in this work.

Reversibility of the ternary composite was successfully achieved after exposing the decomposed sample to 10 bar H_2 pressure and temperature of approximately 365 °C.

8.4.2 $Li_xCa_{1-x}MgH_4$ (x=0.2)

The aim of this section was to synthesise for the first-time quaternary hydride with composition $Li_{0.2}Ca_{0.8}MgH_4$. It was successfully synthesised mixing binary LiH, CaH_2 and MgH_2 hydrides. A small shift to higher diffraction angles was observed. Moreover, lattice parameters and cell volumes of the main $Ca_{19}Mg_8H_{54}$ tend to decrease with increasing milling time.

Thermal decomposition of the milled samples showed one (5,10 h) and two (15h) endothermic reactions. The first associated with the decomposition of the main product, and the second endotherm is associated with the decomposition of $Ca_4Mg_3H_{54}$ into CaH_2 and Mg releasing hydrogen. It was evidenced that 10 h milled $Li_{0.2}Ca_{0.8}MgH_4$ shows the lowest decomposition temperature at 336 °C, while the 5 h milled sample releases the maximum amount of hydrogen (2.76 wt. %) up to 500 °C. This result represents the 52% of the maximum hydrogen capacity (5.4 wt.%) for the $Ca_{19}Mg_8H_{54}$ phase. The possible explanation of this effect, is due to the incomplete dehydrogenation of the CaH_2 phase, given that even at 500 °C remaining of that phase was observed from the XRD.

In-Situ XRD showed the decomposition mechanisms followed. For all samples $Ca_{19}Mg_8H_{14}$ decomposes through $Ca_{19}Mg_8H_{14,}$ approximately at 300 °C, then to CaH_2 and Mg with hydrogen evolution up to 500 °C. Complete dehydrogenation was not successful given that CaH_2 phase remain present in the sample even after heating up to 500 °C.

8.4.3 $Na_xCa_{1-x}MgH_4$ (x=0.2)

Na substitution into the Ca-Mg-H hydride was attempted to try to alter the hydrogen sorption characteristics of the ternary hydride. Samples comprising NaH, CaH_2 and MgH_2 were mechanically milled. Two phases were observed after milling associated with $Ca_{19}Mg_8H_{54}$ and $NaMgH_3$ ternary phases. Lattice parameters and cell volumes of the phases tend to increase with the milling time.

Thermal decomposition from DSC and TGA-MS show that dehydrogenation of the sample proceeds in three-step reaction. The first is related to the decomposition of the $Ca_{19}Mg_8H_{54}$ phase into CaH_2 and Mg approximately at 325 °C. Consequently, the $NaMgH_3$ phase starts to decompose at 350 C into NaH and Mg and finally NaH decomposed into Na to complete the

third endothermic reaction at 375 C approximately. A maximum of 3.47 wt. % of H_2 was released from 297.83 to 385.88 °C. However, that amount of H_2 evolution accounts for 56 wt. % of the total (6.15 wt. %) H_2 evolution expected for the mixture. Therefore, it can be inferred that complete dehydrogenation was not achieved at the investigated temperature range (>500 ^{o}C). It can be assumed that this effect is due to the fact that CaH_2 phase was not entirely decomposed, inferring that higher temperatures (>500 ^{o}C) were required for its complete decomposition.

When further milling the sample for 10 and 15 hours no enhancement neither in the desorption temperature nor in the H_2 release was detected. Hence, reducing the crystallite size of the samples seams to not have a destabilizing effect in this particular mixture.

In-Situ XRD corroborate the findings from the DSC measurements showing that samples decompose in three-steps. Moreover, complete dehydrogenation was not achieved due to the CaH_2 diffractions observed after heating the sample up to 500 °C. Therefore, is suggested that higher temperatures would be necessary to decompose this phase.

Overall, these new synthesised compounds need more research in terms of reversibility. Due to the relatively low hydrogen content and the high temperatures required for the hydrogen desorption, these hydrides would not be suitable for on-board applications. However, might be still of interest for high temperature applications.

CHAPTER IX

9. GENERAL DISCUSION

Mg was considered as the base sample for the hydrides due to the high gravimetric and volumetric hydrogen storage densities. For sample synthesis, a mechanical milling technique was employed in which the conditions were varied, according to the needed final product and its characteristics.

Different compounds were produced and characterised via X-ray diffraction, Raman, to study the composition of the materials, differential scanning calorimetry, thermogravimetric analysis, mass spectrometry (DSC-TGA-MS); to clarify the changes in thermodynamics of the as prepared samples such as decomposition reactions and temperatures, in addition to the analysis of evolution of gases. Moreover, the compositional changes were investigated via in-situ XRD, and finally the reversibility was tested using either in-situ XRD or DSC measurements.

In this work, Chapter 4 shows that MgH_2 thermodynamic characteristics of absorption/desorption can be lowered via mechanically milling as previously reported by (Zaluska et al., 1999), (Suryanarayana, 2001b), (Jain et al., 2010b). Reduction in grain size enhances the diffusion of hydrogen substantially lowering the decomposition temperatures. Thus, after milling MgH_2 for 10h (Ar), a reduction in crystallite size from 200 nm for the as received material to 18 nm was observed, decreasing the desorption temperature from 395 to 325 °C. After milling MgH_2 for 10h (H_2), similar results as in the Ar milled samples were obtained, hence, a reduction in crystallite size of ~182 nm from the as received and 10 h milled MgH_2 leads to a decrease in the decomposition temperature of 80 °C. Milled MgH_2 decomposes in one single step reaction.

$$MgH_2 \xrightarrow{380\ ^{o}C} Mg + H_2 \quad (9.1)$$

XRD data shows peaks of tetragonal α – MgH_2 and orthorhombic γ – MgH_2. The intensity of the MgH_2 peaks is dependant to the milling time. With increasing the milling time, α – MgH_2 peak intensities decrease and broaden, whereas the peak intensities of γ – MgH_2 increase. The increase in the peak width shows a reduction in the grain size enhancing the hydrogen sorption.

The unit cell parameters of the milled MgH_2 in Ar, show a cell expansion on the 2 and 5h milled samples, after milling for 10h there is a minor contraction on the unit cell. Whereas, MgH_2 milled in H_2 shows a steady and constant increase in lattice parameters. The change in lattice parameters suggest a reduction in grain size, allowing a faster dehydrogenation, this is consistent with results reported by Jain et al., 2010 for milled MgH_2.

Raman performed on the milled MgH_2 in Ar and H_2 showed 3 vibrational modes at 317.8 (B_{1g}), 947.6 (E_g) and 1257.9 cm^{-1} (A_{1g}) related to the α – MgH_2 phase. Additionally, weak modes were also detected at 179.6, 657.3, 253.5 and 586.9 cm^{-1} associated with γ – MgH_2 phase. This Raman modes are consistent with previous investigations by Reed and Book, 2011, Santisteban et al., 2000 and Kuzovnikov et al., 2013.

As for hydrogen storage capacity, the largest amount of hydrogen desorbed (6.6 wt.%) was found in the 2 h milled MgH_2 in Ar and 100 bar H_2, this corresponds to 87 % of the total capacity for the MgH_2 (7.6 wt.%). Longer milling times led to lower hydrogen capacities i.e. (5.7 wt.%) for the 10h milled MgH_2 in Ar.

Nevertheless, desorption temperatures were lowered around 120 °C none of the samples experimentally investigated in this work were able to approach to the theoretical hydrogen capacity for the MgH_2 or meet the target criteria for on-board storage proposed by the DOE.

Therefore, further work is necessary to find novel additives, which meet the thermodynamic requirements of a real system.

The direct hydrogenation of a Li-rich Li-Mg ribbon via reactive high-pressure milling reported by (Guo, 2015) was attempted in this work with several modifications in the milling conditions (100 rpm) and shorter milling times (15, 30 and 60 min) (Chapter 5). Direct hydrogenation was achieved after 60 min milling the sample (Li-Mg ribbon) into a powder containing the Li and Mg hydride phases.

A minor peak at 26.2 $2\theta^{o}$ was detected in the milled samples, which is not related to known oxides, hydroxides or to the theoretical $LiMgH_3$ and Li_2MgH_4 (Li et a., 2011, Vajeeston et al., 2008).

The decomposition of the hydride Li-Mg samples starts with the dehydrogenation of its phases into elemental Li and Mg at ~ 194 °C, consequently Li substitutes Mg to form a hcp Mg(Li) solid solution. The degree of substitution increases leading to a slight reduction in hcp-Mg cell volume from 200 °C, based on the Li-Mg phase diagram the solubility of Li in Mg is (Li >17 at%).

DSC under Ar and H_2 show an endothermic reaction starting at 189 °C up to 210 °C which can be linked to the decomposition of MgH_2 but at much lower temperature than for the milled MgH_2 at 360 °C reported by Varin et al., 2006. The amount of hydrogen desorbed accounts for 0.19 wt.% up to 250 °C. However, due to the small peaks of MgH_2 detected at this temperature (250 °C), it can be assumed that not complete dehydrogenation was achieved. Therefore, the total amount of hydrogen released may be increased.

Results experimentally obtained in this work present similar dehydrogenation pathways than previous reported studies (Guo, 2015). However, the reactions occur at lower temperatures. Thus, for the dehydrogenation of the milled Li-Mg ribbon Guo, S. reported a decomposition

temperature of 425 °C with a hydrogen evolution of 0.17 wt.%. In this work, a total amount of (0.19 wt.%) of H_2 was desorbed at 250 °C, showing that changing milling parameters has a positive effect in the thermodynamics of the milled material.

It is important to highlight, that this work was carried out to investigate the possible formation of Li-Mg-H ternary phases from the rapid hydrogenation of a Li-Mg alloy. However, no traces of these theoretical ternary phases were observed.

Although, hydrogenation of the Li-Mg alloy was achieved under relatively low temperature and pressure conditions, the amount of hydrogen that can be desorbed (~ 0.19 wt. %) it is extremely low for practical applications.

Continuing studies on the synthesis of ternary hydrides comprising mixtures of NaH and MgH_2 under Ar atmosphere reported by (Reardon, 2013), this work investigates the synthesis, sorption properties and rehydrogenation ability of $NaMgH_3$ hydrides mechanically milled under an Ar and H_2 atmospheres in Chapter 6. Synthesis of the ternary $NaMgH_3$ (orthorhombic, Pnma space group) under Ar and H_2 was achieved after 2 h milling the binary compounds. X-ray diffractions showed phases related to $NaMgH_3$ and NaH, no traces of remaining MgH_2 were detected and it is assumed that this effect was due to the relatively intensive milling conditions (400 rpm; ball to powder ratio 50:1). Peak intensities increased with the milling, therefore it is inferred that facile $NaMgH_3$ synthesis is possible without the use of high pressure techniques.

Refinement of the structure converged in good agreement with previous reported data (Ikeda, 2005, Reardon, 2013). Lattice parameters tend to linearly expand with increasing the milling time, resulting in larger cell volumes for milled samples under Ar and H_2.

Thermal decomposition occurs in two-step reaction represented by endothermic curves with hydrogen evolution.

$$NaMgH_3 \xrightarrow{330\,^{\circ}C} NaH + Mg \quad (9.2)$$

$$NaH + Mg \xrightarrow{350\,^{\circ}C} Na + Mg + 1/2H_2 \quad (9.3)$$

Dehydrogenation under Ar, showed two endothermic reactions linked to the decomposition of $NaMgH_3$ at 330 °C and NaH at 350 °C with a hydrogen evolution of 5.8 wt.% (2h milled), 5 wt.% (5 h milled) and 4.7 wt.% (15 h milled). Whereas, dehydrogenation under H_2 showed two reactions peaking at same temperatures than in Ar (330 and 350 °C) with 5.2 wt.% (2h milled) and 5.1 wt.% (5h milled) H_2 released. These results are slightly lower than the theoretical maximum for the $NaMgH_3$ ternary hydride (6 wt.%), but comparable to previous reported by (Ikeda, 2005). However, using Ar instead of H_2 for the synthesis. Nevertheless, dehydrogenation temperature (350 °C) remains high for applications therefore, there is a need to lower the hydrogen desorption temperatures.

Rehydrogenation of the $NaMgH_3$ phase from the decomposed Na and Mg products was successfully obtained after exposing the dehydrogenated samples to 10 bar H_2. However, not complete reabsorption was achieved. From the refinement of the sample 27% corresponds to $NaMgH_3$ reformed from the decomposed sample, the remaining products are related to oxides and NaH phases.

Chapter 7 summarises the attempts to decrease the thermodynamic characteristics of the $NaMgH_3$ by substituting Na by Li as suggested by (Reardon, 2013); a series of different molar (x= 0, 0.2, 0.5, 0.8) compositions were investigated. Novelty of this work is highlighted in the synthesis of the sample, for the first time $Li_xNa_{1-x}MgH_3$ system was synthesised in argon alone without the need of high pressure techniques reported in literature (Ikeda et al., 2007, Martínez-Coronado et al., 2012, Wang et al., 2016).

XRD showed the formation of (orthorhombic, Pnma space group) $NaMgH_3$ with a shift to higher diffraction angles attributed to the Li substitution into the hydride for the molar compositions x=0 and 0.2. In addition, for the x=0.5 and 0.8 traces of MgH_2 and NaH were detected. Peak intensity of the main $NaMgH_3$ phase decrease when increasing the amount of Li added. This effect suggest that Na can be substituted by Li up to a certain point (0.5 molar in this research) (Ikeda et al., 2007). This event, have been calculated based on the tolerance factor (t=0.7 to 1) to predict the structural stability of perovskites-type hydrides reported by Ikeda et al., 2007.

The lattice parameters and cell volumes obtained from the refinement of the samples tend to decrease as Li is added, this can be explained by the smaller Li^+ ionic size, showing a shift to higher diffraction angles (Fig. 7.1 inset).

Thermal analysis showed two (x=0, 0.2) and three (x=0.5, 0.8) endothermic reactions (equations 9.4-9.6) related to the decomposition of the samples with hydrogen evolution. DSC and TGA-MS, showed lower decomposition temperatures and higher H_2 capacity when increasing the amount of Li added into the system. Thus, Li x=0 decomposes into Na and Mg in two steps peaking at 369 °C and 390 °C respectively with a maximum hydrogen capacity of 4.6 wt.%. While, Li x=0.8 decomposes in three steps peaking at 314, 332 and 350 °C with a total amount of 5.2 wt.% H_2 released. These results show lower hydrogen capacity in comparison to the theoretical maximum for the $NaMgH_3$ (6 wt.%). However, decomposition temperatures showed a decrease of ~50 °C when more Li was added.

$$NaMgH_3+MgH_2 \xrightarrow{310\,^{\circ}C} NaMgH_3+Mg+H_2 \quad (9.4)$$

$$NaMgH_3+Mg+H_2 \xrightarrow{330\,^{\circ}C} NaH+2Mg+2H_2 \quad (9.5)$$

$$NaH+2Mg+2H_2 \xrightarrow{350\,^{\circ}C} Na+2Mg+5/2H_2 \quad (9.6)$$

Reversibility of the main $NaMgH_3$ phase (x=0.2) was achieved after exposing the sample to 10 bar H_2 and 250 °C. The degree of reabsorption accounted for ~ 43 %. The remaining was linked to NaH and oxides. Although, not complete rehydrogenation was observed, it was found that replacing Li into the $NaMgH_3$ seems to be beneficial for the rehydrogenation process as more percentage of the recombined sample (43 %) was achieved in comparison with the 27 % for $NaMgH_3$. To the best of the author's knowledge the rehydrogenation ability of the $Li_xNa_{1-x}MgH_3$ sample was observed and reported for the first time in this work.

Ternary mixtures composed from CaH_2 and MgH_2 binary hydrides and further substitution of (M=Na, Li) into the $M_{1-x}Ca_xMgH_4$ system were examined in Chapter 8. Synthesis was carried out via reactive milling under argon for 5, 10 and 15h. XRD diffractions showed the formation of $Ca_{19}Mg_8H_{54}$ (cubic, space group Im-3) reported by Bertheville and Yvon, 1999 and Santori et al., 2009, and $Ca_4Mg_3H_{14}$ (hexagonal, space group P62m) reported by Gingl, Bonhomme, and Yvon, 1992, after milling.

Lattice parameters and cell volume of the ternary hydride shows a slight decrease in the structure when increasing the milling time. This effect may be explained by the reduction in the crystallite size.

Thermal decomposition of the main phase was observed in two-step reaction (equations 9.7, 9.8) peaking at 383 and 405 °C associated with the decomposition of the $Ca_{19}Mg_8H_{54}$ phase into $Ca_4Mg_3H_{14}$ and Mg, and further decomposition of $Ca_4Mg_3H_{14}$ into CaH_2 and Mg with a total amount of 2.4 wt.% of H_2 released. This represents ~45% of the theoretical maximum for the $Ca_{19}Mg_8H_{54}$ (5.40 wt.%). The evidence suggested that not complete decomposition of the CaH_2 phase was achieved up to 500 °C. Therefore, it is proposed that higher temperatures are needed for the complete dehydrogenation of the ternary $Ca_{19}Mg_8H_{54}$ hydride and a higher H_2 yield.

$$Ca_{19}Mg_8H_{54} \xrightarrow{380\,^{\circ}C} Ca_4Mg_3H_{14} + Mg \quad (9.7)$$

$$Ca_4Mg_3H_{14} \xrightarrow{405\,^{\circ}C} CaH_2 + Mg \quad (9.8)$$

Reversibility was tested on the ternary Ca-Mg-H under 10 bar flowing H_2 at 100 ml/min using the DSC showed that $Ca_{19}Mg_8H_{54}$ phase can be reversibly formed at approximately 360 °C up to 410 °C. The yield of the rehydrogenation was not possible to obtain from this experimental technique, although form Fig. 8.13 is clear that not complete recombination of the main phase was achieved. Therefore, further investigation to clarify the extent of rehydrogenation and cyclability is advised.

When Li substitutes Ca in molar ratio x=0.2, a quaternary system was formed with $Ca_{19}Mg_8H_{54}$ as main phase. Lattice parameters and cell volume decrease on increasing the milling time showing a small shift to higher diffraction angles.

Thermal decomposition showed one and two-step reactions (equations 9.7 and 9.8) related with the dehydrogenation of $Ca_{19}Mg_8H_{54}$ into CaH_2 and Mg peaking at 325 and 353 °C respectively (10 h milled), with a maximum hydrogen evolution of 2.8 wt.% (15 h milled) up to 500 °C. This result represents the 52% of the maximum hydrogen capacity (5.4 wt.%) for the $Ca_{19}Mg_8H_{54}$ phase. The possible explanation of this effect, is due to the incomplete dehydrogenation of the CaH_2 phase, given that even at 500 °C remaining of that phase was observed from the XRD.

On substitution of Ca by Na with molar composition x=0.2, quaternary system with composition $Na_{0.2}Ca_{0.8}MgH_4$ was formed. X-ray diffraction showed the formation of $Ca_{19}Mg_8H_{54}$ and $NaMgH_3$ phases. Peak intensities decreased when increasing the milling time

showing broader peaks. Lattice parameters and cell volumes of the phases increased with the milling showing a shift to a higher diffraction angles (inset Fig. 8.23).

Thermal decomposition showed three-step dehydrogenation was followed, associated with the decomposition of $Ca_{19}Mg_8H_{54}$ into CaH_2 and Mg releasing hydrogen peaking at 325 ^oC. Consequently, $NaMgH_3$ decomposed into NaH and Mg at 350 ^oC, and further decomposition of NaH into Na was detected peaking at 375 ^oC. A total amount of 3.5 wt. % of hydrogen was released up to 386 ^oC. This H_2 evolution represents 56 % of the calculated theoretical maximum (6.15 wt.%) hydrogen content for the quaternary $Na_{0.2}Ca_{0.8}MgH_4$ hydride. It can be assumed that this effect is due to the fact that CaH_2 phase was not entirely decomposed, inferring that higher temperatures (>500 ^oC) were required for its complete decomposition.

A summary of the peak temperatures and reaction products of the Mg-based hydrides investigated in this thesis is shown in Table 9.1

Table 9.1 Summary of peak temperatures, mass loss and reaction products after decomposition of the Mg-based hydrides investigated in this thesis.

Sample	Tpeak (^oC)	Mass Loss (wt. %)	Observed products
MgH_2	380	6	Mg (MgO)
Li-Mg	250	0.19	-
$NaMgH_3$	330	4.7	Na, Mg (MgO)
$Li_xNa_{1-x}MgH_3$	320	5.1	Na, Mg (MgO)
Ca-Mg-H	380	2.2	CaH_2, Mg (MgO)
$Li_xCa_{1-x}MgH_3$	330	2.7	CaH_2, Mg (MgO)
$Na_xCa_{1-x}MgH_3$	350	3.5	CaH_2,Na, Mg (MgO)

From the experimental point of view of investigations performed in this thesis, it is implausible that at this stage any of the compounds herein investigated would be used for on-board hydrogen applications, given that absorption/desorption temperatures remain high and therefore need to be optimised.

CHAPTER X

10. CONCLUSIONS & FUTURE WORK

10.1 Conclusions

The main aim of this research was to investigate the hydrogen sorption mechanisms and thermodynamic behaviour of Mg-based hydrides, to try to produce novel materials with improved properties, i.e. with lower hydrogen desorption temperature (< 400 ^{o}C), high hydrogen content (> 5 wt. % H_2) and easily reversible.

From the research was found that:

- MgH_2
  - To the best of the authors knowledge, Raman spectroscopy of milled MgH_2 under Ar and H_2 was tested for the first time, showing that milled MgH_2 was Raman active. The vibrational modes were consistent with previous studies from the literature(Reed and Book, 2011)
- Mg-Li Alloy
  - Direct hydrogenation of Mg-Li alloy was achieved after 1 h milling the sample under 100 bar H_2.
  - Dehydrogenation temperature was decreased from 284 ^{o}C to 250 ^{o}C, releasing a total amount of 0.19 wt. % H_2.
- $NaMgH_3$
  - $NaMgH_3$ ternary hydride was synthesised under an Ar atmosphere only.
  - A total amount of 5.8 wt % H_2 was released after milling NaH + MgH_2 for 2 h with an onset temperature of 290 ^{o}C.
  - Reversibility was successfully achieved at ~200 ^{o}C and 10 bar H_2 pressure.

- $Li_xNa_{1-x}MgH_3$
  - To the best of the author's knowledge reversibility of $Li_xNa_{1-x}MgH_3$ was investigated for the first time, showing the ability of the sample to reabsorb H_2 at ~200 ^oC and 10 bar H_2.
- Ca-Mg-H
  - Ca-Mg-H ternary hydride was synthesised milling CaH_2 and MgH_2 under argon alone.
  - Reversibility was successfully achieved after exposing the ternary hydride to 10 bar H_2 pressure and 365 ^oC.
- $(Li/Na)_xCa_{1-x}MgH_4$
  - The synthesis and hydrogen sorption properties of quaternary hydrides with composition $Li_{0.2}Ca_{0.8}MgH_4$ and $Na_{0.2}Ca_{0.8}MgH_4$ were investigated for the first time.

Mg was considered as the base sample for the hydrides due to the high gravimetric and volumetric hydrogen storage densities. For sample synthesis, a mechanical milling technique was employed in which the conditions were varied, according to the needed final product and its characteristics.

Different compounds were produced and characterised via X-ray diffraction, Raman, to study the composition of the materials, differential scanning calorimetry, thermogravimetric analysis, mass spectrometry (DSC-TGA-MS); to clarify the changes in thermodynamics of the as prepared samples such as decomposition reactions and temperatures, in addition to the analysis of evolution of gases. Moreover, the compositional changes were investigated via in-situ XRD, and finally the reversibility was tested using either in-situ XRD or DSC measurements.

10.2 Future Work

Future investigations should be focused on gaining a better understanding in the reversibility of the Mg-based compounds to verify the capacity of the samples after several dehydrogenation/re-hydrogenation cycles and thereby identify possible applications in terms of the characteristics of each mixture. To achieve this, to a certain point in-situ XRD and DSC techniques were employed in this work. Nevertheless, those techniques were not suitable for continuous desorption/absorption cycles. Hence, methods such as Intelligent Gravimetric Analyser (IGA), High-pressure analyser for the measurement of hydrogen storage (HTP) by Sievert's Method.

Another important investigation following the experimental work in this thesis should be dedicated to achieving a better understanding on the synthesis and decomposition pathways of all the Mg-based hydrides in attempt to modify "enhance" the hydrogen sorption characteristics for instance lower the temperature of hydrogen desorption, fasten the kinetics and achieve reversibility.

The possibility to synthesise high hydrogen capacity ternary hydrides Li-Mg-H via mechanical milling remains of interest due to the important properties it presents for hydrogen storage. The synthesis of this hypothetic hydrides from Li-Mg alloys need to be investigated further altering milling conditions, backpressure, incorporation of Li or Mg hydrides in order to optimise the hydrogenation/dehydrogenation properties. Furthermore, reversibility need to be tested.

Finally, novel hydrides might be investigated comprising Mg-based mixtures with lightweight metals in an effort to find a suitable candidate for on-board hydrogen storage. On the other hand, investigate the different application alternatives not only for mobile applications, but for stationary and high temperature uses.

PUBLICATIONS

- ✓ **Vasquez, L. F. C.**, Liu, Y., Paterakis, C., Reed, D., & Book, D. (2017). Hydrogen sorption properties of $Li_xNa_{1-x}MgH_3$ (x= 0, 0.2, 0.5 & 0.8). *International Journal of Hydrogen Energy*.

- ✓ **Vasquez, L.F.C.**, Book D. (2017). Hydrogen sorption properties of mechanically milled Li and Na substitutions into Ca-Mg-H ternary hydride. *Journal of Alloys and Compounds*. To be submitted (Dec. 2017)

- ✓ Liu, Y., Reed, D., Paterakis, C., **Vasquez, L. C.**, Baricco, M., & Book, D. (2017). Study of the decomposition of a 0.62 LiBH 4–0.38 NaBH 4 mixture. *International Journal of Hydrogen Energy*.

- ✓ Paterakis, C., Guo, S., Heere, M., Liu, Y., **Contreras, L. F**., Sørby, M. H., ... & Book, D. (2017). Study of the NaBH 4–NaBr system and the behaviour of its low temperature phase transition. *International Journal of Hydrogen Energy*.

PRESENTATIONS

Dec 2013 Hydrogen & Fuel Cell SUPERGEN Researcher Conference (United Kingdom) – Mechanochemical Synthesis of Magnesium Alloys for Hydrogen Storage

Dec 2014 Hydrogen & Fuel Cell SUPERGEN Researcher Conference (United Kingdom) – Magnesium Alloys for Energy Storage

Nov 2015 UKES 2015, UK Energy Storage Conference (United Kingdom) – Poster presentation,

Aug 2016 15^{th} International Symposium on Metal-Hydrogen Systems (MH2016) (Switzerland) – Hydrogen sorption properties of $Li_xNa_{1-x}MgH_3$

REFERENCES

(DOE), U. D. O. E. 2012a. *Department of Energy targets for Onboard hydrogen storage.* [Online]. Available: https://energy.gov/sites/prod/files/2015/01/f19/fcto_myrdd_table_onboard_h2_storage_systems_doe_targets_ldv.pdf [Accessed 22/03 2017].

(DOE), U. D. O. E. 2012b. *Hydrogen Storage* [Online]. Available: https://energy.gov/eere/fuelcells/hydrogen-storage [Accessed 22/03/2017].

(DOE), U. D. O. E. 2014. *Space-Based Solar Power* [Online]. Available: https://energy.gov/articles/space-based-solar-power [Accessed 28/03/2017].

(DOE), U. S. D. O. E. 2006. Hydrogen Hydrogen Posture Plan an Integrated Research, Development and Demonstration Plan.

(EF), E. C. E. F. 2010. *Disadvantages of Fossil Fuels* [Online]. Available: http://www.conserve-energy-future.com/disadvantages_fossilfuels.php [Accessed 28/03/2017].

(EIA), U. S. E. I. A. 2017. *Annual Energy Outlook 2017* [Online]. Available: https://www.eia.gov/outlooks/aeo/ [Accessed 28/03/2017].

(FCT), F. 2012. *Fuel Cell Technologies* [Online]. Available: http://www.fuelcelltoday.com/technologies/pafc [Accessed 22/03/2017].

(IEA), I. E. A. 2016. *World Energy Outlook 2016* [Online]. Available: http://www.iea.org/newsroom/news/2016/november/world-energy-outlook-2016.html [Accessed 28/03/2016].

(RSOC), R. S. O. C. 2016. *Climate change* [Online]. Available: http://www.rsc.org/campaigning-outreach/global-challenges/environment/#climate-change [Accessed 28/03/2016].

AHLUWALIA, R., HUA, T., PENG, J.-K., LASHER, S., MCKENNEY, K., SINHA, J. & GARDINER, M. 2010. Technical assessment of cryo-compressed hydrogen storage tank systems for automotive applications. *International journal of hydrogen energy,* 35**,** 4171-4184.

AN, E. 2002. Socio-economic Aspects of the Hydrogen Economy Development.

ARES, J., AGUEY-ZINSOU, K.-F., KLASSEN, T. & BORMANN, R. 2007. Influence of impurities on the milling process of MgH 2. *Journal of alloys and compounds,* 434**,** 729-733.

ASANO, K., SAKAKI, K., LIU, X. & AKIBA, E. 2009. Hydrogenation of CaLi 2− x Mg x (0≤ x≤ 2) with C14 Laves phase structure. *Journal of Alloys and Compounds,* 482**,** L18-L21.

ATKINS, P. 2010. *Shriver and Atkins' inorganic chemistry*, Oxford University Press, USA.

ATTEBERRY, J. 2009. *Jonathan Atteberry-How Scanning Electron Microscopes Work* [Online]. Available: http://science.howstuffworks.com/scanning-electron-microscope.htm [Accessed 19/01/2017].

BARKHORDARIAN, G., KLASSEN, T. & BORMANN, R. 2004. Effect of Nb 2 O 5 content on hydrogen reaction kinetics of Mg. *Journal of Alloys and Compounds,* 364**,** 242-246.

BASTIDE, J.-P., BONNETOT, B., LETOFFE, J.-M. & CLAUDY, P. 1980. Polymorphism of magnesium hydride under high pressure. *Materials Research Bulletin,* 15**,** 1215-1224.

BERTHEVILLE, B. & YVON, K. 1999. Ca 19 Mg 8 H 54, a new salt-like ternary metal hydride. *Journal of alloys and compounds,* 290**,** L8-L10.

BOGDANOVIĆ, B., BOHMHAMMEL, K., CHRIST, B., REISER, A., SCHLICHTE, K., VEHLEN, R. & WOLF, U. 1999a. Thermodynamic investigation of the magnesium–hydrogen system. *Journal of Alloys and compounds,* 282**,** 84-92.

BOGDANOVIĆ, B., BOHMHAMMEL, K., CHRIST, B., REISER, A., SCHLICHTE, K., VEHLEN, R. & WOLF, U. 1999b. Thermodynamic investigation of the magnesium–hydrogen system. *Journal of Alloys and Compounds,* 282**,** 84-92.

BOGDANOVIĆ, B., FELDERHOFF, M. & STREUKENS, G. 2009. Hydrogen storage in complex metal hydrides. *Journal of the Serbian Chemical Society,* 74**,** 183-196.

BORGSCHULTE, A., ZUTTEL, A. & WITTSTADT, U. 2008. Hydrogen production. *Hydrogen as a Future Energy Carrier*, 149-164.

BORTZ, M., BERTHEVILLE, B., BÖTTGER, G. & YVON, K. 1999. Structure of the high pressure phase γ-MgH 2 by neutron powder diffraction. *Journal of Alloys and Compounds*, 287, L4-L6.

BOUAMRANE, A., LAVAL, J., SOULIE, J.-P. & BASTIDE, J. 2000. Structural characterization of NaMgH 2 F and NaMgH 3. *Materials research bulletin*, 35, 545-549.

BOUAMRANE, A., SOULIE, J.-P. & BASTIDE, J. 2001. Standard enthalpies of formation of KCaH 3− x F x with x= 1, 1.5, 2, 2.5. *Thermochimica acta*, 375, 81-84.

BOUHADDA, Y., BOUDOUMA, Y., FENNINECHE, N.-E. & BENTABET, A. 2010. Ab initio calculations study of the electronic, optical and thermodynamic properties of NaMgH 3, for hydrogen storage. *Journal of Physics and Chemistry of Solids*, 71, 1264-1268.

BOUHADDA, Y., BOUOUDINA, M., FENINECHE, N. & BOUDOUMA, Y. 2013. Elastic properties of perovskite-type hydride NaMgH 3 for hydrogen storage. *International Journal of Hydrogen Energy*, 38, 1484-1489.

BOUOUDINA, M., GRANT, D. & WALKER, G. 2006. Review on hydrogen absorbing materials—structure, microstructure, and thermodynamic properties. *International Journal of Hydrogen Energy*, 31, 177-182.

BP. 2016. *BP Statistical Review of World Energy* [Online]. Available: https://www.bp.com/content/dam/bp/pdf/energy-economics/statistical-review-2016/bp-statistical-review-of-world-energy-2016-full-report.pdf [Accessed 28/03/2017].

BRITANNICA, E. 1999. *Encyclopædia Britannica-Bragg law* [Online]. Encyclopædia Britannica, inc. Available: https://www.britannica.com/science/Bragg-law [Accessed 01/15/2017].

BRITANNICA, E. 2007. *fuel cell: proton exchange membrane fuel cell.* [Online]. Available: http://kids.britannica.com/comptons/art-106689 [Accessed 22/03/2017].

BUCHNER, H. & POVEL, R. 1982. The daimler-benz hydride vehicle project. *International Journal of Hydrogen Energy*, 7, 259-266.

BURSTOW, C. 2002. Magnesium: the impact of projected new supply on prices over the next five years. *Mineral Processing and Extractive Metallurgy*, 111, 62-64.

CANSIZOGLU, M. & KARABACAK, T. Enhanced Hydrogen Storage Properties of Magnesium Nanotrees with Nanoleaves. MRS Proceedings, 2009. Cambridge Univ Press.

CHAUDHARY, A.-L., PASKEVICIUS, M., SHEPPARD, D. A. & BUCKLEY, C. E. 2015. Thermodynamic destabilisation of MgH 2 and NaMgH 3 using Group IV elements Si, Ge or Sn. *Journal of Alloys and Compounds*, 623, 109-116.

CHENG, F., TAO, Z., LIANG, J. & CHEN, J. 2012. Efficient hydrogen storage with the combination of lightweight Mg/MgH 2 and nanostructures. *Chemical Communications*, 48, 7334-7343.

CHUSID, O., GOFER, Y., GIZBAR, H., VESTFRID, Y., LEVI, E., AURBACH, D. & RIECH, I. 2003. Solid-State Rechargeable Magnesium Batteries. *Advanced Materials*, 15, 627-630.

CUI, J., WANG, H., LIU, J., OUYANG, L., ZHANG, Q., SUN, D., YAO, X. & ZHU, M. 2013. Remarkable enhancement in dehydrogenation of MgH 2 by a nano-coating of multi-valence Ti-based catalysts. *Journal of Materials Chemistry A*, 1, 5603-5611.

CUNNINGHAM, D. 2006. *The Politics of a Hydrogen Economy:*

Networks and the Role for

Industry, Government, NGOs, and Citizens [Online]. Available: https://www.uvic.ca/research/centres/globalstudies/assets/docs/publications/DianneCunninghamWorkshop.pdf [Accessed].

DARNAUDERY, J., DARRIET, B. & PEZAT, M. 1983. The Mg2Ni0. 75M0. 25 alloys (M= 3d element): their application to hydrogen storage. *International journal of hydrogen energy*, 8, 705-708.

DAVIS, J. R. 2001. *Surface engineering for corrosion and wear resistance*, ASM international.

DORNHEIM, M. 2011. *Thermodynamics of Metal Hydrides: Tailoring Reaction Enthalpies of Hydrogen Storage Materials, Thermodynamics - Interaction Studies - Solids, Liquids and Gases* [Online]. InTech. Available: https://www.intechopen.com/books/thermodynamics-interaction-

studies-solids-liquids-and-gases/thermodynamics-of-metal-hydrides-tailoring-reaction-enthalpies-of-hydrogen-storage-materials [Accessed 31/03/2017 2017].

DORNHEIM, M., DOPPIU, S., BARKHORDARIAN, G., BOESENBERG, U., KLASSEN, T., GUTFLEISCH, O. & BORMANN, R. 2007. Hydrogen storage in magnesium-based hydrides and hydride composites. *Scripta Materialia,* 56**,** 841-846.

DORNHEIM, M., EIGEN, N., BARKHORDARIAN, G., KLASSEN, T. & BORMANN, R. 2006. Tailoring hydrogen storage materials towards application. *Advanced Engineering Materials,* 8**,** 377-385.

EBERLE, U., FELDERHOFF, M. & SCHUETH, F. 2009. Chemical and physical solutions for hydrogen storage. *Angewandte Chemie International Edition,* 48**,** 6608-6630.

ENERGY, E. E. R. *Fuel Cell Technologies Office Accomplishments and Progress* [Online]. Available: https://energy.gov/eere/fuelcells/fuel-cell-technologies-office-accomplishments-and-progress [Accessed 28/07/2017].

ENERGY, U. D. O. *Hydrogen Production and Distribution* [Online]. Available: https://www.afdc.energy.gov/fuels/hydrogen_production.html [Accessed 15/06/2017].

ER, S., VAN SETTEN, M. J., DE WIJS, G. A. & BROCKS, G. 2010. First-principles modelling of magnesium titanium hydrides. *Journal of physics: Condensed matter,* 22**,** 074208.

EVA, B. 2016. *BRUKER. EVA Software -The next era in phase analysis n.d.* [Online]. Available: https://www.bruker.com/products/x-ray-diffraction-and-elemental-analysis/x-ray-diffraction/xrd-software/eva/overview.html [Accessed 10/10/2016].

FORNARI, M., SUBEDI, A. & SINGH, D. J. 2007. Structure and dynamics of perovskite hydrides A Mg H 3 (A= Na, K, Rb) in relation to the corresponding fluorides: A first-principles study. *Physical Review B,* 76**,** 214118.

FOURNIER, V., MARCUS, P. & OLEFJORD, I. 2002. Oxidation of magnesium. *Surface and interface analysis,* 34**,** 494-497.

FUKAI, Y. 1993. The Metal-Hydrogen System, Basic Bulk Properties. 1993. Heidelberg: Springer-Verlag.

GINGL, F., BONHOMME, F., YVON, K. & FISCHER, P. 1992a. Tetracalcium trimagnesium tetradecahydride, Ca4Mg3H14: the first ternary alkaline earth hydride. *Journal of alloys and compounds,* 185**,** 273-278.

GINGL, F., YVON, K. & FISCHER, P. 1992b. Strontium magnesium tetrahydride (SrMgH4): a new ternary alkaline earth hydride. *Journal of alloys and compounds,* 187**,** 105-111.

GINGLA, F., VOGT, T., AKIBA, E. & YVON, K. 1999. Cubic CsCaH 3 and hexagonal RbMgH 3: new examples of fluoride-related perovskite-type hydrides. *Journal of alloys and compounds,* 282**,** 125-129.

GOLDMAN, A. 2012. *Wave Energy Facts* [Online]. Available: http://www.renewablegreenenergypower.com/wave-energy-facts/ [Accessed 28/03/2017].

GRIGOROVA, E., KHRISTOV, M., KHRUSSANOVA, M., BOBET, J.-L. & PESHEV, P. 2005. Effect of additives on the hydrogen sorption properties of mechanically alloyed composites based on Mg and Mg2Ni. *International journal of hydrogen energy,* 30**,** 1099-1105.

GROCHALA, W. & EDWARDS, P. P. 2004. Thermal decomposition of the non-interstitial hydrides for the storage and production of hydrogen. *Chemical reviews,* 104**,** 1283-1316.

GUERVÓS SÁNCHEZ, M. 2003. Principales técnicas de almacenamiento de hidrógeno. Pg.

GUO, S. 2015. *Light metal borohydrides and Mg-based hydrides for hydrogen storage.* University of Birmingham.

HANADA, N., ICHIKAWA, T. & FUJII, H. 2006a. Catalytic effect of niobium oxide on hydrogen storage properties of mechanically ball milled MgH 2. *Physica B: Condensed Matter,* 383**,** 49-50.

HANADA, N., ICHIKAWA, T., HINO, S. & FUJII, H. 2006b. Remarkable improvement of hydrogen sorption kinetics in magnesium catalyzed with Nb2O5. *Journal of Alloys and Compounds,* 420**,** 46-49.

HANNINK, R. H. & HILL, A. J. 2006. *Nanostructure control of materials,* Woodhead Publishing.

HANWHA. 2013. *Hydrogen Storage Materials* [Online]. Available: https://hcc.hanwha.co.kr/eng/business/nano_ox.jsp [Accessed 22/03 2017].

HARRIS, R., BOOK, D., ANDERSON, P. & EDWARDS, P. 2004. Hydrogen storage: the grand challenge. *The Fuel Cell Review,* 1**,** 17-23.

HEMMINGER, W. & SARGE, S. 1998. Handbook of thermal analysis and calorimetry. *Principles and practice. Amsterdam: Elsevier*.

HERBSTEIN, F. & AVERBACH, B. L. 1956a. The structure of lithium-magnesium solid solutions—I: Measurements on the Bragg reflections. *Acta metallurgica,* 4**,** 407-413.

HERBSTEIN, F. & AVERBACH, B. L. 1956b. The structure of lithium-magnesium solid solutions—II: Measurements of diffuse X-ray scattering. *Acta Metallurgica,* 4**,** 414-420.

HÖHNE, G. W. H., HEMMINGER, W. & FLAMMERSHEIM, H.-J. 1996. Theoretical Fundamentals of Differential Scanning Calorimeters. *Differential Scanning Calorimetry*. Springer.

HUA, T., AHLUWALIA, R., PENG, J.-K., KROMER, M., LASHER, S., MCKENNEY, K., LAW, K. & SINHA, J. 2011. Technical assessment of compressed hydrogen storage tank systems for automotive applications. *International Journal of Hydrogen Energy,* 36**,** 3037-3049.

HUANG, B., GINGL, F., FAUTH, F., HEWAT, A. & YVON, K. 1997. New tetragonal metal hydrides BaMg2TH8 (T= Ru, Os) containing octahedral [TH6] 4− complex anions and hydride anions. *Journal of alloys and compounds,* 248**,** 13-17.

HUANG, B., YVON, K. & FISCHER, P. 1992a. Ca4Mg4Fe3H22, a new quaternary transition metal hydride containing octahedral [FeH6] 4− complex anions. *Journal of alloys and compounds,* 190**,** 65-68.

HUANG, B., YVON, K. & FISCHER, P. 1992b. Strontium dimagnesium iron octahydride, SrMg2FeH8, containing octahedral [FeH6] 4-complex anions. *Journal of alloys and compounds,* 187**,** 227-232.

HUANG, B., YVON, K. & FISCHER, P. 1993. Synthesis, structure and thermal stability of Yb4Mg4Fe3H22. *Journal of alloys and compounds,* 197**,** 65-68.

HUANG, B., YVON, K. & FISCHER, P. 1995a. Ca4Mg4Co3H19 and Yb4Mg4Co3H19, containing orientationally disordered square-pyramidal [CoH5] 4− anions. *Journal of alloys and compounds,* 227**,** 116-120.

HUANG, B., YVON, K. & FISCHER, P. 1995b. New iron (II) complex metal hydrides with SrMg2FeH8 type structure. *Journal of alloys and compounds,* 227**,** 121-124.

HUGHES, L. J. 2016. *Hydrogen sorption properties of magnesium-based thin films.* University of Birmingham.

HUHN, P.-A., DORNHEIM, M., KLASSEN, T. & BORMANN, R. 2005. Thermal stability of nanocrystalline magnesium for hydrogen storage. *Journal of Alloys and Compounds,* 404**,** 499-502.

HUMPHRIES, T. D., MATSUO, M., LI, G. & ORIMO, S.-I. 2015a. Complex transition metal hydrides incorporating ionic hydrogen: thermal decomposition pathway of Na 2 Mg 2 FeH 8 and Na 2 Mg 2 RuH 8. *Physical Chemistry Chemical Physics,* 17**,** 8276-8282.

HUMPHRIES, T. D., TAKAGI, S., LI, G., MATSUO, M., SATO, T., SØRBY, M. H., DELEDDA, S., HAUBACK, B. C. & ORIMO, S.-I. 2015b. Complex transition metal hydrides incorporating ionic hydrogen: Synthesis and characterization of Na 2 Mg 2 FeH 8 and Na 2 Mg 2 RuH 8. *Journal of Alloys and Compounds,* 645**,** S347-S352.

HUOT, J., LIANG, G., BOILY, S., VAN NESTE, A. & SCHULZ, R. 1999. Structural study and hydrogen sorption kinetics of ball-milled magnesium hydride. *Journal of Alloys and Compounds,* 293–295**,** 495-500.

HUOT, J., LIANG, G. & SCHULZ, R. 2001. Mechanically alloyed metal hydride systems. *Applied Physics A: Materials Science & Processing,* 72**,** 187-195.

HUOT, J., LIANG, G. & SCHULZ, R. 2003. Magnesium-based nanocomposites chemical hydrides. *Journal of Alloys and Compounds,* 353**,** L12-L15.

HYDROPOL. 2017. *Hydrogen storage* [Online]. Available: https://hydropole.ch/en/hydrogen/storage/ [Accessed 20/03 2017].

ICEWIND. 2017. *Wind Power* [Online]. Available: http://icewind.is/en/wind-power/ [Accessed 15/08/2017].

ICSD. 2017. *ICSD Inorganic Chemical Database Service* [Online]. Available: http://icsd.cds.rsc.org/search/basic.xhtml;jsessionid=82761CD648F766CC9CA76BDA84933E21?cdsrdr=3 [Accessed 03/03/2017].

IKEDA, K., KATO, S., SHINZATO, Y., OKUDA, N., NAKAMORI, Y., KITANO, A., YUKAWA, H., MORINAGA, M. & ORIMO, S. 2007a. Thermodynamical stability and electronic structure of a perovskite-type hydride, NaMgH 3. *Journal of Alloys and Compounds,* 446**,** 162-165.

IKEDA, K., KOGURE, Y., NAKAMORI, Y. & ORIMO, S. 2005a. Reversible hydriding and dehydriding reactions of perovskite-type hydride NaMgH 3. *Scripta materialia,* 53**,** 319-322.

IKEDA, K., KOGURE, Y., NAKAMORI, Y. & ORIMO, S. 2007b. Formation region and hydrogen storage abilities of perovskite-type hydrides. *Progress in solid state chemistry,* 35**,** 329-337.

IKEDA, K., NAKAMORI, Y. & ORIMO, S. 2005b. Formation ability of the perovskite-type structure in Li x Na 1− x MgH 3 (x= 0, 0.5 and 1.0). *Acta materialia,* 53**,** 3453-3457.

IMAMURA, H., MASANARI, K., KUSUHARA, M., KATSUMOTO, H., SUMI, T. & SAKATA, Y. 2005. High hydrogen storage capacity of nanosized magnesium synthesized by high energy ball-milling. *Journal of Alloys and Compounds,* 386**,** 211-216.

JAIN, I., LAL, C. & JAIN, A. 2010a. Hydrogen storage in Mg: a most promising material. *International Journal of Hydrogen Energy,* 35**,** 5133-5144.

JAIN, I. P., LAL, C. & JAIN, A. 2010b. Hydrogen storage in Mg: A most promising material. *International Journal of Hydrogen Energy,* 35**,** 5133-5144.

JEHAN, M. & FRUCHART, D. 2013. McPhy-Energy Proposal for Solid Hydrogen Storage Materials and Systems.

JORGENSEN, S. W. 2011. Hydrogen storage tanks for vehicles: Recent progress and current status. *Current Opinion in Solid State and Materials Science,* 15**,** 39-43.

KILNER, J. A., SKINNER, S., IRVINE, S. & EDWARDS, P. 2012. *Functional materials for sustainable energy applications,* Elsevier.

KLASSEN, T., OELERICH, W. & BORMANN, R. Nanocrystalline Mg-based hydrides: Hydrogen storage for the zero-emission vehicle. Materials Science Forum, 2001. Transtec Publications; 1999, 603-608.

KOHNO, T., YOSHIDA, H., KAWASHIMA, F., INABA, T., SAKAI, I., YAMAMOTO, M. & KANDA, M. 2000. Hydrogen storage properties of new ternary system alloys: La 2 MgNi 9, La 5 Mg 2 Ni 23, La 3 MgNi 14. *Journal of Alloys and Compounds,* 311**,** L5-L7.

KOMIYA, K., MORISAKU, N., RONG, R., TAKAHASHI, Y., SHINZATO, Y., YUKAWA, H. & MORINAGA, M. 2008. Synthesis and decomposition of perovskite-type hydrides, MMgH 3 (M= Na, K, Rb). *Journal of Alloys and Compounds,* 453**,** 157-160.

KUZOVNIKOV, M., EFIMCHENKO, V., FILATOV, E., MAKSIMOV, A., TARTAKOVSKII, I. & RAMIREZ-CUESTA, A. 2013. Raman scattering study of α-MgH< sub> 2</sub> and γ-MgH< sub> 2</sub>. *Solid State Communications,* 154**,** 77-80.

LANGMI, H., WALTON, A., AL-MAMOURI, M., JOHNSON, S., BOOK, D., SPEIGHT, J., EDWARDS, P., GAMESON, I., ANDERSON, P. & HARRIS, I. 2003. Hydrogen adsorption in zeolites A, X, Y and RHO. *Journal of Alloys and Compounds,* 356**,** 710-715.

LI, D., ZHANG, T., YANG, S., TAO, Z. & CHEN, J. 2011. < i> Ab initio</i> investigation of structures, electronic and thermodynamic properties for Li–Mg–H ternary system. *Journal of Alloys and Compounds,* 509**,** 8228-8234.

LI, H.-W., KIKUCHI, K., NAKAMORI, Y., OHBA, N., MIWA, K., TOWATA, S. & ORIMO, S. 2008. Dehydriding and rehydriding processes of well-crystallized Mg (BH 4) 2 accompanying with formation of intermediate compounds. *Acta Materialia,* 56**,** 1342-1347.

LIANG, G., HUOT, J., BOILY, S., VAN NESTE, A. & SCHULZ, R. 1999. Catalytic effect of transition metals on hydrogen sorption in nanocrystalline ball milled MgH 2–Tm (Tm= Ti, V, Mn, Fe and Ni) systems. *Journal of Alloys and Compounds,* 292**,** 247-252.

LIU, C. & RAO, Z. 2017. Challenges in various thermal energy storage technologies. *Science Bulletin,* 62**,** 231-233.

LIU, X., ASANO, K., TERASHITA, N. & AKIBA, E. 2009. Hydrogenation of C14 Laves phase alloy: CaLi 2. *International journal of hydrogen Energy,* 34**,** 1472-1475.

LU, J., CHOI, Y. J., FANG, Z. Z., SOHN, H. Y. & RÖNNEBRO, E. 2009. Hydrogen storage properties of nanosized MgH2− 0.1 TiH2 prepared by ultrahigh-energy− high-pressure milling. *Journal of the American Chemical Society,* 131**,** 15843-15852.

MARTIN, M., GOMMEL, C., BORKHART, C. & FROMM, E. 1996. Absorption and desorption kinetics of hydrogen storage alloys. *Journal of Alloys and Compounds,* 238**,** 193-201.

MARTÍNEZ-CORONADO, R., SÁNCHEZ-BENÍTEZ, J., RETUERTO, M., FERNÁNDEZ-DÍAZ, M. & ALONSO, J. 2012. High-pressure synthesis of Na 1− x Li x MgH 3 perovskite hydrides. *Journal of Alloys and Compounds,* 522**,** 101-105.

MATAR, S. F., NAKHL, M., AL ALAM, A. F., ZAKHOUR, M. & OUAÏNI, N. 2011. Ab initio investigations of the perovskite and K 2 NiF 4 phases in the Cs–Ca–H system. *Solid State Sciences,* 13**,** 569-573.

MATHESON, R. 2014. *High-flying turbine produces more power* [Online]. Available: http://news.mit.edu/2014/high-flying-turbine-produces-more-power-0515 [Accessed 23/03/2017].

MAURON, P., BUCHTER, F., FRIEDRICHS, O., REMHOF, A., BIELMANN, M., ZWICKY, C. N. & ZÜTTEL, A. 2008. Stability and reversibility of LiBH4. *The Journal of Physical Chemistry B,* 112**,** 906-910.

MCPHY. *Solid Hydrogen Storage* [Online]. Available: http://www.mcphy.com/en/products/solid-hydrogen-storage/ [Accessed 02/03/2017].

MEDELLÍN, A. M. 2006. El hidrógeno y la energía.

MORIWAKI, T., AKAHAMA, Y., KAWAMURA, H., NAKANO, S. & TAKEMURA, K. 2006. Structural phase transition of rutile-type MgH2 at high pressures. *Journal of the Physical Society of Japan,* 75**,** 074603-074603.

NAKAMORI, Y., LI, H.-W., MATSUO, M., MIWA, K., TOWATA, S. & ORIMO, S. 2008. Development of metal borohydrides for hydrogen storage. *Journal of Physics and Chemistry of Solids,* 69**,** 2292-2296.

NAYAK, V. & VERMA, U. 2016. Phase transition and optoelectronic properties of MgH2. *Phase Transitions,* 89**,** 437-447.

NAYEB-HASHEMI, A., CLARK, J. & PELTON, A. 1984. The Li-Mg (lithium-magnesium) system. *Journal of Phase Equilibria,* 5**,** 365-374.

NESPER, R. & MILLER, G. J. 1993. A covalent view of chemical bonding in Laves phases CaLixAl2− x. *Journal of alloys and compounds,* 197**,** 109-121.

NOBUKI, T., CHIBA, M. & KUJI, T. 2007. Synthesis of CaMg-based bcc alloys and their hydrogenation properties. *Journal of Alloys and Compounds,* 446**,** 152-156.

NOMURA, K., ISHIDO, Y. & ONO, S. 1978. Newly synthesized metal hydride MgCaH 3.72. *Yogyo-Kyokai-Shi,* 86**,** 67-72.

NORITAKE, T., AOKI, M., TOWATA, S., SENO, Y., HIROSE, Y., NISHIBORI, E., TAKATA, M. & SAKATA, M. 2002. Chemical bonding of hydrogen in MgH 2. *Applied physics letters,* 81**,** 2008-2010.

OELERICH, W., KLASSEN, T. & BORMANN, R. 2001. Comparison of the catalytic effects of V, V 2 O 5, VN, and VC on the hydrogen sorption of nanocrystalline Mg. *Journal of Alloys and Compounds,* 322**,** L5-L9.

ORIMO, S.-I., NAKAMORI, Y., ELISEO, J. R., ZÜTTEL, A. & JENSEN, C. M. 2007. Complex hydrides for hydrogen storage. *Chemical Reviews,* 107**,** 4111-4132.

PACESILA, M., BURCEA, S. G. & COLESCA, S. E. 2016. Analysis of renewable energies in European Union. *Renewable and Sustainable Energy Reviews,* 56**,** 156-170.

PADRÓ, C. E. G. & PUTSCHE, V. 1999. *Survey of the economics of hydrogen technologies*.

PALMER, D. 2008. Hydrogen in the Universe. *NASA. Retrieved***,** 02-05.

PARKER, M. 2014. *Geothermal Power Plants* [Online]. Available: https://theconversation.com/drilling-surprise-opens-door-to-volcano-powered-electricity-22515 [Accessed 28/03/2017].

PARKER, S. F., WILLIAMS, K. P., BORTZ, M. & YVON, K. 1997. Inelastic neutron scattering, infrared, and Raman spectroscopic studies of Mg2FeH6 and Mg2FeD6. *Inorganic Chemistry,* 36**,** 5218-5221.

PASKEVICIUS, M., SHEPPARD, D. A. & BUCKLEY, C. E. 2010. Thermodynamic changes in mechanochemically synthesized magnesium hydride nanoparticles. *Journal of the American chemical Society,* 132**,** 5077-5083.

PESCHKA, W. & PESCHKA, W. 1992. Hydrogen Liquefaction. *Liquid Hydrogen: Fuel of the Future***,** 17-70.

PFROMMER, B., ELSÄSSER, C. & FÄHNLE, M. 1994. Possibility of Li-Mg and Al-Mg hydrides being metallic. *Physical Review B,* 50**,** 5089.

PICKERING, L. 2014. *Ti-V-Mn based metal hydrides for hydrogen storage and compression applications.* University of Birmingham.

PINKERTON, F. & MEYER, M. 2008. Reversible hydrogen storage in the lithium borohydride—calcium hydride coupled system. *Journal of Alloys and Compounds,* 464**,** L1-L4.

PORTO, S., FLEURY, P. & DAMEN, T. 1967. Raman Spectra of Ti O 2, Mg F 2, Zn F 2, Fe F 2, and Mn F 2. *Physical Review,* 154**,** 522.

POTTMAIER, D., PINATEL, E. R., VITILLO, J. G., GARRONI, S., ORLOVA, M., BARÓ, M. D., VAUGHAN, G. B., FICHTNER, M., LOHSTROH, W. & BARICCO, M. 2011. Structure and thermodynamic properties of the NaMgH3 perovskite: a comprehensive study. *Chemistry of Materials,* 23**,** 2317-2326.

PRABHUKHOT PRACHI, R. & WAGH MAHESH, M. 2016. A Review on Solid State Hydrogen Storage Material. *Advances in Energy and Power,* 4**,** 11-22.

REARDON, H. 2014. *Synthesis, structure and characterisation of novel lightweight energy materials based on group I & II metal compounds.* University of Glasgow.

REARDON, H., MAZUR, N. & GREGORY, D. H. 2013. Facile synthesis of nanosized sodium magnesium hydride, NaMgH 3. *Progress in Natural Science: Materials International,* 23**,** 343-350.

REED, D. & BOOK, D. 2011. Recent applications of Raman spectroscopy to the study of complex hydrides for hydrogen storage. *Current Opinion in Solid State and Materials Science,* 15**,** 62-72.

REED, D. T. 2010. *An investigation into the synthesis and characterisation of metal borohydrides for hydrogen storage*. PhD, University of Birmingham

REILLY JR, J. J. & WISWALL JR, R. H. 1968. Reaction of hydrogen with alloys of magnesium and nickel and the formation of Mg2NiH4. *Inorganic Chemistry,* 7**,** 2254-2256.

REISER, A., BOGDANOVIĆ, B. & SCHLICHTE, K. 2000. The application of Mg-based metal-hydrides as heat energy storage systems. *International Journal of Hydrogen Energy,* 25**,** 425-430.

RENISHAW. 2016. *Renishaw-Raman spectroscopy* [Online]. Available: http://www.renishaw.com/en/raman-spectroscopy--6150 [Accessed 05/04/2017].

REULE, H., HIRSCHER, M., WEIßHARDT, A. & KRONMÜLLER, H. 2000. Hydrogen desorption properties of mechanically alloyed MgH2 composite materials. *Journal of Alloys and Compounds,* 305**,** 246-252.

RÖNNEBRO, E., NORÉUS, D., KADIR, K., REISER, A. & BOGDANOVIC, B. 2000. Investigation of the perovskite related structures of NaMgH 3, NaMgF 3 and Na 3 AlH 6. *Journal of alloys and compounds,* 299**,** 101-106.

ROSI, N. L., ECKERT, J., EDDAOUDI, M., VODAK, D. T., KIM, J., O'KEEFFE, M. & YAGHI, O. M. 2003. Hydrogen storage in microporous metal-organic frameworks. *Science,* 300**,** 1127-1129.

SAKINTUNA, B., LAMARI-DARKRIM, F. & HIRSCHER, M. 2007. Metal hydride materials for solid hydrogen storage: a review. *International Journal of Hydrogen Energy,* 32**,** 1121-1140.

SAN-MARTIN, A. & MANCHESTER, F. 1987. The H− Mg (Hydrogen-Magnesium) system. *Journal of phase equilibria,* 8**,** 431-437.

SANDROCK, G. & BOWMAN, R. C. 2003. Gas-based hydride applications: recent progress and future needs. *Journal of Alloys and Compounds,* 356**,** 794-799.

SANTISTEBAN, J., CUELLO, G., DAWIDOWSKI, J., FAINSTEIN, A., PERETTI, H., IVANOV, A. & BERMEJO, F. 2000. Vibrational spectrum of magnesium hydride. *Physical Review B,* 62**,** 37.

SARTORI, S., LÉON, A., ZABARA, O., MULLER, J., FICHTNER, M. & HAUBACK, B. C. 2009. Studies of mixed hydrides based on Mg and Ca by reactive ball milling. *Journal of Alloys and Compounds,* 476**,** 639-643.

SCHLAPBACH, L. & ZUTTEL, A. 2001. Hydrogen-storage materials for mobile applications. *Nature,* 414**,** 353-8.

SCHLAPBACH, L. & ZÜTTEL, A. 2001. Hydrogen-storage materials for mobile applications. *Nature*, 414**,** 353-358.

SCHMITTINGER, W. & VAHIDI, A. 2008. A review of the main parameters influencing long-term performance and durability of PEM fuel cells. *Journal of power sources,* 180**,** 1-14.

SCHULZ, R., BOILY, S., ZALUSKI, L., ZALUSKA, A., TESSIER, P. & STROM OLSEN, J. 1995. Nanocrystalline materials for hydrogen storage. Technomic Publishing Co., Lancaster, PA (United States).

SCHULZ, R., HUOT, J., LIANG, G., BOILY, S., LALANDE, G., DENIS, M. & DODELET, J. 1999. Recent developments in the applications of nanocrystalline materials to hydrogen technologies. *Materials Science and Engineering: A,* 267**,** 240-245.

SEN, S. & GANGULY, S. 2016. Opportunities, barriers and issues with renewable energy development–A discussion. *Renewable and Sustainable Energy Reviews*.

SHEPPARD, D. A., PASKEVICIUS, M. & BUCKLEY, C. E. 2011. Thermodynamics of hydrogen desorption from NaMgH3 and its application as a solar heat storage medium. *Chemistry of Materials,* 23**,** 4298-4300.

SHEVLIN, S. & GUO, Z. 2013. MgH2 dehydrogenation thermodynamics: nanostructuring and transition metal doping. *The Journal of Physical Chemistry C,* 117**,** 10883-10891.

SHI, Z., LIU, M., NAIK, D. & GOLE, J. L. 2001. Electrochemical properties of Li–Mg alloy electrodes for lithium batteries. *Journal of Power Sources,* 92**,** 70-80.

SMITH, K. C., FISHER, T. S., WAGHMARE, U. V. & GRAU-CRESPO, R. 2010. Dopant-vacancy binding effects in Li-doped magnesium hydride. *Physical Review B,* 82**,** 134109.

SNELLINGS, R., MACHIELS, L., MERTENS, G. & ELSEN, J. 2010. Rietveld refinement strategy for quantitative phase analysis of partially amorphous zeolitized tuffaceous rocks. *Geologica Belgica*.

SONG, G. & KRAL, M. 2005. Characterization of cast Mg–Li–Ca alloys. *Materials Characterization,* 54**,** 279-286.

STOLLE, A. 2014. *Ball milling towards green synthesis: applications, projects, challenges*, Royal Society of Chemistry.

SURYANARAYANA, C. 2001a. Mechanical alloying and milling. *Progress in materials science,* 46**,** 1-184.

SURYANARAYANA, C. 2001b. Mechanical alloying and milling. *Progress in Materials Science,* 46**,** 1-184.

TAKAGI, S., HUMPHRIES, T. D., MIWA, K. & ORIMO, S.-I. 2014. Enhanced tunability of thermodynamic stability of complex hydrides by the incorporation of H–anions. *Applied Physics Letters,* 104**,** 203901.

TERASHITA, N., KOBAYASHI, K., SASAI, T. & AKIBA, E. 2001. Structural and hydriding properties of (Mg 1− x Ca x) Ni 2 Laves phase alloys. *Journal of alloys and compounds,* 327**,** 275-280.

TESSIER, J.-P., PALAU, P., HUOT, J., SCHULZ, R. & GUAY, D. 2004. Hydrogen production and crystal structure of ball-milled MgH 2–Ca and MgH 2–CaH 2 mixtures. *Journal of alloys and compounds,* 376**,** 180-185.

THOMAS, K. M. 2007. Hydrogen adsorption and storage on porous materials. *Catalysis today,* 120**,** 389-398.

TOPAS, B. 2017. *BRUKER. TOPAS Software n.d.* [Online]. Available: https://www.bruker.com/products/x-ray-diffraction-and-elemental-analysis/x-ray-diffraction/xrd-software/topas.html [Accessed 10/10/2016].

TÖPLER, J. 2016. Hydrogen as energy-storage-medium and fuel-A strong partner of renewable energies. *Renewable Energy and Environmental Sustainability,* 1**,** 31.

TOYOTA. 2015. *Toyota Mirai technical specifications* [Online]. Available: http://blog.toyota.co.uk/toyota-mirai-technical-specifications-vs-fchv-adv [Accessed 24/03/2017].

TSUSHIO, Y., ENOKI, H. & AKIBA, E. 1998. Hydrogenation properties of MgNi 0.86 M1 0.03 (M1= Cr, Fe, Co, Mn) alloys. *Journal of alloys and compounds,* 281**,** 301-305.

TURNER, J. A. 2004. Sustainable hydrogen production. *Science,* 305**,** 972-974.

UMEGAKI, T., YAN, J.-M., ZHANG, X.-B., SHIOYAMA, H., KURIYAMA, N. & XU, Q. 2009. Boron-and nitrogen-based chemical hydrogen storage materials. *international journal of hydrogen energy,* 34**,** 2303-2311.

US DEPARTMENT OF ENERGY, D. 2000. Handbook, Fuel Cell National Energy Technology Laboratory, B. T books.

VAJEESTON, P., RAVINDRAN, P. & FJELLVÅG, H. 2010. Structural investigation and thermodynamical properties of alkali calcium trihydrides. *The Journal of chemical physics,* 132**,** 114504.

VAJEESTON, P., RAVINDRAN, P., HAUBACK, B., FJELLVÅG, H., KJEKSHUS, A., FURUSETH, S. & HANFLAND, M. 2006. Structural stability and pressure-induced phase transitions in MgH 2. *Physical Review B,* 73**,** 224102.

VAJEESTON, P., RAVINDRAN, P., KJEKSHUS, A. & FJELLVÅG, H. 2008. First-principles investigations of the MMgH< sub> 3</sub>(M= Li, Na, K, Rb, Cs) series. *Journal of Alloys and Compounds,* 450**,** 327-337.

VAJO, J. J., SALGUERO, T. T., GROSS, A. F., SKEITH, S. L. & OLSON, G. L. 2007. Thermodynamic destabilization and reaction kinetics in light metal hydride systems. *Journal of Alloys and Compounds,* 446**,** 409-414.

VARIN, R., CZUJKO, T. & WRONSKI, Z. 2006. Particle size, grain size and γ-MgH2 effects on the desorption properties of nanocrystalline commercial magnesium hydride processed by controlled mechanical milling. *Nanotechnology,* 17**,** 3856.

VARIN, R. A., ZBRONIEC, L., POLANSKI, M. & BYSTRZYCKI, J. 2010. A review of recent advances on the effects of microstructural refinement and nano-catalytic additives on the hydrogen storage properties of metal and complex hydrides. *Energies,* 4**,** 1-25.

WALKER, G. 2008. *Solid-state hydrogen storage: materials and chemistry*, Elsevier.

WANG, Z.-M., LI, J.-J., TAO, S., DENG, J.-Q., ZHOU, H. & YAO, Q. 2016. Structure, thermal analysis and dehydriding kinetic properties of Na 1− x Li x MgH 3 hydrides. *Journal of Alloys and Compounds,* 660**,** 402-406.

WAVEMETRICS. 2017. *WaveMetrics-Igor Pro* [Online]. Available: https://www.wavemetrics.com/products/igorpro/igorpro.htm [Accessed 15/09/2016].

WESTERWAAL, R. & HAIJE, W. 2008. Evaluation solid-state hydrogen storage systems. *ECN Hydrogen and Clean Fossil Fuels*.

WIKIPEDIA. 2015. *Growth of photovoltaics* [Online]. Available: https://en.wikipedia.org/wiki/Growth_of_photovoltaics [Accessed 28/03/2017].

WOLF, J. 2010. Liquid hydrogen technology for vehicles. *Handbook of Fuel Cells*.

WONG-FOY, A. G., MATZGER, A. J. & YAGHI, O. M. 2006. Exceptional H2 saturation uptake in microporous metal− organic frameworks. *Journal of the American Chemical Society,* 128**,** 3494-3495.

WU, H., ZHOU, W., UDOVIC, T. J., RUSH, J. J. & YILDIRIM, T. 2008. Crystal chemistry of perovskite-type hydride NaMgH3: implications for hydrogen storage. *Chemistry of Materials,* 20**,** 2335-2342.

WURSTER, R. 2002. Pathways to a Hydrogen Refuelling Infrastructure Between today and 2020–Time Scale& Investment Costs. *PPP, Brussels***,** 11-12.

XIAO, X.-B., TANG, B.-Y., LIAO, S.-Q., PENG, L.-M. & DING, W.-J. 2009. Thermodynamic and electronic properties of quaternary hydrides Li x Na 1− x MgH 3. *Journal of Alloys and Compounds,* 474**,** 522-526.

XIAO, Y., WU, C., WU, H. & CHEN, Y. 2011. Hydrogen generation by CaH 2-induced hydrolysis of Mg 17 Al 12 hydride. *international journal of hydrogen energy,* 36**,** 15698-15703.

YUAN, P. P., LIU, B. H. & LI, Z. P. 2011. A comparative study of LiBH 4-based composites with metal hydrides and fluorides for hydrogen storage. *international journal of hydrogen energy,* 36**,** 15266-15272.

YÜRÜM, Y., TARALP, A. & VEZIROGLU, T. N. 2009. Storage of hydrogen in nanostructured carbon materials. *International journal of hydrogen energy,* 34**,** 3784-3798.

YVON, K. & BERTHEVILLE, B. 2006. Magnesium based ternary metal hydrides containing alkali and alkaline-earth elements. *Journal of alloys and compounds,* 425**,** 101-108.

ZALUSKA, A., ZALUSKI, L. & STRÖM-OLSEN, J. O. 2001. Structure, catalysis and atomic reactions on the nano-scale: a systematic approach to metal hydrides for hydrogen storage. *Applied Physics A,* 72**,** 157-165.

ZALUSKA, A., ZALUSKI, L. & STRÖM–OLSEN, J. O. 1999. Nanocrystalline magnesium for hydrogen storage. *Journal of Alloys and Compounds,* 288**,** 217-225.

ZALUSKI, L., ZALUSKA, A. & STRÖM-OLSEN, J. O. 1997. Nanocrystalline metal hydrides. *Journal of Alloys and Compounds,* 253–254**,** 70-79.

ZHANG, Q. & ZHAO, G. 2007. Effects of Mg content on the crystal structures and hydrogenation behavior of (Ca 1− x Mg x) Al 2 alloys. *Materials chemistry and physics,* 104**,** 373-376.

ZHAO-KARGER, Z., HU, J., ROTH, A., WANG, D., KÜBEL, C., LOHSTROH, W. & FICHTNER, M. 2010. Altered thermodynamic and kinetic properties of MgH 2 infiltrated in microporous scaffold. *Chemical Communications,* 46**,** 8353-8355.

ZHU, L., KIM, D., KIM, H., MASEL, R. & SHANNON, M. 2008. Hydrogen generation from hydrides in millimeter scale reactors for micro proton exchange membrane fuel cell applications. *Journal of Power Sources,* 185**,** 1334-1339.

ZHU, M., WANG, H., OUYANG, L. Z. & ZENG, M. 2006a. Composite structure and hydrogen storage properties in Mg-base alloys. *International journal of hydrogen energy,* 31**,** 251-257.

ZHU, M., WANG, H., OUYANG, L. Z. & ZENG, M. Q. 2006b. Composite structure and hydrogen storage properties in Mg-base alloys. *International Journal of Hydrogen Energy,* 31**,** 251-257.

ZÜTTEL, A. 2003. Materials for hydrogen storage. *Materials today,* 6**,** 24-33.

ZÜTTEL, A. 2004. Hydrogen storage methods. *Naturwissenschaften,* 91**,** 157-172.

ZÜTTEL, A., BORGSCHULTE, A. & SCHLAPBACH, L. 2011. *Hydrogen as a future energy carrier,* John Wiley & Sons.

ZÜTTEL, A., REMHOF, A., BORGSCHULTE, A. & FRIEDRICHS, O. 2010. Hydrogen: the future energy carrier. *Philosophical Transactions of the Royal Society of London A: Mathematical, Physical and Engineering Sciences,* 368**,** 3329-3342.